Modeling and experimental identification of vibrating structures: localized and distributed nonlinearities

Dario Anastasio

* * * * * *

Supervisor
Prof. Stefano Marchesiello

Doctoral Examination Committee
Prof. Gianluca Gatti, Università della Calabria, Italia
Prof. Jean-Claude Golinval, University of Liège, Belgium

Politecnico di Torino
April, 2020

I hereby declare that, the contents and organisation of this dissertation constitute my own original work and does not compromise in any way the rights of third parties, including those relating to the security of personal data.

Dario Anastasio
Turin, April 6, 2020

Acknowledgments

First, I would like to express my sincere gratitude to my tutor Prof. Stefano Marchesiello for the trust and the constant support provided since my master's degree. Your experience and advices have been of fundamental importance, and your passion for the subject truly inspiring.

I would also like to thank Prof. Luigi Garibaldi and Prof. Alessandro Fasana for your assistance during these years and for involving me in your academic and research activities,

Prof. Gaëtan Kerschen, Dr. Jean-Philippe Noël and all the members of the Space Structures and System Laboratory of University of Liège for welcoming me during my staying there and for your support and fresh ideas,

Prof. Gianluca Gatti and Prof. Jean-Claude Golinval for your constructive revision of this thesis.

The PhD is a long journey and it wouldn't have been such a beautiful experience without my friends and colleagues: thanks for all the moments together, the *gourmet* lunches at mensa, the laughs and the fruitful discussions.

Finally, thanks Elisa for having such a positive impact on my life, and thanks to my family: you are the most precious gift even at hundreds of kilometers of distance.

Cheers,
Dario

There is a theory which states that if ever anyone discovers exactly what the Universe is for and why it is here, it will instantly disappear and be replaced by something even more bizarre and inexplicable.

There is another theory which states that this has already happened.

Douglas Adams,
The Restaurant at the End of the Universe

Summary

Nonlinearity is a frequent companion of engineering structures: it occurs anytime the outputs of a system cannot be expressed in terms of linear superposition of the inputs, a rare circumstance in the real world. Despite the long tradition of studies in nonlinear systems theory, the transposition of such knowledge to the structural engineering world is quite recent and has gained more importance in the very last decades, to address the ever-increasing demand of improved performances driven by industrial needs.

In this framework, nonlinear features often represent obstacles or unwanted effects that might compromise the behavior of the engineering structures, or even bring dangerous consequences. For this reason, it is important to be able to recognize and characterize them, both from modeling and experimental point of views. The latter case can be implemented via nonlinear system identification techniques, that allow the extraction of information about the dynamical behavior of a structure from the measured data. Fairly, this is just a part of the story, as a structure can be also designed to behave nonlinearly, to take advantage of some nonlinear effects that would not exist in the linear regime. This is for instance the case of negative stiffness absorbers, composites, nonlinear (meta)materials or slender elements.

This doctoral dissertation attempts to develop robust techniques for nonlinear vibrating structures, in order to give a contribution to the current unsolved challenges in the field, by identifying nonlinear features from real structures. Complex nonlinear dynamical phenomena are observed and modeled, considering both scaled-laboratory and real-life applications. In particular, the techniques presented in this thesis are based on the nonlinear subspace identification (NSI) method. NSI is meant to extract information about the nonlinear behavior of structures directly from the measured data, including the classical modal parameters (natural frequencies, damping ratios, mode shapes), plus details about the nonlinearity itself. The method was originally designed to work with input-output data of systems with localized

nonlinearities, but the extension to output-only free-decay measurements is presented, as well as to the case of distributed nonlinearities. The latter in particular has a wide range of applications, from wind turbines to aerospace vehicles.

The developed techniques are compared with the ones available in the literature, and numerical examples are very often proposed to assess the presented strategies. Eventually, the final application is related to the railway field and concerns the interaction between pantograph and catenary for high speed trains. The focus here is on improving the performances of the system by designing ad-hoc nonlinear damping elements. Therefore, the design process is presented, from the nonlinear modeling of the structure via a custom FE implementation, to the experimental testing and the nonlinear system identification with NSI.

Results show a high degree of confidence in the adopted methodologies and pave the way to the application of nonlinear tools such as NSI to the industrial world.

Contents

List of figures

List of tables

List of acronyms

ARMA	Auto-regressive moving average
BLA	Best linear approximation
CRP	Conditioned reverse path
DOF	Degree of freedom
FEM	Finite element method
FNSI	Frequency-domain nonlinear subspace identification
FRF	Frequency response function
HBM	Harmonic balance method
HSR	High speed rail
LLE	Largest Lyapuv exponent
LNM	Linear normal mode
LS	Least square
MAC	Modal assurance criterion
NARMAX	Nonlinear ARMA with exogenous input
NFRC	Nonlinear frequency response curve
NIFO	Nonlinear identification through feedback of the outputs
NNM	Nonlinear normal mode
NPR	Nonlinear phase resonance
NSI	Nonlinear subspace identification
OCL	Overhead contact line
PNLSS	Polynomial nonlinear state-space
RFS	Restoring force surface
RMS	Root mean square
RP	Reverse path
SI	Subspace identification
SVD	Singular value decomposition
TNSI	Time-domain nonlinear subspace identification
ULS	Underlying-linear system

Notes on the nomenclature

The following nomenclature rules are adopted, unless specified otherwise:

- Matrices and vectors are written in boldface;
- Matrices are labeled with capital letters, vectors with small letters;
- Signals in the time domain are labeled with small letters and their frequency-domain counterparts (spectra or FFTs) with the corresponding capital letters.
- The ith mass of a discrete system is generally referred to as "DOF i" (degree-of-freedom).

The following symbols are commonly adopted:

$\boldsymbol{M}$	Mass matrix
$\boldsymbol{K}$	Stiffness matrix
$\boldsymbol{C_v}$	Viscous damping matrix
t	Time variable
ω	Frequency variable
$\boldsymbol{f}$	Forcing input
$\boldsymbol{G}$	Frequency response function (FRF) matrix
ω_r	Natural frequency of the rth mode
ζ_r	Damping ratio of the rth mode
$\boldsymbol{\psi}_r$	Unit-scaled mode shape of the rth mode
m_r	Modal mass of the rth mode
α_r	Scaling factor of the rth mode
μ_j	Coefficient of the jth nonlinearity
ξ_j	Nonlinear basis function of the jth nonlinearity

$\boldsymbol{L}_j$ Location vector of the jth nonlinearity

$\bullet^{\dagger}$ Pseudo-inverse matrix

$\bullet^{T}$ Transposed matrix

$\bullet^{H}$ Hermitian transposed matrix

$\bullet^{id}$ Superscript for "identified"

$\bullet^{e}$ Superscript for "extended"

$\bullet^{nl}$ Superscript for "nonlinear"

Specific symbols are defined in each chapter.

Chapter 1

Introduction

All the world is a nonlinear system
He linearised to the right
He linearised to the left
Till nothing was right
And nothing was left

S.A. Billings, University of Sheffield

Nonlinear phenomena can be found in nearly every scientific area, from physics to biology, therefore the study of their mathematical representation has intrigued scientists for a long time. The nonlinear dynamics theory can be fairly traced back to the late 1800s with the intuitions of H. Poincaré, who was the first to glimpse the possibility of *chaos* [1].

Regardless of such a long tradition, the practical transposition of nonlinear features to structural dynamics is pretty recent and has gained more importance during the very last decades, as a consequence of the continual industrial interest in improving design and performances of structures. This very often brings the need of characterizing nonlinear features, as the structure may involve, to cite a few: flexible regimes, where large-amplitude motions are likely to occur; high speeds, where nonlinear fluid-structure interaction is significant; tight tolerances, with contact and friction dynamics [2].

Although nonlinearity does not necessarily imply *complexity*, most real systems do exhibit some nonlinear feature causing complex dynamics, difficult to handle and conceivably associated to undesired or unsafe effects. For instance, the occurrence of limit cycles in an aircraft, i.e. large amplitude self-sustained motions, seriously compromises its fatigue life [3]; looseness of joints may result in clearances, friction, and possibly lead to failure; large-amplitude oscillations in cable-based structures (cable-stayed bridges, overhead power lines,…) couple different planes of motions, resulting in galloping phenomena [2]. Nonlinearity is also of use to the diagnosis of faults in structures, as it is very likely that the occurrence of a fault in an initially-linear structure will result in a nonlinear behavior [3,4]. These few examples confirm the importance of developing reliable tools to recognize and characterize nonlinearity, aiming to avoid such unwanted effects. A way to do this is by performing the *nonlinear system identification* of the structure under test, that is the extraction of a nonlinear model from the measured data. The identified model should in principle be related to components and behaviors of the system under study, to reproduce its (nonlinear) dynamical characteristics and, wherever possible, to reveal the *rules* that represent the system [5]. Nonlinearity can also be a precise design choice, to benefit of the wide range of opportunities nonlinear features might bring – opportunities that allow to expand the performances of the designed structure and that simply do not exist in the linear world. Of course, this carries the need of nonlinear modelling techniques, which might be dispendious in terms of complexity, time and resources.

It should be highlighted though that there exists no unique approach in nonlinear design and identification, as the methods developed so far are generally valid for a subset of nonlinear phenomena or systems. On the contrary, linear systems theory is well consolidated, with the advantages of commercial tools and shared techniques. It is therefore necessary to carefully evaluate the need of a nonlinear study: as a matter of fact, cases exist where a linear or *linearized* model may be enough [6]. Linearization techniques are well known nowadays [7], although it should be kept in mind that nonlinearity might be still around the corner, as a linearized model is generally valid only for small deviations from a given working position. The decision of using (or not) nonlinear models should be therefore made on a single-case basis, depending on the purposes of the model itself and on the structure under study. For this decision to be consciously taken, one should be aware of two factors:

- The possible sources of nonlinearity in the considered system;
- The possible effects of a nonlinear behavior, so as to be able to recognize it.

As for the first point, nonlinearity can originate from several sources, and the following ones happen to be very common in mechanical structures [8,9]:

- Geometrical nonlinearity: it arises when a structure undergoes large-amplitude vibrations. For instance, a test rig involving a beam with geometrical nonlinearity is analyzed in [10–12]. Large deformations of flexible elastic continua also belong to this category, as they result in a distributed nonlinear strain-displacement relation. A practical example of this kind of nonlinear behavior will be studied in Chapter 5.
- Inertia nonlinearity: it may be caused by the presence of concentrated or distributed masses, or by Coriolis acceleration in motions of bodies moving relative to rotating frames. In [13] the effects of longitudinal and rotary nonlinear inertia forces are investigated on a hinged beam, retrieving a predominant softening behavior. More recently, nonlinear formulations involving inertia nonlinearities have been proposed for cantilever carbon nanotubes [14] and energy harvesters [15].
- Material nonlinearity: it occurs when the stresses are nonlinear functions of the strains, such as in foams [16] and rubbers [17].
- Nonlinear boundary conditions: these are very common in real-life structures, such as impacts in loose joints [18] and clearances [19].
- Damping dissipation: the classical viscous damping assumption is not necessarily the most appropriate representation of the physical dissipation phenomena, although it is surely convenient from a mathematical point of view. Indeed, nonlinear dissipation models are quite difficult to estimate, and the two most important examples are hysteretic damping and dry friction [3].

The effects of these nonlinear sources are wide, including: non-invariance of the frequency response functions (FRFs), possibility of multiple solutions, bifurcations, new resonances, loss of periodicity, chaos, … [1,20]. Many of these phenomena will be observed and discussed throughout the thesis, and frequently they will be used to characterize the dynamics of the structure under test and detect a possible nonlinear behavior.

1.1. Thesis objectives and outline

The objective of this doctoral dissertation is to develop robust and reliable techniques for nonlinear vibrating structures. Complex nonlinear dynamical phenomena are studied and experimentally characterized, involving localized and distributed nonlinearities, as well as bifurcations and chaos. The developed methods have the purpose of giving a contribution to the current unsolved challenges in the field, such as the identification of distributed nonlinearities and the identification of nonlinear structures from output-only

measurements. The final application is the design and the experimental identification of a nonlinear improved dropper for high-speed railway overhead contact lines.

The present manuscript is organized as follows:

In Chapter 2 an overview of nonlinear structural dynamics is presented. Numerical examples are adopted to introduce and discuss classical nonlinear phenomena: harmonic distortions, nonlinear frequency response curves, stability issues, bifurcations and chaos. Eventually, the effects of different kind of excitations to nonlinear systems are investigated, with emphasis on random and multisine signals.

In Chapter 3 the nonlinear system identification of mechanical structures is introduced, starting from a literature review about the major contributions in the field. The nonlinear subspace identification (NSI) method is presented in detail, as it will be adopted and improved throughout the thesis. A demonstrative experimental application with a clearance nonlinearity is also proposed.

In Chapter 4 a novel technique to perform nonlinear system identification with output-only free-decay measurements is presented, called Free-decay-NSI. The methodology is based on NSI in combination with a mass change technique, and it is first tested on a numerical example with Coulomb friction. An experimental test rig is eventually proposed, involving a scaled five-levels building with a polynomial nonlinearity on the top floor.

In Chapter 5 the problem of identifying a distributed nonlinear behavior is faced and a strategy proposed. The technique is tested on a slender clamped-clamped beam subjected to large-amplitude vibrations, which is first modelled using a nonlinear modal model. The study and the experimental tests were carried out while visiting Prof. Gaetan Kerschen and his research group at the Space Structures and Systems Laboratory of the University of Liège, Belgium. The proposed identification technique, called Modal-NSI, is compared with a non-parametric method named Polynomial Nonlinear State-Space (PNLSS).

In Chapter 6 the design and experimental identification of a nonlinear damping system for railway overhead contact lines is presented. The study was carried out in collaboration with Fratelli Bertolotti S.p.A. and Rete Ferroviaria Italiana. The techniques seen in the previous chapters are here adopted to validate the design choices, comparing experimental tests with numerical outcomes. Nonlinear system identification is performed to extract the model parameters from the measured data, where typical nonlinear phenomena are observed: jumps, harmonic distortions and chaotic behavior. Eventually, the designed model is updated on the base of the experimental identification to build the final prototype of the dropper.

In Chapter 7 conclusions are finally drawn, together with the main contributions of this doctoral thesis and the directions for future research.

Chapter 2

Nonlinear dynamics in structures: an overview

2.1. Introduction

As stated in the first chapter, the study of the dynamical behavior of nonlinear systems has a long story. It is not the purpose of this thesis to give an exhaustive review of nonlinear systems theory, as it would be a far too vast subject, but the reader can refer to the books of S. Strogatz [1] and D.W. Jordan [21] for a comprehensive mathematical outlook on nonlinear dynamical phenomena. Instead, an illustration of the classical symptoms of nonlinearity will be covered here, to discuss some phenomena that will often recur throughout the thesis in the numerical and experimental applications proposed.

To begin with, the first symptom of nonlinearity may be derived from the definition of *linear* itself: *linear systems can be broken down into parts* [1], being based on the principle of superposition. The principle of superposition can be applied statically or dynamically and states that the total response of a linear system to a set of simultaneous inputs can be decomposed into the sum of individual inputs and outputs. This is simply not true for *nonlinear* systems, and it is basically the reason why they are so much harder to analyze than linear ones. The consequences of the breaking down of the superposition principle truly characterize the nonlinear dynamical behavior, and they will be briefly covered in the subsequent sections by means of numerical examples.

For the sake of simplicity, let us consider a nonlinear single-degree-of-freedom-system, defined by the equation:

$$\ddot{y}(t) + \alpha \dot{y}(t) + \beta y(t) + \gamma y(t)^3 = f(t) \tag{2.1}$$

where $y(t)$ is the displacement, t is the time variable, α the damping parameter, β the linear stiffness parameter, γ the cubic stiffness parameter and $f(t)$ an external forcing input. Eq. (2.1) is known as Duffing equation, named after the German engineer G. Duffing [22]. It will be adopted in the following to demonstrate the effects of several nonlinear phenomena.

With $\gamma = 0$, Eq. (2.1) reduces to the forced linear oscillator, whose natural frequency is called ω_0. On the other hand, with $\gamma \neq 0$, Eq. (2.1) describes a forced nonlinear oscillator, which is characterized by a nonlinear force–displacement relationship. Due to the time-dependent forcing input, the Duffing equation (2.1) can be considered as a second-order nonautonomous system [22].

Considering first the homogeneous equation ($f = 0$), the state-space representation can be adopted by setting $y_1 = y, y_2 = \dot{y}$. This yields:

$$\begin{cases} \dot{y}_1 = y_2 \\ \dot{y}_2 = -\alpha y_2 - y_1(\beta + \gamma y_1^2) \end{cases} \tag{2.2}$$

If $\dot{y}_1 = y_2 = 0$ the *fixed* (or *equilibrium*) *points* (y_1^*, y_2^*) can be computed as:

$$\begin{cases} y_2^* = 0 \\ y_1^*(\beta + \gamma y_1^{*2}) = 0 \end{cases} \tag{2.3}$$

If $\beta\gamma > 0$ there is only one trivial fixed point $(y_{1,0}^*, y_{2,0}^*) = (0,0)$, while if $\beta\gamma < 0$ there are two more nontrivial fixed points: $(y_{1+}^*, y_{2+}^*) = (\sqrt{-\beta/\gamma}, 0)$ and $(y_{1-}^*, y_{2-}^*) = (-\sqrt{-\beta/\gamma}, 0)$. The stability of these points can be checked, and a full analysis is reported in [22].

Substituting $y_1 = y_1^* + \Delta y_1$ ($|\Delta y_1| \ll 1$) and $y_2 = y_2^* + \Delta y_2$ ($|\Delta y_2| \ll 1$) into Eq. (2.2), the following second-order system of the variable Δy_1 can be derived:

$$\Delta\ddot{y}_1 + \alpha\Delta\dot{y}_1 + (\beta + 3\gamma y_1^{*2})\Delta y_1 = 0 \tag{2.4}$$

whose characteristic equation is:

$$\lambda^2 + \alpha\lambda + \beta + 3\gamma y_1^{*2} = 0 \tag{2.5}$$

The solution of the last equation gives the eigenvalues λ_1 and λ_2 that determine the stability of the fixed points.

The dynamics of the system depend on the choice of the coefficients describing the characteristic equation, and several scenarios can be considered. Assuming the damping coefficient α to be positive, the most interesting cases for the purposes of this thesis are the following two:

a) $\beta = \omega_0^2, \gamma > 0, 0 < \alpha < 2\omega_0$: the eigenvalues of the system are complex conjugate with a negative real part; there is one trivial fixed point, which is a stable focus. In this case, all the possible trajectories of the system eventually lead to the stable focus, with a phase portrait like the one in Figure 2.1a.

b) $\beta = -\omega_0^2, \gamma > 0, 0 < \alpha < 2\sqrt{2}\omega_0$: the eigenvalues of the system are complex conjugate with a negative real part. The trivial fixed point is called *saddle* in this case and is inherently unstable, in the sense that a small displacement from the equilibrium state will generally take the system on to a phase path which leads it away from the equilibrium state [21]. The two nontrivial fixed points are stable equilibrium positions. The corresponding phase portrait is shown in Figure 2.1b.

Other cases depend on the choice of the damping coefficient α: negative values lead to unstable solutions, positive values can lead to oscillatory stable and unstable behaviors (like cases a) and b)), or to non-oscillatory overdamped solutions. It is out of the objectives of this thesis to analyze all the possible scenarios, but the reader can refer to [22] for a comprehensive study. The two cases discussed here clearly underline how nonlinearity in dynamical system can lead to complex and rich responses, with multiple stable and unstable solutions. Experimental evidences of such behaviors have been widely observed in nature, and a practical example in the case of mechanical systems is presented in Chapter 6.
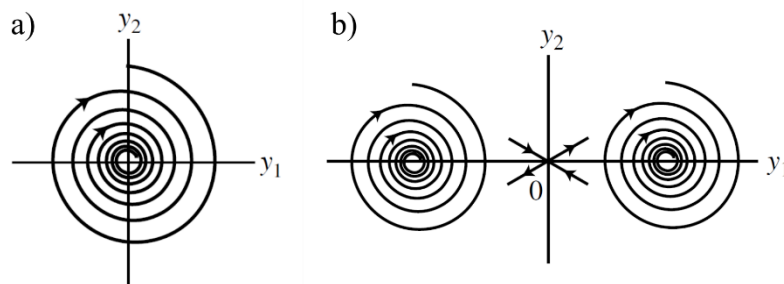
Figure 2.1: Phase portraits of a Duffing oscillator, from [22]. Positive linear stiffness in (a) and negative linear stiffness in (b).

2.2. Harmonic distortions

Let us consider now the case of harmonic excitation in Eq. (2.1): $f(t) = f_0 \sin(\omega t)$. A synchronous solution of the type $y(t) = y_0 \sin(\omega t + \phi)$ can be

sought, exactly like linear systems. However, in this case it is possible to demonstrate that a sinusoidal term of argument $3\omega t$ shows up in the output relation [3]: this term contains the third harmonic of the excitation frequency ω, and more importantly it is not balanced. Thus, a simple synchronous solution is not suitable in this case. Interestingly, if the third harmonic is included in the solution, with an expression like $y(t) = y_{01}\sin(\omega t + \phi_1) + y_{03}\sin(3\omega t + \phi_3)$, higher unbalanced odd harmonics show up in the output relation, in particular terms containing $5\omega, 7\omega, 9\omega$. This process can be repeated infinitely, therefore the only possible solution must include all the odd harmonics, yielding:

$$y(t) = \sum_{j=1}^{\infty} y_{0,2j+1} \sin\big([2j+1]\omega t + \phi_{2j+1}\big) \tag{2.6}$$

Note that the odd harmonics appear due to the cubic stiffness term γy^3; if even nonlinear terms are present as well, both odd and even harmonics show up in the output relation.

The presence of harmonics in the response may have a huge influence in the overall dynamical behavior of a structure and it is generally referred to as *harmonic distortion*. For instance, in the multi-degree-of-freedom case a mode that is not directly excited by the external forcing input can be triggered by one harmonic of another mode. Similarly, two or more closely spaced modes can exchange energy when nonlinearly excited. These two phenomena are usually called *modal interactions* or *internal resonances* [23], and they occur frequently in real structures with complex nonlinear behaviors and multiple modes of vibration. Examples in the scientific literature can be found for panels [24], aerospace structures [25,26] or components with friction [27].

2.3. Nonlinear frequency response curves and path stability

The solution expressed in Eq. (2.6) contains an infinite number of harmonics. While this being correct from a formal point of view, it is not feasible in a computational perspective. Luckily, a few harmonics are generally enough to describe the behavior of nonlinear structures with a decent accuracy, and methods exist to numerically find periodic solutions of nonlinear differential equations with a truncated number of harmonics. The harmonic balance method (HBM) is certainly one of the most common and versatile. It is also known as the Fourier-Galerkin method, since it consists in the application of the Galerkin method with Fourier basis and test functions [26]. The periodic signals are expanded as Fourier series up to N_h harmonics, and the Fourier coefficients of the series become the new unknowns of the problem. The harmonic balance method can be used to compute the nonlinear frequency

response curves (NFRCs) of nonlinear systems when combined with an iterative continuation technique [28].

Referring to the Duffing oscillator described by Eq. (2.1), the nonlinear frequency response curve (NFRC) is computed using the HB technique and considering 7 harmonics (both odd and even). The parameters of the system are listed in Table 2.1, and two levels of amplitude f_0 of the excitation are considered.

Table 2.1: Parameters of the Duffing equation for the computation of the NFRC.

$\alpha \left(\dfrac{\text{N s}}{\text{m kg}} \right)$	$\beta \left(\dfrac{\text{N}}{\text{m kg}} \right)$	$\gamma \left(\dfrac{\text{N}}{\text{m}^3 \text{ kg}} \right)$
0.1	1	1

The NFRCs are depicted in Figure 2.2 in terms of amplitude of the response (maximum of $y(t)$ in the time domain) over f_0. The linear response is also reported as a comparison.
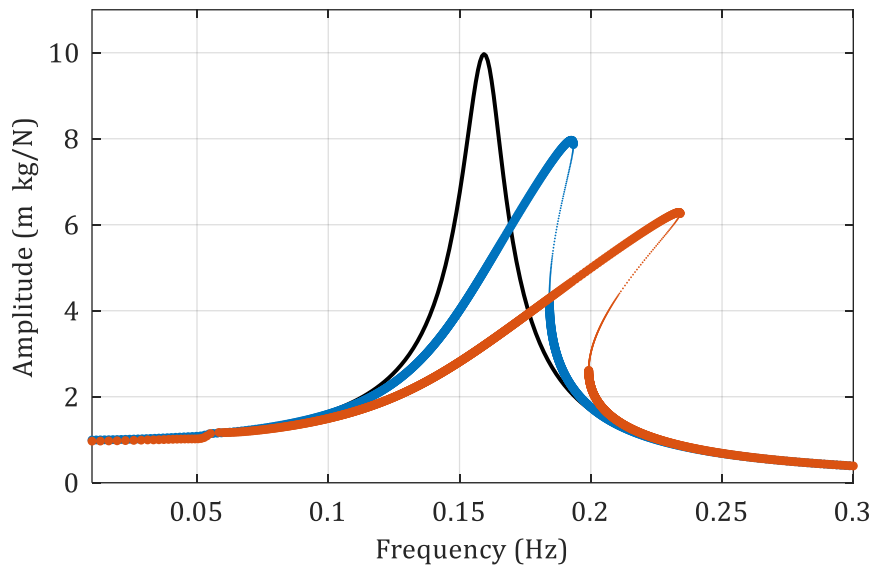
Figure 2.2: NFRCs of the Duffing oscillator of Table 2.1, computed with HBM. Black line: linear FRF; thick dots: NFRC, stable paths; small dots: NFRC, unstable paths. Blue: f_0=0.1 N/kg. Orange: f_0=0.2 N/kg.

It is worth recalling that FRFs are invariant for linear systems because of their *homogeneity* property: a proportional increase in the input level corresponds to the same increase in the output. This is not true for nonlinear ones, as clearly represented in Figure 2.2. In particular, a classical *hardening* effect can be noticed, meaning that the frequency associated to the amplitude peak increases with increasing excitation level f_0. This originates from the fact that the cubic stiffness term γ is chosen as positive. On the contrary, if $\gamma < 0$ the system is *softening*, and the frequency associated to the amplitude peak

decreases with increasing excitation level [3]. An unstable path is also highlighted in Figure 2.2 for each NFRC, which is another typical nonlinear phenomenon. In this context, a system is defined as *stable* if small perturbations do not lead to a significantly different system response [26]. Unstable paths cause sudden changes in the magnitude of the FRF, called *jumps* [3,21]. The jump phenomenon occurs in the frequency region where multiple solutions exist, as the system suddenly tries to reach a stable path. A numerical example is provided later on in this chapter.

For representation purposes it is convenient to normalize the single harmonic contributions $y_{0,k}$ with respect to the total harmonic contributions, as in [26]:

$$\sigma_k = 100 \frac{y_{0,k}}{\sum_{j=1}^{N_h} y_{0,j}} \tag{2.7}$$

The evolution of the normalized harmonic coefficients σ_k is depicted in Figure 2.3 for the 0.2 N/kg case.
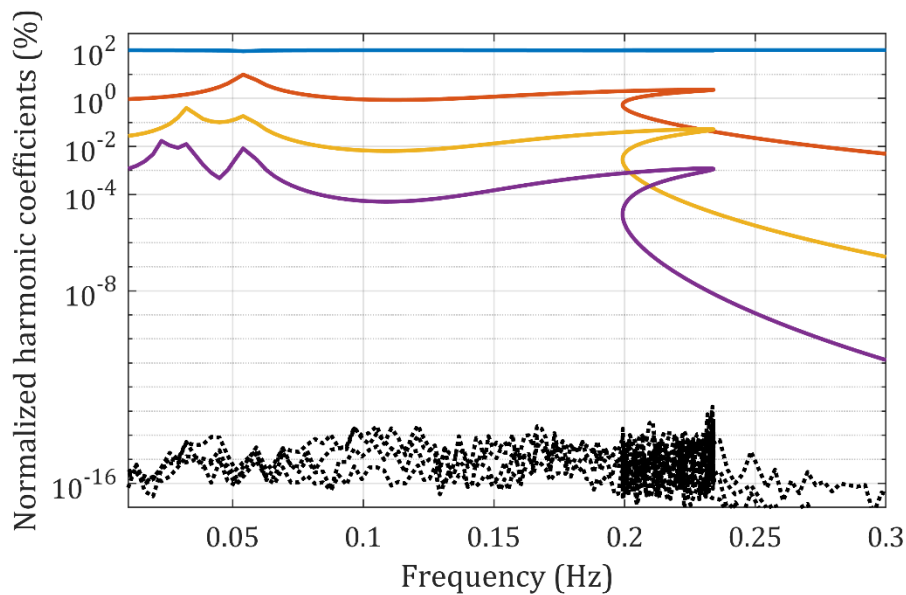
Figure 2.3: Normalized harmonic coefficients of the Duffing oscillator of Table 2.1 in logarithmic scales. Black dots: even harmonics. Blue line: 1st (fundamental) harmonic. Orange line: 3rd harmonic. Yellow line: 5th harmonic. Purple line: 7th harmonic.

The response is dominated by the first (fundamental) harmonic, although the third harmonic also plays an important role. This is particularly true around the jumping region, where the nonlinearity dominates the response, but also at around 0.053 Hz. In this region, the excitation frequency is roughly 1/3 of the natural frequency of the system, the latter being 0.16 Hz. Since the system responds also with the third harmonic of the excitation frequency, a

resonance is created, known as *superharmonic resonance* [22]. As expected, no even harmonics are present in the response.

As for the jump phenomenon, an example is depicted in Figure 2.4, where the time response to a linear sine-sweep is computed using the Newmark method [29], with $f_0 = 0.1$ N/kg.

When a sweep-up excitation is applied, the system response jumps down towards lower levels after reaching the maximum amplitude. Instead, when a sweep-down excitation is applied, a jump-up phenomenon is observed.

Two *bifurcation points* are located right before and after the unstable path. Bifurcations occur when fixed points are created or destroyed, resulting in qualitative changes in the system dynamical behavior [1].
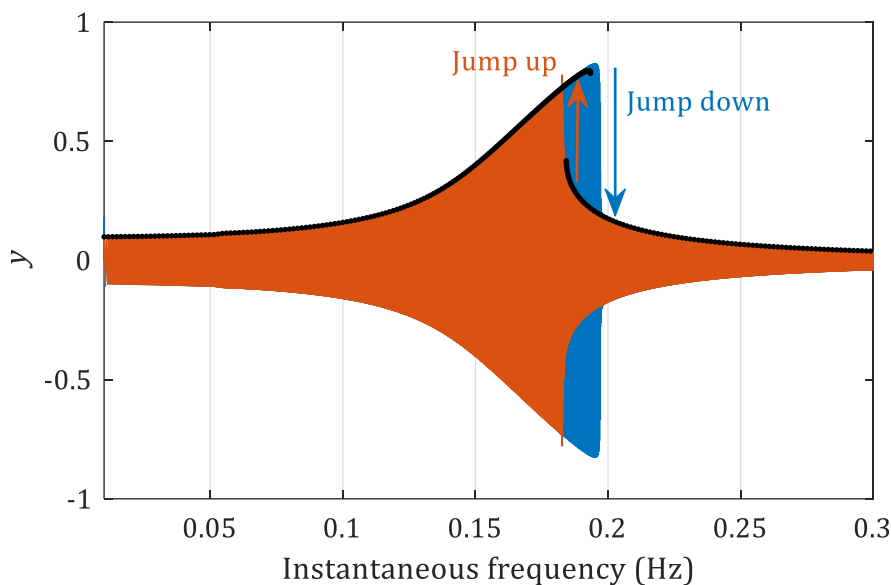
Figure 2.4: Jump phenomena on the Duffing oscillator of Table 2.1, f_0=0.1 N/kg. Blue line: response to a sweep-up excitation; orange line: response to a sweep-down excitation; black dots: NFRC, stable path.

Several types of bifurcations exist, and the most common ones are [30]:

- Fold (or saddle-node) bifurcations: trace the locus of the frequency response peaks and are responsible of the jump phenomenon.
- Neimark-Sacker bifurcations: create or eliminate quasi-periodic oscillations;
- Branch-point bifurcations: detect the beginning of two stable branches out of one;
- Flip (or period-doubling) bifurcations: create a new branch of periodic solutions, with a period doubled compared to the solution of the original branch. When they appear in cascade, flip bifurcations can lead to chaos.

A number of methods exist to discover and track bifurcations in NFRCs, and the reader can refer to [31] for a comparison paper. The *Hill's method* is adopted in this thesis, which is the frequency-domain variant of the *Floquet theory* [28].

Eventually, the spectrogram of the time response can be computed to see the time-frequency contents of the signal. The result is shown in Figure 2.5 for the sweep-up simulation, and it clearly highlights the presence of odd harmonics in the response, as well as the jump-down phenomenon.
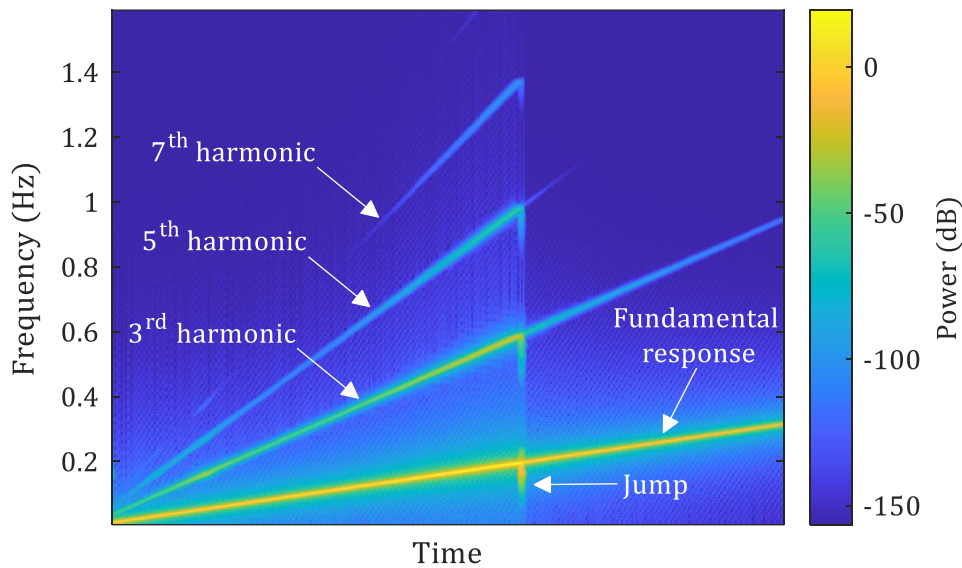
Figure 2.5: Spectrogram of the Duffing oscillator of Table 2.1, sweep-up excitation.

2.4. Bifurcation map and chaos

Harmonic distortions in nonlinear systems may not involve just higher harmonics, but also *subharmonics*. These latter occur when the system responds at periods that are integer multipliers of the excitation period, which in terms of frequencies means $1/2\,\omega, 1/3\,\omega, 1/4\,\omega, \ldots$ Although it is rather difficult that subharmonics arise in weakly nonlinear systems, they are important as transition phenomena to more complex dynamical behaviors, including chaos. An example is provided by considering the Duffing oscillator of Table 2.2.

Table 2.2: Parameters of the Duffing equation for the computation of the bifurcation diagram.

$\alpha\left(\dfrac{\text{N s}}{\text{m kg}}\right)$	$\beta\left(\dfrac{\text{N}}{\text{m kg}}\right)$	$\gamma\left(\dfrac{\text{N}}{\text{m}^3\,\text{kg}}\right)$
0.3	-1	1

Since a negative linear stiffness is considered, the system is characterized by a phase portrait like the one in Figure 2.1b, with two stable equilibrium positions $(y_+^*, 0)$, $(y_-^*, 0)$ and one central saddle point $(y_0^*, 0)$, as in Eq. (2.3). Applying a harmonic excitation, the so-called *bifurcation map* of the system can be built for a specific excitation frequency ω. The bifurcation map is a snapshot of the kind of steady-state solutions that can be obtained for a given excitation frequency when ranging over the excitation amplitude f_0. The initial conditions in this case are $(y_0, \dot{y}_0) = (y_+^*, 0)$, the excitation frequency is $\omega = 0.2$ Hz and time responses are computed again using the Newmark scheme. The bifurcation map is depicted in Figure 2.6, together with the phase diagrams for three different values of f_0.

Each point in the map represents the amplitude(s) of the steady-state solution for a specific value of the excitation amplitude f_0. At first, f_0 is low and one periodic solution is obtained (called *period-1* solution), represented in Figure 2.6a. At some point a series of bifurcations start to show up, creating the so-called *period doubling cascade*: a rapidly accelerating sequence of bifurcations, which eventually doubles to infinity leaving an "oscillation" without any obvious periodic behavior [21]. As an illustration, a *period-2* solution is obtained for the excitation level of Figure 2.6b, meaning that the response is periodic with twice the period of the excitation signal. Thus, the subharmonic $1/2\,\omega$ shows up and two nested orbits are present in the phase diagram.
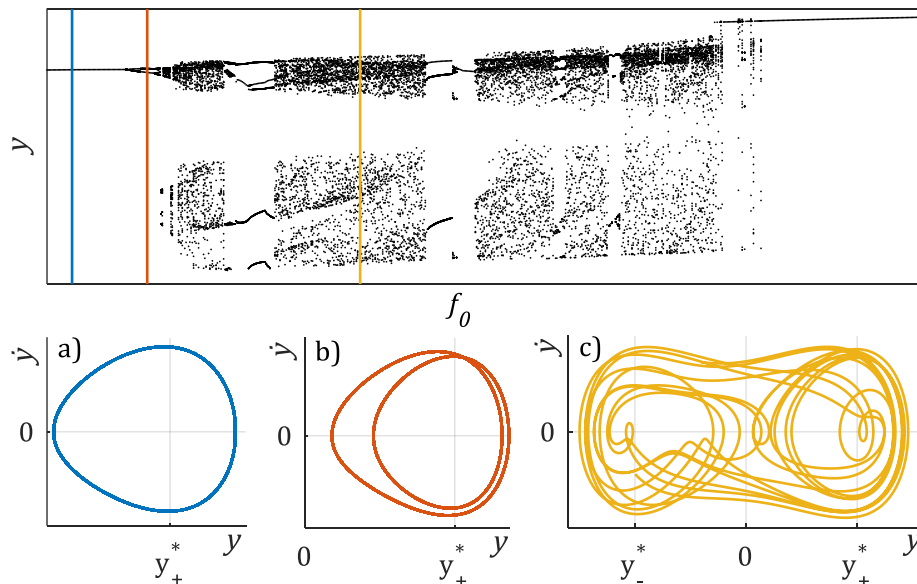
Figure 2.6: Bifurcation map of the Duffing oscillator and phase diagrams in three cases: a) Periodic solution, f_0=0.2 N/kg; b) Period doubling solution, f_0=0.28 N/kg; c) Chaos, f_0=0.45 N/kg.

Instead, no evidence of periodic behavior can be deduced for the excitation amplitude of Figure 2.6c. The solution in this case is bounded but not periodic,

and it continuously crosses the two stable equilibrium points (cross-well motion). This kind of response is a symptom of *chaotic* behavior. It is worth reminding that no definition of *chaos* is universally accepted; the definition given by S. Strogatz in [1] is adopted in this thesis, and reads:

Chaos is aperiodic long-term behavior in a deterministic system that exhibits sensitive dependence on initial conditions.

This definition is essentially based on three foundations:

1. "Aperiodic long-term behavior" means that there are trajectories which do not settle down to fixed points, periodic orbits, or quasiperiodic orbits as $t \to \infty$.
2. "Deterministic" means that the system has no random or noisy inputs or parameters.
3. "Sensitive dependence on initial conditions" means that nearby trajectories separate exponentially fast.

The last point can be quantified by means of the largest Lyapunov exponent (LLE) of the system [1]. A positive sign of the LLE means chaotic motion, while a negative sign is representative of a periodic orbit. The computation of the LLE from an experimental time series is presented in Chapter 6.

2.5. Poincaré map

The *Poincaré map* was originally derived for autonomous nonlinear differential equations. It can be imagined as the intersection of a periodic orbit in the state-space of a dynamical system with a certain lower-dimensional subspace Σ, called *Poincaré section*, transversal to the flow of the system. For the purposes of this thesis, it is actually more useful to adopt the extension of Poincaré maps to nonautonomous systems [21]. Considering the nonautonomous Duffing equation (2.1), the corresponding three-dimensional autonomous system can be derived by considering t as a third state-variable in addition to y_1 and y_2 [22]. Thus, the extended state-space system becomes:

$$\begin{cases} \dot{y}_1 = y_2 \\ \dot{y}_2 = -\alpha y_2 - y_1(\beta + \gamma y_1^2) + f_0 \sin(\omega t) \\ \dot{t} = 1 \end{cases} \tag{2.8}$$

Since the forcing input is periodic with period $T = \omega/2\pi$, the solutions are invariant to a translation in time by T. This observation can be used to build the Poincaré sections of the system. Starting at an initial time $t = t_0$, the points

on a suitable surface (Σ, the Poincaré section) can be collected by stroboscopically monitoring the state variables at intervals of the period T [22]. The Poincaré sections can be computed starting from any initial time t_0, with a certain phase φ with respect to the forcing term (called *phase synchronization angle*).

Considering again the parameters listed in Table 2.2, the Poincaré map is computed considering a forcing level of $f_0 = 0.45$ N/kg and an excitation frequency of $\omega = 0.2$ Hz. Results are depicted in Figure 2.7, where the Poincaré sections are stacked together in a polar plot, building the typical shape of a *strange attractor* [32].
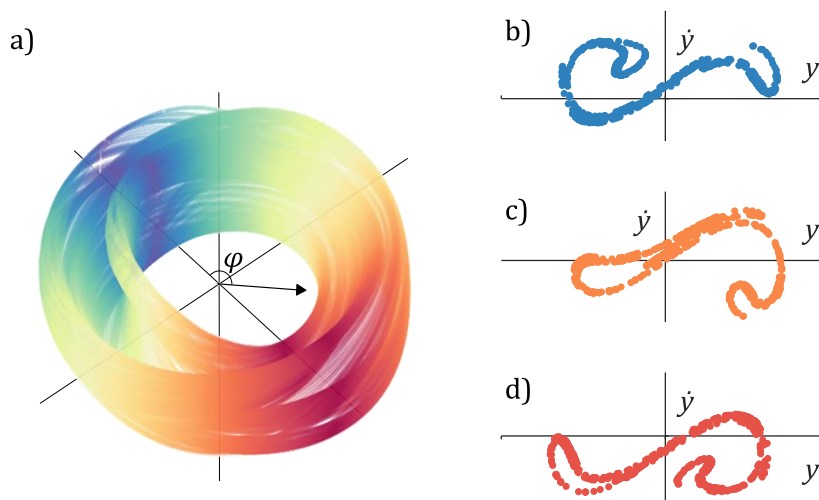
Figure 2.7: Poincaré sections of the Duffing oscillator, f_0=0.45 N/kg. a) Polar representation of the attractor surface; b) Poincaré section, φ=15°; c) Poincaré section, φ=135°; c) Poincaré section, φ=205°.

2.6. **Random excitation in nonlinear systems**

The classical theory of nonlinear dynamics involves harmonically excited systems, resulting in the phenomena discussed so far. Nevertheless, random excitations (usually band-limited) are usually more convenient from a practical point of view, as a broadband frequency range is simultaneously excited with a (theoretical) flat spectrum.

Nonlinear systems respond differently to different kind of excitations, and random signals have a completely different impact when compared to harmonic ones. An example comes from jumps and harmonics: despite them being clear signs of a nonlinear behavior, they are strictly associated to harmonic excitations. The FRF of a nonlinear structure obtained from random excitation on the other hand may appear just "noisy", with no link to any nonlinear phenomena at a first sight. The only way in which random excitation

can assist in detecting nonlinearity is for several tests to be carried out at different RMS levels of the input excitation and the resulting FRFs overlaid to test for homogeneity [3]. An example is depicted in Figure 2.8 considering the Duffing oscillator of Table 2.1. Three levels of excitation are taken into account, and results are plotted in terms of estimated FRFs $G(\omega)$ and coherence functions. The FRFs $G(\omega)$ are estimated using classical linear tools, given the simulated input and output time histories.

Clearly, an increase in the RMS level of the excitation corresponds to a "noisier" and shifted FRF. Since FRFs are invariant for linear systems, these changes can be used to detect a nonlinear behavior. This method will be applied several times in the experimental cases proposed throughout this thesis. The coherence function can be adopted as an indicator of a potential nonlinear behavior as well. However, it should be highlighted that the coherence is not a direct measure of nonlinearity, but an indicator of the *causality* between input and output. Therefore, noise in the acquisition data affects the coherence as well.
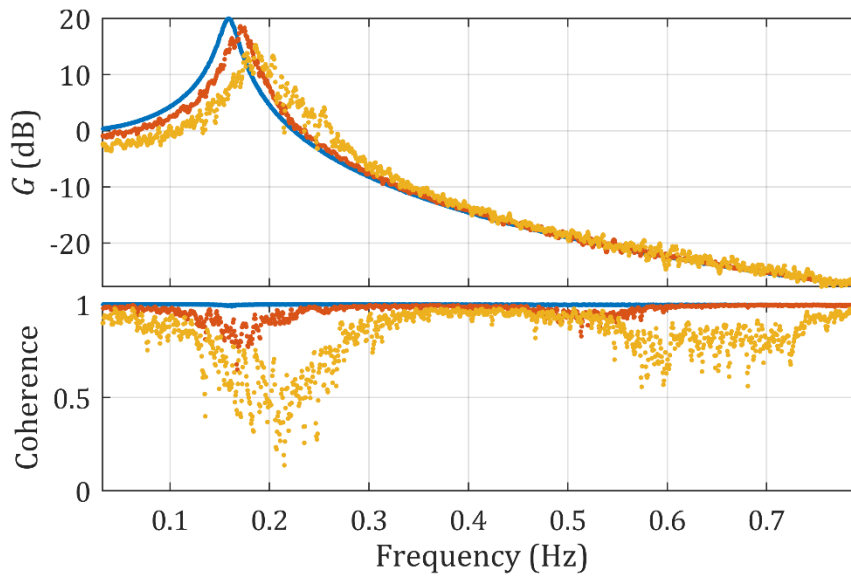
Figure 2.8: FRFs of the Duffing oscillator of Table 2.1 under several random excitations. Blue: f_0=0.1 N/kg RMS. Orange: f_0=1 N/kg RMS. Yellow: f_0=2 N/kg RMS.

2.6.1. Multisine excitation with random phase

A particular class of random excitations consists of random-phase multisines. A random-phase multisine is a periodic signal, defined as a sum of harmonically related sine waves [33,34]:

$$f(t) = \frac{1}{\sqrt{N}} \sum_{k=-N}^{N} F_k e^{i(2\pi k \tilde{f} t + \phi_k)} \qquad (2.9)$$

with $\phi_{-k} = -\phi_k, F_k = F_{-k} = F(k\tilde{f})$ and $\tilde{f} = f_s/N = 1/T$. The sampling frequency to generate the signal is f_s, the period of the multisine is T, and k is the frequency line index. The amplitudes F_k are chosen in a custom way, according to the user-defined power spectrum that should be realized. A typical choice consists of a flat spectrum inside a given frequency range. The randomness of the generated signal comes from the phases ϕ_k, which are realizations of an independent distributed random process such that $E[e^{i\phi_k}] = 0$. Usually the phases are uniformly distributed over $[0,2\pi)$ [6,34]. The major advantage of the random-phase multisine is that it still has (asymptotically for sufficiently large *N*) all the nice properties of Gaussian random noise, while it also has the advantages of a deterministic signal:

1. The amplitude spectrum does not show dips at the excited frequencies, in contrast to purely random signals with no control over the amplitudes.
2. Since the multisine input is periodic with period T, the periodicity of the outputs can be exploited as well. Linear systems respond to periodic inputs with same-period outputs. Nonlinear systems may show periodicity-breaks for strong nonlinear levels. An example of this case will be discussed in Chapter 5.
3. In practical situations when noise is present in the measurement chain, multisines may allow to separate nonlinear distortions to uncorrelated noise. By analyzing the variations of the periodic input and output signals over the measurements of the repeated periods, the sample mean and the sample covariance of the input and the output disturbing noise can be calculated, as a function of the frequency. Although the disturbing noise varies from one period to the other, the nonlinear distortions do not [6]. This allows to separate noise from nonlinear distortions in the FRFs.
4. The amount of even and odd nonlinearities can be detected by carefully choosing the excited frequency lines. Assuming that the input spectrum contains only odd frequency lines and some of them are randomly missing, these lines will not be present in the output as well if the system behaves linearly. Instead, different scenarios are possible if nonlinearities are present [6]:
    *   If the output spectrum contains even frequency lines, then these are necessarily due to a source of even nonlinearity. That is because even frequency lines are not excited, and even nonlinearities show up at these lines because an even number of odd frequencies is added together;
    *   Odd nonlinearities are present only at the odd frequency lines because an odd number of odd frequencies is added together. At the odd frequencies that are not excited at the input, the odd

nonlinear distortions become visible at the output because the linear part of the model does not contribute to the output at these frequencies.

This class of multisine inputs, is called *odd-random multisines*. An example is illustrated in Figure 2.9, while a practical application of this methodology will be implemented in the experimental measurements of Chapter 5.
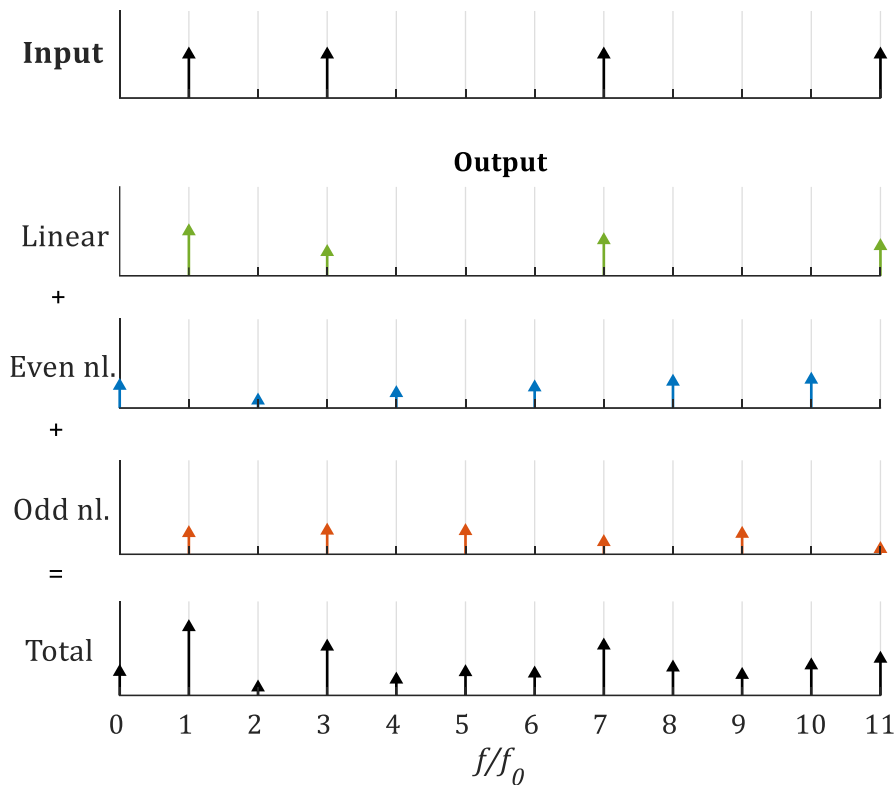
Figure 2.9: A design of a multisine excitation for a nonlinear analysis, elaborated from [6].

Chapter 3

Nonlinear system identification of mechanical structures

3.1. Introduction

Nonlinear phenomena can be complex to model and understand, and frequently numerical tools alone are not enough to gain the desired confidence in the dynamical representation of the structure under test. Even more often, some lack of information may be present in the numerical model that has to be filled by experimental data, for instance via *system identification*.

This process generally refers to the extraction of information directly from the measured data [35], and it may or may-not involve a model, depending on the information that is sought and on the algorithms that are adopted. As a general distinction, methods for system identification are classified according to a *palette of grey shades*, from white-box to black-box models [36], depending on the amount of physical insights needed by the model itself (Figure 3.1). White-box models are physically-based, i.e. they rely on a full physical interpretation of the structural behavior. In other words, the underlying processes characterizing the system are fully known. On the contrary, black-box models do not take into account any underlying physics, and generally they are based on some fitting of flexible functions. The huge class of grey-box (hybrid) methods lays in between these two extremes, where some physical insights are mixed to non-parametric or stochastic functions to account for the missing information.
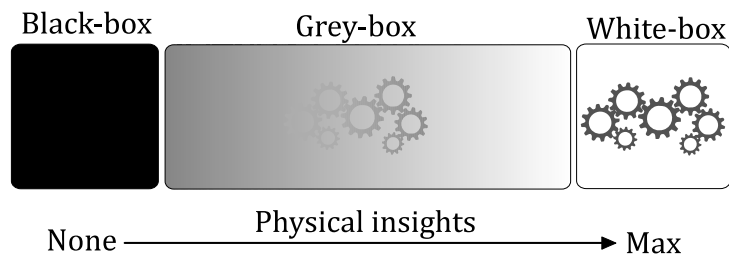
Figure 3.1: Palette of grey shades in experimental testing

This distinction is particularly useful when the system behaves nonlinearly, i.e. in the case of *nonlinear system identification*, as the description of the nonlinearity itself can be physically-based or not.

Despite the *shade* of the adopted algorithm, the nonlinear identification process can be regarded as a progression through three steps: detection, characterization and parameter estimation [9], as outlined in Figure 3.2.
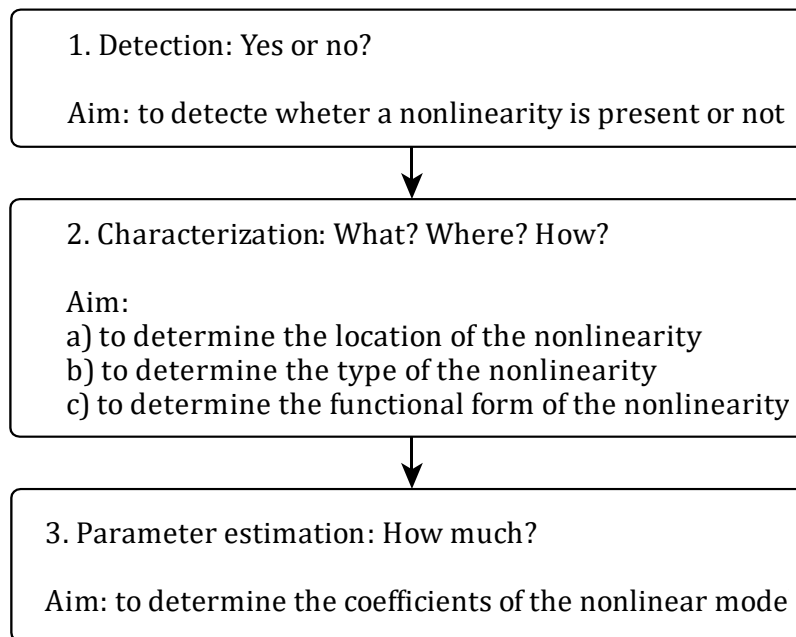
Figure 3.2: Nonlinear system identification process.

Several methods have been developed to accomplish the first step, that is detecting whether a system is behaving nonlinearly, and an extensive literature review can be found in [3]. Generally, these methods aim to reject some hypothesis that hold only for linear systems, to prove that the structure under test is indeed nonlinear. In principle, all the symptoms of nonlinearity seen in Chapter 2 are valid candidates for the detection purpose: harmonic distortions, jumps, non-homogeneity of the FRFs, bifurcations, ...

The second step of the identification process is the characterization, which essentially is about determining which kind of nonlinear behavior is occurring

and where. The latter in particular should be intended in a broad sense, as the nonlinearity may be either localized around a particular spot or distributed along the geometrical extension of the structure.

The last step of the flowchart in Figure 3.2 involves the parameters estimation, i.e. the identification of the coefficients defining the nonlinear behavior. This step highly depends on the algorithm used for performing the nonlinear system identification, as also is the interpretation of the estimated coefficients. A variety of methods exist in the technical literature to perform such a task, and an exhaustive literature review can be found in [9,37]. Some techniques among the others are quite established nowadays, in particular:

Restoring force surface method (RFS): initially developed by Masri and Caughey for SDOF systems in the late 70s [38,39], it relies on the representation of the restoring force (scattered) surface starting from the measured data, followed by a surface interpolation. It has been extended to MDOF systems in the 80s [39] and it has been improved and adopted a lot up to recent years ([40–44]). Its most appealing application is still with SDOF systems, where the functional form of the nonlinearity can be easily visualized just by data manipulation. A practical example comprising a double-well Duffing oscillator will be given in Chapter 6.

Nonlinear ARMA with exogenous input (NARMAX): it is a time-series analysis method, derived from the linear counterpart ARMA (auto-regressive moving average). Proposed by Leontaritis and Billings in the 80s ([45]), it provides a very versatile nonlinear model structure and in most cases it can exploit well-established linear-algebraic means of least-squares estimation. For these reasons, there have been many developments during the years, for instance the inclusion in neural networks [46].

Reverse path and conditioned reverse path methods (RP, CRP): the reverse path analysis has been used to develop spectral methods for nonlinear system identification starting from the late 80s (Rice and Fitzpatrick, [47,48]). The "conditioned" version ([49–51]) estimates both the nonlinear coefficients and the underlying-linear structure.

Nonlinear identification through feedback of the outputs (NIFO): it is a frequency-domain method proposed by Adams and Allemang [52] in 2000. The cornerstone of the method is the idea of treating the nonlinear forces as internal feedbacks to the so-called underlying-linear system.

Nonlinear subspace identification methods (NSI): developed in the time domain by Marchesiello and Garibaldi [53] in 2008 (called TNSI), and in the frequency domain by Noël and Kerschen [54] (called FNSI), they are extension of linear subspace methods (Appendix A) to nonlinear systems. The method relies on the same feedback interpretation proposed by Adams and Allemang ([52]), but in the case of NSI the measured data is processed using

the subspace formulation, providing a fully nonlinear state-space model of the system. This method will be intensively adopted and improved in the next chapters; therefore an in-deep description is provided in the following section.

Polynomial nonlinear state-space models (PNLSS): proposed by Paduart et al. in 2010 [34], it is a non-parametric method based on a multivariate polynomial nonlinear state-space representation of the system, obtained by optimizing the state-space matrices over the residuals between measured and simulated outputs. The detailed formulation of PNLSS is described in Appendix B, and its implementation in the case of a distributed nonlinear behavior will be discussed in Chapter 5.

Nonlinear phase resonance (NPR): linear phase resonance tests have been widely used with linear structures and consist of single modes excitations using a multipoint monoharmonic forcing input at the corresponding natural frequency. This idea was brought to nonlinear systems by Peeters, Kerschen and Golinval in 2011 [55], introducing the nonlinear phase lag quadrature criterion in conjunction with the theory of nonlinear normal modes (NNMs) [56].

Bayesian model updating methods: the use of non-deterministic approaches for linear and nonlinear system identification has gained a lot of attention in the last decades, as an opportunity to enlarge the versatility of the predicted model to catch the uncertainties associated to the estimated parameters. In particular, the stochastic framework based on Bayes' theorem has proved to be the most prevalent approach for model updating of nonlinear systems (Green and Worden, 2015 [57,58]), combined with effective Markov Chain Monte Carlo simulation techniques.

The high number of methods developed for nonlinear system identification proves the interest of the research community around this topic. However, a common framework has not been developed yet, and the state-of-the-art methods are generally intended for ad-hoc applications or model structures. Of course, this originates from the intrinsic difficulty of dealing with nonlinear phenomena, from both theoretical and experimental point of views. Among the proposed techniques, nonlinear subspace methods (TNSI and FNSI) have proven to be very robust in several situations, including real-life nonlinear structures [59]. For this reason, this class of methods will be widely used in this thesis, with several improvements and novel applications. The time domain version will be generally used, and it will be referred to as NSI, unless specified otherwise. A description of the method is provided in the subsequent section, followed by a demonstrative experimental application.

3.2. Nonlinear subspace identification (NSI)

As briefly introduced, NSI is a nonlinear system identification algorithm based on the feedback interpretation proposed by Adams and Allemang ([52]), in conjunction with the subspace formulation. A nonlinear state-space model of the system is gained as outcome, containing the FRF matrix of the so-called *underlying-linear system* and a full description of the nonlinear part of the system. The inputs required by the method are the input-output measured data and the knowledge of the nonlinear basis functions, i.e. the functional form of the nonlinearities. This requirement classifies the method as grey-box, so that a certain amount of physical insights can be gathered from the outcomes of the method.

3.2.1. Problem statement

Let us consider a generic discrete nonlinear vibrating system with N degrees of freedom (DOFs). Its equations of motion can be written in the form:

$$\boldsymbol{M}\ddot{\boldsymbol{y}}(t) + \boldsymbol{C}_v\dot{\boldsymbol{y}}(t) + \boldsymbol{K}\boldsymbol{y}(t) + \boldsymbol{f}^{nl}(t) = \boldsymbol{f}(t) \tag{3.1}$$

where $\boldsymbol{M}$, $\boldsymbol{C}_v$ and $\boldsymbol{K} \in \mathbb{R}^{N \times N}$ are the mass, linear viscous damping and linear stiffness matrices, respectively, while $\boldsymbol{y}(t)$ and $\boldsymbol{f}(t) \in \mathbb{R}^N$ are the displacement and external force vectors. The nonlinear part of the equation is described by the term $\boldsymbol{f}^{nl}(t) \in \mathbb{R}^N$, representing the nonlinear restoring force. Generally, it is a function of displacements $\boldsymbol{y}(t)$ and/or velocities $\dot{\boldsymbol{y}}(t)$. It is assumed that $\boldsymbol{f}^{nl}$ can be decomposed into J distinct nonlinear contributions using a linear-in-the-parameters model, thus yielding:

$$\boldsymbol{f}^{nl}(t) = \sum_{j=1}^{J} \mu_j \boldsymbol{L}_j \xi_j(t) \tag{3.2}$$

μ_j being the coefficient of the jth nonlinearity and ξ_j a scalar function defining the shape of the jth nonlinearity, called nonlinear basis function. The vector $\boldsymbol{L}_j \in \mathbb{B}^N$ is the Boolean location vector of the jth nonlinearity, whose entries can be 1, -1 or 0. The term $\boldsymbol{f}^{nl}$ is shifted to the right-hand side of Eq. (3.1), becoming and additional forcing term:

$$\boldsymbol{M}\ddot{\boldsymbol{y}}(t) + \boldsymbol{C}_v\dot{\boldsymbol{y}}(t) + \boldsymbol{K}\boldsymbol{y}(t) = \boldsymbol{f}(t) - \boldsymbol{f}^{nl}(t) \tag{3.3}$$

In this way it can be seen as a feedback to the system described by the left-hand side of the equation, called *underlying-linear system*, as in Figure 3.3.
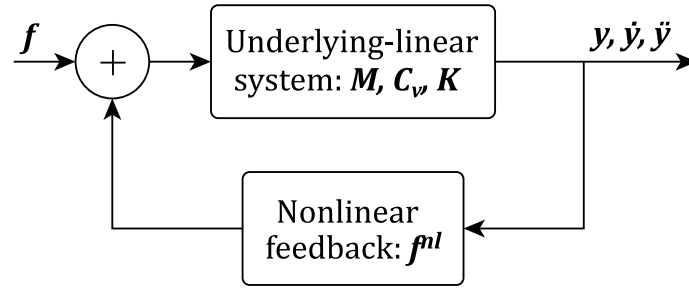
Figure 3.3: Nonlinear feedback interpretation.

An extended input vector $\boldsymbol{f}^e(t)$ is defined as:

$$\boldsymbol{f}^e(t) = \left[\boldsymbol{f}(t)^{\mathrm{T}}, \quad -\xi_1(t), \quad \dots, \quad -\xi_J(t)\right]^{\mathrm{T}} \tag{3.4}$$

Introducing now the state vector $\boldsymbol{x} = [\boldsymbol{y}^{\mathrm{T}}, \dot{\boldsymbol{y}}^{\mathrm{T}}]^{\mathrm{T}}$, a state-space formulation can be retrieved:

$$\begin{cases} \boldsymbol{x}(\tau + 1) = \boldsymbol{A}\boldsymbol{x}(\tau) + \boldsymbol{B}^e \boldsymbol{f}^e(\tau) \\ \boldsymbol{y}(\tau) = \boldsymbol{C}\boldsymbol{x}(\tau) + \boldsymbol{D}^e \boldsymbol{f}^e(\tau) \end{cases} \tag{3.5}$$

τ being the sampled time. The matrices $\boldsymbol{A}, \boldsymbol{B}^e, \boldsymbol{C}, \boldsymbol{D}^e$ are the state, extended input, output and extended direct feedthrough matrices, respectively. Subspace identification can be performed to identify the state-space matrices, rearranging the measured displacements into Hankel-type block matrices. The idea is borrowed from the linear subspace identification theory (SI) [60,61], and detailed steps can be found in Appendix A.

It is worth noticing that the matrix $\boldsymbol{A}$ is the classical state-matrix of a linear state-space model, but related just to the underlying-linear system in this case. This means that the underlying-linear dynamics of the structure can be easily exploited by classical eigenvalue decomposition of $\boldsymbol{A}$ [62], obtaining the natural frequencies ω_r, the damping ratios ζ_r and the linear normal modes (LNMs) $\boldsymbol{\psi}_r$, for each identified mode r. It is assumed hereafter that the LNMs are normalized according to the unit-scale normalization, unless specified otherwise.

3.2.2. Underlying-linear FRFs and nonlinear coefficients

The so-called *extended FRF matrix* $\boldsymbol{G}^e(\omega)$ can be obtained from:

$$\boldsymbol{G}^e(\omega) = \boldsymbol{D}^e + \boldsymbol{C}(z\boldsymbol{I} - \boldsymbol{A})^{-1}\boldsymbol{B}^e, \quad z = e^{i\omega\Delta t} \tag{3.6}$$

where $\boldsymbol{I}$ is the identity matrix and i is the imaginary unit. $\boldsymbol{G}^e(\omega)$ has the same structure as the extended force vector $\boldsymbol{f}^e$:

$$G^e(\omega) = \begin{bmatrix} G(\omega), & G(\omega)\mu_1 L_1, & \dots, & G(\omega)\mu_J L_J \end{bmatrix} \quad (3.7)$$

so that its first block $G(\omega)$ is the FRF matrix of the underlying-linear system. The coefficients μ_j can eventually be deduced from the remaining blocks of $G^e(\omega)$ [53]. For instance, if a single forcing input is applied at DOF u, then the jth coefficient μ_j can be computed from:

$$\mu_j G(\omega) L_j = \mu_j \begin{bmatrix} ? & ? & ? & \cdots & ? \\ \vdots & \ddots & & & \vdots \\ G_{u,1} & G_{u,2} & \ddots & \cdots & G_{u,N} \\ \vdots & & & \ddots & \vdots \\ ? & ? & ? & \cdots & ? \end{bmatrix} L_j = \begin{bmatrix} ? \\ \vdots \\ G^e_{u,j+N} \\ \vdots \\ ? \end{bmatrix} \quad (3.8)$$

where the symbol ? represents an unknown quantity. A 2 DOFs numerical example taken from [53] is proposed in the following to better understand Eq. (3.8). The system is depicted in Figure 3.4 and it comprises three nonlinear stiffness terms: a quadratic and a cubic nonlinear stiffness between the first mass and the ground, and a cubic nonlinear stiffness between masses 1 and 2.
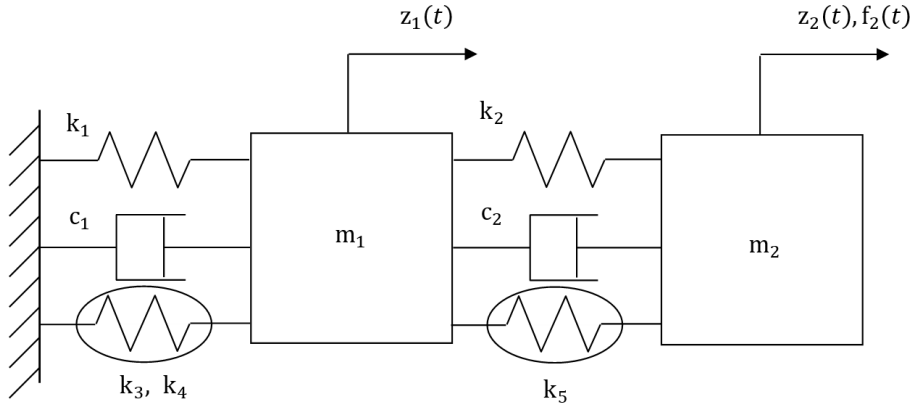
Figure 3.4: 2 DOF numerical example.

Therefore $J = 3$ and the three nonlinear contributions are:

$$\mu_1 L_1 \xi_1(t) = k_3 \begin{bmatrix} 1 \\ 0 \end{bmatrix} z_1^3,$$

$$\mu_2 L_2 \xi_2(t) = k_4 \begin{bmatrix} 1 \\ 0 \end{bmatrix} z_1^2, \quad (3.9)$$

$$\mu_3 L_3 \xi_3(t) = k_5 \begin{bmatrix} -1 \\ 1 \end{bmatrix} (z_2 - z_1)^3$$

The FRF matrix of the ULS $G(\omega)$ is a 2×2 matrix of the type:

$$G = \begin{bmatrix} G_{11} & G_{12} \\ G_{21} & G_{22} \end{bmatrix} \quad (3.10)$$

and since the force is applied at DOF 2, only the second column of G can be estimated. It should be noted that the reciprocity property of the FRF matrix holds in this case, as G is a linear FRF. Thus, it is possible to write $G_{12} = G_{21}$. These considerations made, Eq. (3.8) can be explicitly written for the considered case as:

$$\mu_1 G \, L_1 = \mu_1 \begin{bmatrix} ? & G_{12} \\ G_{21} & G_{22} \end{bmatrix} \begin{bmatrix} 1 \\ 0 \end{bmatrix} = \begin{bmatrix} ? \\ \mu_1 G_{12} \end{bmatrix} = \begin{bmatrix} ? \\ G_{23}^e \end{bmatrix},$$

$$\mu_2 G \, L_2 = \mu_2 \begin{bmatrix} ? & G_{12} \\ G_{21} & G_{22} \end{bmatrix} \begin{bmatrix} 1 \\ 0 \end{bmatrix} = \begin{bmatrix} ? \\ \mu_2 G_{12} \end{bmatrix} = \begin{bmatrix} ? \\ G_{24}^e \end{bmatrix}, \qquad (3.11)$$

$$\mu_3 G \, L_3 = \mu_3 \begin{bmatrix} ? & G_{12} \\ G_{21} & G_{22} \end{bmatrix} \begin{bmatrix} -1 \\ 1 \end{bmatrix} = \begin{bmatrix} ? \\ \mu_3(G_{12} - G_{22}) \end{bmatrix} = \begin{bmatrix} ? \\ G_{25}^e \end{bmatrix}$$

Note that this operation results in a frequency-dependent and complex-valued quantity, called $\mu_j^{id}(\omega) \in \mathbb{C}$. Since the true coefficient μ_j is supposed to be a real number, no dependence on the frequency should be expected from the identified counterpart μ_j^{id}, as well as null imaginary part. However, this happens only in complete absence of noise and nonlinear modeling errors. Instead, when real measurements are performed, a non-zero imaginary part $\Im[\mu_j^{id}]$ is generally retrieved, although it is expected to be much smaller than the real part $\Re[\mu_j^{id}]$. That being said, the ratio between real and imaginary parts can be adopted as a tool to assess the quality of the identification outcome. Examples of this idea will be given in the next chapters.

3.2.3. Stabilization diagram and modal contributions

A crucial step of the identification process is the selection of the order of the state-space model in Eq. (3.5). This task may be non-trivial also for the linear identification case, as noise in the data is likely to have an impact on the estimated poles of the system. Also, in modal analysis one is usually not interested in a good model as such, but rather in the modal parameters extracted from that model. An over-specification of the model order might be necessary in order to ensure a good accuracy of the estimated modal parameters, but this results in a number of spurious numerical modes [62]. The stabilization diagram [63] is a common tool to discard spurious poles from the identification. The poles corresponding to a certain model order are compared to the ones related to the previous order: if the differences in the modal parameters are within certain user-defined limits, the pole is defined as stable. Since spurious modes are assumed to have stochastic or computational nature, they should not be stable across different model orders. Stabilization diagrams can be used in NSI by checking the stabilization of the modal parameters of the ULS across several model orders. Generally, stabilization is checked for eigenfrequencies, damping ratios and mode shapes. These latter,

in particular, can be compared adopting the modal assurance criterion (MAC) [64]. Practical implementations of the stabilization diagram will be given throughout the thesis every time system identification is performed.

Furthermore, using the state-space formulation, the contributions of single modes to the system FRFs can be easily decoupled, and this hold for both SI and NSI [65]. One of the advantages of this operation is that the capabilities of the stabilization diagram can be expanded by checking also the stabilization of the estimated modal mass m_r of each mode r.

In NSI, it is possible to split the single modes contributions to the jth nonlinearity by expanding the modal contributions to the extended FRF $G^e(\omega)$. In particular, if displacements are measured the corresponding receptance can be written as:

$$G^e(\omega) = \sum_{r=1}^{N} \frac{\widetilde{C}_r \widetilde{B}_r}{(z - \lambda_r)} = \sum_{r=1}^{N} {}_r G^e(\omega), \quad z = e^{i\omega\Delta\tau} \tag{3.12}$$

where $\widetilde{C}_r$ is the rth column of $\widetilde{C} = C\Psi$, $\widetilde{B}_r$ is the rth row of $\widetilde{B} = \Psi^{-1}B^e$ and λ_r is the rth discrete eigenvalue of A. The matrix Ψ is the modal matrix, which stacks the eigenvectors ψ_r by column, and the contribution of the rth mode to G^e is called ${}_r G^e$. If accelerations are measured:

$$G^e(\omega) = \sum_{r=1}^{N} \frac{(z - 1)\widetilde{C}_r \widetilde{B}_r}{(\lambda_r - 1)(z - \lambda_r)} = \sum_{r=1}^{N} {}_r G^e(\omega), \quad z = e^{i\omega\Delta\tau} \tag{3.13}$$

It is therefore possible to estimate the coefficient μ_j from each modal contribution:

$$_r G^e(\omega) = \begin{bmatrix} {}_r G(\omega), & {}_r G(\omega)\mu_1 L_1, & \dots, & {}_r G(\omega)\mu_J L_J \end{bmatrix} \tag{3.14}$$

where $_r G(\omega)$ is the contribution of the rth mode to $G(\omega)$. Since this operation can be repeated for each identified mode $r = 1, \dots, N$, there are in principles N estimations of each μ_j^{id}. Nevertheless, different modes respond differently to the nonlinear excitation, and some of them may not be affected by the nonlinearity at all. Therefore, no general rule can be defined about how to treat the different single-modes estimations, but considerations can be made on single-case basis.

Once spurious modes have been detected using the stabilization diagram, these can be removed from the computation of the coefficients, selecting only the physical modes in Eq. (3.14). Practical examples of such an implementation will be given in the next chapters. Please note that this approach does not alter the state-space matrices, as the spurious poles are detected a posteriori. Ways exist to remove them directly from the identified nonlinear state-space model, for instance via modal reduction [66].

3.3. Experimental application: identification of a non-smooth nonlinearity

A three-degrees-of-freedom system is considered, composed by three masses linked by thin plate-like springs. A schematic representation of the system is depicted in Figure 3.5, and a photo of the setup in Figure 3.6a. A non-smooth piecewise spring is located between the third mass and the ground, achieved by means of two additional springs added to the sides of the third mass. Each additional spring presents a small gap with respect to the grounding spring, g^- on the left and g^+ on the right, as shown in Figure 3.6b. The measure of the gaps is really challenging since they are very small and the system is quite flexible. An indicative maximum value of gaps measured with a feeler gauge is $|g^-| = g^+ = 0.35$ mm. Additional details on the test-rig can be found in [67–69].

The system is excited with a Gaussian random force in the frequency range $0 - 21$ Hz applied to mass 1, and the responses are measured for 300 s with a sampling frequency of $f_s = 102.4$ Hz. The displacements and accelerations of the three DOFs are measured by means of three laser displacement sensors and three accelerometers, which will be referred to as S1, S2, S3 respectively for DOF 1, DOF 2 and DOF 3. The acquisitions are performed with six different values of RMS driving voltage supplied to the amplifier, listed in Table 3.1.
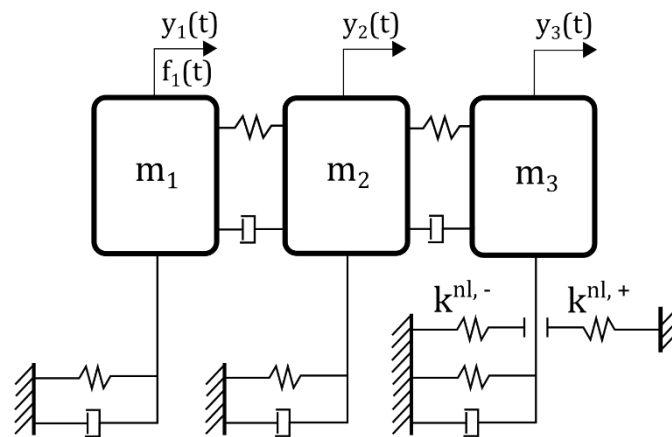
Figure 3.5: Schematic representation of the non-smooth system.

A first characterization of the nonlinearity is carried out by just processing the input-output data. The objective of this first step is to have a clearer idea of the dynamical behavior of the system, especially when the nonlinearity is activated. The information collected will be used afterwards to estimate the nonlinear basis functions required by NSI to perform the identification.
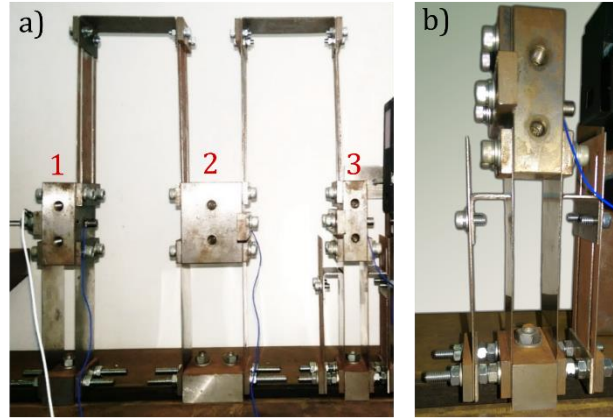
Figure 3.6: Photo of the non-smooth experimental test-rig in (a) and detail of the piecewise nonlinear spring in (b).

Table 3.1: RMS force values, non-smooth nonlinear system.

Name	Driving voltage RMS (V)	Excitation force RMS (N)
F1	0.1	1.52
F2	0.2	3.05
F3	0.3	4.67
F4	0.4	6.12
F5	0.5	7.71
F6	0.6	9.23

3.3.1. Nonlinear characterization

The piecewise nonlinearity is supposed to add a positive contribution to the stiffness of the system when the gap is closed, so as to obtain a hardening effect. To check whether this happens, the system is driven through several levels of excitation. The lowest level assures that the gap is always open, so not to trigger the nonlinearity and have a linear reference. On the contrary, the higher levels of excitation are chosen so as to progressively excite more the nonlinearity. The experimental FRFs obtained processing the input-output data are shown in Figure 3.7 for the excitation levels F1, F4 and F6.

A distinct increase of the frequency associated to the third mode can be noted when increasing the input level, together with a reduction of the amplitude. This is particularly evident in Figure 3.7c, showing the FRF $G_{31}(\omega)$. Concerning the other two modes, different behaviors can be noted. The first mode seems not to be much affected by the nonlinearity, as neither its frequency nor its amplitude shows significant changes. Instead, the second mode seems to exhibit a slight softening behavior, so that its frequency reduces for increasing excitation levels. This is combined to a decrease of its amplitude, as for the third mode.
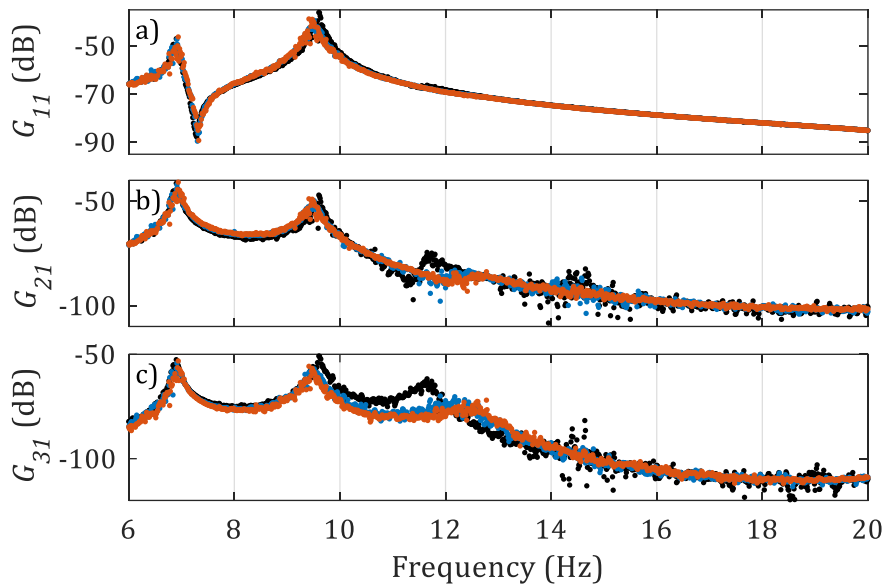
Figure 3.7: Receptance of the system for different excitation levels in dB scales (ref. 1 m/N). Black line: F1; blue line: F4; orange line: F6. a) G_{11}; b) G_{21}; c) G_{31}.

Some more insights about the nature of the frequency shift for the third mode can be gathered when looking at Figure 3.8, showing the spectrogram of DOF 3 for several levels of excitation stacked into one single stepped-random series. Three main frequency lines corresponding to the three modes are clearly visible, and not a big change can be observed for the first two modes, as previously seen. Instead, the third one shows an increase in its frequency due to the non-smooth nonlinearity. In particular, the highest frequency shift is observed switching from level F2 to F3. As for the higher levels of excitation, it has been observed during the experimental tests that the gap was almost always closed, practically obtaining a new linear (but stiffer) system.

Theoretically, the only piecewise nonlinearity does not justify the softening behavior of the second mode. This may suggest that some other nonlinear sources may be present in the considered system. Nevertheless, the most evident nonlinear phenomenon is still related to the hardening effect associated to the non-smooth nonlinearity. Therefore, the other nonlinear phenomena are neglected in the following, and just the theoretical nonlinear basis functions related to the non-smooth stiffness are considered. This choice implies that there will still be a minor part of the nonlinear behavior of the system that is not represented by the identified model.
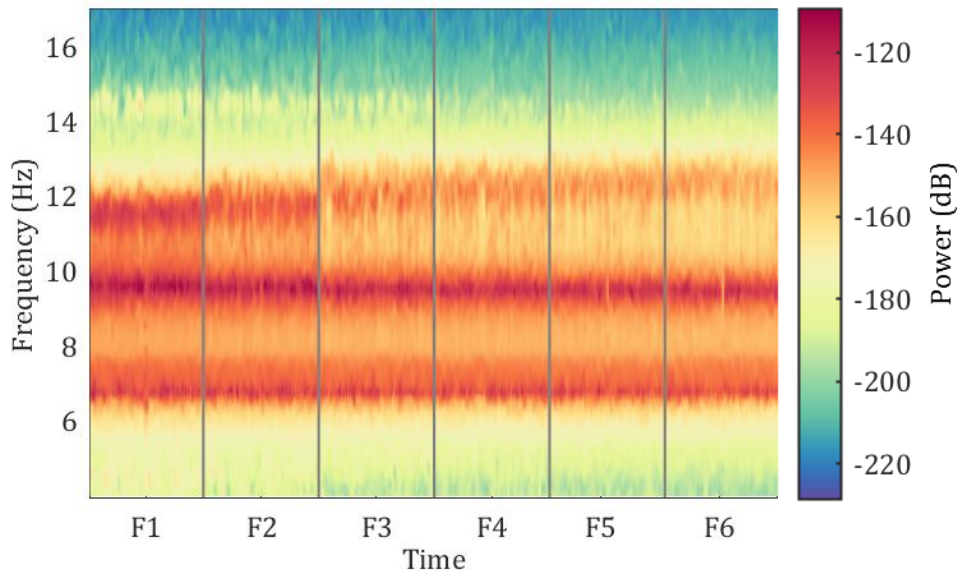
Figure 3.8: Spectrogram of DOF 3 for different excitation levels.

3.3.2. Nonlinear identification

A suitable excitation level should be chosen to estimate positive and negative gaps. Indeed, the excitation should be able to properly trigger the nonlinearity, so that a good number of samples outside the negative and positive gaps are present. On the other hand, a decent number of samples inside the inner dead-space should be present to help the identification of the underlying-linear dynamics. Also, it has been already observed that the most noticeable frequency increase is obtained when going from level F2 to F3. Lower excitation levels do not guarantee a proper nonlinear behavior, while higher levels tend to "saturate" the nonlinearity. A middle-level excitation seems then the best choice, corresponding to the 0.3 V test (F3).

The identification of the gaps is performed by considering a set of guess values for both the positive gap g^+ and the negative gap g^-. This prevents any symmetry constraint during the estimation, as positive and negative gaps may differ due to assembly inaccuracy. The two sets of guess values are called, respectively, $\boldsymbol{g}^+ = \left[g_1^+, \ldots, g_p^+\right]$ and $\boldsymbol{g}^- = \left[g_1^-, \ldots, g_n^-\right]$. Note that in principle they might have a different number of components, i.e. $p \neq n$. The total guess set $\boldsymbol{g} = [\boldsymbol{g}^-, \boldsymbol{g}^+] \in \mathbb{R}^{p+n}$ is eventually assembled, so that the nonlinear basis functions ξ_j can be defined using a piecewise formulation:

$$\xi_j(t) = \begin{cases} y_3(t) - g_j & \text{for } y_3(t) > g_j \text{ and } g_j > 0 \\ y_3(t) - g_j & \text{for } y_3(t) < g_j \text{ and } g_j < 0, \\ 0 & \text{elsewhere} \end{cases}$$
(3.15)

$$\boldsymbol{L}_j = [0\ 0\ 1]^{\mathrm{T}}$$

The final nonlinearity is then built by summing the different contributions ξ_j, each one multiplied by the corresponding identified coefficient μ_j. In this way, the choice of the different guess values g_j can be very rough and just intended to define a realistic range. The guess set is chosen equal to $\boldsymbol{g}$ = [-0.4, -0.3, -0.2, -0.1, 0.1, 0.2, 0.3, 0.4] mm, and it contains a total of 8 values. Thus, J = 8 nonlinear contributions are taken into account, and the jth nonlinear basis function ξ_j can be computed from Eq. (3.15) considering the jth element of $\boldsymbol{g}$. The resulting nonlinear basis functions are depicted in Figure 3.9.
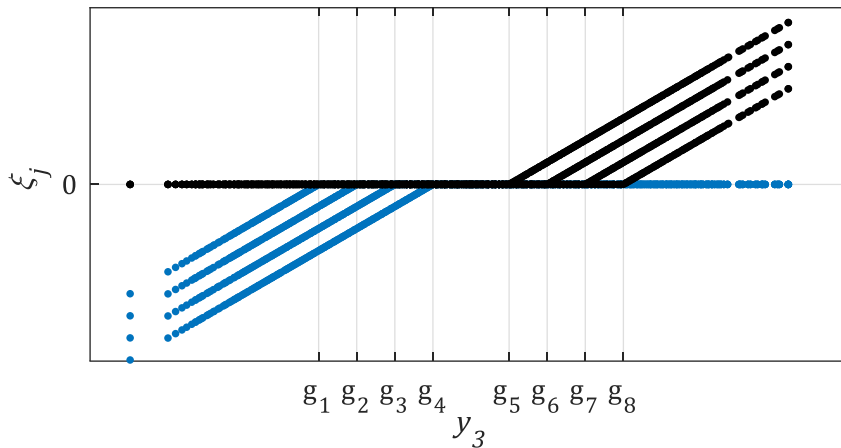
Figure 3.9: Nonlinear basis functions ξ_j for the gaps estimation with guess set $\boldsymbol{g}$. Black dots: positive set; blue dots: negative set.

The stabilization diagram of the underlying-linear system is reported in Figure 3.10 and stability is checked for frequencies, damping ratios, MACs and modal masses.

The three translational modes of the system are clearly visible in the stabilization diagram starting from a model order equal to 10. For this reason, 10 is selected as the order of the state-space model. It is worth highlighting that the selected model order does not directly correspond to the "physical" order, which would be 6 (3 DOFs) in this case. This is a common phenomenon in both linear and nonlinear system identification, when real measurements are considered, and noise plays an important role. In the nonlinear case there might be also nonlinear residuals due to nonlinear modeling errors. The result is that the model order extracted from the stabilization diagram might not be linked to the physical degrees-of-freedom of the considered structure.

The nonlinear coefficients associated to the chosen model order are extracted and listed in Table 3.2 in terms of real spectral mean $\bar{\mu}_j^{id}$ plus its standard deviation σ_j, computed in the frequency range $0 - 15\ Hz$. Also, the ratio between the real and the imaginary parts $E[\Re/\Im]_j$ is reported for each coefficient.
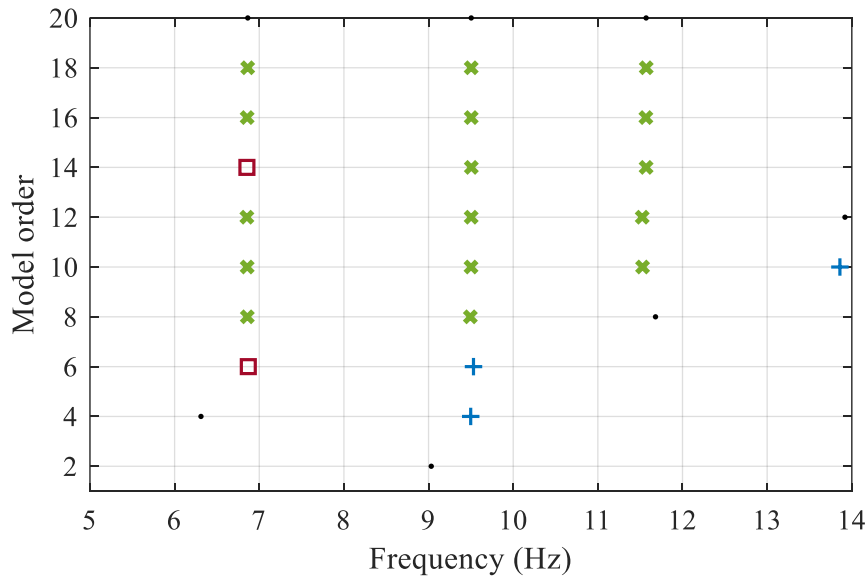
Figure 3.10: Stabilization diagram of the ULS. Stabilization thresholds for natural frequency, damping ratio, MAC and modal mass are 0.5%, 20%, 99%, 20%, respectively. Black dot: new (not stable) pole; blue plus: pole stable in frequency; red square: pole stable in frequency and MAC; orange circle: pole stable in frequency, MAC and damping; green cross: pole stable in frequency, MAC, damping and modal mass.

Table 3.2: Identified coefficients for the gaps estimation.

Direction	Coefficient	$\bar{\mu}^{id}$ (N/m)	σ (N/m)	$E[\Re/\Im]$
	μ_1^{id}	-646	10	14
	μ_2^{id}	1306	10	26
Positive	μ_3^{id}	606	7	10
	μ_4^{id}	-161	1	12
	μ_5^{id}	664	10	7
	μ_6^{id}	479	6	17
Negative	μ_7^{id}	-360	1	76
	μ_8^{id}	225	2	12

The nonlinear function $f^{nl}(y_3)$ is then computed and the result is shown in Figure 3.11, where the single contributions are also depicted.
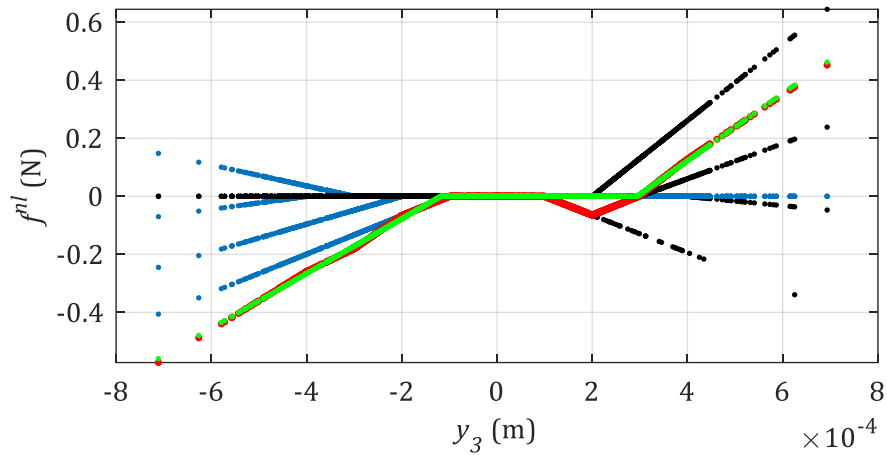
Figure 3.11: Nonlinear function f^{nl} for the gaps estimation. Black dots: positive set; blue dots: negative set; red circles: nonlinear function; green line: piecewise-linear fitting.

The nonlinear function is eventually fitted to a piecewise-linear formulation, whose roots give the estimated values for the positive and negative gaps, yielding:

$$g^- = -0.12 \text{ mm}$$
$$g^+ = +0.28 \text{ mm}$$

(3.16)

A new identification can eventually be carried out fixing the positive and negative gaps to the identified ones. The remaining coefficients to identify are then the slopes associated to the negative and positive piecewise nonlinearities. Thus, only two nonlinear basis functions are considered, which can be still written as in Eq. (3.15), with the only difference that the new set is $\boldsymbol{g} = [-0.12, +0.28]$ mm. The stabilization diagram of the new underlying-linear system is reported in Figure 3.12 and stability is checked for frequencies, damping ratios, MACs and modal masses.

The three translational modes of the system are clearly visible in the stabilization diagram obtained with NSI, and a model order equal to 10 is chosen also in this case. The identified linear modal parameters are reported in Table 3.3.

Also, linear system identification is performed considering the low-level test (level F1) assumed as linear, in order to validate the estimation of the underlying-linear system. Linear subspace identification (SI, Appendix A) is used to extract the state-space model of the linear reference and the obtained linear modal parameters are compared with the ones estimated by NSI from the nonlinear test.

A good correspondence is retrieved on the identified natural frequencies and modal masses. In particular, the discrepancies between SI and NSI are in the order of 1% for the natural frequencies, and NSI estimations are always lower than the SI counterparts. This is very likely related to the already

discussed softening phenomenon; thus, further investigations about the softening nonlinearity may improve this result.
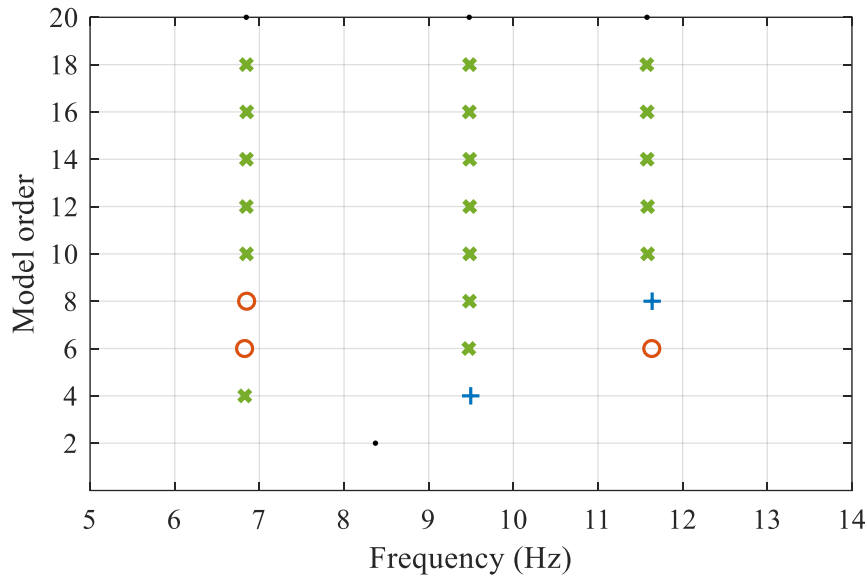
Figure 3.12: Stabilization diagram of the ULS. Stabilization thresholds for natural frequency, damping ratio, MAC and modal mass are 0.5%, 20%, 99%, 20%, respectively. Black dot: new (not stable) pole; blue plus: pole stable in frequency; red square: pole stable in frequency and MAC; orange circle: pole stable in frequency, MAC and damping; green cross: pole stable in frequency, MAC, damping and modal mass.

Table 3.3: Identified modal parameters of the underlying-linear system and comparison with the linear identification.

Mode number	Frequency (Hz)			Damping ratio (%)			Modal mass (kg)		
	SI	NSI	Δ (%)	SI	NSI	Δ (%)	SI	NSI	Δ (%)
1	6.90	6.85	0.81	0.39	0.46	16.70	2.95	2.86	2.99
2	9.59	9.49	1.15	0.60	0.82	37.13	1.42	1.41	0.93
3	11.63	11.59	0.38	1.30	1.53	17.34	1.13	1.12	0.66

As for the damping ratios, greater discrepancies are retrieved between NSI and SI estimations. In particular, NSI always identifies higher damping ratios, perhaps symptom of some source of nonlinear damping which has not been included in the nonlinear basis functions. A possible explanation is that the energy dissipated during the contact with the damper may play a role in the damping distribution of the system. It should be recalled that the nonlinear basis functions adopted here cannot account for these two phenomena; instead, the only hardening effect related to the piecewise nonlinearity is considered. The FRFs of the underlying-linear system are reported in Figure 3.13.
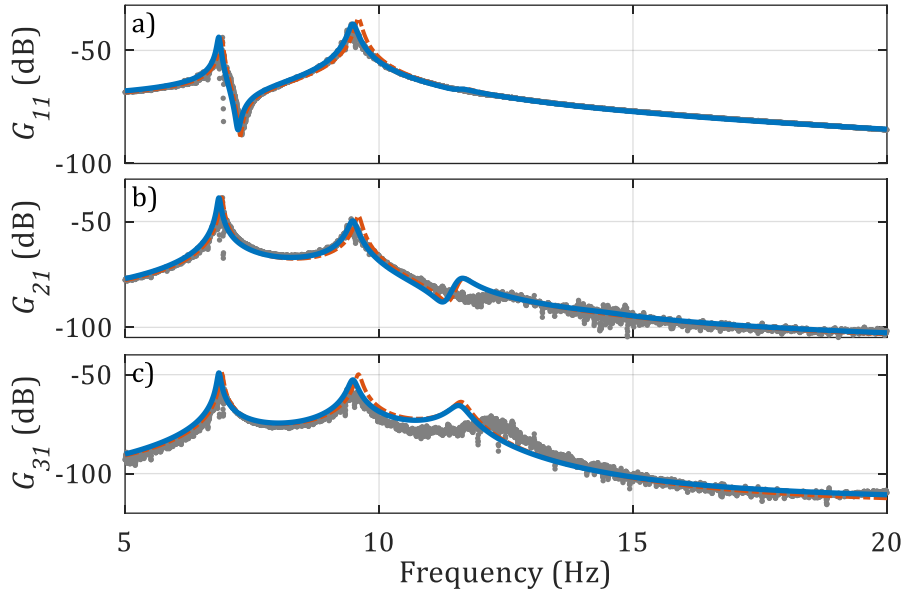
Figure 3.13: Receptances of the underlying-linear system in dB scales (ref. 1 m/N). Grey dots: measured receptance of the nonlinear test; orange dashed-dotted line: SI estimation of the linear FRF from the low-level test; blue line: NSI estimation of the underlying-linear FRF. a) G_{11}; b) G_{21}; c) G_{31}.

It can be noted in Figure 3.13 that the hardening effect on the third mode is correctly caught, as a consequence of the piecewise nonlinear basis functions adopted. Also, the discrepancies in the natural frequencies between NSI and SI estimations are clearly visible, as the peaks of the blue curves (NSI) are all shifted to the left with respect to the orange dashed-dotted curves (SI).

Eventually, the coefficients of the nonlinearities are computed from the nonlinear state-space model and depicted in Figure 3.14 in their real and imaginary parts. It should be recalled that two nonlinear basis functions are considered, associated to the negative and positive gaps, respectively. Thus, two coefficients μ_1^{id}, μ_2^{id} are identified. A list is reported in Table 3.4 in terms of real spectral mean $\bar{\mu}_j^{id}$ plus its standard deviation σ_j, and ratio between the real and the imaginary parts $E[\mathfrak{R}/\mathfrak{I}]_j$.

Table 3.4: Identified coefficients for piecewise nonlinearity estimation.

Coefficient	$\bar{\mu}^{id}$ (N/m)	σ (N/m)	$E[\mathfrak{R}/\mathfrak{I}]$
μ_1^{id}	1340	2	153
μ_2^{id}	2170	2	261

The spectrum of the real part of the identified coefficients is practically flat, with a standard deviation around 0.1% of the mean value. Also, the real part is much higher that the imaginary part for both the coefficients, thus the estimation should be considered reliable.
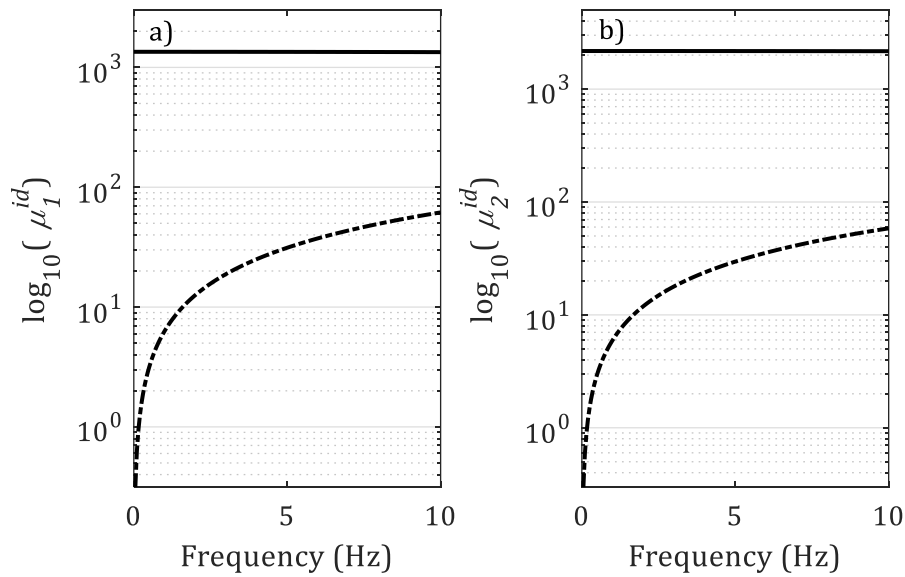
Figure 3.14: Identified coefficients of the piecewise nonlinearity in logarithmic scales. Continuous line: real part; dashed-dotted line: imaginary part. a) $\mu_1{}^{id}$; b) $\mu_2{}^{id}$.

The spectral means of the two coefficients $\bar{\mu}_1^{id}$ and $\bar{\mu}_2^{id}$ are then taken as the final values for the slopes associated to the negative and positive gaps. The parameters defining the nonlinearity are eventually summarized in Table 3.5, and their graphical representation is shown in Figure 3.15.

Table 3.5: Final parameters of the piecewise nonlinearity.

Direction	Gap (mm)	Slope (N/m)
Positive	+0.28	2170
Negative	-0.12	1340
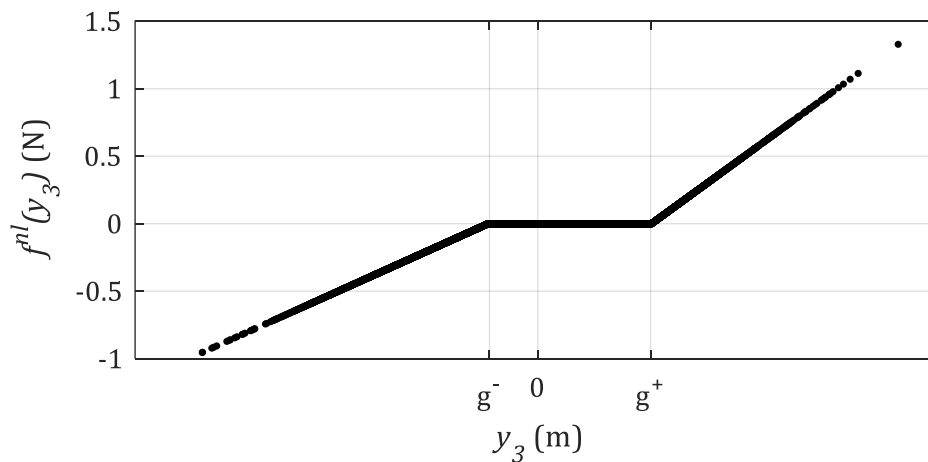
Figure 3.15: Identified nonlinear function $f^{nl}(y_3)$.

Finally, the identified nonlinear model is validated over the residuals with the measured outputs $\boldsymbol{y}^{val}(t)$ of the validation set. Three validation sets with

increasing excitation levels are considered, namely F3, F4 and F6. The simulated outputs $y^{id}(t)$ are first generated using the identified state-space model given as input the measured force $f^{val}(t)$ of each validation set. The residual with the measured output $\|y^{id}(t) - y^{val}(t)\|$ is then computed both in time and frequency domains. The comparison is depicted in Figure 3.16 in the frequency domain.
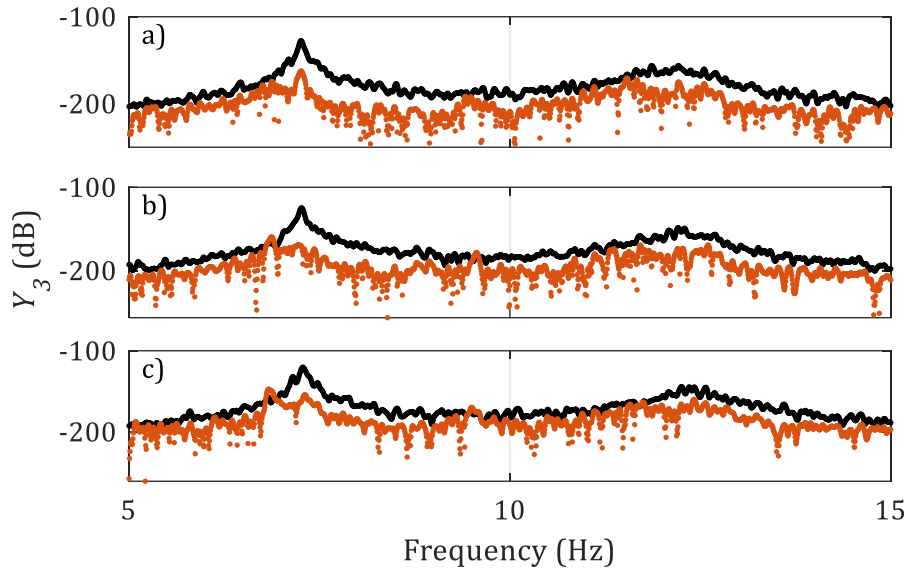
Figure 3.16: Validation of the nonlinear identification in the frequency domain. Black line: spectrum of the measured output in dB scales (ref. 1 m²/Hz), S3; orange line: residual with the spectrum of the simulated output. a) Validation set from level F3; b) Validation set from level F4; c) Validation set from level F6.

The relative RMS deviation between measured and simulated outputs in the considered frequency range is approximately 2% for the level F3, 3% for the level F4 and 5% for the level F6. As expected, the error is minimum for level F3, being the same level used for the identification, and increases for increasing excitation amplitude. In any case, there is a good match between simulations and measurements also for the highest level, whose detailed response in the time domain is shown in Figure 3.17.

To sum up, the identification has been carried out with a two-step procedure using NSI, first estimating the gaps and then the piecewise slopes. Also, both the underlying-linear system and the fully nonlinear state-space model are retrieved. The validation of the obtained model shows a good accuracy, especially when comparing measured and simulated outputs. However, some discrepancies are present in the underlying-linear system when compared with the result of a low-level linear identification. This is presumably related to a softening effect that is visible in the measurement, but not included in the nonlinear identification, as not related to the piecewise

behavior. Allegedly, this phenomenon is associated to the own weights of the moving plates and masses, influencing the dynamics of the system.
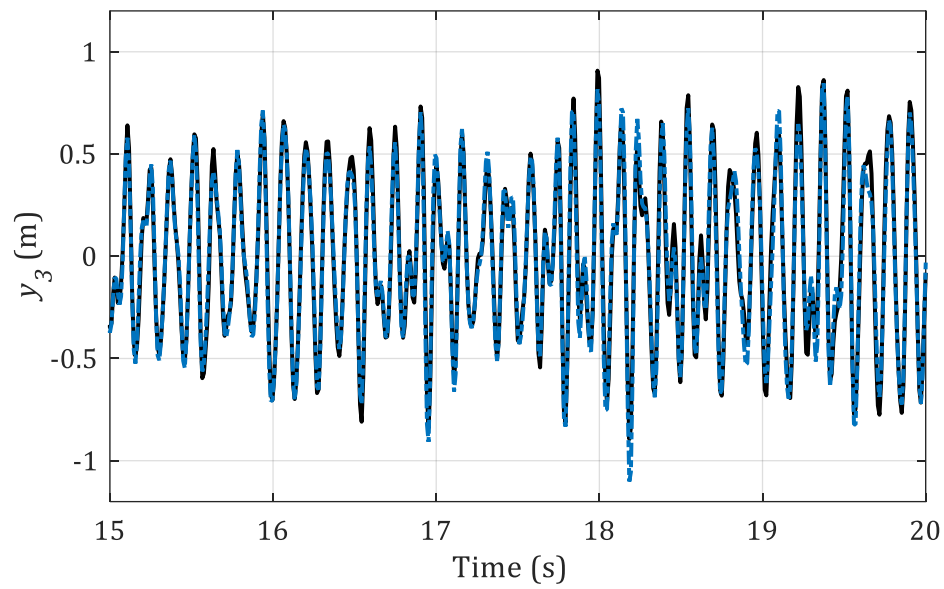
Figure 3.17: Validation of the nonlinear identification in the time domain, S3, validation set from level F6. Black line: measured output; blue line: simulated output.

Chapter 4

Free-decay-NSI via mass-change scheme

4.1. Introduction

As described in Chapter 3, NSI in its classical form needs input-output data to properly work, so that a persistent measured excitation must be provided to the structure under test. This is a general requirement of the methods developed so far for nonlinear system identification, and it originates from the very basic principle defining the nonlinear systems: the breaking of the superposition principle, and thus of the invariance of the FRFs (see Chapter 2). Since the response of a nonlinear system is nonlinearly linked to the energy provided to the system itself, it is straightforward that the latter should be known (or measured). Conversely, linear system identification with output-only data is a consolidated practice nowadays, and it is referred to as *stochastic identification* if the unmeasured input is assumed to be a realization of a stochastic process [62].

This need may be an issue in situations where providing and measuring a continuous input is difficult, or it simply alters the structure under testing. A practical example of the latter case will be given in Chapter 5, where an experimental nonlinear beam is excited with a shaker: given the slenderness of the beam, the attachment with the shaker deeply alters its dynamical response and its symmetry properties.

Attempts have already been made to identify nonlinear systems with output-only measurements, although no *true* nonlinear-stochastic identification method has been developed yet [37]. In [70] a time and frequency domain approach based on the RFS method and the NIFO method has been developed, to work with nonlinear systems with unmeasured input. In [71] RFS is adopted again, but in conjunction with the direct parameter identification method [72]. In [73] structural health monitoring is performed by identifying a black-box nonlinear environmental model for the slow variations of the damage-sensitive features due to changing environmental and operational conditions.

In this work, a novel version of NSI is proposed, to work in situations where no continuous input can be provided to the system under test. In particular, the case of free-decay measurements is considered, and NSI is combined with a mass-change technique to fill the missing information needed to complete the nonlinear model [74]. The method is referred to as "Free-decay-NSI" and it is validated on numerical and experimental data.

4.2. Description of the method

Referring to Eq. (3.1), the equation of motion can be written as a response to some given initial conditions if no forcing input is provided to the structure:

$$\begin{cases} M\ddot{y}(t) + C_v\dot{y}(t) + Ky(t) + f^{nl}(t) = 0 \\ y(t = 0) = y_0, \quad \dot{y}(t = 0) = \dot{y}_0 \end{cases} \tag{4.1}$$

The nonlinear restoring force is still $f^{nl}(t)$, as in Eq. (3.2). Instead, the extended input vector $f^e(t)$ of Eq. (3.4) reduces now to a vector containing only the nonlinear basis function, called $\xi^{nl}(t)$:

$$\xi^{nl}(t) = \begin{bmatrix} -\xi_1(t), & \dots, & -\xi_J(t) \end{bmatrix}^{\mathrm{T}} \tag{4.2}$$

so that the state-space formulation becomes:

$$\begin{cases} x(\tau + 1) = Ax(\tau) + B^{nl}\xi^{nl}(\tau) \\ y(\tau) = Cx(\tau) + D^{nl}\xi^{nl}(\tau) \end{cases} \tag{4.3}$$

The matrices A, B^{nl}, C, D^{nl} can be identified again using the subspace formulation. In particular, the underlying-linear dynamics are expressed by the state matrix A, as in Eq. (3.5). However, in contrast to the original formulation of NSI, the state-space model of Eq. (4.3) does not allow the identification of the FRFs of the underlying-linear system. Therefore, the coefficients μ_j cannot be estimated yet. Instead, the FRF matrix of the nonlinear feedbacks $G^{nl}(\omega)$ can be defined as:

$$\boldsymbol{G}^{nl}(\omega) = \boldsymbol{D}^{nl} + \boldsymbol{C}(z\boldsymbol{I} - \boldsymbol{A})^{-1}\boldsymbol{B}^{nl}, \quad z = e^{i\omega\Delta\tau} \tag{4.4}$$

$\boldsymbol{G}^{nl}(\omega)$ has the same structure as the vector of nonlinear basis functions $\boldsymbol{\xi}^{nl}$:

$$\boldsymbol{G}^{nl}(\omega) = \left[\boldsymbol{G}(\omega)\mu_1\boldsymbol{L}_1, \quad \dots, \quad \boldsymbol{G}(\omega)\mu_J\boldsymbol{L}_J\right] \tag{4.5}$$

The FRF matrix of the underlying-linear system $\boldsymbol{G}(\omega)$ is unknown in this case, but the modal parameters of the underlying-linear system $(\omega_r, \zeta_r, \boldsymbol{\psi}_r)$ can still be estimated by performing the eigenvalue decomposition of $\boldsymbol{A}$.

Of course, knowing these modal parameters is not sufficient, as the nonlinear part of the equation of motion must be identified as well. Looking at Eq. (4.5), it seems that this requires the knowledge of $\boldsymbol{G}(\omega)$, which should be somehow estimated. It is worth recalling that the FRF of the underlying-linear system can be assembled as a sum of single modes contributions in the case of underdamped modes. In terms of receptance it yields:

$$G_{pq}(\omega) = \sum_{r=1}^{N} \frac{{}_rA_{pq}}{\omega_r^2 - \omega^2 + 2i\omega\omega_r\zeta_r} \tag{4.6}$$

where ${}_rA_{pq} = \alpha_r^2\psi_{pr}\psi_{qr}$ is the residue of the rth mode, depending on the so-called *scaling factor* α_r. The problem reduces then to the estimation of this quantity for each identified mode, since all the other quantities are known so far. It should be noted that the scaling factors are related to the modal masses by the relation:

$$\alpha_r = \frac{1}{\sqrt{m_r}} \tag{4.7}$$

A common technique to estimate the scaling factors in linear operational modal analysis consists of adding known lumped masses to the structure in order to exploit the changes in natural frequencies and LNMs. This technique is generally referred to as *mass-change* [75–77]. The idea proposed here is based on the same approach, but brought to the nonlinear case.

It is assumed that the mass matrix $\boldsymbol{M}$ is modified by a quantity $\Delta\boldsymbol{M}$, leading to a modified structure, labeled with subscript $\bullet_I$. A new equation of motion can therefore be written:

$$\begin{cases} (\boldsymbol{M} + \Delta\boldsymbol{M})\ddot{\boldsymbol{y}}_I(t) + \boldsymbol{C}_v\dot{\boldsymbol{y}}_I(t) + \boldsymbol{K}\boldsymbol{y}_I(t) + \boldsymbol{f}^{nl}(t) = \boldsymbol{0} \\ \boldsymbol{y}_I(t=0) = \boldsymbol{y}_{I0}, \quad \dot{\boldsymbol{y}}_I(t=0) = \dot{\boldsymbol{y}}_{I0} \end{cases} \tag{4.8}$$

A new state-space formulation is inferred for the modified structure, represented by the matrices $\boldsymbol{A}_I, \boldsymbol{B}_I^{nl}, \boldsymbol{C}_I, \boldsymbol{D}_I^{nl}$, which can be identified again

using the subspace formulation. The set of modal parameters of the modified underlying-linear system can be obtained by performing the eigenvalue decomposition of $\boldsymbol{A}_I$, obtaining the natural frequencies ω_{Ir}, the damping ratios ζ_{Ir} and the unit-scaled mode shapes $\boldsymbol{\psi}_{Ir}$ for $r = 1, \dots, N$.

The next step of the technique involves the estimation of the scaling factors α_r, for which several methods have been developed for linear systems.

4.2.1. Estimation of the scaling factors

The mass-change technique consists of attaching masses to points of the structure where the mode shapes of both unmodified and modified structures are known [77]. This approach has been widely used in linear OMA, such as in bridges [75] and buildings [78], or in conjunction with FEM models [79].

The original idea arises from Parloo et al. [75], who estimated the scaling factors using a first-order approximation for the sensitivity of the natural frequencies with respect to the mass for light-damped structures. The method requires small changes in the natural frequencies, and thus low mass modifications. Other methods have been developed to improve the original one, and an comprehensive literature review can be found in [77]. In this chapter, the method proposed by Bernal [76] is adopted, which does not impose limitations on the spatial distribution or magnitude of the added masses.

The method requires the definition of an auxiliary matrix, called $\boldsymbol{\Lambda}$ and equal to:

$$\boldsymbol{\Lambda} = \boldsymbol{\Psi}^\dagger \, \boldsymbol{\Psi}_I \tag{4.9}$$

where the matrix $\boldsymbol{\Psi}_I$ is the modal matrix of the modified structure, containing the eigenvectors $\boldsymbol{\psi}_{Ir}$, while the matrix $\boldsymbol{\Psi}^\dagger$ is the pseudo-inverse modal matrix of the unmodified structure.

The modal scaling factors of the unmodified structure can therefore be computed by:

$$\alpha_r^2 = \frac{(\omega_r^2 - \omega_{Ir}^2)}{\omega_r^2} \frac{\Lambda_{rr}}{\boldsymbol{\psi}_r^{\mathrm{T}} \boldsymbol{\Delta M} \boldsymbol{\psi}_{Ir}}, \quad r = 1, \dots, N \tag{4.10}$$

where Λ_{rr} is the rth diagonal entry of $\boldsymbol{\Lambda}$. It should be noted that Eq. (4.10) is an exact formulation when a full set of modes is used to compute $\boldsymbol{\Lambda}$. Instead, the estimation of the scaling factors is approximated when a truncated set of modes is adopted. Luckily, the truncation error is expected to be small in the diagonal terms of $\boldsymbol{\Lambda}$, which are the only ones showing up in Eq. (4.10), therefore providing a reasonable accuracy in the estimation of the scaling factors [77].

4.2.2. Underlying-linear FRFs and nonlinear coefficients

Since all the quantities in Eq. (4.10) have been estimated by NSI, the scaling factors can be computed, and thus the FRF matrix G from Eq. (4.6). The coefficients of the nonlinearities μ_j can be estimated as well from Eq. (4.5). A flowchart of the identification process is shown in Figure 4.1.
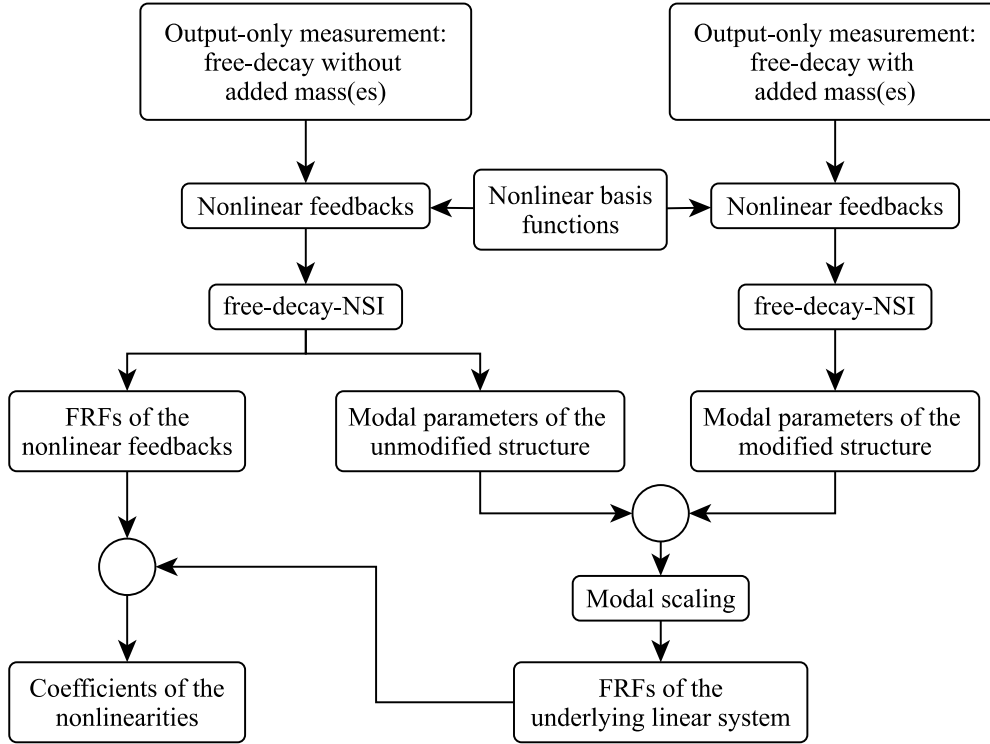
Figure 4.1: Flow-diagram of the free-decay-NSI identification.

It worth highlighting that the full FRF matrix is retrieved in this case, thus yielding:

$$\mu_j \boldsymbol{G} \boldsymbol{L}_j = \mu_j \begin{bmatrix} G_{11} & G_{12} & \cdots & G_{1N} \\ G_{21} & G_{22} & & \\ \vdots & & \ddots & \vdots \\ G_{N1} & & \cdots & G_{NN} \end{bmatrix} \boldsymbol{L}_j = \begin{bmatrix} G_{1j}^{nl} \\ G_{2j}^{nl} \\ \vdots \\ G_{Nj}^{nl} \end{bmatrix} \qquad (4.11)$$

The coefficient μ_j can be computed from Eq. (4.11) starting from any row of $\boldsymbol{G}$. This leads to an intrinsic redundancy of the methodology, as there are in principle N estimations of each coefficient. Conversely, when classical input-output NSI is used, the number of known rows of $\boldsymbol{G}$ is equal to the number of physical forcing inputs, that is generally one (Eq. (3.8)). Practically, it is possible to solve Eq. (4.11) in a least-square (LS) sense with respect to μ_j, also considering an appropriate weighting function. The choice of the weighting function can be deduced recalling that NSI does not estimate directly the

coefficient μ_j, but a frequency-dependent and complex-valued quantity $\mu_j^{id}(\omega) \in \mathbb{C}$. Based on this fact, two considerations can be made:

- A flat dependency on the frequency is expected, therefore a possible choice for the weighting function can be the inverse covariance matrix of the N estimations.
- The imaginary part should be negligible with respect to the real part, therefore the ratio between real and imaginary parts of $\mu_j^{id}(\omega)$ can be used as a possible weighting function.

These two considerations hold also in the case of standard NSI, as already discussed in Chapter 3. Eventually, a combination of the two considerations seems to give the best results, and it will be used in the following applications. Calling $\boldsymbol{W}_j(\omega)$ the weighting vector of the jth nonlinearity, it is therefore possible to write the following minimization problem:

$$\underset{\mu_j^{id}(\omega)}{\arg\min}\{\boldsymbol{\varepsilon}_j^{\mathrm{H}} \operatorname{diag}(\boldsymbol{W}_j)\,\boldsymbol{\varepsilon}_j\}, \quad \boldsymbol{\varepsilon}_j(\omega) = \begin{bmatrix} G_{1j}^{nl} \\ \vdots \\ G_{Nj}^{nl} \end{bmatrix} - \mu_j^{id}\boldsymbol{GL}_j \qquad (4.12)$$

with $\boldsymbol{\varepsilon}_j(\omega)$ being the residue at the frequency ω, and $\bullet^{\mathrm{H}}$ indicating the Hermitian transpose. The LS solution of Eq. (4.12) gives the complex-valued quantity $\mu_j^{id}(\omega)$. Moreover, it is possible to split the single modes contributions to the jth nonlinearity, as in the classical NSI approach (Eqs. (3.12)-(3.14)).

4.3. Numerical application: 4DOFs nonlinear system with friction

A four degrees-of-freedom train of masses is considered, in the presence of Coulomb friction between DOFs 3 and 4. A representation of the system is depicted in Figure 4.2, where the nonlinear link is also shown, while the system parameters are summarized in Table 4.1. The free-decay response of the system is simulated by applying an impulsive force on mass 1 at the time $t = 0\ s$. The sampling frequency is $f_s = 500\ \text{Hz}$ and the total time of the simulation is 30 seconds. Time histories are obtained with the Newmark time integration scheme, and 1% of zero-mean Gaussian noise is added to each simulated output.

Table 4.1: Parameters of the 4 DOFs train of masses

Mass (kg)	Stiffness (kN/m)	Damping coefficients	Friction coefficient (N)
$m_1 = 1; m_2 = 5;$ $m_3 = 3; m_4 = 1.$	$k_1 = 6; k_2 = 5;$ $k_3 = 10; k_4 = 9.$	$\alpha = 0.1;$ $\beta = 10^{-4}.$	$c^{nl} = 5$
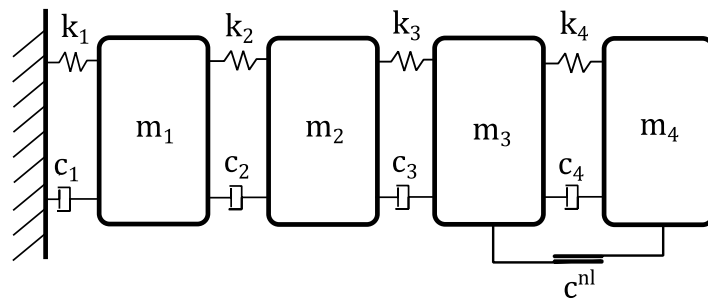
Figure 4.2: 4 DOFs nonlinear system with friction between DOF 3 and 4.

The displacements of the four DOFs are reported in Figure 4.3, while the spectrogram of DOF 4 is shown in Figure 4.4.
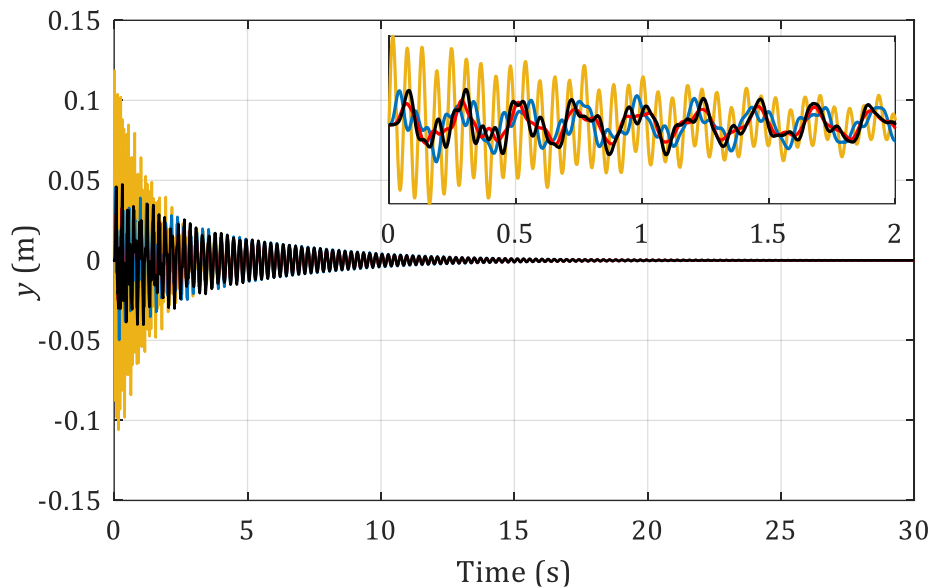
Figure 4.3: Displacements of the 4 DOFs system with zoom around the first 2 seconds. Yellow line: DOF 1; blue line: DOF 2; red line: DOF 3; black line: DOF 4.

The frequency values reported in the y-axis of the spectrogram are the natural frequencies of the underlying-linear system. It can be noted that the frequency content of the response is a lot richer than the only natural frequencies lines, allegedly due to the nonlinear nature of the simulated outputs.
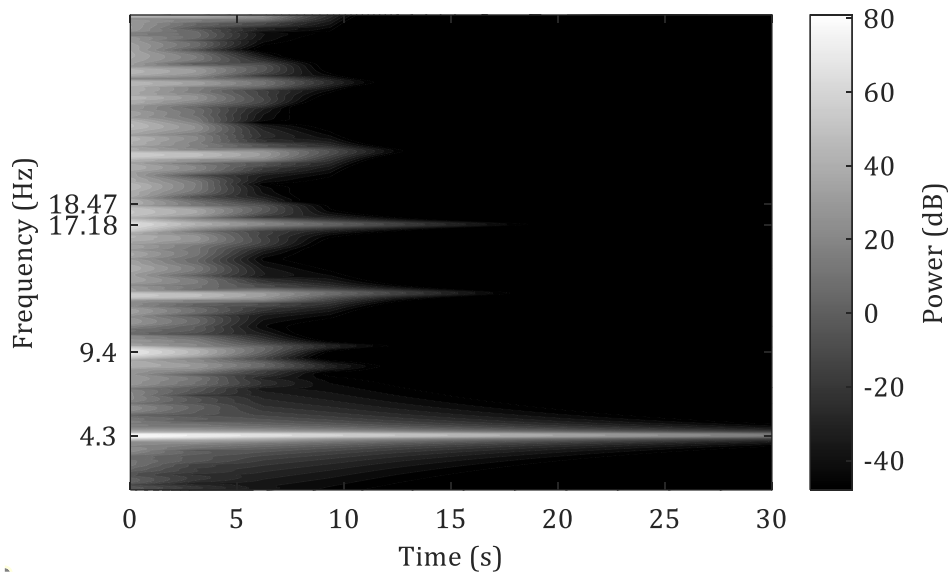
Figure 4.4: Acceleration spectrogram of DOF 4. The frequency values reported in the y-axis are the natural frequencies of the underlying-linear system.

The identification is performed with free-decay-NSI considering the nonlinear basis function $\xi(t) = \text{sign}(\dot{y}_4 - \dot{y}_3)$ with location vector $\boldsymbol{L} = [0 \quad 0 \quad -1 \quad 1]^{\text{T}}$.

The stabilization diagram of the underlying-linear system is depicted in Figure 4.5, obtained by increasing the model order from 2 to 20. Stabilization is checked for frequencies, damping ratios and MACs, and a model order equal to 8 is eventually chosen.

The set of identified modal parameters of the underlying linear system $\{\omega, \zeta, \boldsymbol{\psi}\}_{r=1,...,4}$ is extracted and reported in Table 4.2 in terms of natural frequencies and damping ratios.

The whole process is then repeated with the modified structure, where a change in the mass distribution is accomplished by increasing each lumped mass by 10%. The new set of identified modal parameters of the underlying-linear system for the modified structure $\{\omega_I, \zeta_I, \boldsymbol{\psi}_I\}_{r=1,...,4}$ is referred to as "Set I" and it is reported in Table 4.2 in terms of natural frequencies. The associated damping ratios are not listed, as they are not needed in the methodology.
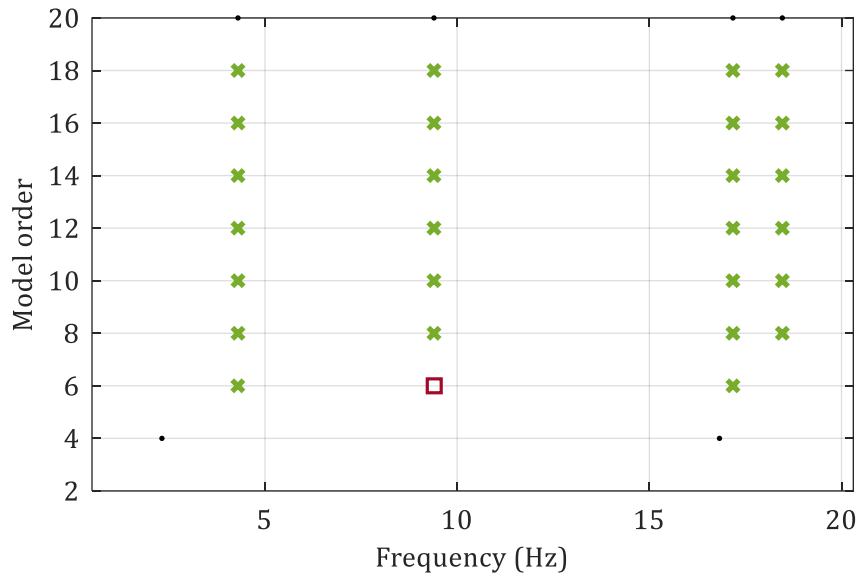
Figure 4.5: Stabilization diagram of the ULS. Stabilization thresholds: 0.5%, 10% and 99.5% for frequencies, damping ratios and MACs respectively. Black dot: new pole; blue plus: pole stable in frequency; red square: pole stable in frequency and MAC; green cross: pole stable in frequency, MAC and damping.

Table 4.2: Identified modal parameters of the 4 DOFs system.

| Mode | Frequency (Hz) | | Damping ($\%$) |
	Unmodified	Set I	Unmodified
1	4.30	4.10	0.32
2	9.40	8.97	0.38
3	17.17	16.38	0.59
4	18.46	17.59	0.69

The modal scaling factors and the modal masses are eventually computed from Eq. (4.10) and Eq. (4.7), respectively. The identified modal masses are then compared with the theoretical ones in Table 4.3, where a decent agreement can be noted.

Table 4.3: Identified modal masses of the 4 DOFs system.

Mode	Identified modal mass (kg)	Theoretical modal mass (kg)	Difference (%)
1	8.25	8.09	1.98
2	6.09	5.92	2.90
3	1.11	1.10	0.49
4	1.68	1.71	1.72

The FRF matrix of the underlying linear system is then built according to Eq. (4.6), and the FRF $G_{11}(\omega)$ is depicted in Figure 4.6 and compared with the theoretical one. A great correspondence is retrieved also in this case between

identified and theoretical results. As for the nonlinear identification, the coefficient of the nonlinearity $\mu_1 = c^{nl}$ is identified solving Eq. (4.12) in a LS sense. Since the full FRF matrix is available, $N = 4$ estimations of μ_1 are retrieved considering the 4 DOFs as inputs for each mode $r = 1, \dots, 4$. Thus, a total of 16 possible estimations can be obtained. As pointed out in the previous section, not all the modes equally contribute to the nonlinear part of the response. Indeed, the LS solution should take into account this information, and this can be done automatically by choosing the weighting function according to the guidelines provided in the previous section. Eventually, the final value for the nonlinear coefficient can be obtained by considering the spectral mean $\bar{\mu}_1^{id}$ of the real part of the weighted LS solution $\Re[\mu_1^{id}(\omega)]$. The result is $\bar{\mu}_1^{id} = 4.96\,N$ with a standard deviation of $0.20\,N$, providing a percentage error of 0.79% from the true value.
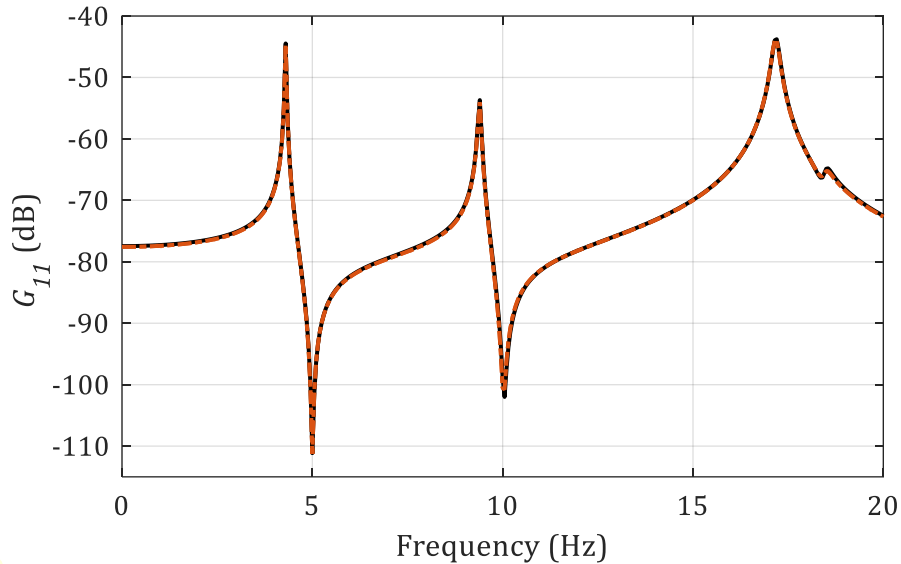
Figure 4.6: Driving-point linear FRF G_{11} for the 4 DOFs system in dB scales (ref. 1 m/N). Continuous black line: identified FRF; dashed-dotted orange line: theoretical FRF.

Real and imaginary parts of the LS solution μ_1^{id} are depicted in Figure 4.7. It should be noted that the imaginary part is always several orders of magnitude lower than the real part, assessing the goodness of the identification.
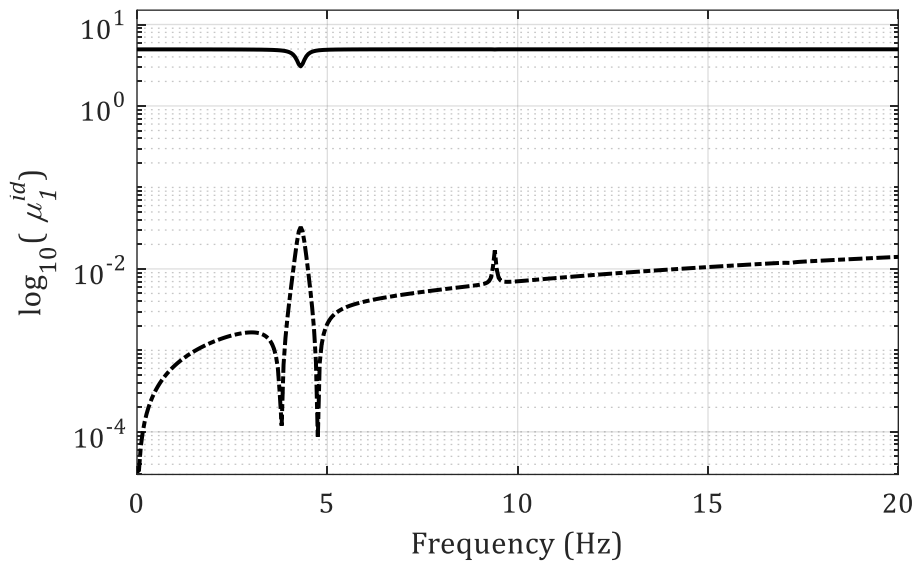
Figure 4.7: Coefficient of the nonlinearity for the 4 DOFs system in logarithmic scale. Continuous black line: real part of the LS solution; dashed-dotted black line: imaginary part of the LS solution.

4.4. Experimental application: nonlinear scaled building

The experimental application is composed of five aluminum plates connected by thin steel beams (Figure 4.8) [65]. It can be assumed that the vertical beams provide just a flexural stiffness contribution, thus the rig may be reasonably considered as a 5 DOFs system. Three photos of the experimental setup are reported in Figure 4.9 and the characteristics of the structure are reported in Table 4.4. The nonlinearity is introduced by a thin pretensioned metallic wire connected to the fifth floor (Figure 4.9c). This acts like a nonlinear stiffness when the wire undergoes large amplitude oscillations. The restoring force produced by the wire can be written as a series expansion comprising a linear stiffness term k^{lin} plus a cubic one [80], thus having a nonlinear restoring force $f^{nl} = \mu_1 y_5^3$.
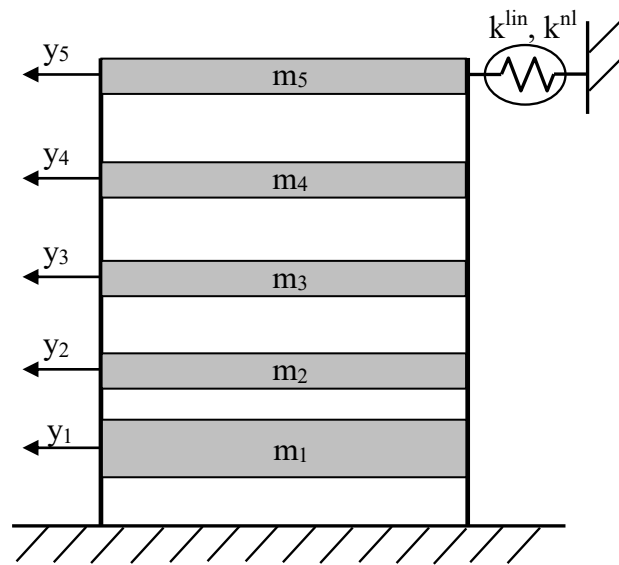
Figure 4.8: Multi-story building with nonlinearity produced by a thin wire.

Table 4.4: Characteristics of the experimental setup.

#	Plate Mass (kg)	Width (mm)	Length (mm)	Thickness (mm)	Vertical beam Length (mm)	Section (mm^2)
1	4.30	270	250	24	50	60×0.3
2	2.15	270	250	12	30	60×0.3
3	1.97	270	250	10	60	60×0.3
4	1.79	270	250	10	60	60×0.3
5	1.99	270	250	10	60	60×0.3

The free-decay response is recorded with 5 accelerometers positioned at each floor plus one on the ground, with sampling frequency $f_s = 409.6 \ Hz$ and duration of 40 s. The displacement of the fifth floor $y_5(t)$ is obtained by double integrating its measured acceleration $\ddot{y}_5(t)$.

A first characterization is carried out just processing the measured (output-only) data, to check whether the system truly behaves nonlinearly.

Figure 4.9: Photos of the experimental setup. a) Overall view with nonlinear link highlighted in red; b) Overall view with motion directions in green; c) Particular of the nonlinear link (thin wire).

4.4.1. Nonlinear characterization

The thin metallic wire is supposed to add a nonlinear stiffness contribution to the structure when it undergoes large amplitude oscillations. Since an impulsive response is considered, this allegedly happens at the beginning of the decay and vanishes as the time goes-by. In other words, the energy provided to the structure is not constant, as it would be in the case of external random excitation. This is not the ideal situation from a nonlinear identification point of view, as the nonlinear response itself depends on the energy given to the system. The nonlinear behavior is therefore expected to be dominant during the first instants of the response. Afterwards, a linear regime should be reached. For these reasons, the only frequency analysis of the output spectra is not helpful anymore. A time-frequency analysis, on the other hand, seems to be the best choice, as changes in the natural frequencies over time can be exploited, if the structure behaves nonlinearly. In particular, they will generally tend to the linear natural frequencies starting from a shifted (presumably higher) value in this case.

The spectrogram of the output $\ddot{y}_2(t)$ is shown in Figure 4.10a, and the instantaneous frequency of the five modes is directly extracted. The other sensors show a similar behavior. The percentage frequency shifts of the five extrapolated modes are depicted in Figure 4.10b, taking as starting values the instantaneous frequencies at $t = 0\ s$. A relatively high frequency shift is detected for the first mode of the structure, and it progressively dies out as the mode number increases. The frequency associated to the fifth mode seems not

to be affected by the nonlinearity at all. The instantaneous frequencies seem to stabilize after almost 15 seconds, meaning that a linear regime is reached.
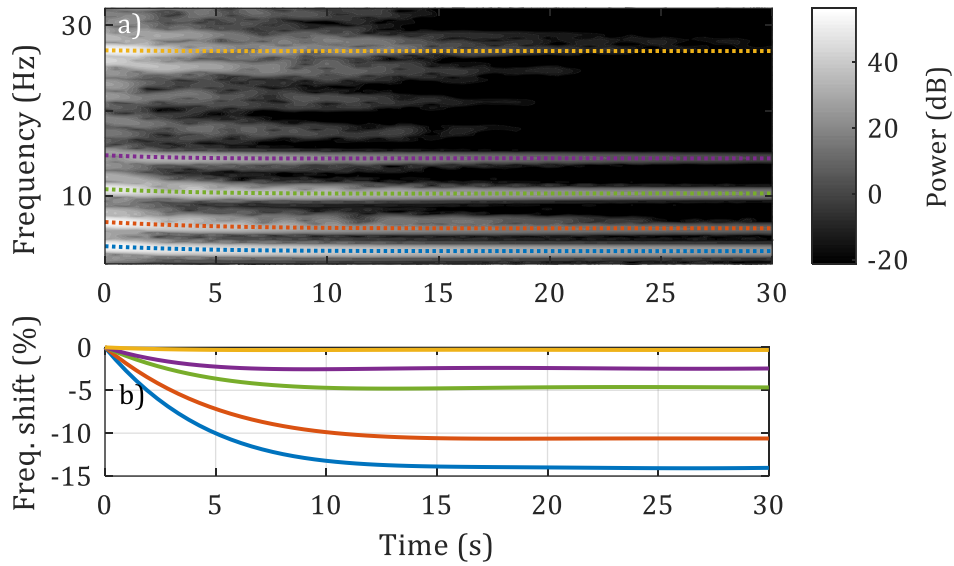
Figure 4.10: Time-frequency analysis of the multi-story building. a) Spectrogram of the acceleration of y_2; b) Frequency variations of the five modes. Blue line: mode 1; orange line: mode 2; green line: mode 3; purple line: mode 4; yellow line: mode 5.

A nonlinear response is then retrieved during the first instants of the acquisition, and therefore nonlinear system identification can be applied.

4.4.2. Nonlinear identification

The identification is performed with free-decay-NSI considering the following nonlinear basis functions and location vectors:

$$\begin{array}{ll} \xi_1(t) = y_5(t)^3 & \xi_2(t) = y_5(t)^2 \\ \boldsymbol{L}_1 = [0\ 0\ 0\ 0\ 1]^T & \boldsymbol{L}_2 = [0\ 0\ 0\ 0\ 1]^T \end{array} \tag{4.13}$$

A quadratic nonlinear basis function ξ_2 is also added to DOF 5 to account for possible asymmetries in the nonlinear restoring force, generally present in real structures.

The stabilization diagram of the underlying-linear system is obtained by increasing the model order from 2 to 20 and it is depicted in Figure 4.11. Stabilization is checked for frequencies, damping ratios and MACs, and the set of identified modal parameters of the underlying-linear system $\{\omega, \zeta, \boldsymbol{\psi}\}_{r=1,\dots,N}$ is eventually extracted and reported in Table 4.5 in terms of natural frequencies and damping ratios. The model order for each mode is selected according to the median-damping criterion [81].
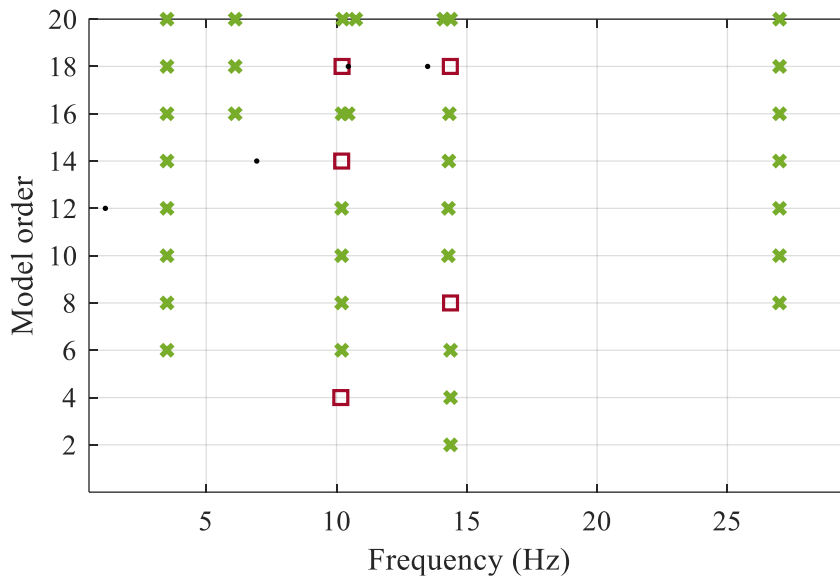
Figure 4.11: Stabilization diagram of the ULS. Stabilization thresholds: 0.5%, 10% and 99.5% for frequencies, damping ratios and MACs respectively. Black dot: new pole; blue plus: pole stable in frequency; red square: pole stable in frequency and MAC; green cross: pole stable in frequency, MAC and damping.

The whole process is then repeated with the modified structure, where a change in the mass distribution is considered. In this case, this is accomplished by adding a mass equal to 1.99 kg first on the fifth floor and then on the third floor. The reason of this choice can be found when looking at the identified mode shapes of the unmodified structure, reported in Figure 4.12. It can be seen that the fifth identified mode has a node on the fifth floor. Thus, adding a mass there does not affect the corresponding mode, making the estimation of the fifth modal mass unreliable. For this reason, the latter is estimated by adding the mass on the third floor.

Output-only-NSI is applied with both the modifications, leading to two sets of underlying-linear modal parameters:

- Set I, $\{\omega_I, \zeta_I, \boldsymbol{\psi}_I\}_{r=1,...,N}$ with the mass on the fifth floor;
- Set II, $\{\omega_{II}, \zeta_{II}, \boldsymbol{\psi}_{II}\}_{r=1,...,N}$ with the mass on the third floor.

The identified natural frequencies related to the two sets are listed in Table 4.5.
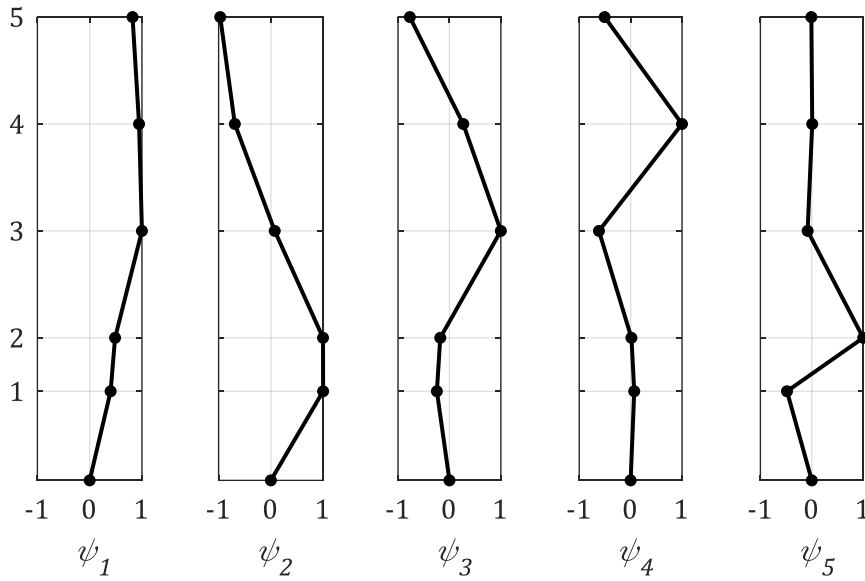
Figure 4.12: Linear mode shapes of the multi-story building.

Table 4.5: Identified modal parameters of the multi-story building.

| Mode | Frequency (Hz) | | | Damping (%) |
	Unmodified	Set I: Mass on the 5th floor	Set II: Mass on the 3rd floor	Unmodified
1	3.49	3.02	3.06	0.49
2	6.11	5.46	6.08	0.48
3	10.20	8.93	8.61	0.25
4	14.38	13.34	14.31	0.18
5	27.00	26.61	26.85	0.53

As for the variations in the mode shapes, the MACs between the unmodified and the modified mode shapes are shown in Figure 4.13. It can be seen that the MAC between $\boldsymbol{\psi}_5$ and $\boldsymbol{\psi}_{I5}$ is equal to 1, as expected. Eq. (4.10) is then applied to the two configurations, and the final modal scaling factors are computed by averaging the two set of estimations, except for the cases of unitary MAC for either one of the two sets. The identified values for the modal masses are listed in Table 4.7. Also, a comparison with the results obtained performing the (linear) stochastic subspace identification on the last part of the response (linear behavior) is presented in the following sub-section.
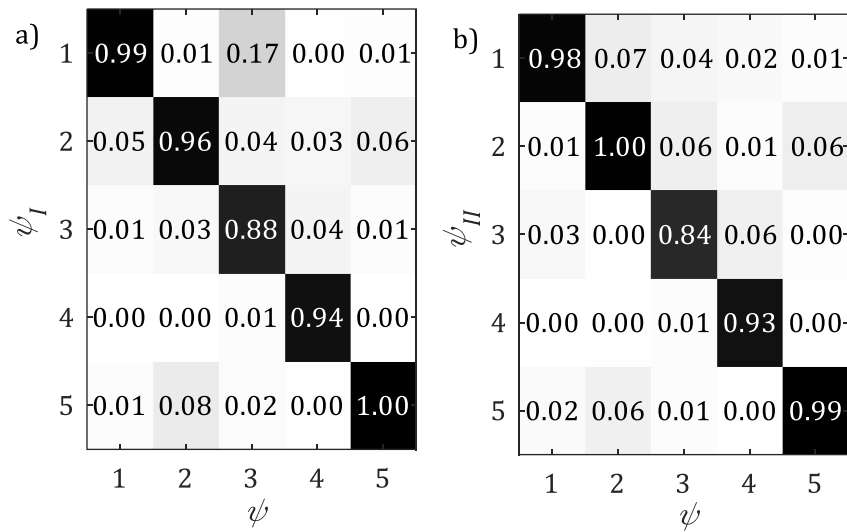
Figure 4.13: MAC between the mode shapes of the building in the unmodified and modified configurations. a) Set I, mass added on the fifth floor; b) Set II, mass added on the third floor.

Comparison with the linear identification

Since the mass-change method has been originally developed for linear systems, it is useful to check what happens with linear measurements, also to validate the results obtained with the free-decay-NSI method. Thus, the same free-decay dataset used so far is considered here, but the first part is cut off to let just the linear response to be present. Referring to Figure 4.10, the instantaneous frequencies stabilize after almost 15 seconds, so this value is chosen as cutting time. Stochastic subspace identification (SSI) is then performed considering the unmodified structure and the two sets of modifications, to retrieve the linear modal parameters and to estimate the modal masses of the unmodified configuration.

The stabilization diagram of the unmodified structure is depicted in Figure 4.14, and the model order for each mode is selected according to the median-damping criterion. The identified modal parameters for the three situations are listed in Table 4.6.

A decent correspondence is retrieved between the results listed in Table 4.5 (underlying-linear systems with free-decay-NSI) and the results of Table 4.6 (linear identification with SSI). In particular, the deviation on the identified natural frequencies is generally below 1%, while a higher dispersion is retrieved for the damping ratios. This is very common, as uncertainties in the damping estimation are always quite high. Furthermore, the activation of the stiffness nonlinearity in the complete decay response is likely to trigger some nonlinear dissipation phenomenon as well, possibly related to the contact between the aluminum decks and the vertical slender beams, or also to the thin metallic wire undergoing large amplitude oscillations.

Table 4.6: Identified modal parameters of the multi-story building, linear system identification.

Mode	Frequency (Hz)			Damping (%)
	Unmodified	Set I	Set II	Unmodified
1	3.51	3.05	3.08	0.40
2	6.12	5.42	6.10	0.21
3	10.25	8.94	8.62	0.16
4	14.35	13.34	14.29	0.25
5	27.05	26.47	26.80	0.42

As for the computation of the modal masses, Eqs. (4.10) and (4.7) are applied again, with the considerations previously made about the position of the added mass still holding. The identified modal masses using the free-decay-NSI method (on the full-nonlinear-decay) and the SSI method (on the truncated-linear-decay) are listed in Table 4.7.
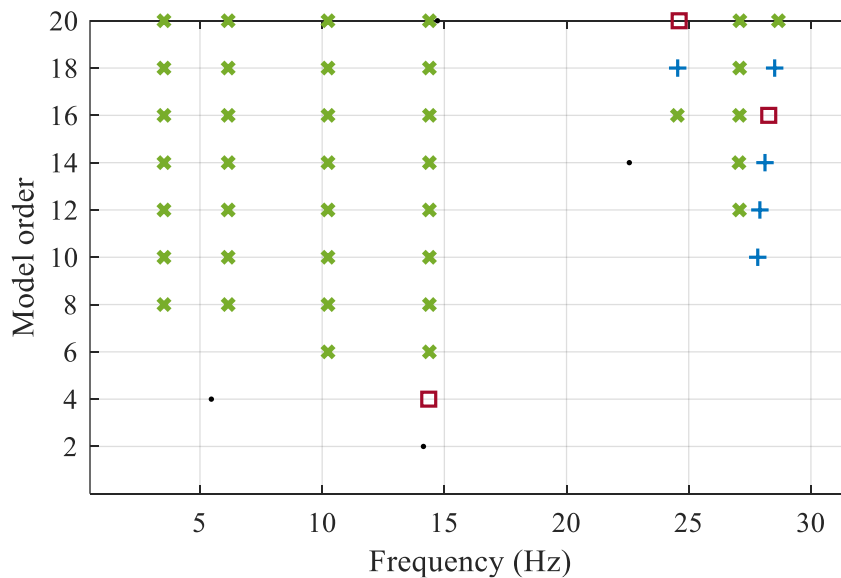
Figure 4.14: Stabilization diagram, linear system identification. Stabilization thresholds: 0.5%, 10% and 99.5% for frequencies, damping ratios and MACs respectively. Black dot: new pole; blue plus: pole stable in frequency; red square: pole stable in frequency and MAC; green cross: pole stable in frequency, MAC and damping.

Table 4.7: Identified modal masses of the multi-story building.

Mode	Modal mass (kg), Free-decay-NSI	Modal mass (kg), SSI	Difference (%)
1	5.47	5.69	4.05
2	6.82	6.26	8.20
3	3.94	3.83	2.67
4	1.34	1.37	2.44
5	0.79	0.47	39.48

Generally, there is a good agreement between the estimation of the modal masses. The only exception is the fifth mode, showing a high percentage deviation. This can be explained by considering that the identification with SSI is performed by cutting away the nonlinear part of the response from the decay. Since the fifth mode decays faster, it is possible that this mode is badly identified from the truncated linear decay. This is also confirmed by the spectrogram of the output no. 2 in Figure 4.10: the power associated to the fifth mode is highly reduced after 15 seconds, in contrast to the other modes. Eventually, the FRFs of the underlying-linear system are estimated for both free-decay-NSI and SSI from Eq. (4.6). A comparison is depicted in Figure 4.15 for the driving point FRFs G_{11} and G_{33}. As expected, the agreement is very good except around the fifth mode, for the aforementioned reasons.
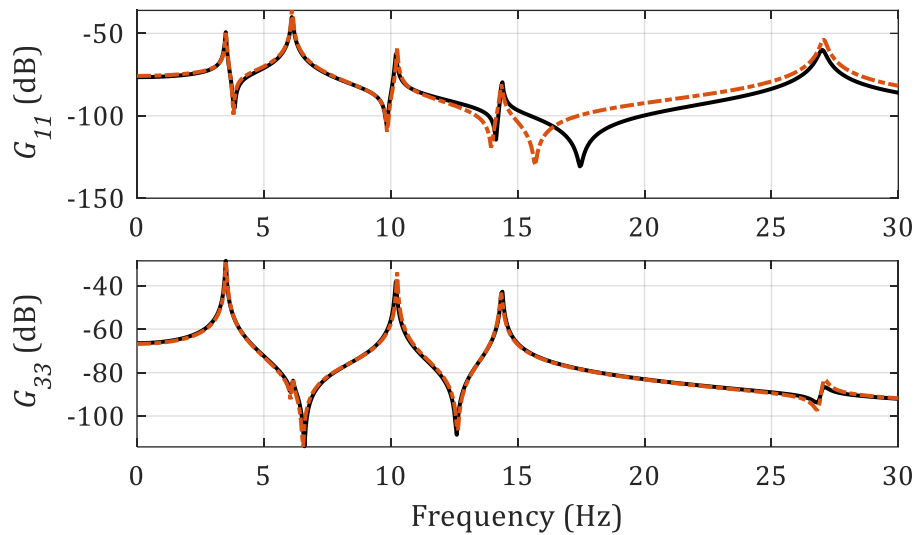
Figure 4.15: Underlying-linear FRFs of the multi-story building in dB scales (ref. 1 m/N). Continuous black line: free-decay-NSI estimation; dashed-dotted orange line: SSI estimation. a) G_{11}; b) G_{33}.

Identification of the nonlinear restoring force

After validating the identification of the underlying-linear system, the nonlinear part of the model of Eq. (4.1) can be estimated as well. According to Eq. (4.13), two nonlinear feedbacks are considered in this case, respectively cubic and quadratic. Thus, two coefficients should be identified in a LS sense. As for the single modes contributions, the first and second identified modes are considered in this case, as they show a higher frequency shift in Figure 4.10. With this choice, the final values for the two coefficients can be obtained as the spectral mean of the real parts of the LS solutions, leading to $\bar{\mu}_1^{id} = 5.2 \cdot 10^7 \text{ N/m}^3$ (with a standard deviation of $2.4 \cdot 10^6 \text{ N/m}^3$) and $\bar{\mu}_2^{id} = 6.7 \cdot 10^4 \text{ N/m}^2$ (with a standard deviation of $5.2 \cdot 10^3 \text{ N/m}^2$). The single estimations are reported in Figure 4.16 in terms of spectral mean of their real

parts. The darkness of the dots is proportional to their weight in the LS solution. Also, the final identified values $\bar{\mu}_{1,2}^{id}$ are depicted.

The contributions associated to the second mode are generally weighted more, except for the third DOF, i.e. the dots labeled as $_2G_{31}^{nl}$ and $_2G_{32}^{nl}$. Interestingly, the third DOF of the mode shape $\boldsymbol{\psi}_2$ is almost a node (Figure 4.12), thus making the estimation of the coefficients unreliable for the combination $u = 3$ (DOF), $r = 2$ (mode). This is correctly caught by the weighting function, which puts almost to zero the corresponding weight.
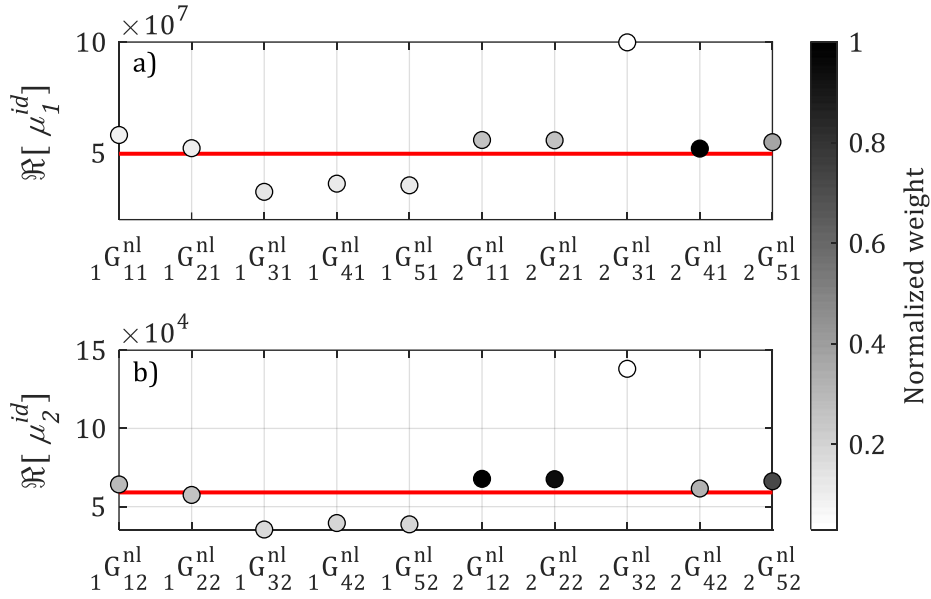
Figure 4.16: Coefficients of the cubic nonlinearity in (a) and the quadratic nonlinearity in (b) of the multi-story building. Red line: real part of the LS solution; dots: single estimations. The intensity of the color of the dots is proportional to their weight in the LS solution.

Eventually, the real and imaginary parts of the LS solutions are depicted in Figure 4.17. It should be noted that the imaginary parts are always several times lower than the real parts.
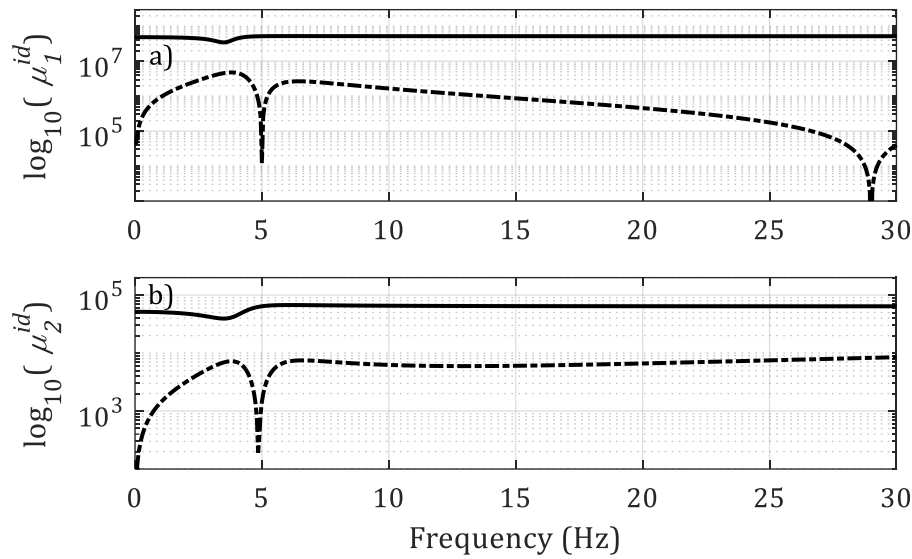
Figure 4.17: Coefficients of the nonlinearities of the multi-story building in logarithmic scales. Continuous black line: real part of the LS solution; dashed-dotted black line: imaginary part of the LS solution. a) Cubic coefficient; b) Quadratic coefficient.

The identified nonlinear restoring force $f^{nl} = \bar{\mu}_1^{id} y_5^3 + \bar{\mu}_2^{id} y_5^2$ is depicted in Figure 4.18 as a function of $y_5(t)$. A zoom around the origin is also reported in Figure 4.18b, where the asymmetry introduced by the quadratic term is visible.
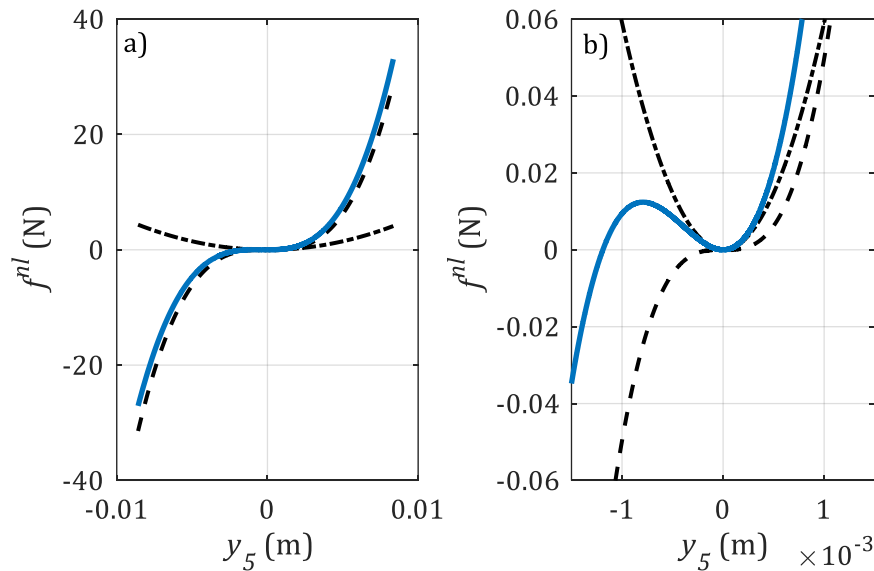
Figure 4.18: Nonlinear restoring force of the multi-story building in (a) and zoom around the origin in (b). Dashed black line: cubic term; dashed-dotted black line: quadratic term; blue line: total force f^{nl}.

The RMS value of cubic component of f^{nl} is approximately 5 times higher then the quadratic one, thus the response in mostly symmetric.

4.5. On the initial energy supply

The method presented in this chapter is based on free-decay measurements of nonlinear structures. This implies that the energy associated to the nonlinear effects varies with the signal decay, as seen in the previous sections. It is therefore useful to investigate the initial energy supplied to the structure, in order to make sure that nonlinearity is properly triggered. A low initial energy would result in a poor nonlinear excitation, and the identification method would struggle to get satisfying results in the estimation of the nonlinearity. On the other hand, other side effects might occur if the initial energy is too high, possibly associated to nonlinear phenomena such as large amplitude vibrations.

The spectrogram of the acceleration of y_2 is depicted in Figure 4.19 for three different excitation levels in the case of no added mass: the first level (Figure 4.19a) is the selected one for the identification in the previous section, the second level (Figure 4.19b) corresponds to a lower initial energy, while the third level (Figure 4.19c) corresponds to a higher initial energy.
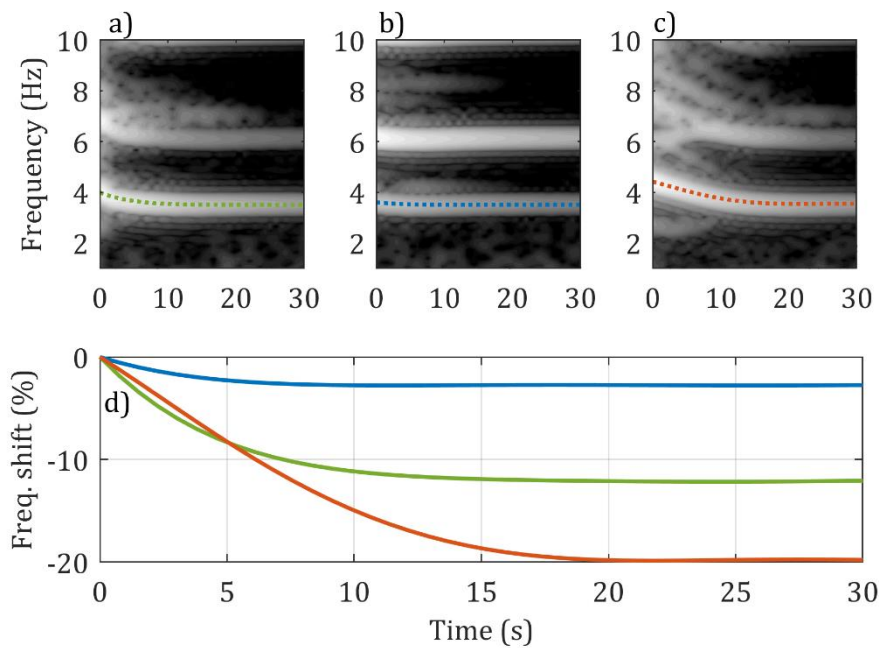
Figure 4.19: Time-frequency analysis of the multi-story building for different initial energy levels. a) Spectrogram of the acceleration of y_2, selected level; b) Spectrogram of the acceleration of y_2, low energy; c) Spectrogram of the acceleration of y_2, high energy; d) Frequency variations of the first mode for the three levels.

Figure 4.19d shows the percentage frequency shifts of the first extrapolated mode for the three excitation levels, taking as starting values the instantaneous frequencies at $t = 0$ s. The selected level has a maximum frequency shift of roughly 12%, while it becomes 2% for the lower level and 20% for the higher one. It is worth recalling that the first mode used to be the

most nonlinear in the previous characterization, which is the reason why it has been chosen here as a comparison feature.

When performing the nonlinear system identification with the proposed method, different scenarios are obtained for the different initial energy levels. The stabilization diagrams of the ULS for the three cases are depicted in Figure 4.20. Only the totally-stable poles are shown, i.e. the poles stable in frequency, MAC and damping. The stabilization diagram of the low-energy level (in blue plus) shows a good stability for the first four modes, while the last one is poorly excited and barely visible. Instead, the stabilization diagram of the high-energy level does not show a decent stability: the second mode is not stable at all, and the third mode is unstable for every model order but one. This excitation level is therefore not appropriate for the proposed method to be applied. The physical reason might be that a very high initial energy possibly triggers some other dynamical phenomena, like geometrically nonlinear effects on the vertical beams.
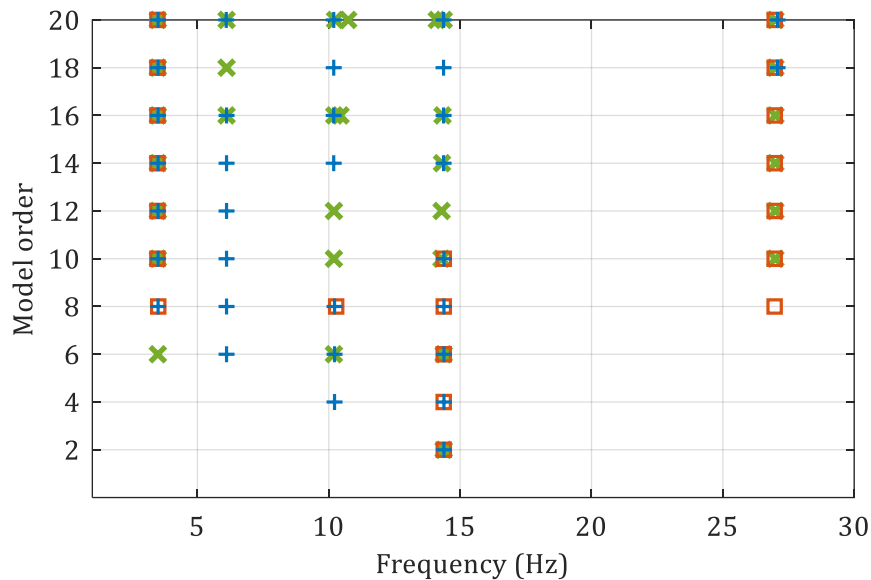
Figure 4.20: Stabilization diagrams of the ULS for the three excitation levels. Stabilization thresholds: 0.5%, 10% and 99.5% for frequencies, damping ratios and MACs respectively. Green cross: totally-stable pole, selected level; blue plus: totally-stable pole, low energy; orange square: totally-stable pole, high energy.

As for the lower excitation level, one can try to use free-decay-NSI to estimate the coefficients of the nonlinearities, although it is very likely that a poor estimation will be obtained. For the sake of completeness, the whole identification process previously seen is repeated, but considering the low-energy measurement of Figure 4.19b when there is no added mass, and two low-energy measurements when the mass is on the fifth floor and on the third floor. The maximum frequency shift for both cases is of the same magnitude of the unmodified setup in Figure 4.19b. The same nonlinear feedbacks of Eq.

(4.13) are considered, respectively cubic and quadratic. Thus, two coefficients can be identified in a LS sense, and real and imaginary parts of the LS solutions are depicted in Figure 4.21.
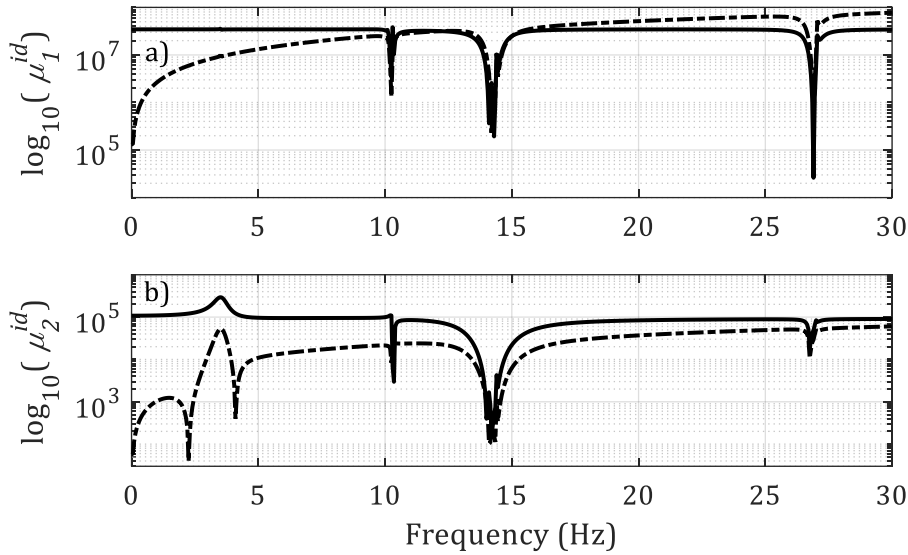
Figure 4.21: Coefficients of the nonlinearities of the multi-story building in logarithmic scales, low energy case. Continuous black line: real part of the LS solution; dashed-dotted black line: imaginary part of the LS solution. a) Cubic coefficient; b) Quadratic coefficient.

As expected, the identification is not successful in this case, as the imaginary parts of the identified coefficients are very high compared to the real parts. Therefore, the confidence in the estimated coefficients is very poor.

This example highlights the importance of choosing an adequate excitation level when performing nonlinear system identification. Indeed, this is a general requirement for nonlinear systems, and it is not restricted to the proposed methodology. The main difference in this case is that no forcing input is present, which makes harder to quantify the entity of the nonlinear distortions. Nevertheless, the time-frequency analysis and the stabilization diagrams can help the user selecting a good initial energy level.

4.6. Concluding remarks

A method has been proposed in this chapter to perform nonlinear system identification of vibrating structures starting from output-only free-decay measurements. To accomplish this task, a modified version of NSI has been developed in combination with a mass-change scheme. Although generally free-decay measurements are not convenient for nonlinear system identification, as the nonlinearity is likely to be poorly excited, the decoupling capability of the presented method allows to maximize the confidence in the identification. This is carried out by weighting the single modes according to

their participation to the nonlinear behavior. The technique has been tested first on a numerical system involving a friction nonlinearity and subsequently on an experimental test bench of a nonlinear scaled building. Results have confirmed the capability of the methodology of identifying the underlying-linear and nonlinear parameters of the considered systems with a satisfying confidence. Therefore, the presented method can be considered suitable if no forcing input can be provided to a nonlinear structure, relying on an easy free-decay test.

Chapter 5

Nonlinear identification of distributed geometrical nonlinearities

5.1. Introduction

The methods and the applications described so far have been developed to identify a nonlinear model structure for localized-only nonlinearities. This certainly covers an extensive range of real-life situations, but it does not comprise the big class of *distributed nonlinearities*. This chapter accounts for this case, considering structures undergoing large-amplitude oscillations, i.e. a geometrically nonlinear behavior. This case is increasingly getting more attention in the research community, driven by the industrial need of designing lighter and more flexible structures to reduce polluting emissions. As an illustration, the *High Level Group on Aviation and Aeronautics Research* in Europe has signed the report *Flightpath 2050: Europe's Vision for Aviation* [82] in 2011, assessing the goals of the European air transports by 2050: reductions of 75% in CO_2 emission and 90% in NO_x emission per passenger kilometer. Because of these ambitious goals, studies on large-amplitude (nonlinear) oscillations are becoming crucial in the design process of vehicles and structures, as well as research on new sustainable and performing materials (e.g. composites).

Interestingly enough, the theory of large-amplitude vibrations of mechanical structures has a long tradition, going back to the 70s. The reader can refer to the work of A.H. Nayfeh and P.F. Pai [8] for an extensive literature review about nonlinear beams, plates and shells. Recently, geometrical nonlinearities have been considered in the design and analysis of several structural applications, such as helicopter blades, deployable solar panels, wind turbines, antennas and cylindrical shells [83,84].

Geometrical nonlinearity associated to large-amplitude oscillations results in a distributed nonlinear strain-displacement relation [85], causing the coupling between different planes of deformation (e.g. bending and in-plane stretching for thin walled structures). In this framework, a nonlinear model is very often obtained by projecting the physical domain onto a reduced-order basis, forming a reduced-order model [86]. The selection of the reduced-order basis becomes then a key step, and a well-known option consists in considering the linear normal modes (LNMs) as a projection space. This choice is straightforward in the case of linear systems, as the LNMs decouple the equations of motion providing a huge benefit in terms of reduction of model complexity and computational burden. In the case of nonlinear systems, this approach can still be chased with some limitations. In fact, a full decoupling is not possible, and the LNMs are able to reproduce the motion for moderately-large amplitudes of vibrations only [87]. Other possibilities are the use of nonlinear normal modes and modal derivatives [87], which enrich the projection space allowing a more complete nonlinear model. The computation of these quantities might be a non-trivial task tough, and an increase in the model complexity is rather sure. In any case, a reduced (still nonlinear) model should be retrieved at the end, defined by a set of parameters. These parameters have to be estimated, and this process is done via nonlinear system identification in this thesis, starting from experimental data.

While the existing literature on numerical studies about large-amplitude vibrations is quite rich, the same cannot be stated when experimental measurements are considered. A few recent works deal with this problem, but their application is generally restricted to harmonic excitations under the assumption of no modal couplings. In [88] the first bending mode of an experimental beam undergoing large-amplitude vibrations is characterized fitting the nonlinear frequency response function (FRF) via harmonic balance method. In [89] an experimental diesis-like structure showing a geometrical nonlinear behavior is considered, and its model parameters estimated under the assumption of no internal resonances fitting again the nonlinear FRF. In [90], the nonlinear normal modes of a shell-like structure are sought by applying the restoring force surface (RFS) method, leading to noticeable modelling errors. All the methods presented in [88–90] work in the modal

domain and rely on not so powerful nonlinear system identification algorithms, which may struggle in the case of multiple modes interactions.

In this chapter, the problem of identifying large-amplitude oscillations is faced by considering a two-steps strategy, proposed in the following section. This novel methodology is intended to work with experimental data under a broadband Gaussian excitation. Therefore, multiple modes are excited simultaneously, and no restrictions about the possible internal interactions are made. This is accomplished by extracting the nonlinear model directly from the measurements via nonlinear system identification in the modal domain, using an appropriate algorithm [91]. Thus, the LNMs are first extracted from the measurements and then they are used to obtain the nonlinear reduced-order model. An ad-hoc version of the NSI algorithm is proposed, called *Modal-NSI*, although it should be noted that the presented methodology can be applied with other nonlinear identification tools as well.

The whole methodology is validated on experimental data of a very thin beam exhibiting a distributed nonlinear behavior, tested at the Space Structures and Systems Laboratory of University of Liège, Belgium. The nonlinear basis functions are deduced from a nonlinear modal model of the beam, which is numerically compared with a commercial FE software (ANSYS, [92]) [93]. Since the expression of the nonlinearity is analytic and in a closed-form in the modal model, it is also possible to compute the nonlinear response using the harmonic balance method [26], for the computation of stable and unstable paths.

Eventually, the nonlinear system identification is performed by applying Modal-NSI on the experimental data. For the sake of completeness, a second nonlinear identification is also performed in the physical domain using the PNLSS black-box algorithm (Appendix B).

5.2. Nonlinear identification of distributed geometrical nonlinearities

The strategy proposed here makes use of the LNMs as reduction basis to create the reduced-order domain. In principle, the methodology can be applied with any nonlinear identification algorithm, in time or frequency domain. Of course, the amount of a-priori information needed depends on the *shade* of the adopted algorithm (see section 3.1). Whatever algorithm is used, the LNMs are needed in order to build the reduced-order domain. It is important to highlight that the LNMs have to be computed just in the points where the sensors are located. In other words, a full analytical description of the mode shapes is not needed. This implies that a low-excitation level test should be performed first to extract the modal parameters using a linear identification algorithm.

5.2.1. Problem statement

Let us consider a generic continuous nonlinear system, whose equation of motion can be written as:

$$M[\ddot{w}(\boldsymbol{x},t)] + C_v[\dot{w}(\boldsymbol{x},t)] + K[w(\boldsymbol{x},t)] = f(\boldsymbol{x},t) - f^{nl}(w,\dot{w}) \qquad (5.1)$$

where $w(\boldsymbol{x},t)$ is the displacement of the spatial coordinate $\boldsymbol{x} \in \mathcal{D}$ in the domain $\mathcal{D}$; M and K are the mass and stiffness linear differential operators [94], C_v is the proportional viscous damping operator, and $f(\boldsymbol{x},t)$ is the forcing input. The term $f^{nl}(w,\dot{w})$ represents again the nonlinear restoring force, i.e. the nonlinear part of the equation. For the case studied here, a distributed nonlinear behavior is considered and the LNMs ψ are used to operate in the modal domain. Using the expansion theorem, the solution of Eq. (5.1) can be expressed as:

$$w(\boldsymbol{x},t) \cong \sum_{j=1}^{N} \psi_j(\boldsymbol{x})\eta_j(t) \qquad (5.2)$$

where $\eta_j(t)$ is the jth modal coordinate and a total of N LNMs are taken into account. This choice is very common when dealing with distributed nonlinearities due to its simplicity. However, the LNMs do not decouple the equations of motion in a nonlinear setting, as stated in the introduction. A good accuracy is preserved for moderately-large amplitude vibrations and when large rotations are not present [95]. The following set of equations can be obtained substituting Eq. (5.2) into Eq. (5.1), and under the assumption of self-adjoint operators:

$$m_r\ddot{\eta}_r + c_r\dot{\eta}_r + k_r\eta_r = q_r - q_r^{nl}, \quad r = 1,2,\dots,N \qquad (5.3)$$

where m_r, c_r and k_r are the modal mass, damping and stiffness respectively, and $q_r(t) = \int_{\mathcal{D}} \psi_r(\boldsymbol{x})f(\boldsymbol{x},t)d\mathcal{D}$ is the modal force. The nonlinearity is now expressed by the term $q_r^{nl}(t) = \int_{\mathcal{D}} \psi_r(\boldsymbol{x})f^{nl}(\psi,\eta,\dot{\eta})d\mathcal{D}$.

A set of N nonlinear equations is obtained, and each one can be identified separately to retrieve a set of nonlinear modal models. The final model in the physical domain can be eventually assembled by performing the direct modal transformation. The nonlinear identification strategy is summarized in Figure 5.1.
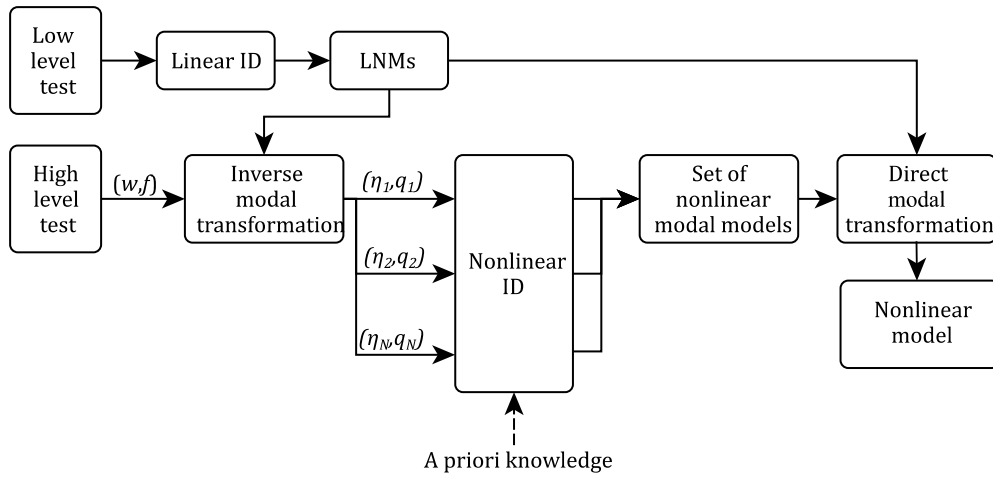
Figure 5.1: Flowchart of the nonlinear system identification strategy.

5.2.2. Modal-NSI

The feedback formulation of standard NSI can be recognized when looking at Eq. (5.3), with the difference that the nonlinear term q_r^{nl} is now in the modal domain. It is assumed hereafter that this term can be written as a linear-in-the-parameters basis function expansion up to a certain number J:

$$q_r^{nl} = \sum_{j=1}^{J} {}_r\mu_j \; {}_r\xi_j(t) \tag{5.4}$$

so that each contribution is defined by an unknown coefficient ${}_r\mu_j$ and a nonlinear basis function ${}_r\xi_j$. The same passages of standard NSI (see section 3.2) can then be repeated when working in the modal domain. In particular, the extended input vector becomes an extended *modal* input vector, called $\boldsymbol{q}_r^e(t)$:

$$\boldsymbol{q}_r^e(t) = \begin{bmatrix} q(t) & \xi_1(t) & \dots & \xi_J(t) \end{bmatrix}_r^{\mathrm{T}} \tag{5.5}$$

The subscript $\bullet_r$ is omitted hereafter to ease the notation, stating that all the steps refer to a single mode. A state vector $\boldsymbol{\lambda} = [\eta \;\; \dot{\eta}]^{\mathrm{T}}$ can be introduced to derive the following nonlinear discrete time (modal) state-space formulation:

$$\begin{cases} \boldsymbol{\lambda}(\tau + 1) = \boldsymbol{A}\boldsymbol{\lambda}(\tau) + \boldsymbol{B}^e \boldsymbol{q}^e(\tau) \\ \eta(\tau) = \boldsymbol{C}\boldsymbol{\lambda}(\tau) + \boldsymbol{D}^e \boldsymbol{q}^e(\tau) \end{cases} \tag{5.6}$$

where τ is the sampled time. The analogy between the state-space model of Eq. (5.6) and the standard one of Eq. (3.5) is evident, although the matrices $\boldsymbol{A}, \boldsymbol{B}^e, \boldsymbol{C}, \boldsymbol{D}^e$ are in this case the state, extended input, output and extended direct feedthrough *modal* matrices, respectively. Also, it follows from Eq. (5.6)

that recasting the nonlinear feedbacks into the extended modal input vector results in a multi-input system, with $J + 1$ forcing functions.

It is worth noticing that Eq. (5.6) represents in principle a single-degree-of-freedom system in the case of linear systems, as it is the result of the modal transformation. The model order in the modal state-space formulation is then theoretically equal to two. Therefore, the abovementioned matrices can be written as follows, assuming that displacements are measured:

$$
A = \begin{bmatrix} 0 & 1 \\ -m^{-1}k & -m^{-1}c \end{bmatrix} \in \mathbb{R}^{2\times2},
$$

$$
B^e = \begin{bmatrix} 0 & 0 & \dots & 0 \\ m^{-1} & m^{-1}\mu_1 & \dots & m^{-1}\mu_J \end{bmatrix} \in \mathbb{R}^{2\times(J+1)},
$$

$$
C = \begin{bmatrix} 1 & 0 \end{bmatrix} \in \mathbb{R}^{1\times2},
$$

$$
D^e = \begin{bmatrix} 0 & 0 & \dots & 0 \end{bmatrix} \in \mathbb{R}^{1\times(J+1)}
$$

(5.7)

For nonlinear systems, the LNMs can be used as a reduction basis in a Galerkin sense, but they do not guarantee a full decoupling. In the following, no assumption is made about the order of the modal model and stabilization diagrams will be used in the practical application to select the best model order on a case-by-case basis [59].

Once the rth state-space model A, B^e, C, D^e is identified, the final step is the estimation of the nonlinear coefficients $\mu_{j=1,\dots,J}$ and of the FRF of the underlying-linear (and modal) system $\Gamma(\omega)$. In particular, the extended FRF matrix $\Gamma^e(\omega)$ can be obtained from:

$$
\Gamma^e(\omega) = D^e + C(zI - A)^{-1}B^e, \quad z = e^{i\omega\Delta t}
$$

(5.8)

where I is the identity matrix and i is the imaginary unit. $\Gamma^e(\omega)$ has the same structure as the extended force vector q^e:

$$
\Gamma^e(\omega) = \begin{bmatrix} \Gamma(\omega), & \mu_1 \Gamma(\omega), & \dots, & \mu_J \Gamma(\omega) \end{bmatrix}
$$

(5.9)

so that its first block $\Gamma(\omega)$ is the FRF of the underlying linear (and modal) system. The nonlinear coefficients μ_j^{id} can eventually be deduced from the remaining blocks [53]. Note that the identified coefficients are still complex-valued frequency-dependent quantities $\mu_j^{id}(\omega) \in \mathbb{C}$, as in standard NSI.

If the steps described in Eqs. (5.4)-(5.9) are repeated for each participating mode r, a set of N nonlinear modal state-space models $\{A, B^e, C, D^e\}_r$ is obtained together with the full matrix of coefficients μ^{id}. The physical nonlinear model can eventually be assembled by computing the direct modal transformation, as in Figure 5.1. Thus, the simulated physical outputs w^{id} can

be computed from Eq. (5.2) when the modal (simulated) outputs η^{id} are considered. The FRF of the physical underlying-linear system, called $G(\omega)$, can be computed similarly by summing the contributions of the considered modes expressed by the modal FRFs $\Gamma_r(\omega)$ of Eq. (5.9), with $r = 1, \dots, N$, and knowing the corresponding LNMs.

5.3. Geometrically nonlinear beam: a modal model

A slender beam undergoing large flexural vibrations is considered. The governing equation is derived in [8] neglecting inertial and curvature nonlinear terms thanks to the slenderness assumption, and it is reported in Eq. (5.10):

$$m\ddot{w} + c_v\dot{w} + EIw^{IV} - EA\left[u^I + \frac{1}{2}(w^{II})^2\right]w^{II} = f(t)\,\delta(x - x_f) \qquad (5.10)$$

where $w(x, t)$ is the flexural displacement, $u(x, t)$ is the axial displacement, m is the linear density (kg/m), c_v is the viscous damping parameter (Ns/m^2), E is the Young's modulus (Pa), I is the moment of inertia (m^4), A is the transversal section of the beam (m^2), $f(t)$ is the external punctual force applied at position x_f and δ is the Dirac's delta. Also, a proportional viscous damping is considered to account for dissipation. When the flexural deflection is large, the axial force plays a significant role in carrying transverse loads, and geometrical nonlinearities couple the equations governing the extension and bending vibrations [96]. This phenomenon is expressed in Eq. (5.10) by the nonlinear term, which depends on a varying tensile force $T(x, t)$ acting on the beam:

$$T(x, t) = EA\left[u^I + \frac{1}{2}(w^{II})^2\right] \qquad (5.11)$$

If the beam has fixed edges, the nonlinear term produces a stretching effect and Eq. (5.10) can be written as [8]:

$$m\ddot{w} + c_v\dot{w} + EIw^{IV} - \frac{EA}{2l}\left[\int_0^l (w^I)^2 dx\right]w^{II} = f(t)\,\delta(x - x_f) \qquad (5.12)$$

where l is the length of the beam (m). Note that a similar expression can also be obtained in the case of non-ideal boundary conditions, which is the case of realistic non-perfect clamps [88]. Solutions to Eq. (5.12) can be found projecting the physical domain onto a convenient reduced-order basis. If LNMs $\psi(x)$ are chosen as projection space, this operation is simply the modal transformation. Eq. (5.12) can then be multiplied by a generic eigenfunction $\psi_r(x)$ and integrated over the spatial domain, yielding:

$$
m \int_l \left(\psi_r \sum_j \psi_j \ddot{\eta}_j \right) dx + c_v \int_l \left(\psi_r \sum_j \psi_j \dot{\eta}_j \right) dx
$$

$$
+ EI \int_l \left(\psi_r \sum_j \psi_j^{IV} \eta_j \right) dx
$$

$$
- \frac{EA}{2l} \int_l \psi_r \left[\int_l \left(\sum_j \psi_j^I \eta_j \right)^2 dx \cdot \sum_j \psi_j^{II} \eta_j \right] dx
$$

$$
= q_r(t)
$$
(5.13)

where $q_r(t) = \int_l \psi_r f(x,t) dx$ is the modal force. In general, the integral $\int_l \left(\sum_j \psi_j^I \eta_j \right)^2 dx$ contains all the terms of the summation:

$$
\int_l \left(\sum_{j=1}^J \psi_j^I \eta_j \right)^2 dx = \int_l \left(\sum_{p=1}^J \psi_p^I \eta_p \right) \left(\sum_{q=1}^J \psi_q^I \eta_q \right) dx
$$
(5.14)

although there are situations where the off-diagonal terms (i.e. the integrals $\int_l \psi_p^I \psi_q^I \, dx$, with $p \neq q$) can be neglected, like the simply supported case. The number of nonlinear couplings is defined by the index J, which is a user-defined quantity and it cannot exceed N, when N modes are taken into the solution. A set of coefficients α_{pq} can be defined as:

$$
\alpha_{pq} = \int_l \psi_p^I \psi_q^I dx, \quad p, q = 1, \dots, J
$$
(5.15)

so as to re-write Eq. (5.13) in the form:

$$
m_r \ddot{\eta}_r + c_r \dot{\eta}_r + k_r \eta_r - \frac{EA}{2l} \sum_{p=1}^J \sum_{q=1}^J (\alpha_{pq} \eta_p \eta_q) \beta_r \eta_r = q_r
$$
(5.16)

where m_r, c_r and k_r are the modal mass, damping and stiffness respectively, and $\beta_r = \int_l \psi_r \psi_r^{II} dx$. Similar formulations to Eq. (5.16) can be found in [86,88,97]. The coefficients α_{pq} and β_r depend only on the geometrical properties of the beam and the boundary conditions, and they can be recast into a matrix $_r\boldsymbol{\mu}$ defined as:

$$
_r\boldsymbol{\mu} = \beta_r \frac{EA}{2l} \begin{bmatrix} \alpha_{11} & \cdots & \alpha_{J1} \\ \vdots & \ddots & \vdots \\ \alpha_{1J} & \cdots & \alpha_{JJ} \end{bmatrix} = \begin{bmatrix} _r\mu_{11} & \cdots & _r\mu_{J1} \\ \vdots & \ddots & \vdots \\ _r\mu_{1J} & \cdots & _r\mu_{JJ} \end{bmatrix}
$$
(5.17)

Thus, Eq. (5.16) can be written as:

$$m_r \ddot{\eta}_r + c_r \dot{\eta}_r + k_r \eta_r + q_r^{nl} = q_r,$$

$$q_r^{nl} = -\sum_{p=1}^{J} \sum_{q=1}^{J} {}_r\mu_{pq}\, \eta_p \eta_q \eta_r \tag{5.18}$$

The model described by Eq. (5.18) is validated numerically in the following section. The nonlinear part of Eq. (5.18) is then used as an a priori information for the experimental identification of a nonlinear beam conducted with NSI.

5.3.1. Comparison with ANSYS

As discussed in the introduction, the modal model (referred to as MM) is compared with ANSYS FE formulation [92].Two cases are considered, both involving a slender beam undergoing large-amplitude vibrations. The first one is a sine-sweep across the first bending mode of the straight beam, while the second one presents an added lumped mass to create an internal nonlinear resonance between first and second bending modes [98]. The properties of the beam are listed in Table 5.1, and a proportional damping distribution is considered with a mass-proportional coefficient equal to 3 s^{-1} and a stiffness-proportional coefficient equal to 2·10^{-6} s.

For the modeling of the beam, a formulation with shear-deformable beam finite elements is used in ANSYS, while the MM method is based on a Euler-Bernoulli formulation (Eq. (5.10)). As it is a thin and slender beam, results from all approaches are comparable to each other. The time integration is performed with the Newmark integration method [29] for all the approaches with a sampling frequency of 5 kHz and a spatial discretization of 40 nodes. In particular, the spatial discretization is an important parameter for the FE code, while it does not play any role in the MM method, since it is based on a modes superposition approach. Instead, the number of retained modes (called N in the previous section) and the number of nonlinear couplings (called J in the previous section) make a difference in the modal model behavior.

Table 5.1: Properties of the numerical beam.

Length (mm)	Width (mm)	Thickness (mm)	Young's Modulus (MPa)	Density (kg/m^3)
500	20	1	200	7800

Straight beam case

In this case, the first resonance frequencies are located at $\omega_1 = 20.75$ Hz, $\omega_2 = 57.21$ Hz and $\omega_3 = 112.15$ Hz. The matrix of coefficients $_1\boldsymbol{\mu}$ associated to the first mode is reported in Figure 5.2 considering $N = J = 5$. Each matrix

$_r\boldsymbol{\mu}$ is symmetric in the case of fixed edges, and the magnitudes of its diagonal entries increase together with the considered mode.
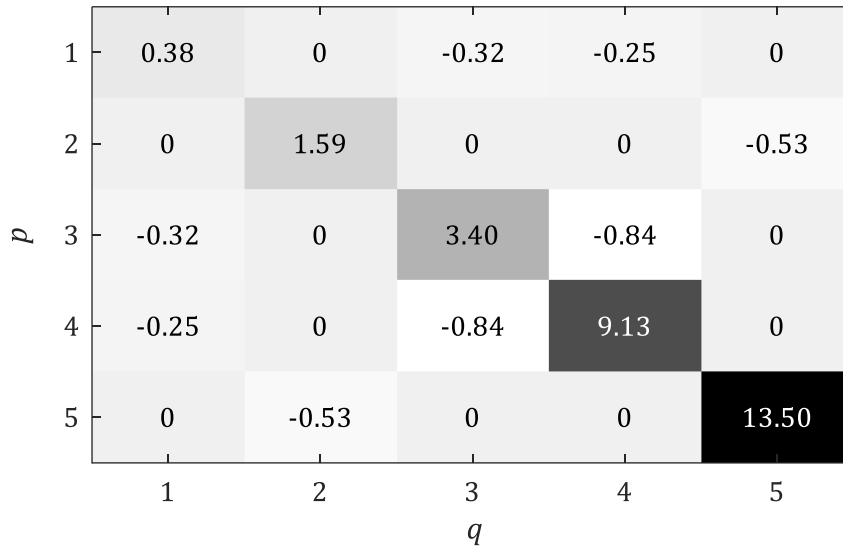
Figure 5.2: Analytical coefficients $_1\boldsymbol{\mu} \times 10^9$ of the numerical beam. The background color of each entry is proportional to its magnitude.

The beam is excited with a frequency sweep over the first mode (from 16 Hz to 28 Hz) considering two different amplitudes and with a sweep rate of 0.1 Hz/s. The lowest excitation level can be considered as linear, with an amplitude of 0.01 N. Instead, the higher excitation level is noticeably nonlinear, with an amplitude of 0.1 N. The excitation is applied at 5 cm from one end, and the response is computed at the mid-span node. Results are reported for the two methods (MM and ANSYS) in the time domain in Figure 5.3.

The two responses are quite close for the lowest excitation level. There is still a minor difference in Figure 5.3a around the resonance peak, which is allegedly due to the different beam models used by the approaches. While MM is based on the Euler-Bernoulli formulation, ANSYS is based on the Timoshenko formulation. The two formulations are indeed very similar for slender beams like the one considered here, but there is still a slight difference in the computation of the first natural frequency, leading to a small phase shift ($\sim 0.3\%$). As for the nonlinear level in Figure 5.3b, a characteristic hardening effect coming from the stretching of the neutral axis is visible and the three methods well agree, though some difference is present around the jumping frequency. This originates from the same reasons as before, plus possible differences in the modeling of the nonlinear behavior.
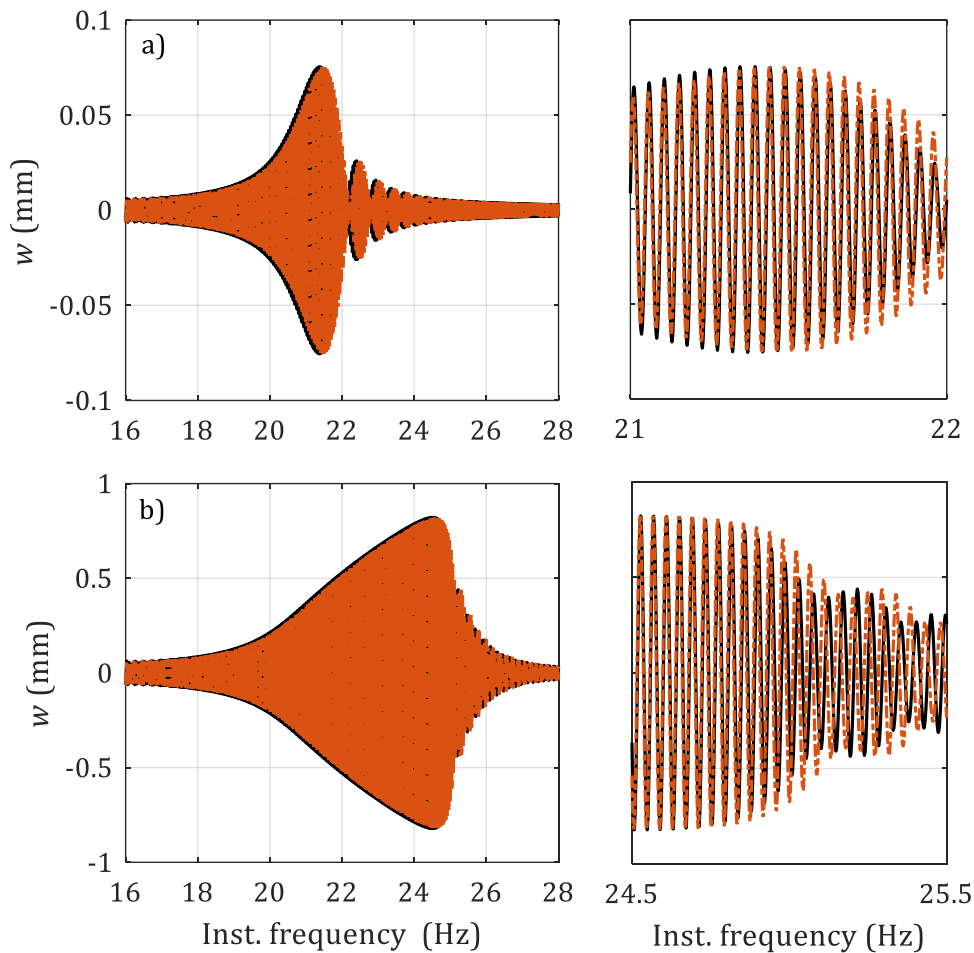
Figure 5.3: Displacement at the mid-span computed with MM and ANSYS. Black line: MM; orange dashed-dotted line: ANSYS. a) Input amplitude of 0.01 N, with zoom around the resonance peak; b) Input amplitude of 0.1 N, with zoom around the jumping frequency.

Some more insights on the nonlinear characteristics of the modal model can be obtained when computing the response with the harmonic balance method (HBM, [26]) using the modal model. Results are plotted in Figure 5.4 considering a point at 1/3 of the length of the beam and for the 0.1 N level of excitation, where a classical hardening nonlinear response can be observed in the nonlinear frequency response curve (NFRC), with the unstable path in dotted line. The NFRC is compared with the response obtained using MM with a sine-sweep excitation of the same amplitude and rate of 0.1 Hz/s, to qualitatively assess the HBM result. Indeed, the envelope of the sine-sweep simulation is almost overlapped to the HBM solution in the regions out of the jumping frequency. Furthermore, a snapshot of the Fourier coefficients of the nonlinear restoring force $F(q_r^{nl})$ is depicted in Figure 5.4b for the first three modes when 5 harmonics are taken into account. As expected, only the first mode plays a noticeable role in the nonlinear response, as it is the only one

excited. Also, only the odd harmonics are present, as the nonlinearity is essentially of cubic type.
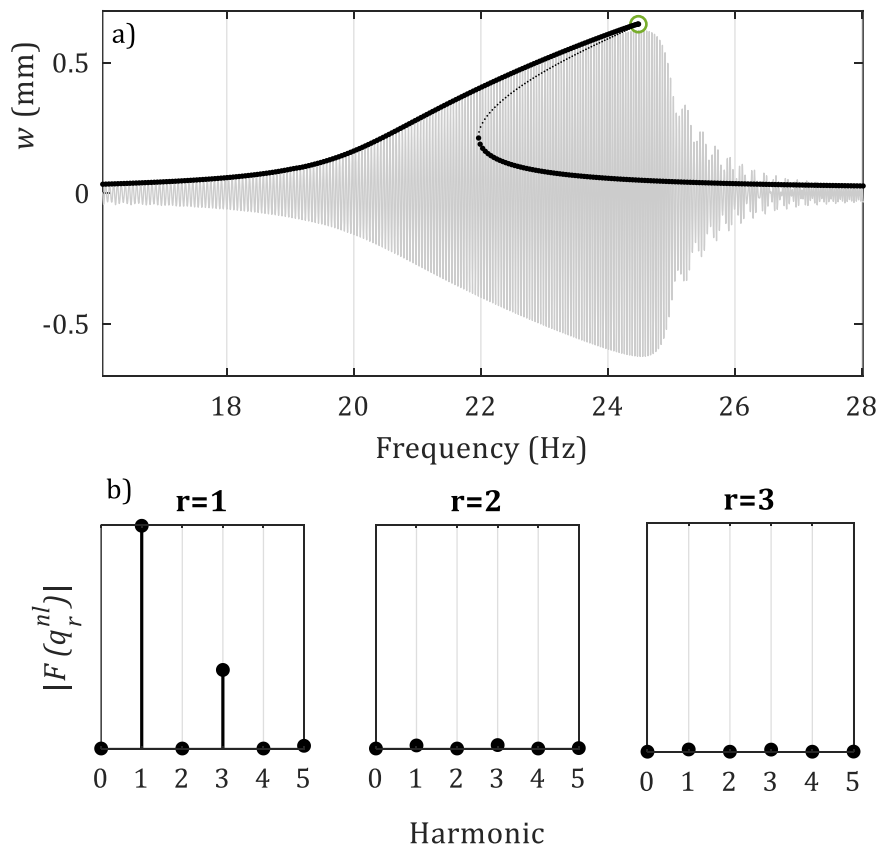
Figure 5.4: HBM results at 1/3 of the length of the beam with input amplitude of 0.1 N. a) Black line: nonlinear frequency response curve, with the unstable path in small dots; grey line: MM simulation; b) Snapshot of the Fourier coefficients of the first three modes with 5 harmonics per mode, computed at the point corresponding to the green circle in (a).

A 3:1 internal resonance case

Internal resonances are interesting nonlinear phenomena, happening when two different modes of vibration exchange energy. The theory of nonlinear normal modes has shed some light on this phenomenon, proving how frequent this can happen in real life structures [99,100]. The easiest case is when two close modes (in terms of natural frequencies) are nonlinearly excited, but other scenarios are possible as well. In particular, it may happen that two different modes have associated natural frequencies in an integer ratio. If then the lower mode is nonlinearly excited and it responds also at its integer harmonics, it excites the higher mode as well.

In this section, the beam of Table 5.1 is considered, but a 3:1 internal resonance between second and first bending modes is created by adding a lumped mass to the structure. The entity and the position of the mass have been selected by solving an optimization problem, with cost function to be

minimized equal to the norm of the distance between the natural frequency of the second mode ω_2 and the third harmonic of the first mode $3\omega_1$. Genetic algorithms [101] have been adopted to find the optimum set of values, corresponding to a lumped mass of 44 grams at 32 cm from one end, as depicted in the scheme of Figure 5.5. The natural frequency associated to the second mode is $\omega_2 = 47.7$ Hz, which is roughly 3 times the one associated to the first mode $\omega_1 = 14.4$ Hz.

When the beam undergoes large-amplitude oscillations, a response of the kind η_1^3 (among the others) is retrieved from Eq. (5.18) and thus the second mode is excited as well.
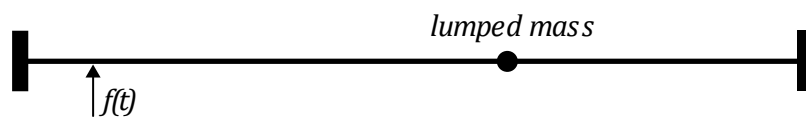
Figure 5.5: Scheme of the numerical beam with a 3:1 internal resonance.

Internal resonances are an interesting test, because the response becomes very sensitive to small perturbations, even numerical ones. The comparison between ANSYS and MM is therefore motivating. The beam is still excited with a frequency sweep over the first mode (from 10 Hz to 20 Hz) with a sweep rate of 0.1 Hz/s and an amplitude of 0.21 N. The excitation is applied at 5 cm from one end, and the response is computed at 1/3 of the length of the beam.

The time response is depicted in Figure 5.6a, with a zoom around the jumping frequency for the two methods. They show a similar behavior, but different distortions can be seen before the jumping frequency for both approaches due to the 3:1 interaction. Interestingly, the spectra of the responses in the frequency domain in Figure 5.6b are quite similar for both MM and ANSYS, at least in the excited frequency range. Also, they both show an important frequency content at around 50 Hz, which is in the range of the second bending mode. Major differences between the two responses can be noticed at the higher harmonics.

It is rather difficult to find an explanation for the differences between the two approaches, mostly because ANSYS does not provide a closed (analytical) nonlinear form. Therefore, the only possible inference is that MM is certainly capable of replicating a hardening effect due to the geometrical nonlinearity, having roughly the same strength of the one predicted by ANSYS. Surely, the contribution of the third harmonic of the excited mode is predominant in both approaches, but other nonlinear couplings are present as well and possibly handled in different ways by the two methods.
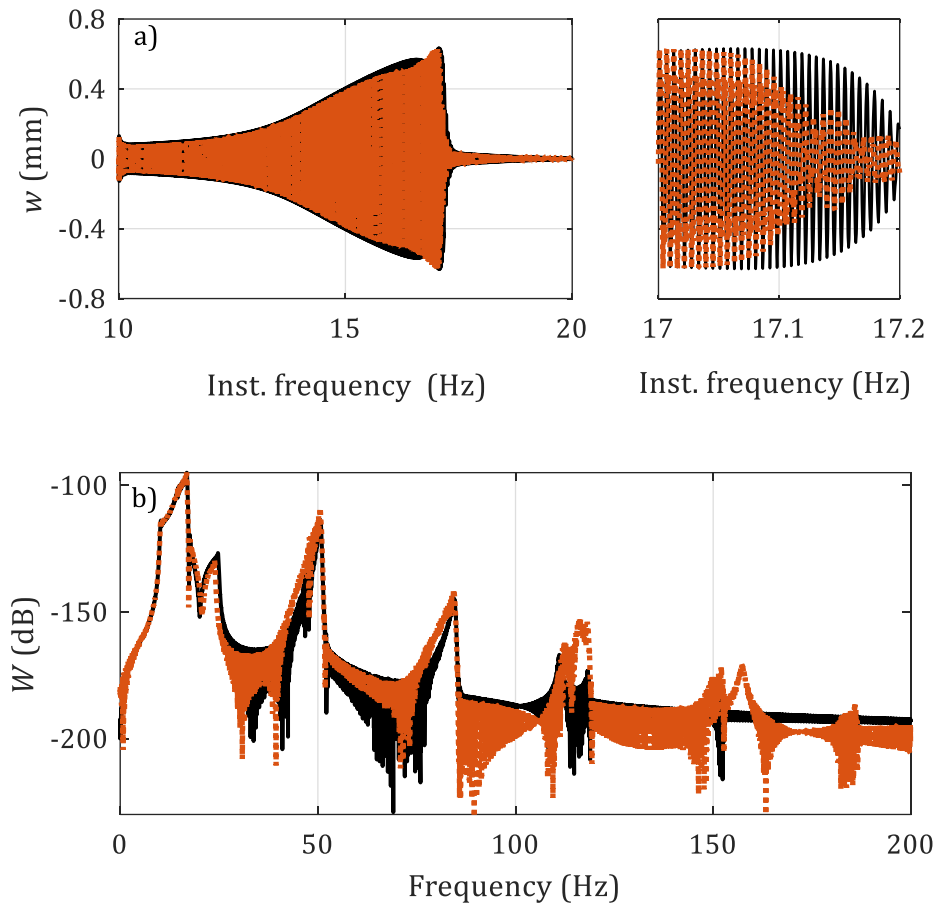
Figure 5.6: Displacement computed with MM and ANSYS in the case of internal resonance with input amplitude of 0.21 N. Black line: MM; orange dashed-dotted line: ANSYS. a) Time response with zoom around the jumping frequency; b) Frequency spectrum of the response.

Eventually, HBM is used also in this case with the MM formulation to build the nonlinear response. The outcome is depicted in Figure 5.7 for several input levels, to clearly see the increasing influence of the 3:1 interaction for increasing excitation amplitude.

The case corresponding to an excitation amplitude of 0.3 N is also depicted in Figure 5.8, with a snapshot of the Fourier coefficients of the nonlinear restoring force $F(q_r^{nl})$ for the first three modes and 5 harmonics. It can be seen how the second mode ($r = 2$) is also responding to the excitation with its odd harmonics in this case.
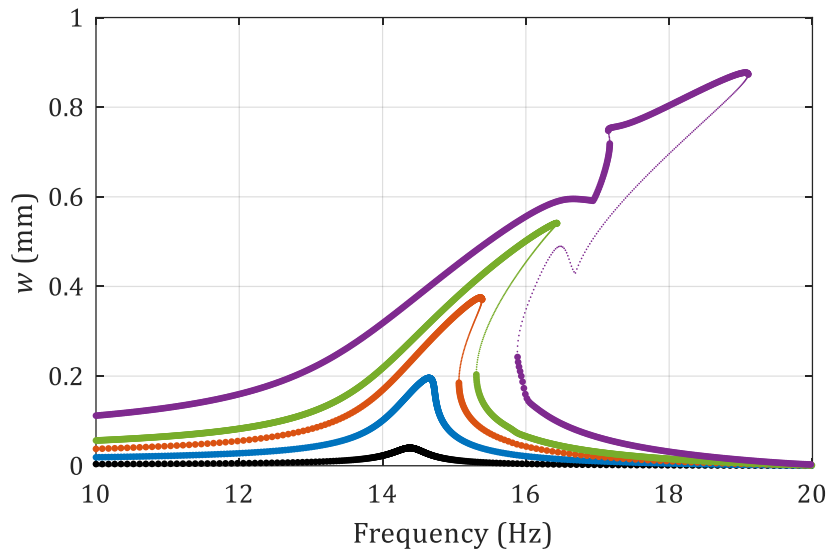
Figure 5.7: HBM results in the case of internal resonance for input amplitudes of 0.01 N (black), 0.05 N (blue), 0.1 N (orange), 0.15 N (green), 0.3 N (purple). Nonlinear responses computed at 1/3 of the length of the beam. Thick dots: stable paths; small dots: unstable paths.
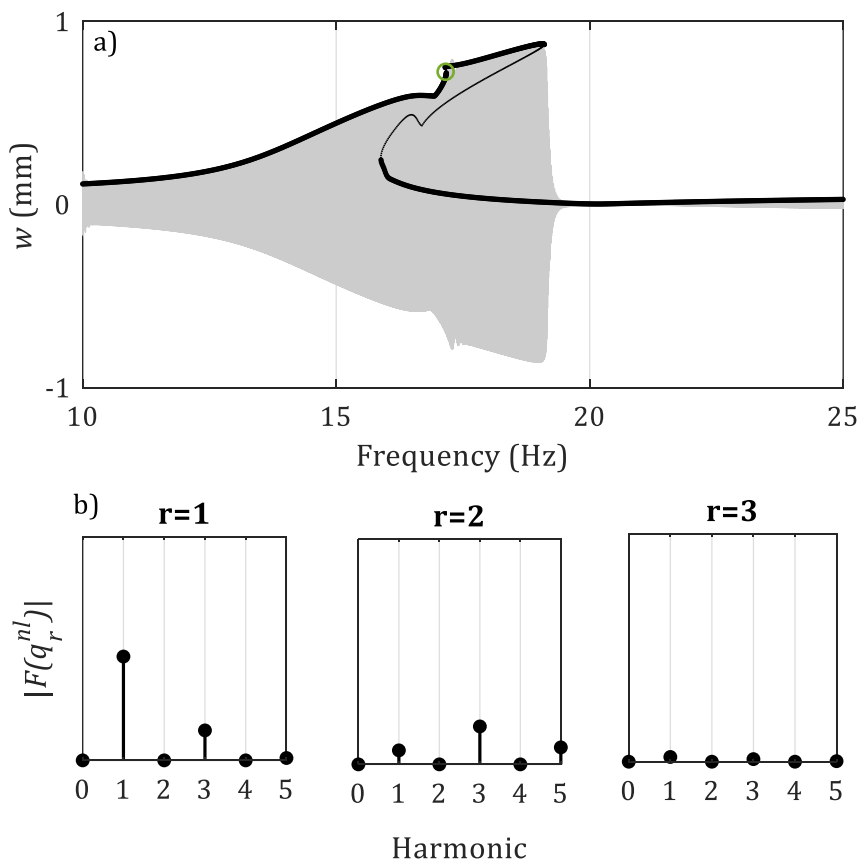
Figure 5.8: HBM results in the case of internal resonance at 1/3 of the length and with input amplitude of 0.3 N. a) Black line: nonlinear frequency response curve, with the unstable path in small dots; grey line: MM simulation; b) Snapshot of the Fourier coefficients of the first three modes with 5 harmonics per mode, computed at the point corresponding to the green circle in (a).

5.4. Experimental tests

Experiments are performed on a clamped-clamped slender beam instrumented with accelerometers and excited with a hanged shaker. A sketch of the test bench is reported in Figure 5.9.
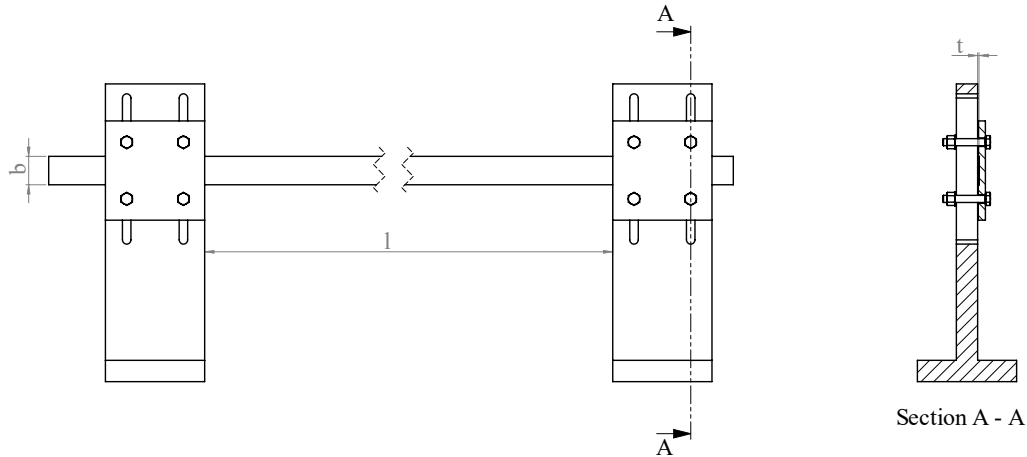
Figure 5.9: Drawing of the experimental test rig.

The properties of the beam are reported in Table 5.2, while some photos of the experimental setup can be seen in Figure 5.10.

Table 5.2: Properties of the experimental beam

Length (mm)	Width (mm)	Thickness (mm)	Material
479	20	0.75	Carbon steel
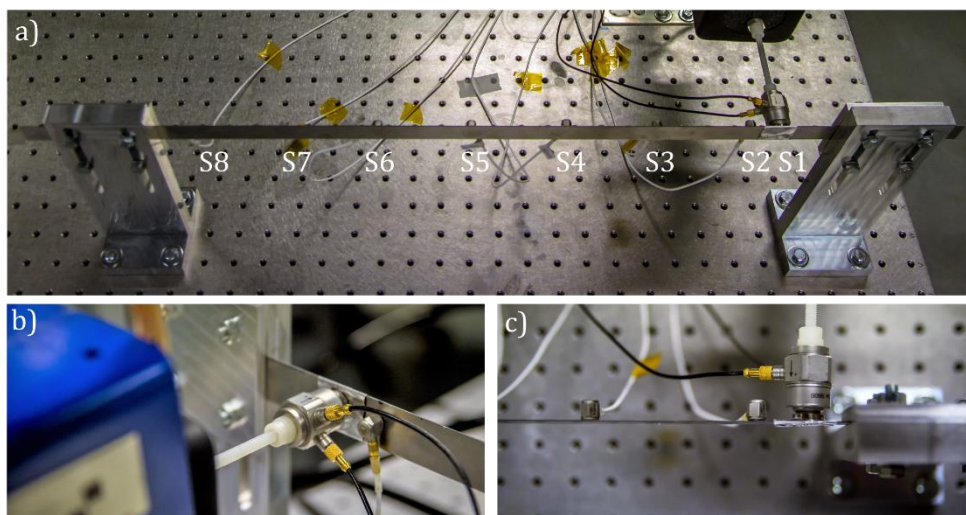
Figure 5.10: Photos of the experimental setup. Global view in (a) and close views of the shaker attachment in (b) and (c).

A total of 8 accelerometers are used to record the output, while a load cell on the head of the shaker is adopted to record the input. The position of the sensors is summarized in Table 5.3.

Table 5.3: Position of the sensors along the length of the beam and type.

Sensor #	Distance from the right end (mm)	Type	Name	Weight (g)
S1	15	Impedance head	Dytran 5860B	60
S2	35			
S3	105			
S4	175			
S5	245	Accelerometer	Dytran 3035B2	2.5
S6	315			
S7	385			
S8	455			

The aim of these experimental tests is to perform the nonlinear system identification of the considered structure when a distributed geometrically nonlinear behavior is retrieved. Some preliminary tests are conducted first to characterize the dynamical behavior of the beam and to check if geometrical nonlinearities can be actually triggered.

5.4.1. Sine-sweep tests

In principle, both Modal-NSI and PNLSS need a broadband input to properly work, and this is obtained in this study by feeding random-phase multisines to the shaker. However, sine-sweep excitations are also considered in this section to better visualize the nonlinear behavior.

A series of up and down linear sine-sweeps is performed with three different input amplitudes and two frequency ranges. The sweep rate is 0.2 Hz/s, with a sampling frequency of 3200 Hz. The considered input amplitudes f_0 are respectively equal to 0.2 N, 0.6 N and 1 N.

The first set of tests are performed into the frequency range $5 - 30$ Hz, and the responses of sensors S3 and S5 to the sweep-up excitation are depicted Figure 5.11. Note that the x-axis reads "sweep frequency", that is the instantaneous frequency of the sine-sweep input computed as the derivative of the phase of the analytic signal of the input using the Hilbert transform [102].

Both sensors show a great increase in the acceleration amplitudes around $20 - 27$ Hz, depending on the excitation level. A clear hardening effect is visible in this frequency region with a jump-down phenomenon, especially for the highest input level. Other small resonances are present below 10 Hz, but these are allegedly due to the shaker-structure interaction or to the suspended shaker itself. The spectrogram of the response S5 is also reported in Figure 5.12 for the highest excitation level.
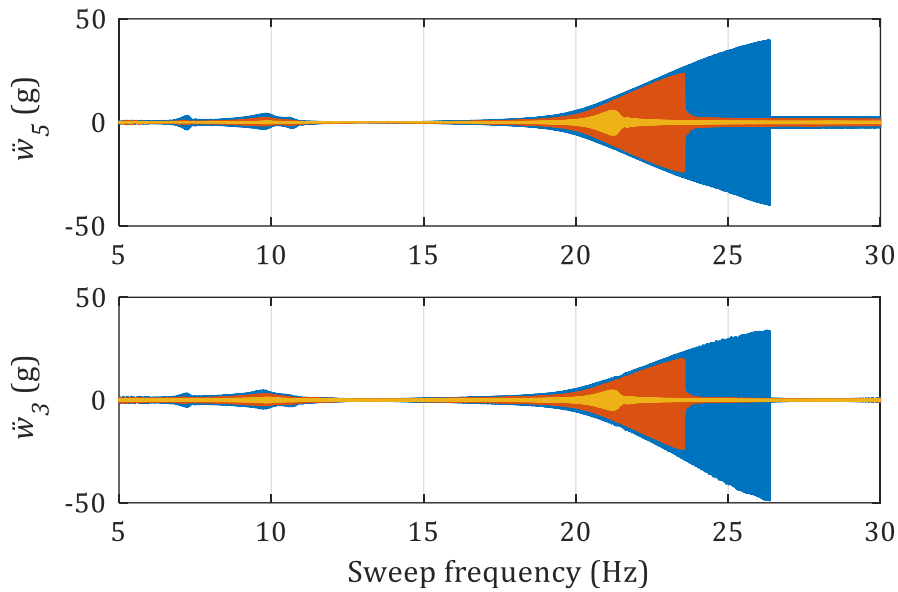
Figure 5.11: Responses S3 and S5 to the sweep-up excitation in the frequency range 5-30 Hz. Yellow line: f_0=0.2 N; orange line: f_0=0.6 N; blue line: f_0=1 N.

The jump-down phenomenon can be observed again around 27 Hz, but more interestingly the harmonics of the response can be noted as well. It is worth highlighting that both even and odd harmonics can be observed in the spectrogram, symptom of a nonlinear behavior even more complex than the one predicted by the modal model of section 4.3. More in-depth discussion about this result are presented in section 4.4.2.
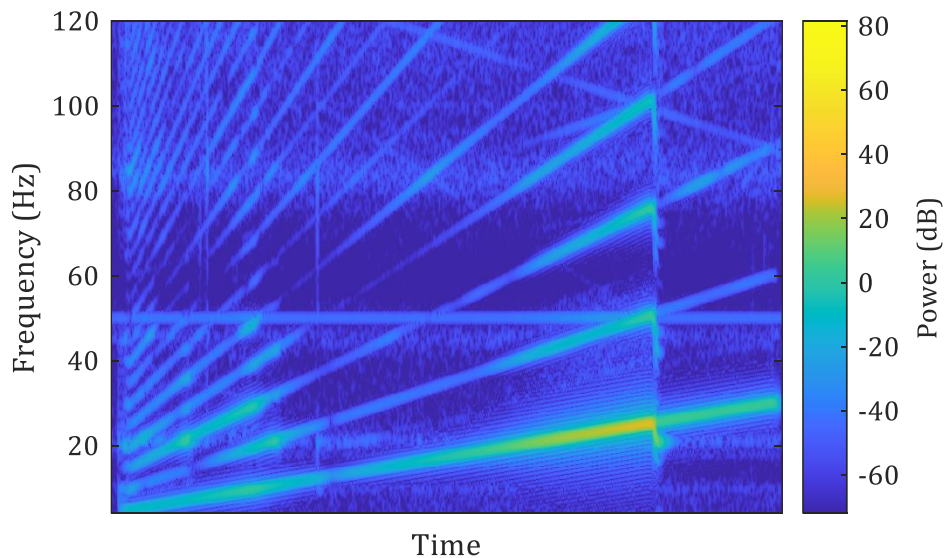
Figure 5.12: Spectrogram of S5, f_0=1 N.

The second set of tests is performed into the frequency range $40 - 60$ Hz, and the responses of sensors S3 and S5 to the sweep-up excitation are depicted in Figure 5.13.
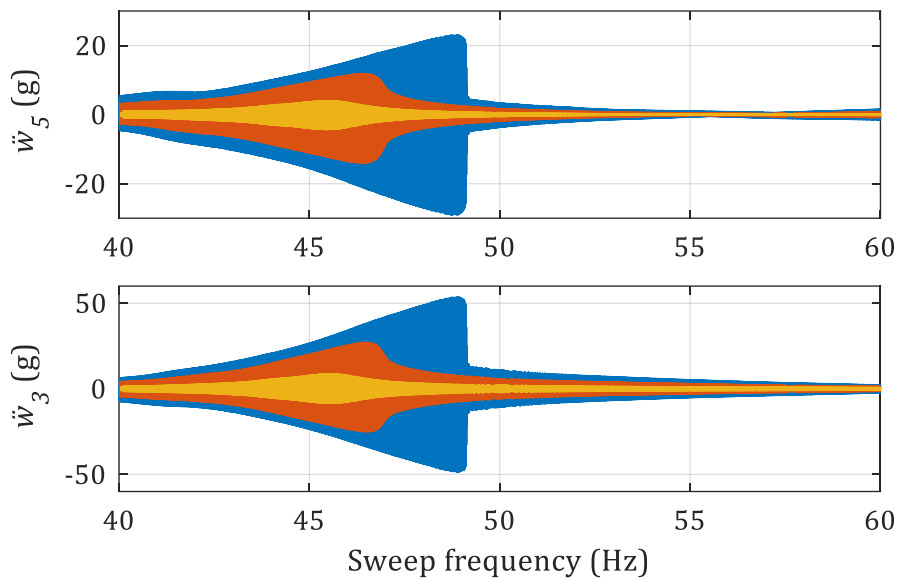
Figure 5.13: Responses S3 and S5 to the sweep-up excitation in the frequency range 40-60 Hz. Yellow line: f_0=0.2 N; orange line: f_0=0.6 N; blue line: f_0=1 N.

The second bending mode is presumably excited, and a hardening effect can be noted also in this case, with a jumping frequency at around 49 Hz for the highest excitation level.

Results obtained with the sweep-down tests are equivalent to the ones seen so far, and a comparison between the sweep-up and the sweep-down responses of sensor S6 is depicted in Figure 5.14 as an illustration.
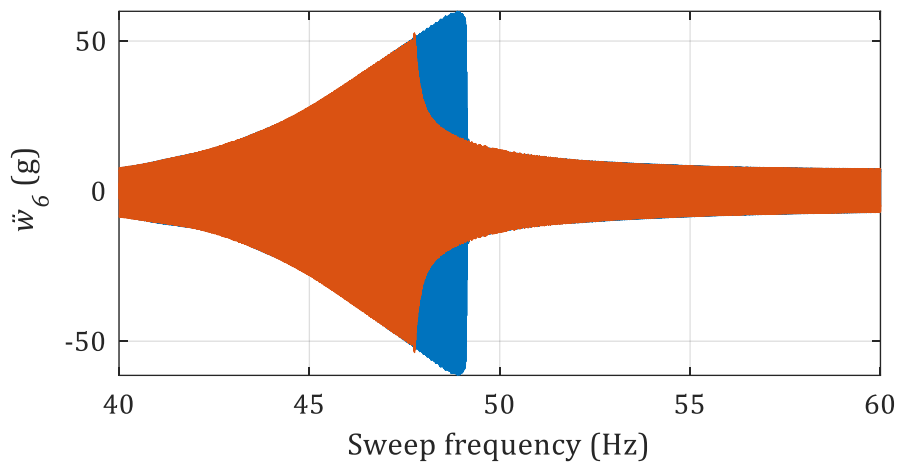
Figure 5.14: Response of S6 to the sine-sweep excitation, f_0=1 N. Blue line: sweep-up; orange line: sweep-down.

The two responses are perfectly overlapped everywhere except in the "unstable" region, where the jump-down and jump-up phenomena occur.

5.4.2. Random-phase multisine tests

Random-phase multisine tests (see section 2.6.1) are performed in the frequency range 14-100 Hz, where the first three bending mode of the structure are located. The sampling frequency is $f_s = 6400$ Hz, and a total of $M = 5$ realizations with $P = 6$ periods and $N_s = 65536$ spectral lines per period are considered. The different periods and realizations are used in this section to characterize the nonlinearity. Several forcing levels are considered, ranging from a linear behavior ($f_0 = 0.2$ N RMS) to a highly nonlinear one ($f_0 = 3$ N RMS).

Figure 5.15a represents the acceleration of S5 over the first realization for different forcing levels in the time domain. The corresponding experimental FRF is depicted in Figure 5.15b together with the coherence function. A hardening effect is clearly visible in Figure 5.15b, confirming the results of the previous section. A decrease of the coherence around the resonance regions is also retrieved.
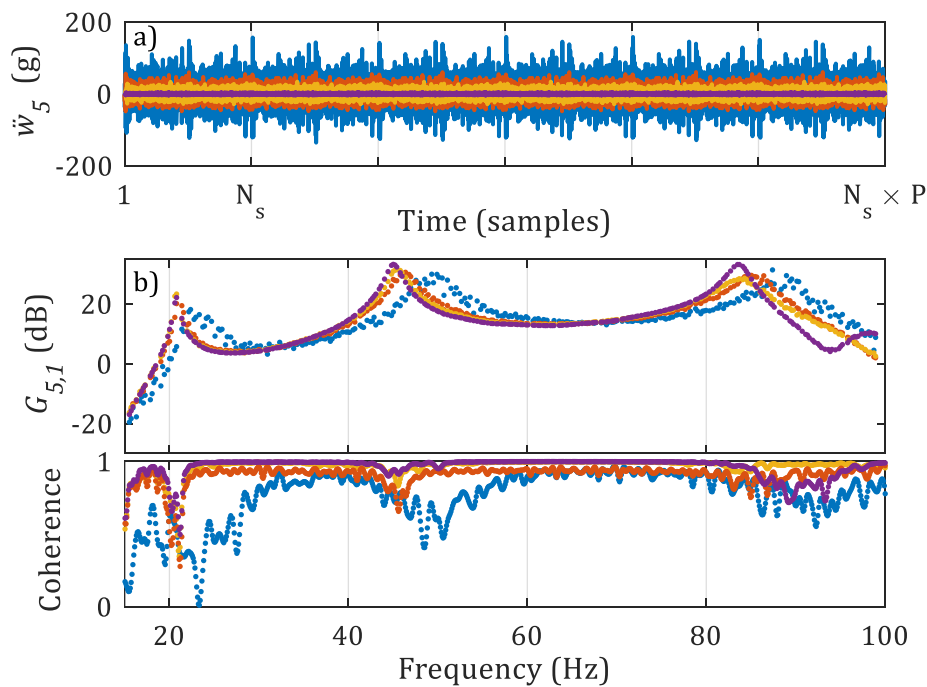
Figure 5.15: First realization output of S5 and corresponding FRFs for different forcing levels f_0. Purple: f_0=0.2 N; yellow: f_0=1 N; orange: f_0=1.7 N; blue: f_0=3 N. a) Time domain; b) Experimental FRF (inertance) in dB scales (ref. 1 g²/N) and coherence plot.

The measured acceleration in the frequency domain A_5 is reported in Figure 5.16 for several odd-random multisine levels. Recalling that noise and nonlinear distortions can be separated with random-phase multisine excitations due to their periodicity, the spectra of the disturbing noise and of the odd and even nonlinearities are also shown. It can be seen that the levels

of noise and nonlinearities are similar for the lowest forcing level (Figure 5.16a), while their difference becomes more important as the forcing level increases. Also, both even and odd nonlinearities are clearly present in the output response, as already seen in Figure 5.12.
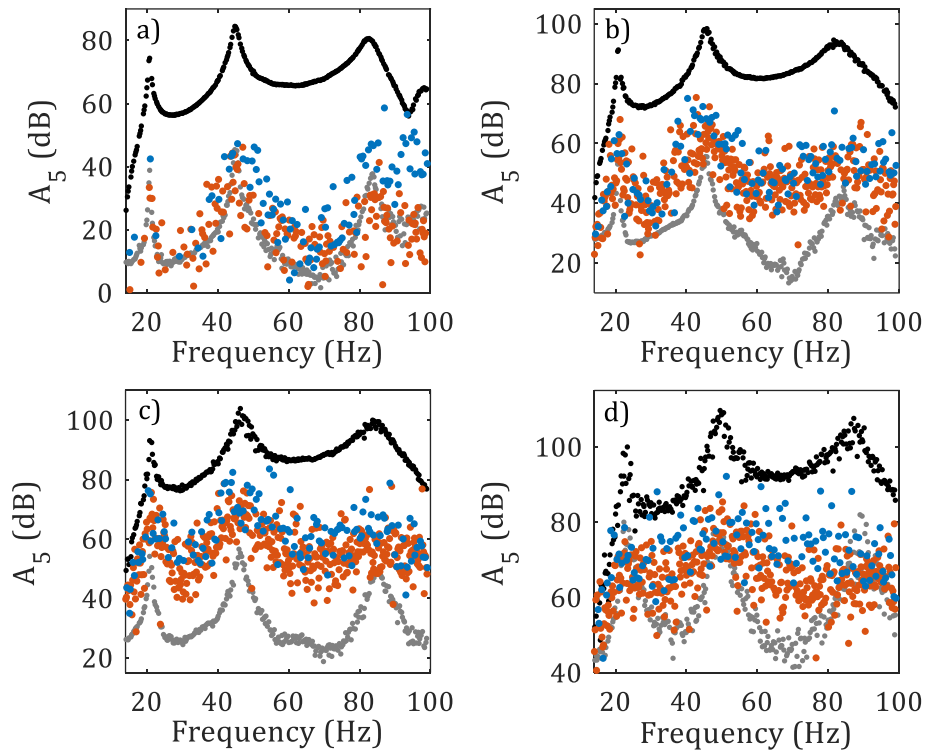
Figure 5.16: Odd-random multisine output for different forcing levels in dB scales (ref. 1 g^2/Hz). Black: output spectrum; grey: disturbance noise level; blue: odd nonlinearities; orange: even nonlinearities. a) f_0=0.2 N; b) f_0=1 N; c) f_0=1.7 N; d) f_0=3 N.

It is worth recalling that the model presented in section 5.3 is not capable of featuring an even nonlinear behavior. That is because, generally, even nonlinearities are associated with some asymmetry in the response, which in principle should not appear in the case of a straight clamped-clamped beam. Nevertheless, there might be several sources of even behavior when the real structure is considered: imperfection of the clamps, possible non-planarity of the section of the beam along its length, the added mass of the shaker and the accelerometers on one side of the beam, nonlinear damping... It is not straightforward to investigate the effects related to each source, but even nonlinearities should be taken into account when proceeding with the system identification.

Eventually, the total distortion level (sum of even and odd nonlinear distortions) of S5 is reported in Figure 5.17 for the two highest level, confirming that the amount of the total distortions is very high, comparable to

the level of the output in the resonance regions. The other sensors show a similar behavior.
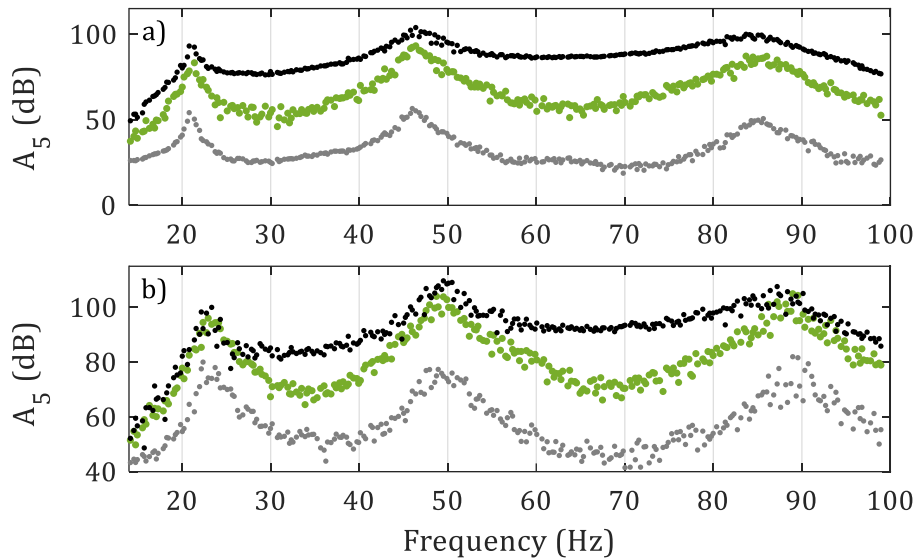
Figure 5.17: Odd-random multisine output for different forcing levels in dB scales (ref. 1 g²/Hz). Black: output spectrum; grey: disturbance noise level; green: total distortions level. a) f_0=1.7 N; b) f_0=3 N.

5.4.3. Identification of the LNMs

Recalling the identification process of Figure 5.1, the first step is the extraction of the LNMs, and this is done here by performing linear subspace identification (SI, Appendix A) on a low-amplitude test. The beam is excited with a full random phase multisine ranging over the first three bending modes. The full multisine is chosen here instead of the odd-random of the previous section to maximize the number of spectral lines for a fixed acquisition length. The test is conducted using the same parameters of section 5.4.2, with an input amplitude of $f_0 = 0.2$ N RMS. The experimental FRF (receptance) related to S2 is reported in Figure 5.18 together with the noise level and the total distortion level, the other sensors showing a similar behavior.

Some difference can be noted between the total distortion level and the noise level, especially around the resonance peaks. This mismatch is supposed to be caused by some source of nonlinearity, and the most likely scenario is that this is due friction between the beam and the clamps and is not related to geometrical effects. In any case, the total distortions are always at least one order of magnitude lower than the FRF. Therefore, the structure can be considered as linear at this level of excitation, and SI can be applied to extract the parameters of interest.

The stabilization diagram obtained applying SI for different model orders is reported in Figure 5.19. Since the object of the linear identification are just

the LNMs, the model order for each mode is chosen adopting a LNMs similarity criterion: all the MACs between the LNMs related to each identified mode are compared and the model order that achieves the best MAC is selected.
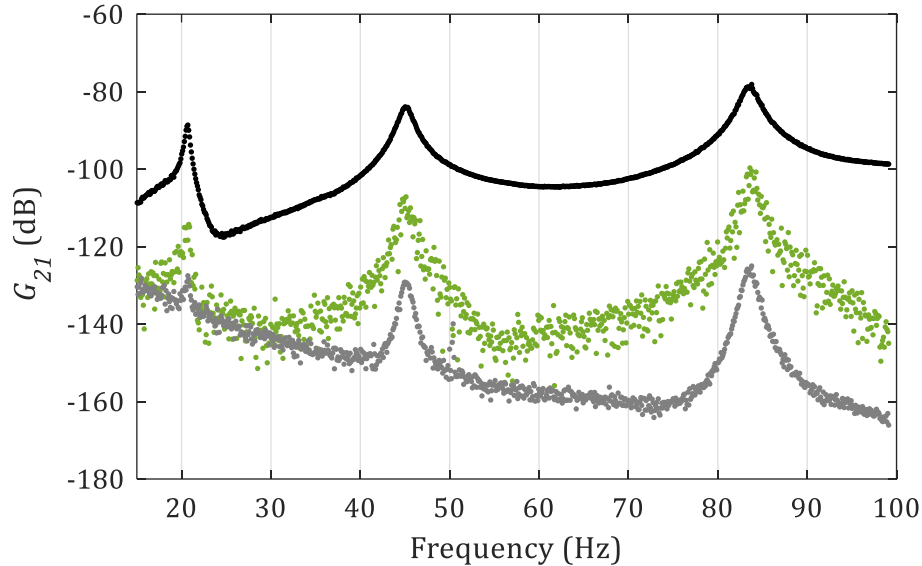
Figure 5.18: Experimental FRF (receptance) of S2 in dB scales (ref. 1 m/N), f_0=0.2 N (RMS). Black: FRF; grey: disturbance noise level; green: total distortions level.
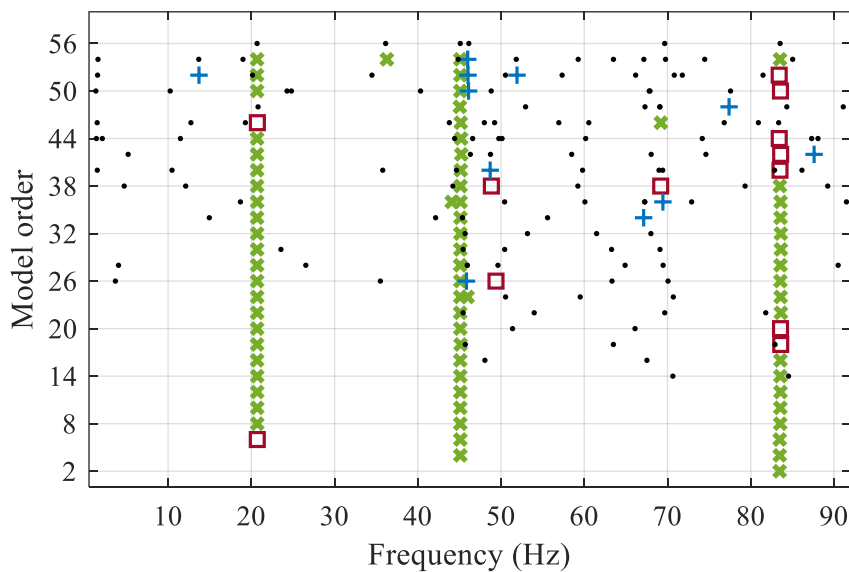
Figure 5.19: Stabilization diagram related to the linear subspace identification at low level. Stabilization thresholds for natural frequency, damping ratio and MAC are 0.5%, 10% and 99.5%, respectively. Black dot: new (not stable) pole. Blue plus: pole stable in frequency. Red square: pole stable in frequency and MAC. Green cross: pole stable in frequency, MAC and damping.

The modal parameters are then extracted and reported in Table 5.4.

Table 5.4: Linear modal parameters identified with SI.

Mode number	Frequency (Hz)	Damping ratio (%)
1	20.7	1.2
2	45.1	1.7
3	83.6	1.1

The deformed shapes of the first three bending modes are eventually depicted in Figure 5.20.
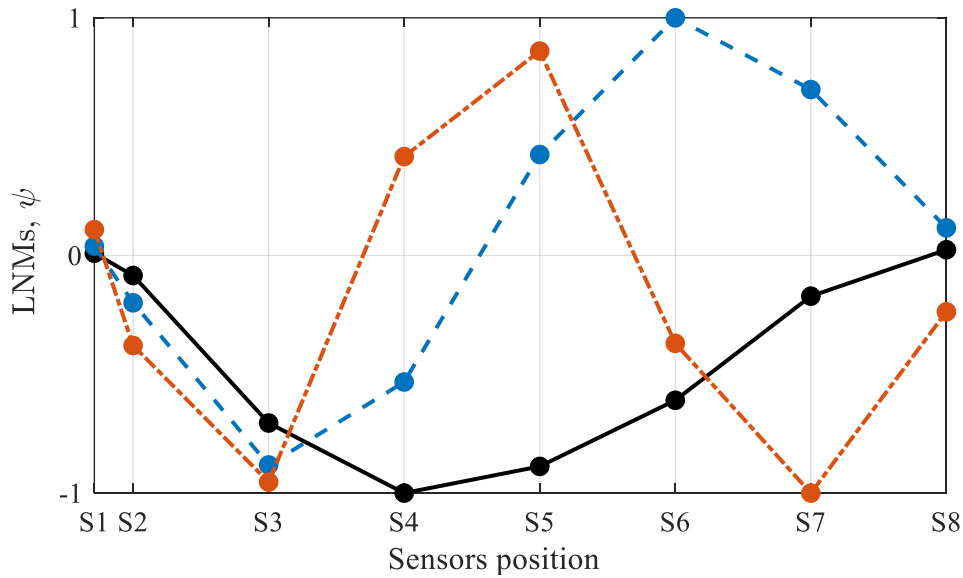
Figure 5.20: Experimental LNMs. Black line: ψ_1; dashed blue line: ψ_2; dashed-dotted red line: ψ_3.

Afterwards, Modal-NSI and PNLSS are used on the same nonlinear dataset.

5.4.4. Nonlinear system identification

The nonlinear system identification strategy proposed in section 5.2 is here applied to the experimental beam structure under test. The beam is excited again with a full random phase multisine ranging over the first three bending mode, with the same parameters of section 5.4.2. Here, 4 realizations out of 5 are used as a training set for the identification, while the last one is used as a validation set. The RMS value of the input force is $f_0 = 2$ N and the experimental FRF (receptance) of S2 is reported in Figure 5.21 together with the noise level and the total distortion level. The other sensors show a similar behavior.
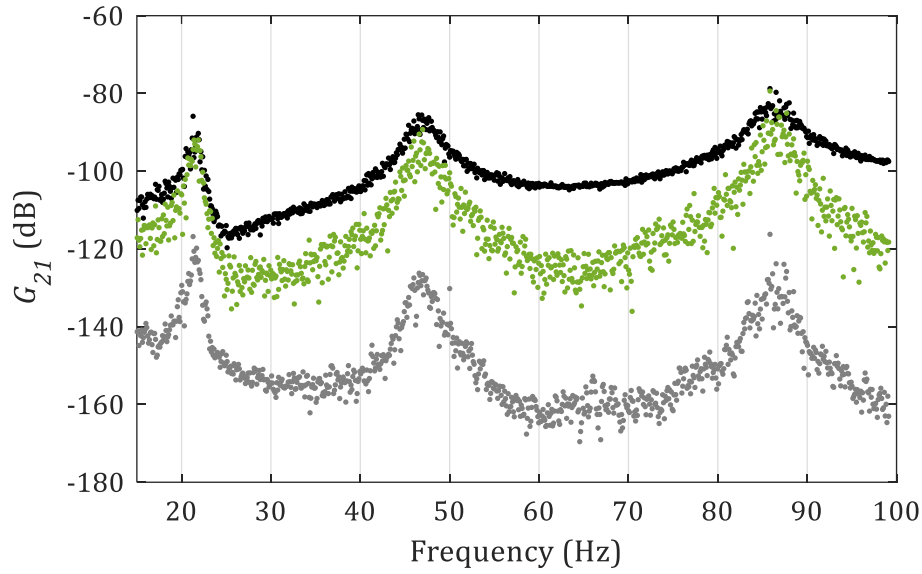
Figure 5.21: Experimental FRF (receptance) of S2 in dB scales (ref. 1 m/N), f_0=2 N (RMS). Black line: FRF; grey line: disturbance noise level; green dots: total distortions level.

The amount of the total distortions almost reaches the level of the signal itself around the resonance peaks, ensuring that the nonlinearity is properly triggered. In terms of shifting of the natural frequencies, all the three modes in Figure 5.21 show a frequency shift of approximately 5% when compared to the ones in Figure 5.18 (linear case).

The inverse modal transformation is first applied to the measured signals to compute the modal coordinates as in Figure 5.1. Afterwards, the nonlinear identification is performed for each mode independently.

Modal-NSI

The vector of nonlinear basis functions $_r\boldsymbol{\xi}$ must be defined for each mode $r = 1, \dots, N$ according to Eq. (5.4). A straightforward choice is to adopt the definition of the nonlinearity described by the modal model of section 4.3, thus obtaining:

$$_r\boldsymbol{\xi} = -\text{vec}\{\eta_p\eta_q\eta_r\}, \quad p, q = 1, \dots, J = N \tag{5.19}$$

Eq. (5.19) follows directly from Eq. (5.18), and each identified nonlinear coefficient $_r\mu_{pq}^{id}$ has the physical meaning of its counterpart in Eq. (5.17). With this choice, the number of unique nonlinear feedbacks per mode is 6 when $J = N = 3$. For instance, the corresponding vector of nonlinear basis functions $_1\boldsymbol{\xi}$ of the first mode is:

$$_1\boldsymbol{\xi} = -[\eta_1^3, \quad \eta_1^2\eta_2, \quad \eta_1^2\eta_3, \quad \eta_2^2\eta_1, \quad \eta_1\eta_2\eta_3, \quad \eta_3^2\eta_1]^{\text{T}} \tag{5.20}$$

Since three modes are excited, a total of 18 coefficients must be retrieved. However, this nonlinear model predicts only an odd nonlinear behavior, as previously discussed. The experimental characterization conducted in section 4.4.2 showed how the system exhibits also a reasonable amount of even nonlinear distortions caused by some even nonlinearity. Since the nonlinear basis functions in Eq. (5.19) are not capable of representing this kind of behavior, there will still be a part of the system response that is not captured by the identified model. A possible improvement will be presented in the following section, where the nonlinear basis functions are expanded to cover also even nonlinear couplings.

The stabilization diagrams of the (modal) underlying-linear systems (ULSs) are computed for each mode in order to select the best model order and they are reported in Figure 5.22. Stability is checked for frequencies, damping ratios, MACs and modal masses.
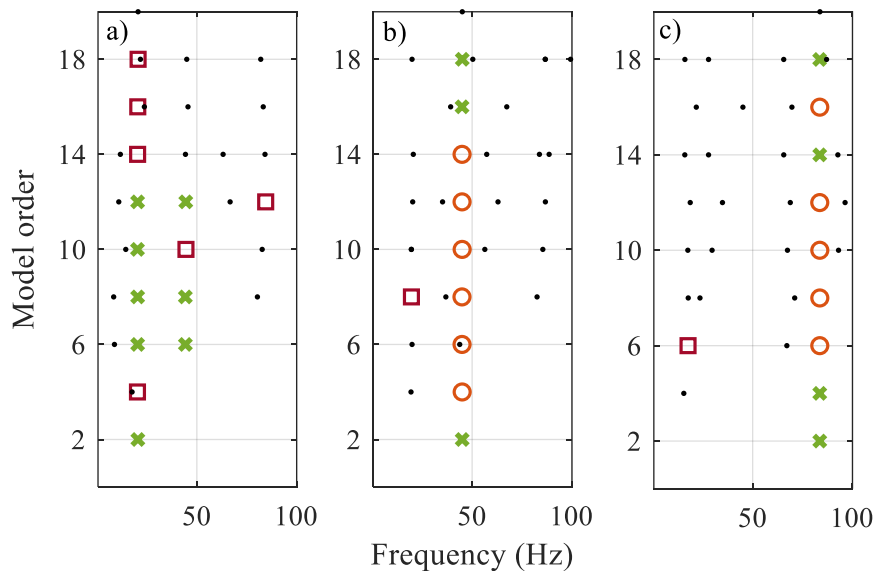
Figure 5.22: Stabilization diagram of the modal ULSs. Stabilization thresholds for natural frequency, damping ratio, MAC and modal mass are 0.5%, 10%, 99.5%, 10%, respectively. Black dot: new (not stable) pole; blue plus: pole stable in frequency; red square: pole stable in frequency and MAC; orange circle: pole stable in frequency, MAC and damping; green cross: pole stable in frequency, MAC, damping and modal mass. a) Mode number 1; b) Mode number 2; c) Mode number 3.

The incomplete decoupling of the equations of motion due to the nonlinearity implies that multiple poles can be identified for each mode, and this is evident in Figure 5.22. Nevertheless, it is a convenient choice to select a model order equal to 2 for each mode, thus including only its main contribution. In fact, including also other poles in the modal state-space model can lead to overfitting and an increased model sensitivity to noise, therefore 2 is selected as model order for each mode. Furthermore, these poles are generally not stabilized.

A further optimization over the residuals of the modal outputs is carried out after the identification of the modal state-space models. Eventually, it is possible to go back to the physical domain by applying the direct modal transformation. In particular, the simulated (physical) outputs are compared with the measured ones of the validation set. The comparison is reported in the time domain in Figure 5.23 for S6, the other sensors showing a similar result. In particular, the measured signal is plotted against its residual with the simulated one both before and after the final optimization. The residual appears to be relatively small, and the relative RMS error between the two signals is approximately 12% before the optimization and 9% after the optimization. This result is replicable also with the other sensors.
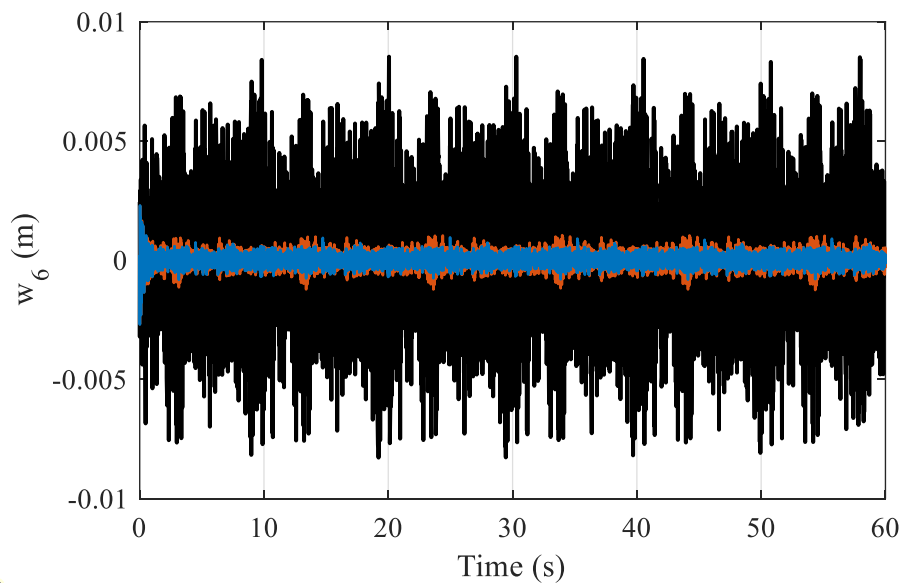
Figure 5.23: Validation of the nonlinear identification in the time domain. Black: measured output, S6, validation set; orange: residual with the simulated output before the optimization; blue: residual with the simulated output after the optimization.

The same comparison is reported also in the frequency domain considering the spectra of the respective signals in the frequency range of interest, and the result is depicted in Figure 5.24. The frequency-domain representation is particularly useful because it clearly shows the regions where the identification struggles. Before the final optimization, the region around the first natural frequency is the most critical, with a residual 14 dB lower than the signal. The final optimization improves this result with a much smaller error. Thus, the optimized identified model is taken as the final one hereafter.
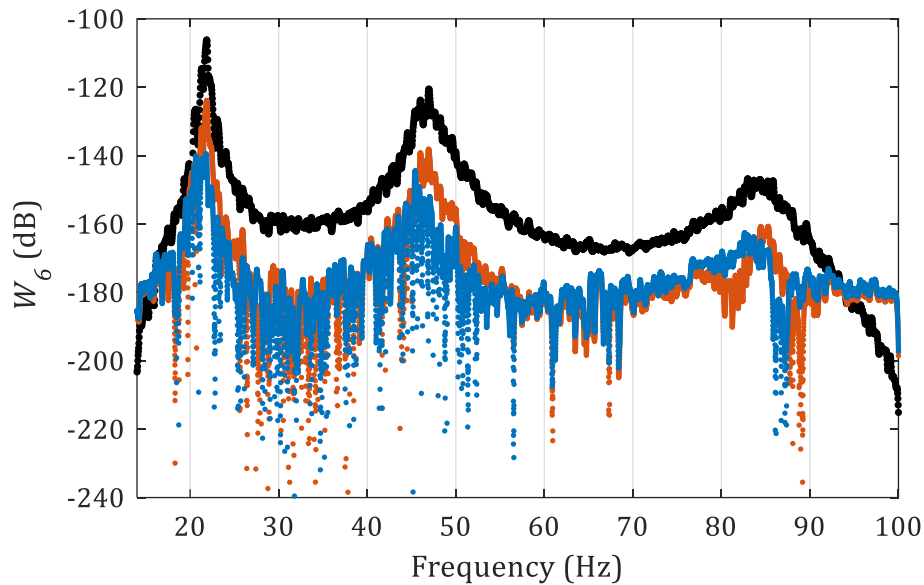
Figure 5.24: Validation of the nonlinear identification in the frequency domain in dB scales (ref. 1 m²/Hz). Black: spectrum of the measured output, S6, validation set; orange: residual with the spectrum of the simulated output before the optimization; blue: residual with the spectrum of the simulated output after the optimization.

Eventually, the first three identified coefficients are reported in Figure 5.25 as frequency-dependent quantities in their real and imaginary parts.
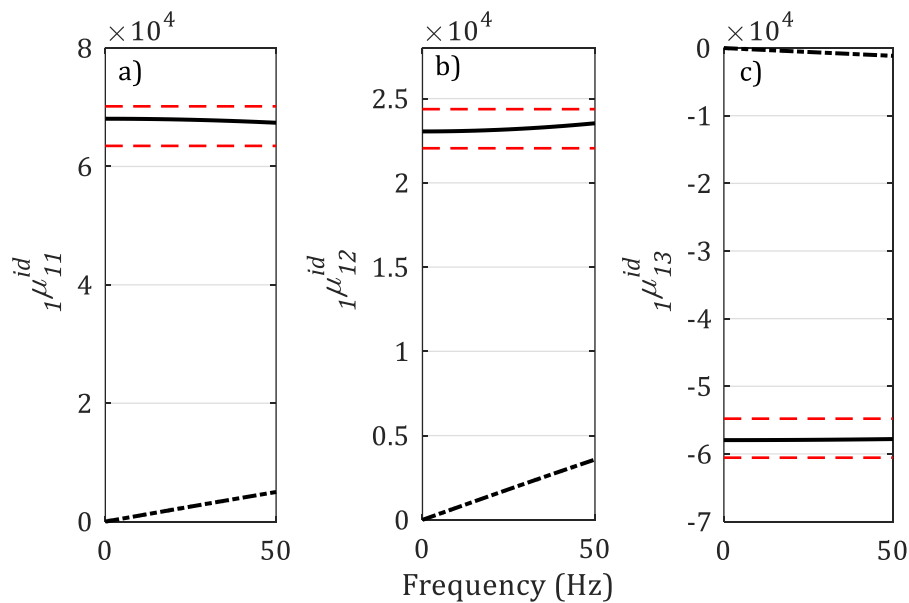
Figure 5.25: First three identified coefficients as frequency dependent quantities. Black continuous line: real part; black dashed-dotted line: imaginary part; red dashed line: ±5% of the mean value. a) Coefficient $_1\mu_{11}{}^{id}$; b) Coefficient $_1\mu_{12}{}^{id}$; c) Coefficient $_1\mu_{13}{}^{id}$.

It is worth highlighting that the imaginary part is always several orders of magnitude lower than the real part, which assesses the goodness of the identification. Also, the real part shows little variations in its spectrum. Thus, the spectral mean of the real part is taken as the final value for the identified coefficients, termed $_r\bar{u}_{pq}^{id}$. The matrix $_1\overline{\boldsymbol{u}}^{id}$ of the identified coefficients related to the first mode is reported in Figure 5.26 together with their percentage deviation in the considered frequency range. Only the upper triangular matrix is shown, as repeated monomials are discarded in the identification (the nonlinear basis functions are the ones in Eq. (5.20)). The small percentage deviation from the mean value confirms the goodness of the choice of the nonlinear basis functions.
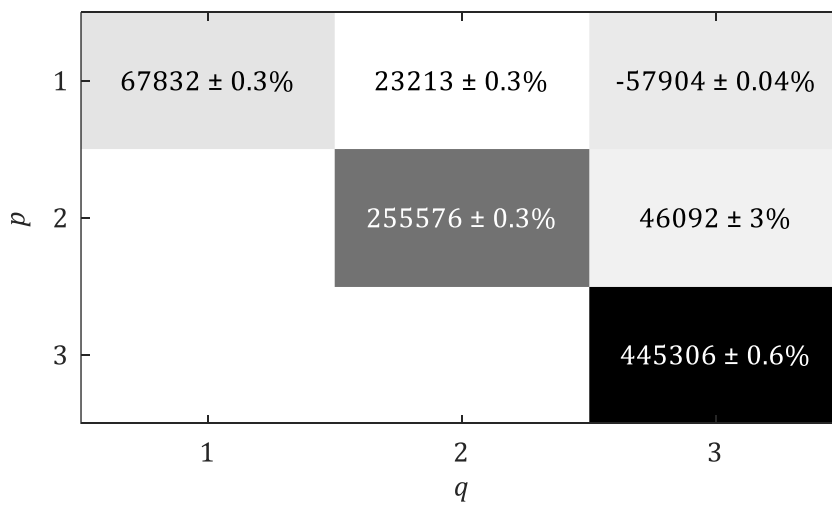
Figure 5.26: Upper triangular matrix of the identified coefficients related to the first mode, with their percentage deviation. The background color of each entry is proportional to its magnitude.

The nonlinear feedbacks of the first mode (Eq. (5.20)) corresponding to the coefficients of Figure 5.26 are depicted in Figure 5.27.

Eventually, the underlying linear system is identified as well and compared with the one obtained applying SI to the low-level test. The comparison is reported in Figure 5.28 in terms of receptances.
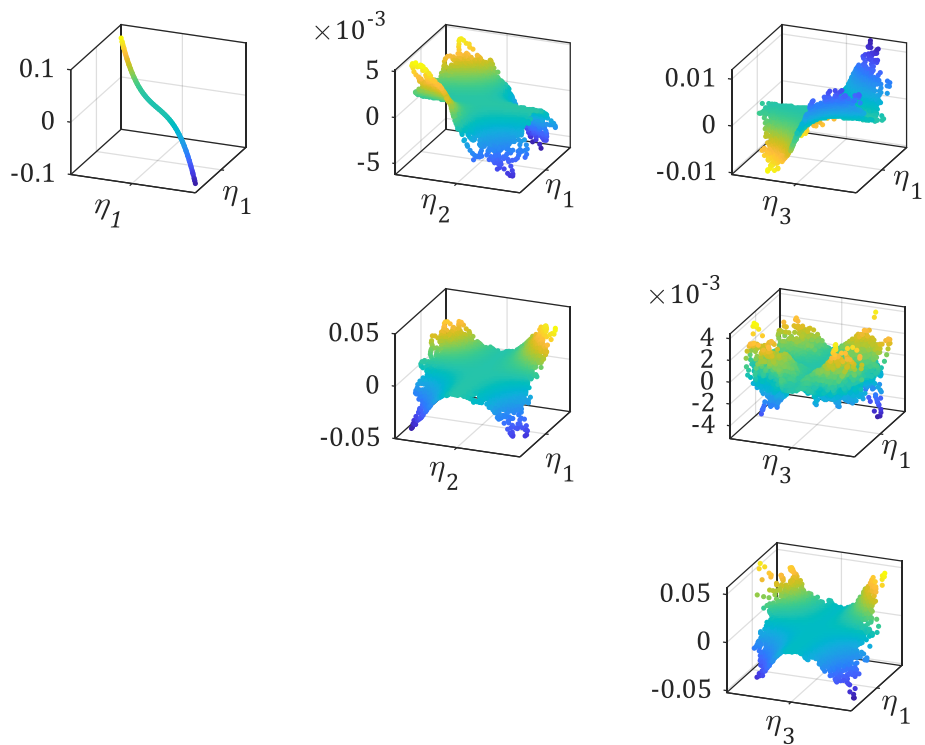
Figure 5.27: Nonlinear feedbacks of the first mode computed with Modal-NSI.
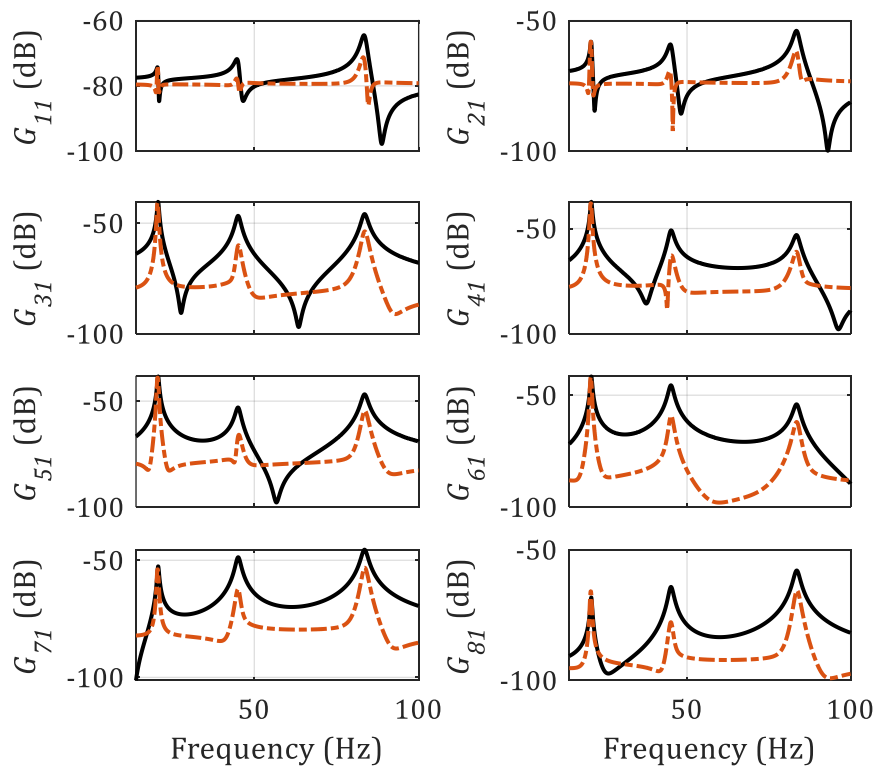
Figure 5.28: Estimated linear FRFs (receptance) in dB scales (ref. 1 m/N) for all the sensors. Black line: SI estimate from the low-level test; dashed-dotted orange line: residual with the NSI estimate from the high-level test.

There is generally a good correspondence between the NSI estimation of the linear FRFs and the SI estimation from the low-level. The highest residual corresponds to the first mode, whose identified natural frequency is slightly different for the two FRFs. The identified modal parameters are reported in the final comparison table (Table 5.5).

Modal-NSI with extended basis functions

An option to improve the results of Modal-NSI could be to expand the basis functions so as to include all the possible couplings between modes (η_p, η_q) for each mode r, with both odd and even degrees. This allows the inclusion of even nonlinearities, which allegedly improve the identified model. In this case, the nonlinear feedbacks can be written as bivariate polynomials of maximum degree equal to 3, yielding:

$$
\begin{aligned}
\boldsymbol{\xi} = -[&\eta_1^2, \quad \eta_1^3, \quad \eta_1\eta_2, \quad \eta_1\eta_2^2, \quad \eta_1^2\eta_2, \quad \eta_1\eta_3, \quad \eta_1\eta_3^2, \\
&\eta_1^2\eta_3, \quad \eta_2^2, \quad \eta_2^3, \quad \eta_2\eta_3, \quad \eta_2\eta_3^2, \quad \eta_2^2\eta_3, \quad \eta_3^2, \\
&\eta_3^3, \quad \eta_1\eta_2\eta_3]^\mathrm{T}
\end{aligned}
\tag{5.21}
$$

Since this vector already includes all the modes, it is possible to compute it just once and then it can be used as a feedback for each mode $r = 1, \dots, N$. The final number of nonlinear feedbacks per mode is 16 when $J = N = 3$.

The stabilization diagrams of the underlying-linear (modal) systems are computed for each mode in order to select the best model order and they are reported in Figure 5.29. Stability is checked also in this case for frequencies, damping ratios, MACs and modal masses. As for the stabilization diagrams of Figure 5.22, the incomplete decoupling of the equations of motion due to the nonlinearity implies that multiple poles can be identified for each mode.

A model order equal to 2 for each mode is considered hereafter, as in the previous case. The simulated (physical) outputs are compared with the measured ones of the validation set. The comparison is reported in the frequency domain in Figure 5.30 for S6, the other sensors showing a similar behavior. In particular, the spectrum of the measured signal is plotted against its residual with the simulated one, both before and after the final optimization. The residual now is smaller than the previous case, and the relative RMS error between the two signals in time is approximately 11% before the optimization and 7% after the optimization. The optimized identified model is taken as the final one hereafter.
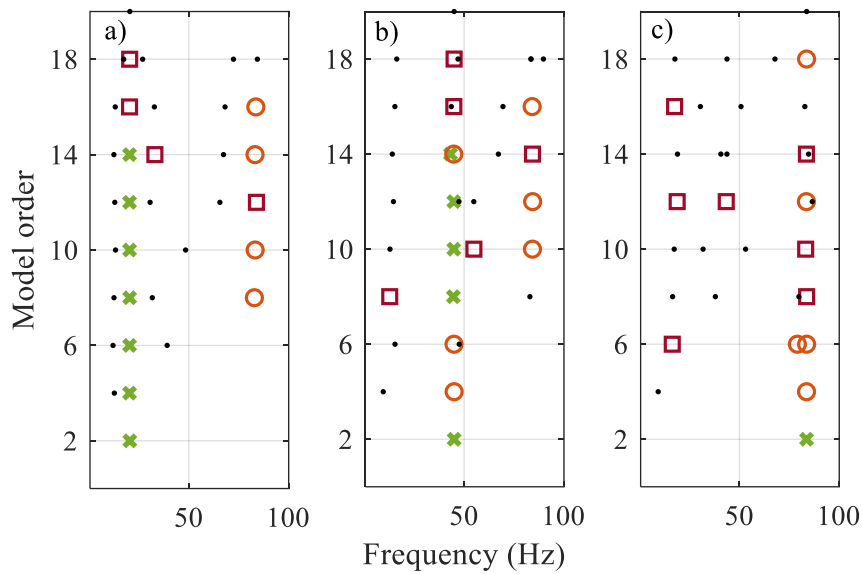
Figure 5.29: Stabilization diagrams of the modal ULSs considering the extended basis functions. Stabilization thresholds for natural frequency, damping ratio, MAC and modal mass are 0.5%, 10%, 99.5%, 10%, respectively. Black dot: new (not stable) pole; blue plus: pole stable in frequency; red square: pole stable in frequency and MAC; orange circle: pole stable in frequency, MAC and damping; green cross: pole stable in frequency, MAC, damping and modal mass. a) Mode number 1; b) Mode number 2; c) Mode number 3.
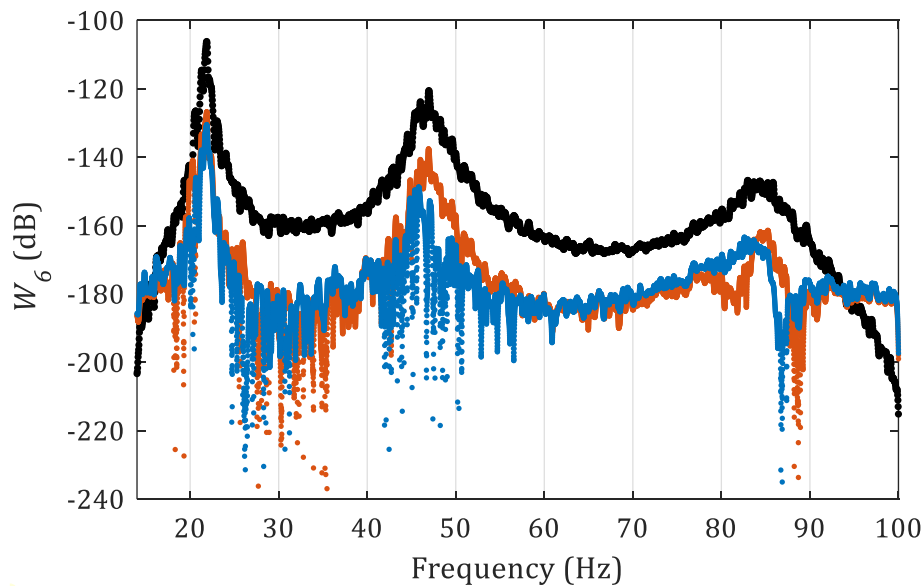
Figure 5.30: Validation of the nonlinear identification in the frequency domain in dB scales (ref. 1 m²/Hz). Black: spectrum of the measured output, S6, validation set; orange: residual with the spectrum of the simulated output before the optimization; blue: residual with the spectrum of the simulated output after the optimization.

As for the coefficients of the nonlinearities, 16 coefficients per mode are identified, as the result of the expansion of the basis functions. While this allows for more flexibility to catch the nonlinear part of the response, it makes the nonlinear coefficients to lose their original physical interpretation. Therefore, the representation of all the identified coefficients is not useful in this case, because no meaning can be directly associated to them. Instead, it may be informative to know which feedbacks are predominant for each identified mode. For this reason, the RMS magnitude of each nonlinear feedback is depicted in Figure 5.31 using a grey-scale colormap. It is clear that the highest RMS on each mode corresponds to the purely cubic basis function $\eta_1^3, \eta_2^3, \eta_3^3$, respectively. Thus, the cubic nonlinearity is dominant for each mode, in accordance with the theory.
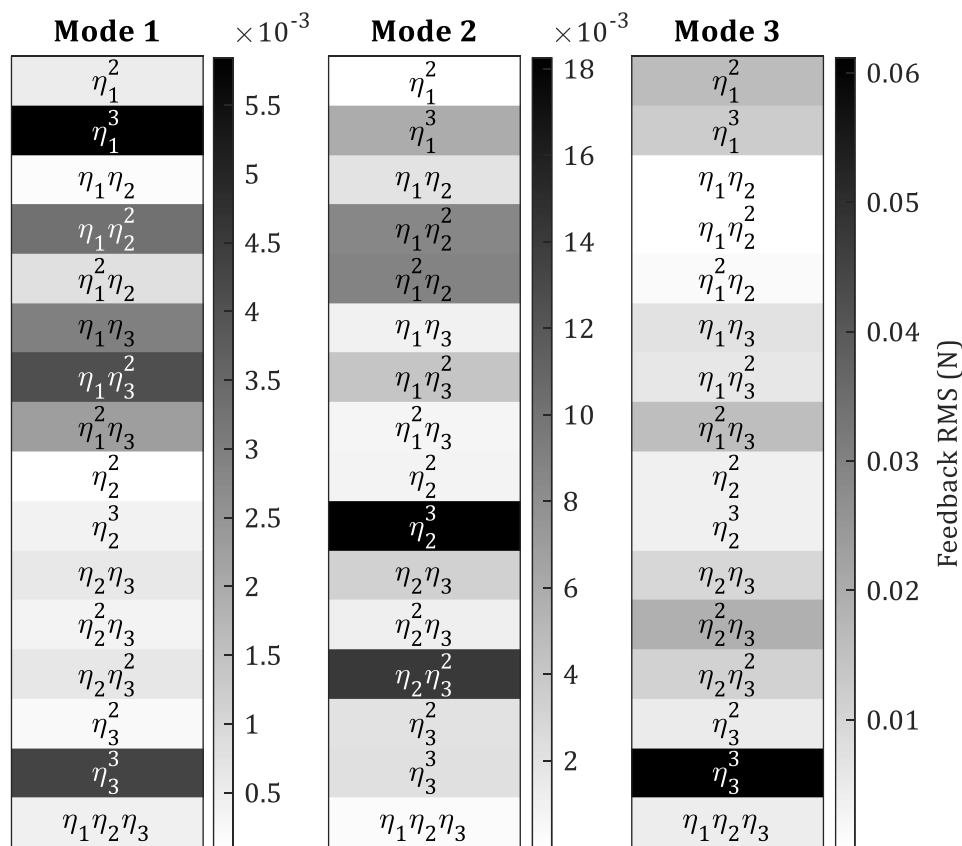
Figure 5.31: RMS magnitudes of the nonlinear feedbacks for the three identified modes with NSI. The background color of each entry is proportional to its magnitude.

The ratios between real and imaginary parts of the identified coefficients are reported in Figure 5.32 for the first mode of the structure. The other modes show a similar behavior, with values that are usually between 10^1 and 10^2.
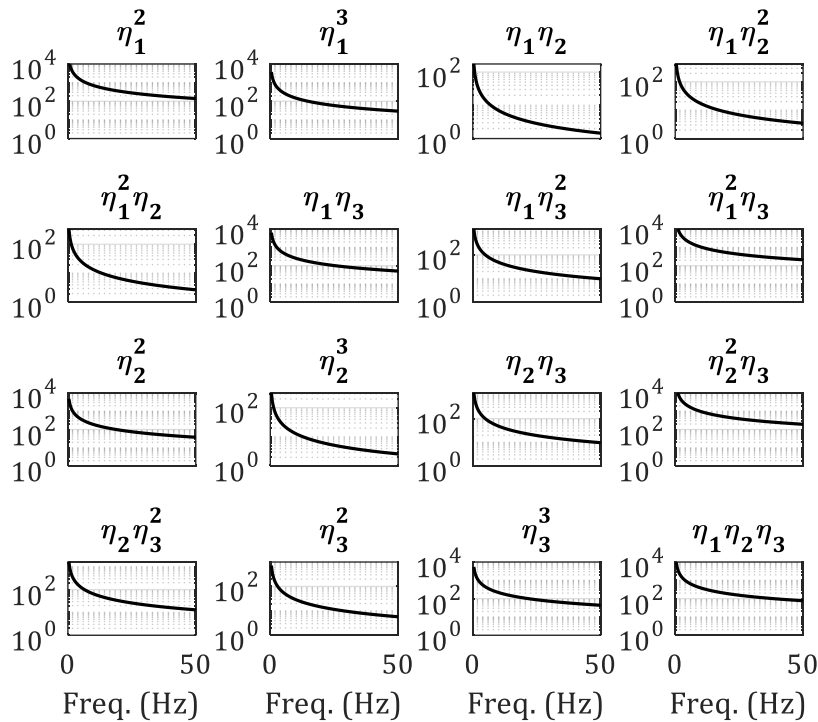
Figure 5.32: Ratios between real and imaginary parts of the identified coefficients related to the first mode, in the frequency range 0-50 Hz.

The underlying linear system is also identified, and it is compared with the one estimated by SI. The comparison is reported in Figure 5.33 in terms of receptance. Figure 5.33 also shows the residual between the linear FRF estimated by SI and the underlying linear FRF estimated by Modal-NSI using the original basis functions. The residuals of the underlying linear FRF computed with Modal-NSI in the two cases (original basis functions and extended ones) seem to be comparable with each other. Therefore, it can be supposed that expanding the nonlinear basis functions in this case mostly affects the nonlinear part of the system, so that the residuals of the outputs drop from 9% to 7%. Indeed, this is generally not true, as linear parameters are affected as well by the choice of the nonlinear basis functions. In this particular case, this result confirms that the main nonlinear contributions come from the original nonlinear basis functions, and in particular from the cubic terms (Figure 5.31). The inclusion of the other coupling terms results just in a slight improvement of the predicted nonlinear response. Eventually, the identified modal parameters are reported in the subsequent comparison table.
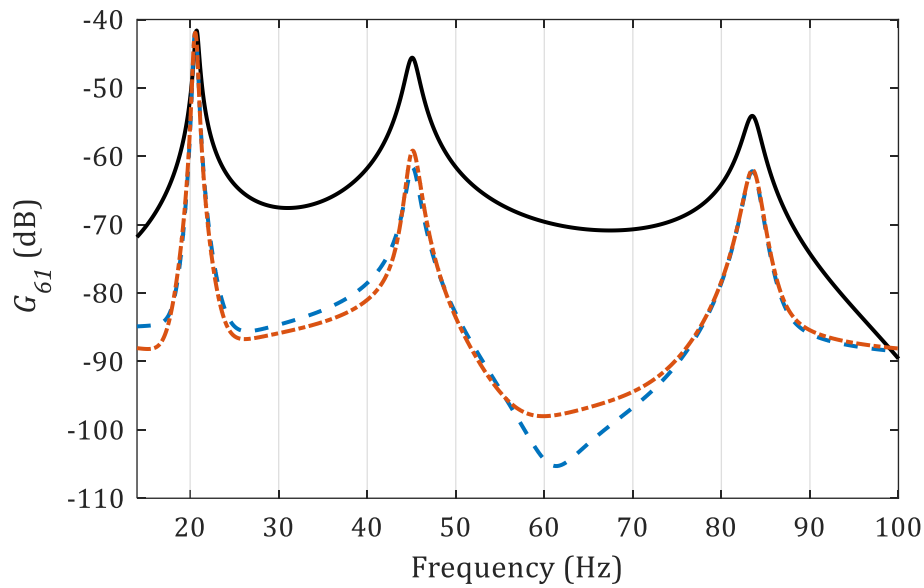
Figure 5.33: Estimated linear FRF (receptance) related to S6 in dB scales (ref. 1 m/N). Black line: SI estimate from the low-level test; dashed-dotted orange line: residual with the NSI estimate from the high-level test and the original basis functions; dotted blue line: residual with the NSI estimate from the high-level test and the extended basis functions.

Table 5.5: Summary of the identified modal parameters: SI, Modal-NSI with the original basis functions (Original Modal-NSI), Modal-NSI with the extended basis functions (Extended Modal-NSI).

Mode number	Frequency (Hz)			Damping ratio (%)		
	SI	Original Modal-NSI	Extended Modal-NSI	SI	Original Modal-NSI	Extended Modal-NSI
1	20.7	20.4	20.5	1.2	1.1	1.2
2	45.1	45.1	45.1	1.7	2.3	2.2
3	83.6	83.8	83.8	1.1	2.0	2.0

There is a very good correspondence in the identification of the natural frequencies, while the results related to the damping ratios are less in agreement with their corresponding low-level estimates. In particular, Modal-NSI generally identifies a higher damping than the low-level test. The reason for that may be a source of nonlinear damping that has not been considered in the model. Thus, a further improvement of the methodology should take into account also the possibility of characterizing the nonlinear damping.

As for the computational burden, Modal-NSI runs in roughly 1-2 minutes including the final optimization, depending on the number of nonlinear basis functions adopted.

Black-box identification with PNLSS

In the case of PNLSS, no basis function must be defined and the working domain is the physical one. This brings the great advantage that no pre-processing of the signal has to be performed, and neither a low-amplitude linear identification. On the other hand, every physical interpretation of the results is lost, and the validation of the model can be performed only on its prediction capabilities.

The degrees of the multivariate polynomials in the state and output equations must be chosen, and a reasonable choice is to consider degrees 2 and 3 in the states, so as to include even and odd nonlinear functions.

The first step of PNLSS is the computation of the BLA. A way to ensure that the BLA is correctly computed is to check first the periodicity of the outputs when a periodic input is applied. In the considered case, a multisine input is provided with 6 periods and 5 realizations. A periodicity analysis it therefore carried out by subtracting every period from the last one for each realization, and results are depicted in Figure 5.34.
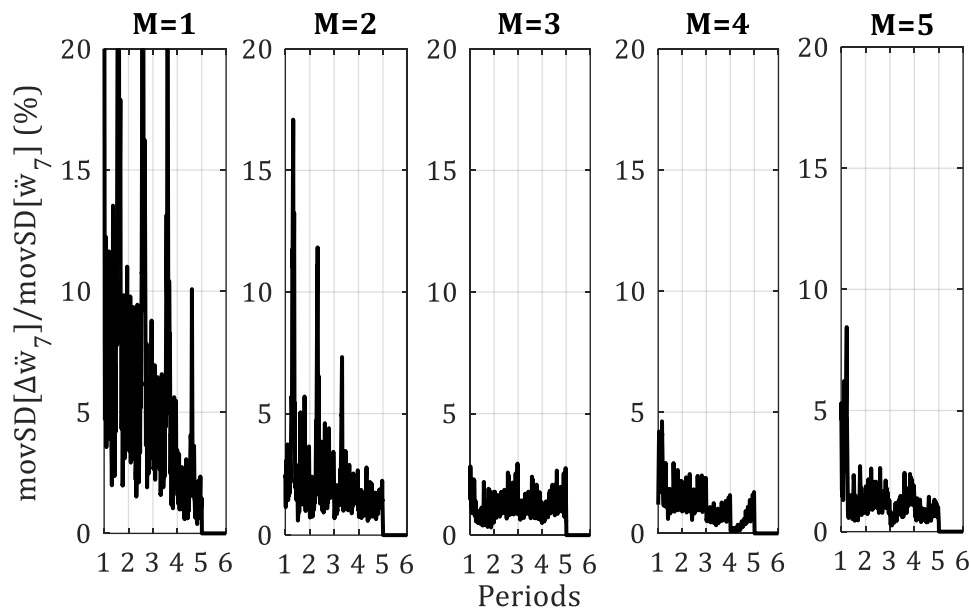
Figure 5.34: Periodicity analysis on the acceleration of S7, f_0=2 N (RMS): moving standard deviation (movSD) of the difference between every period and the last one over the moving standard deviation (movSD) of the last period.

It can be seen that generally the periodicity is not preserved, especially for the first two realizations. This is allegedly due to the strong nonlinear behavior, whose periodicity break is a characteristic phenomenon. For this reason, the first two realizations are excluded from the PNLSS analysis, and the first two periods are removed from the remaining realizations to get rid of transients. This should maximize the confidence in the BLA estimation, which is computed by averaging over different periods and realizations.

The BLA estimations of the FRFs related to S2 and S8 are depicted in Figure 5.35. A state-space model of order equal to 6 is fitted to the BLA to initialize the nonlinear optimization of PNLSS, using the subspace identification algorithm in the frequency domain [61].
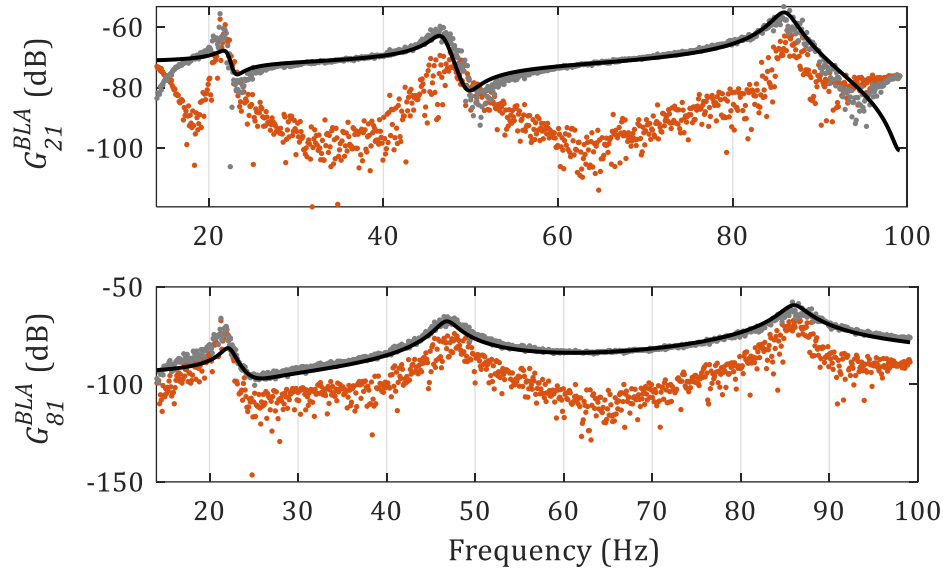
Figure 5.35: BLA analysis on S2 and S8 in dB scales (ref. 1 m/N). Grey dots: experimental BLA; black line: parametric BLA, model order equal to 6; orange dots: residual.

The residuals between the experimental BLA and the parametric BLA are generally quite high, which is somehow expected since the system is inherently nonlinear. The percentage error between measured outputs and predicted ones using the state-space model of the parametric BLA can be computed, and a very high value is retrieved: the average error over the different sensors is 70%. This confirms that even the best possible linear model is inadequate in representing the dynamical behavior of the structure, and a nonlinear model must be considered. Nevertheless, such a high residual might be an inconvenient for the subsequent nonlinear optimization of the state-space model, as the starting point may be very far away from the optimal solution. Such optimization is carried out using the Levenberg–Marquardt algorithm, in order to populate the matrices E and F (Eq. (B1), Appendix B). A total of 462 parameters are optimized, corresponding to the coefficients of the multivariate polynomials in the state equation. To avoid the possibility of being stuck into a local minimum, two sequential optimizations of 60 iterations each have been conducted, plus a third one to assess the result. The starting point of each optimization is the best solution of the previous one, as depicted in Figure 5.36. The high number of iterations is justified by the huge error obtained with the BLA model, which is the starting point of the first optimization. This cascade of optimizations makes the computational effort

quite high, so that PNLSS runs on approximately 45 minutes on the same computer used with Modal-NSI. Therefore, the PNLSS analysis is certainly more dispendious than Modal-NSI.
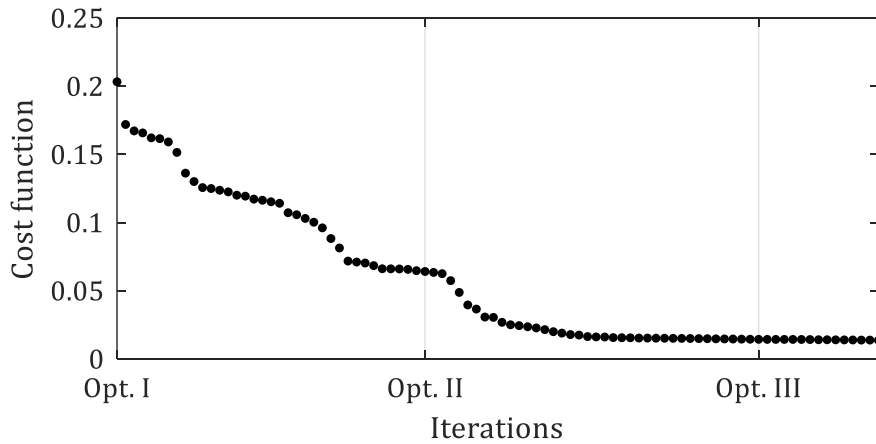
Figure 5.36: Cost function value of the Levenberg–Marquardt optimization cascade with PNLSS.

The final result is shown in Figure 5.37 in terms of output prediction. In particular, the measured displacement of the validation set of S6 is represented in the time and frequency domains and compared with the simulated one using the nonlinear state-space model. The outcome of Modal-NSI with extended basis functions is also reported as a comparison.

The average residual obtained with PNLSS is 19%, which is a huge improvement from the BLA error (70%). However, it is not a satisfactory result when compared to Modal-NSI, whose residual is 7%. This result is replicable for the other sensors as well. By looking at Figure 5.37a, the major issue with PNLSS seems to be the presence of transients. This can be noted by the spikes in the residuals obtained with PNLSS corresponding the be beginning of a new period. It should be recalled that a prior periodicity analysis has already been conducted (Figure 5.34) and the first two periods of each realization already removed. It is likely that the strength of the nonlinearity is high enough to compromise the periodicity of the remaining part of the response as well. A lower excitation level which preserves the periodicity should improve the PNLSS result. It must be said also that Modal-NSI is designed ad-hoc for distributed nonlinearities, while PNLSS provides a flexible model structure that can fit several situations. Also, the time-domain version of NSI has been used to develop Modal-NSI, which is not affected by the presence of transients or periodicity breakdowns. It is likely that the frequency domain counterpart (FNSI) in the modal domain would present the same issues of PNLSS for the considered excitation level.

No more insights can be inferred from the nonlinear state-space model of PNLSS, given the black-box nature of the algorithm. From this point of view,

Modal-NSI is much more informative, as it gives information about both the ULS and the coefficients of the nonlinearities. The use of one method or another depends on the needs of the user and on the purposes of the identified model: control, design, prediction, ...
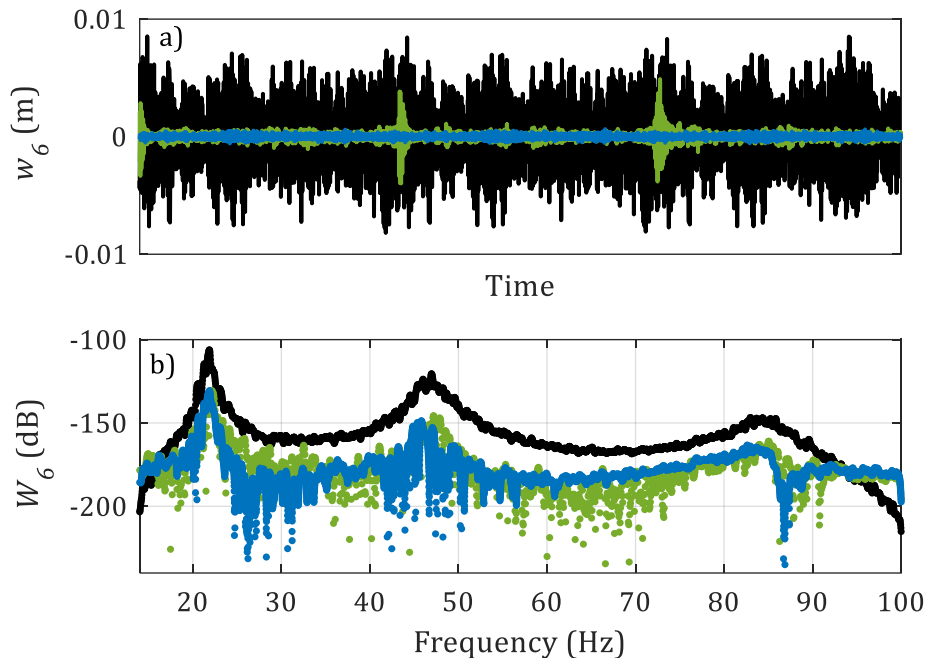
Figure 5.37: Validation of PNLSS. Black: measured output, S6, validation set; blue: residual with the simulated output, Modal-NSI; green: residual with the simulated output, PNLSS. a) Time domain; b) Frequency domain spectra in dB scales (ref. 1 m²/Hz).

5.5. Concluding remarks

In this chapter, a methodology for performing nonlinear system identification on structures exhibiting distributed geometrical nonlinearities was presented. The system identification is performed in a reduced-order domain, obtained by first identifying the linear normal modes of the structure. An ad-hoc version of the NSI method working in the modal domain was adopted, called *Modal-NSI*, although the methodology itself is not restricted to a particular identification method.   The whole approach is applied to experimental data related to a very thin beam exhibiting a distributed nonlinear behavior. A series of tests have been performed to characterize the dynamical behavior of the structure, involving sine-sweeps and multisine excitations.

The nonlinear identification has been performed with Modal-NSI selecting the nonlinear basis functions according to a modal model of a clamped-clamped nonlinear beam. The model itself has been validated numerically by comparing its outcome with a nonlinear FEM (Ansys). In a second step, the

nonlinear basis functions have been extended to cover also even nonlinearities, not present in the model but retrieved in the experimental setup. Results generally show a very good level of accuracy, validating the effectiveness of the methodology. Eventually, PNLSS is also applied on the same dataset as a comparison. Further improvements of Modal-NSI should take into account also nonlinear damping and the possibility to test the method on more complex real-life structures exhibiting large deformations.

Chapter 6

Nonlinear identification for design: application to OCLs

6.1. Introduction

System identification of nonlinear structures has been covered in the previous chapters considering several scenarios, with novel and proven techniques. However, little words have been spent on the final purposes of the extracted model structure, whilst the developing of methods for the identification was the primary focus. It has been discussed in Chapter 3 that several reasons can motivate the need of performing system identification, from control to design. In this chapter, the latter case will be covered by considering the design of a nonlinear improved dropper for railway overhead contact lines (OCLs). The chapter is organized as follows:

- Motivations: limits of the current technologies and reasons for the research of new designs;
- Nonlinear system identification: extraction of the functional parameters of the nonlinear dropper prototype;
- Experimental tests on a reduced test set: check the differences between identified parameters and designed ones, eventually followed by a correction of the design choices;
- Simulations on a high-speed OCL: numerical tests using a FE model (Cateway).

Some context is provided in the subsequent section to introduce railway overhead contact lines with emphasis on the high-speed case.

6.1.1. Railway overhead contact lines (OCLs)

Railway OCLs are complex arrangements of cables and wires that provides the electric energy supply to the train by means of the contact between the pantograph of the vehicle and the catenary. Typically, in the European network the catenary structure is composed of a series of repeating spans having lengths 50-60 meters. Each span is basically made of three main components (Figure 6.1): the contact wire, the messenger (or carrier) wire, and the droppers.
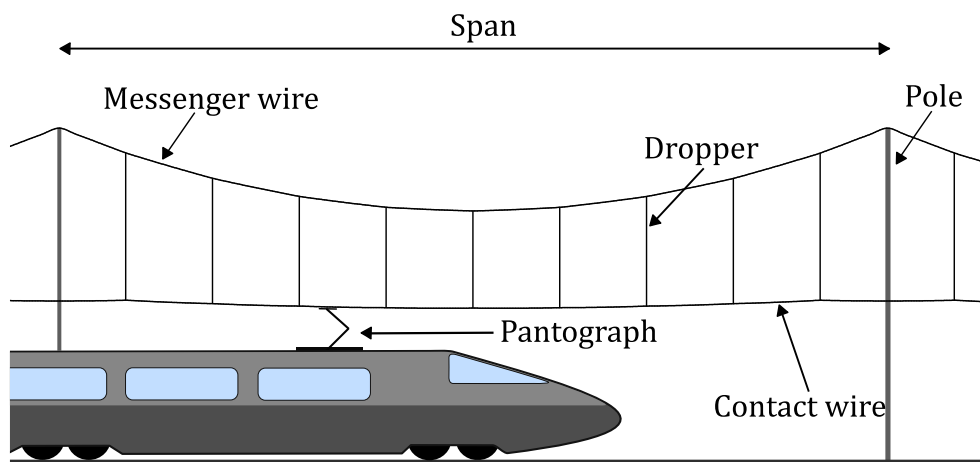
Figure 6.1: 2D scheme of a typical pantograph-catenary system.

From the electrical point of view, the contact wire is the most important component because it is the only responsible for supplying the current to the train. The messenger wire and the droppers are adopted to stiffen the catenary, and the length of the droppers is set so as to realize an almost flat profile of the contact wire in its static configuration. Both messenger and contact wires are tensioned with high axial forces (typically 16-22 kN) to limit the sag and guarantee an appropriate smoothness of contact with the pantograph. The poles delimit each span and bear the brackets to support the messenger wire and to set the classical zig-zag profile of the contact line (called *stagger*) via the steady arms, as in Figure 6.2.

The OCL and the pantograph form a coupled system because of their continuous interaction, which produces very rich and complex dynamics, involving wave propagation phenomena and sources of nonlinearities.
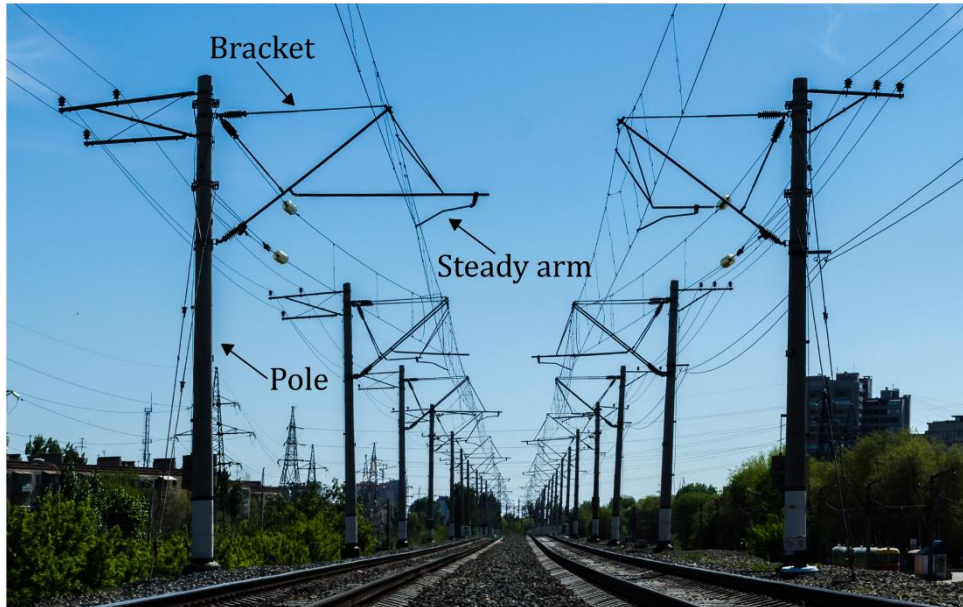
Figure 6.2: Photo of an overhead contact line. Source: http://pxhere.com/en/photo/998878, CC0.

The pantograph itself is the current collector element mounted on the roof of the train. The kinematics of the pantograph allows the elevation of the upper part, carrying the contact elements. These are generally two carbon strips, sliding on the lower surface of the contact wire (Figure 6.3).
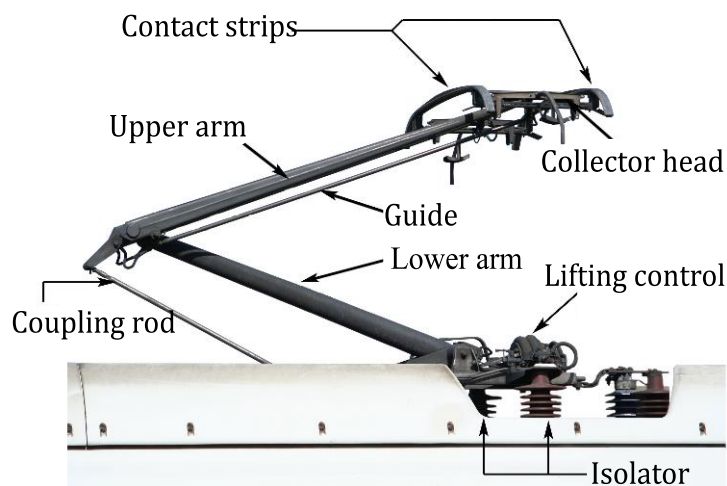
Figure 6.3: Scheme of a pantograph. Source: Rcsprinter123, Pantograph ICE 3, https://commons.wikimedia.org/wiki/File:Pantograph_ICE_3.png, CC BY-SA 3.0.

When the train travels at high speeds, the catenary structure may undergo large displacements, such that the dropper length may occasionally become shorter than the unstretched configuration. In this condition the dropper gets under compression: it becomes unstable and its stiffness becomes almost negligible, as it can be seen in Figure 6.4b. This phenomenon is referred to as

slackening, and it represents one of the principal sources of nonlinearity in the catenary system. Furthermore, the higher the speed of the train is, the more difficult becomes to maintain a smooth and constant contact between the contact wire and the pantograph. The force that the pantograph and the contact wire exchange is generally called *contact force*, and it should be theoretically maintained as constant and smooth as possible, to avoid deterioration of the functional conditions of the two systems in contact. Losses of contact between these two elements are quite frequent in high speed trains though, causing electrical arcs, temporary losses of electrical supply and wear of the components [103]. This phenomenon is photographed in Figure 6.4a.
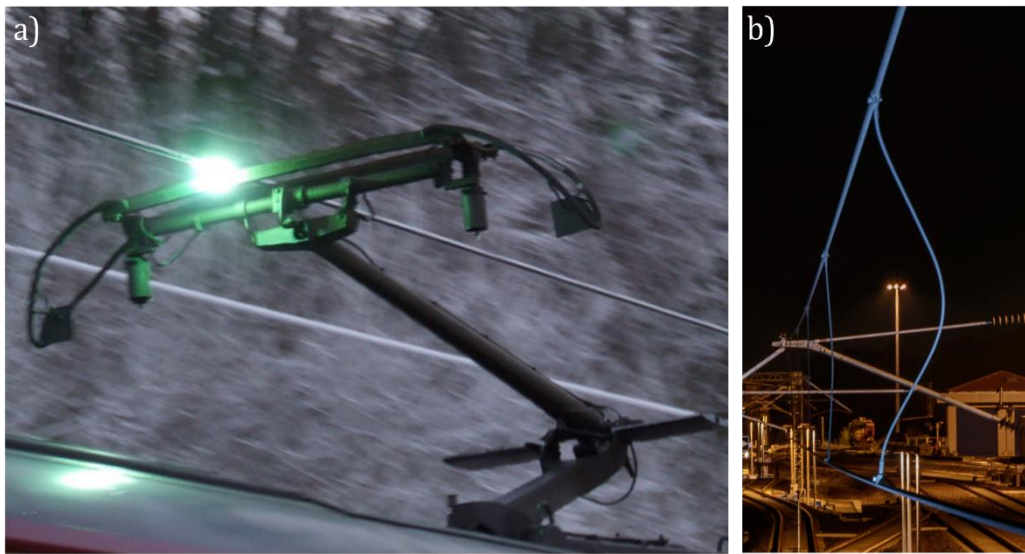
Figure 6.4: a) Electric arc caused by a temporary loss of contact. Source: T. Nugent, Sparking pantograph, https://www.geograph.org.uk/photo/2216440, CC BY-SA 2.0; b) Slackening phenomenon.

The statistical parameters of the contact force are used as an indication of the goodness of the contact both in simulations and experimental measurements. The quality of the pantograph-catenary contact required for high-speed train operations is quantified in current regulations EN50317 [104] and EN50367 [105]. Also, for the European network, the technical specifications for interoperability across the different national networks are defined by the TSI specifications [106]. The most important requirements to be satisfied are:

- The standard deviation σ_c of the contact force f_c must not exceed the value $0.3\, \bar{f}_c$, with $\bar{f}_c$ mean contact force:

$$\sigma_c \leq 0.3\, \bar{f}_c \tag{6.1}$$

The desired value of $\bar{f}_c$ depends on the velocity of the train v, and it is generally estimated by a heuristic quadratic law of the kind [107]: $\bar{f}_c =$

$0.00097v^2 + 70$ N, valid for speeds up to 320 km/h [108]. This value corresponds also to the static preload that the pantograph induces on the contact wire.

- The limit of the maximum contact force is set to: $\max(f_c) \leq 350$ N.
- The maximum uplift of the contact wire in correspondence of the steady arms (at each support) is set to 120 mm.
- The maximum vertical displacement of the pantograph is set to 80 mm.
- The percentage of real arcing must not exceed 0.2%.

Moreover, the maximum allowed operational speed of the train is related to the lowest wave propagation velocity on the contact wire, called critical speed c_{crit} and given by [109]:

$$c_{crit} = \sqrt{\frac{\pi^2 EI}{ml^2} + \frac{T}{m}}$$ (6.2)

where EI is the bending stiffness of the contact wire, m is the contact wire mass per unit length, T is its axial tension and l its length. When the train speed approaches the critical speed of the contact wire, the contact between the pantograph and the catenary is harder to maintain due to increase in the amplitude of catenary oscillations and bending effects. In order to avoid the deterioration of the contact quality, the current regulation imposes a limit to the train speed defined by [107]:

$$v \leq 0.7 c_{crit}$$ (6.3)

Taking the overhead contact line of [110] as an example, the critical speed results in roughly 460 km/h, meaning that the velocity of the train cannot exceed 320 km/h. This is a typical value for standard high-speed European OCLs, and it confirms that technological restrictions are still heavily present despite the huge achievements of the last decades.

6.1.2. Motivations of the current work

Nowadays, more than 46000 km of high-speed rails (HSR) are in operation worldwide [111], with the majority of share belonging to China. Among them, Europe detains more than 9000 km spread across Austria, Belgium, France, Germany, Italy, Poland, Spain, the Netherlands and the United Kingdom (Figure 6.5). As for the speed, the typical maximum speed of HSRs in Europe ranges from 250 km/h to 320 km/h, while it reaches 350 km/h on selected lines in China [112]. This values are valid only for steel-wheels kind of railways, which are the most common. Other technologies, such as magnetic levitation (Maglev train in China) and Hyperloop are promising even faster rail speeds, but require the construction of all new rail lines.
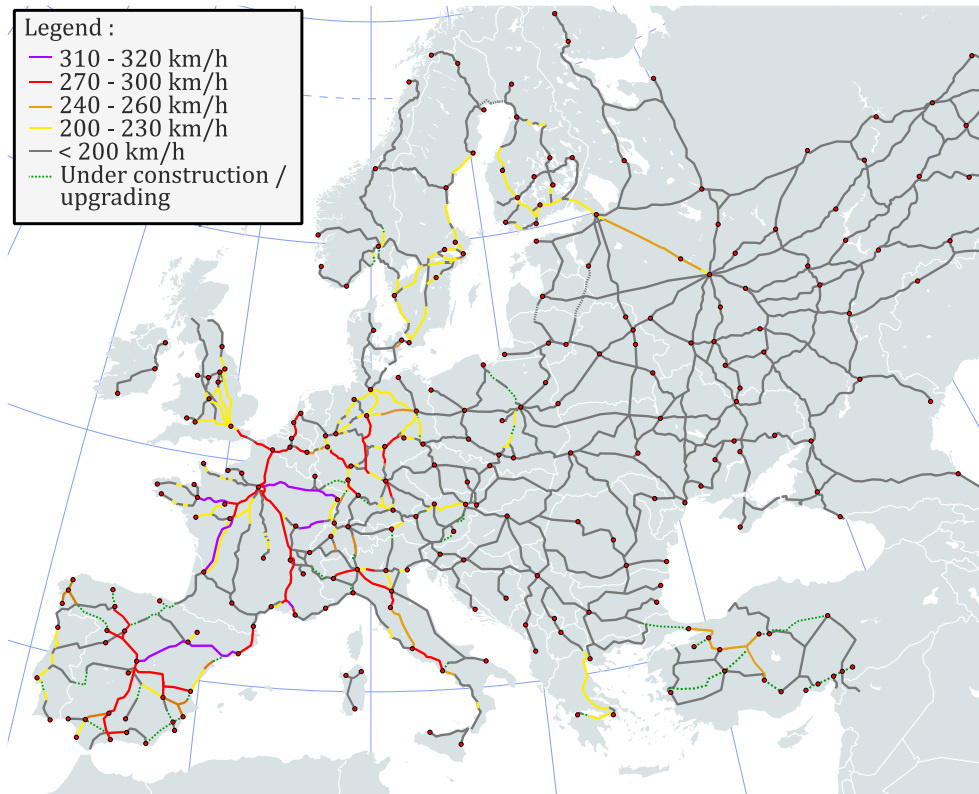
Figure 6.5: High speed railroad map of Europe in 2019. Source: https://commons.wikimedia.org/wiki/File:High_Speed_Railroad_Map_of_Europe.svg, CC BY-SA 3.0.

Expanding the HSRs and improving their performances in a cost-effective way is a demanded goal among railway national services, although it can be a time-consuming and expensive job. "Improving" in this context theoretically means gaining a smoother and constant contact between the OCL and the pantograph(s), as well as the possibility to safely increase the train speed above the current limits. Looking at Eqs. (6.2) and (6.3), it is straightforward to realize that the latter goal can be *easily* achieved by modifying the material characteristics of the contact wire, or its axial tension. For instance, the current world speed record for a commercial train on steel wheels is held by the French TGV at 574.8 km/h [113], and obtained via huge modifications of the catenary infrastructure. In particular, the catenary voltage was increased to 31 kV from the standard 25 kV, and the mechanical tension in the wire to 40 kN from the standard 25 kN. The resulting critical speed reached therefore 610 km/h, providing a sufficient margin of safety beyond the train's maximum speed [114]. Similarly, improvements in the material of the wires composing the OCL can lead to a higher allowed speeds. The main component of contact wires is copper (Cu), but it may host inclusions of elements like magnesium (Mn) or silver (Ag) to increase its tensile strength [115], and thus the allowed axial tension in operational conditions.

Of course, such solutions involves the partial or full replacement of existing lines, with enormous costs and times: on average, it takes around 16 years for brand-new high-speed lines to proceed from the start of works to the beginning of operations [116], with an average cost of almost 30 million €/km [117]. Another possibility would be to act on the preload of the pantographs, to generate higher contact forces. These would lead to less incidents of loss of contact, but would also lead to higher friction forces and, consequently, to higher wear of the catenary contact wire and pantograph strip [118]. Further strategies have been proposed to improve the current quality collection, such as: extra lumped masses [119], auxiliary pantographs [120], or variations of the pantograph characteristics [121,122].

The idea pursued in this project is instead related to the damping distribution of the OCL, and involves the design of nonlinear droppers with increased damping capabilities. It should be highlighted that standard droppers used in railway OCLs do not add any significant damping contributions to the structure: they are needed to adjust the stiffness of the catenary system and regularize the height of the contact wire. The addition of damping-droppers would allow to keep existing lines in operation, with just localized upgrades. The idea comes from the consideration that OCLs are very lightly damped structures [81,123,124], and therefore easily subjected to undesired long-lasting oscillations. Moreover, as long tensioned wires are involved, low-frequency modes are dominant in the response. Reducing these vibrations would possibly help the dynamical pantograph-catenary interaction, gaining a smoother contact force.

This idea has been investigated considering numerical simulations and experimental tests, and detailed information can be found in the master theses recently developed at the Dynamics and Identification Research Group of Politecnico di Torino by B. Villen [125], L. Dellavalle [126] and D. Lucio [127].

6.2. An improved nonlinear dropper

The design of the improved dropper for OCLs is inspired from negative stiffness absorbers. Devices and materials exhibiting a negative stiffness region are often used as vibration isolators due to their amplified damping properties [128,129]. In particular, in the case of engineering structures, such devices are usually designed adopting discrete macroscopic elements, such as post-buckled beams, plates, shells and pre-compressed springs, arranged in appropriate geometrical configurations. Examples can be found in automotive suspensions [130,131] or seismic isolation [132,133]. The central concept of these approaches is to significantly reduce the stiffness of the isolator and consequently of the natural frequency of the system even at almost zero levels [134]. In this way, the transmissibility of the system for all operating

frequencies above the natural frequency is reduced, resulting to enhanced vibration isolation [129].

Details about the design stages of the improved dropper are reported in the master theses [125,127]. Due to difficulties in performing experimental tests in real OCLs, the first prototype is designed considering a reduced test set, involving a 30 meters long tensioned contact wire. Performances are evaluated in terms of absorbed vibrations. This is justified by considering that low-frequency modes at around 1 Hz dominate the oscillations of the contact wires in OCLs. Because of the little damping of such structures, these low-frequency modes have a very long decay, lasting for minutes after a train passage. Moreover, the wave propagation phenomenon has a huge impact on the dynamical response of the OCL [81], especially in relation with the pantograph interaction. It is therefore plausible that damping out these modes results in a smoother contact with the pantograph, as reported in [135], reducing also propagation and reflection of waves.

6.2.1. Design and experimental characterization

The main element of the dropper is a U-shaped frame, anchored to the messenger wire and connected through rods to a central moving point. A schematic representation is depicted in Figure 6.6, where the sub-part of the dropper containing the frame is drafted as a rectangle.
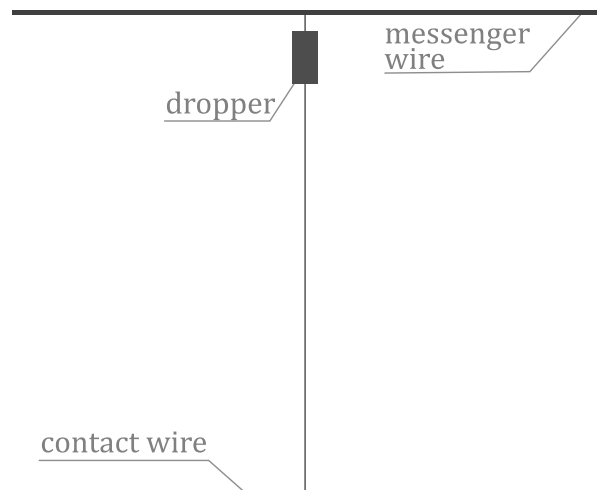
Figure 6.6: Schematic representation of the position of the dropper.

The design process of the elements of the device is reported in the already mentioned master theses, while the experimental characterization and identification is pursued here, to validate the adopted model and eventually perform a nonlinear model updating. To do so, the upper (flat) surface of the frame is attached to a shaking table, so that a displacement $b(t)$ can be imposed to the structure. In this configuration, the system can be treated as a

double-well Duffing oscillator, like the one discussed in Chapter 2. Two photos of the experimental setup are reported in Figure 6.7, showing the system in its two equilibrium positions.
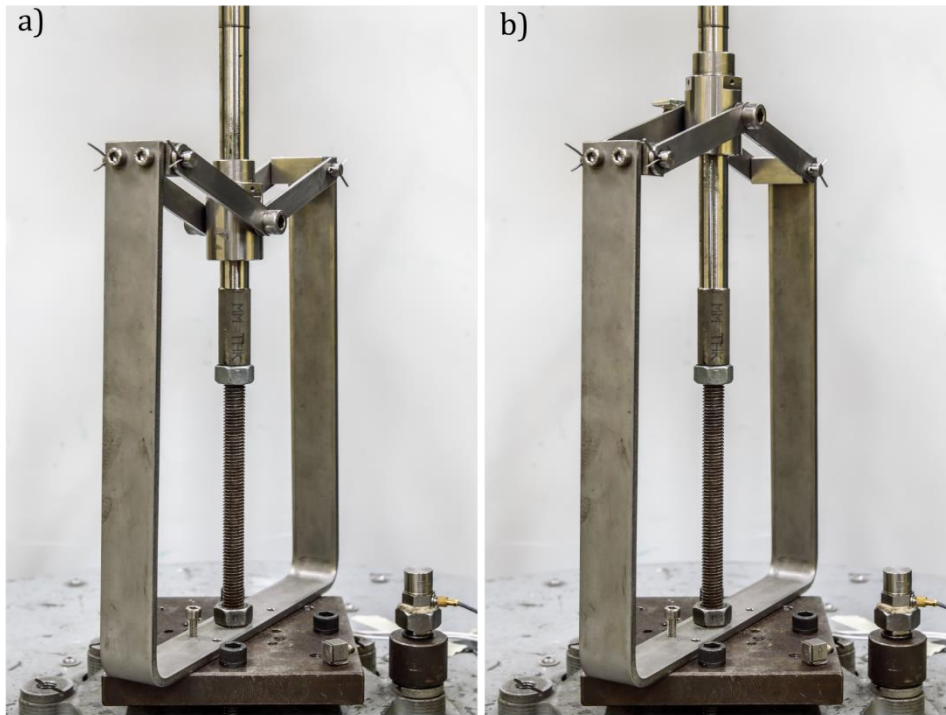
Figure 6.7: Photos of the experimental setup. a) Negative equilibrium position; b) Positive equilibrium position.

It is assumed that the inertia of the moving parts can be concentrated into one central point with mass m, comprising the mass of the central bushing and the equivalent inertia of the rods. The vertical movement of this point is described by the coordinate $y(t)$, while the rotation of the rods is called θ. The elastic deformation of the frame exerts a compression force $p(\theta)$ on the rods, considered as infinitely rigid.

A schematic representation of the functional model here described is reported in Figure 6.8, together with the free-body-diagram of the mass m.

The equilibrium equation along the vertical coordinate is:

$$m\ddot{y}(t) + 2p\big(\theta(t)\big)\sin\big(\theta(t)\big) + mg = 0 \qquad (6.4)$$

Calling $z(t) = y(t) - b(t)$, it yields:

$$m\ddot{z}(t) + 2p\big(\theta(t)\big)\sin\big(\theta(t)\big) + mg = -m\ddot{b}(t) \qquad (6.5)$$

Since the system is a SDOF, the displacement $z(t)$ is taken as independent variable and both θ and $p(\theta)$ are written as a function of z.
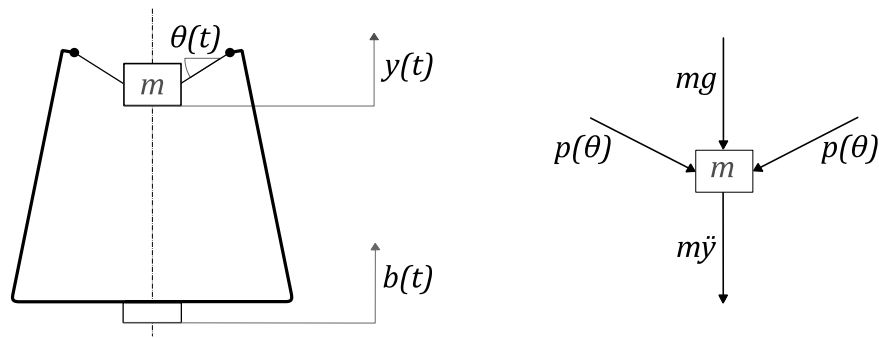
Figure 6.8: Model of the negative stiffness oscillator and free-body-diagram of m.

The elasticity of the frame is studied in [125] to analytically derive the force $p(\theta)$ that the frame transmits to the rods. This is obtained by considering a physically-based model of half the frame, with the elasticity of the different segments modelled using beam elements. The model itself is defined by the following set of parameters (see [125] and Figure 6.9):

- Dimensions of the frame: a, h, s_1, s_2, d
- Length of the rods: r
- Angle of the frame: α
- Young's modulus: E
- Mass of the moving point: m
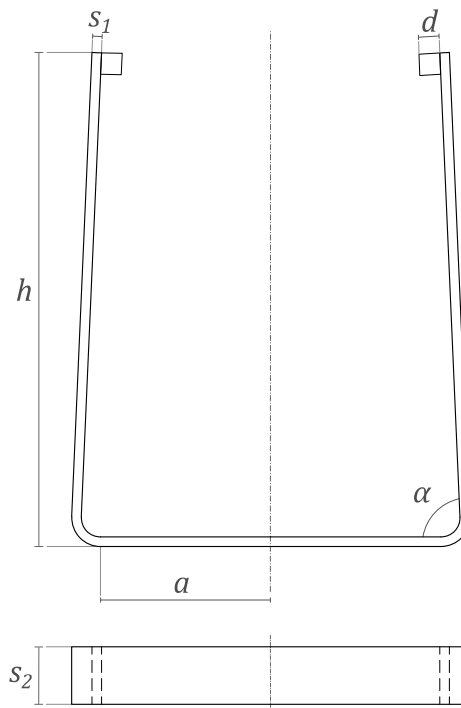
Figure 6.9: Physical parameters of the model.

A qualitative representation of the vertical component $p_v = 2\,p(\theta)\sin(\theta)$ of p is depicted in Figure 6.10 as a function of $z(\theta)$. The quantitative

representation instead is provided later on, when the experimental measurements are considered.
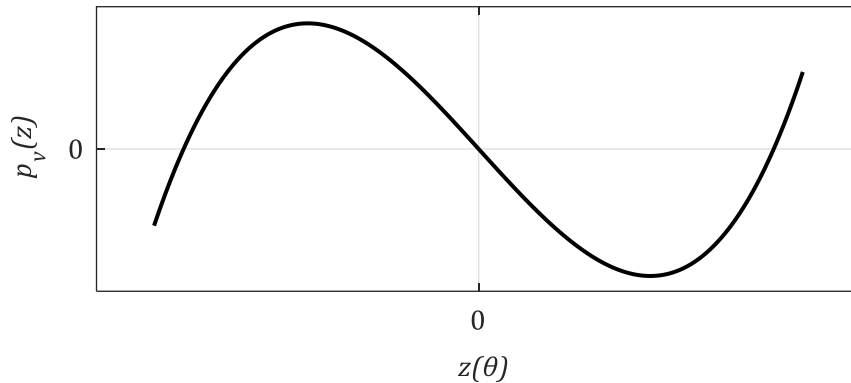
Figure 6.10: Qualitative graph of the force p_v.

It can be seen that $p_v(z)$ has three roots and crosses the origin with a negative slope, which gives a negative stiffness contribution. A much more informative representation of $p_v(z)$ can be found by writing the force as a polynomial expansion. This can be done considering that it is a continuous function, and it yields:

$$p_v(z) = k_3 z^3 + k_2 z^2 - k_1 z \tag{6.6}$$

The choice of such representation is based on the following considerations:

- The linear coefficient k_1 accounts for the negative stiffness contribution;
- The quadratic coefficient k_2 accounts for the vertical asymmetry of the U-shaped frame;
- The cubic coefficient k_3 accounts for the overall shape of $p_v(z)$, which appears to be mainly a cubic function.

The equation of motion can eventually be written as:

$$m\ddot{z} + k_3 z^3 + k_2 z^2 - k_1 z + k_0 = -m\ddot{b} \tag{6.7}$$

where $k_0 = mg$. Eq. (6.7) has the form of a negative-stiffness Duffing equation. The restoring force K of the system and the elastic potential U are defined as:

$$K(z) = k_3 z^3 + k_2 z^2 - k_1 z + k_0 \tag{6.8a}$$

$$U(z) = \frac{1}{4} k_3 z^4 + \frac{1}{3} k_2 z^3 - \frac{1}{2} k_1 z^2 + k_0 z \tag{6.8b}$$

A qualitative representation of the potential is shown in Figure 6.11. The quantitative representation instead is provided later on, when the experimental measurements are considered. Its asymmetric double-well

characteristic can be observed, together with the three equilibrium positions z^* obtained by setting $K(z^*) = 0$. As in Chapter 2, two out of three positions represent a stable equilibrium, namely z_-^* and z_+^*, while the central position z_0^* is an unstable point.

The oscillations of the moving point are said to be *in-well* when the motion is bounded around one of the two stable equilibrium positions $z_\pm^*$. The associated linear natural frequency $\omega_\pm$ can be computed by:

$$\omega_\pm = \sqrt{\frac{U''\left(z_\pm^*\right)}{m}} \tag{6.9}$$

$U''\left(z_\pm^*\right)$ being the second derivative of $U(z)$ computed in z_-^* or z_+^*.

As for the experimental setup, the moving mass is instrumented with an accelerometer to measure its absolute acceleration $\ddot{y}(t)$ and a laser vibrometer to measure its absolute displacement $y(t)$. The zero position of $y(t)$ corresponds to the horizontal configuration of the rods ($\theta = 0$). The acceleration of the base $\ddot{b}(t)$ is also recorded through a second accelerometer, so as to obtain the displacement $z(t)$ as the difference between the laser measure $y(t)$ and the displacement of the base $b(t)$. The latter is obtained by integrating twice the measured acceleration.
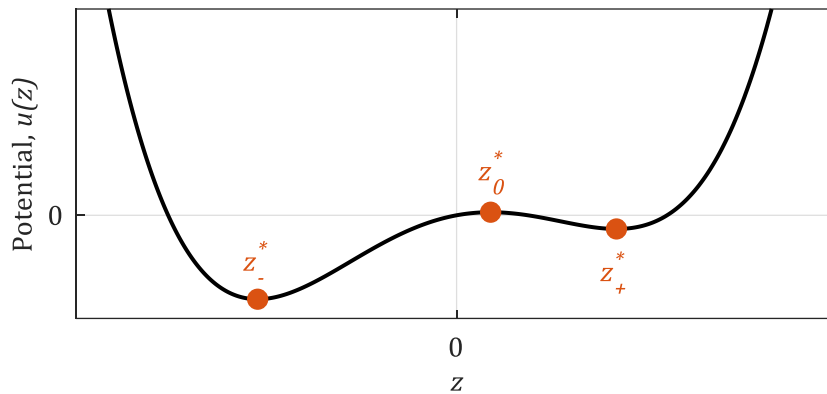
Figure 6.11: Potential of the double-well Duffing oscillator. Orange dots: equilibrium positions.

Random tests

Random tests are performed to check the non-homogeneity of the FRFs with increasing excitation levels, as a proof of nonlinearity. The frequency range is $7 - 50$ Hz, with a sampling frequency of 512 Hz and a duration of 300 s. Several forcing levels are applied, expressed as RMS values of the acceleration of the base $\ddot{b}$, and the starting position is z_-^*. Results are depicted in Figure 6.12 in terms of time series and transmissibility T, defined as the ratio between the output acceleration $\ddot{z}$ and the input $\ddot{b}$. In-well oscillations in the neighborhood of the negative equilibrium position can be observed, which in this case is approximately at -3 cm from the horizontal configuration of the rods ($\theta = 0$). Also, an increasingly asymmetric behavior with respect to z_-^* can be noted for increasing forcing levels, as the system tries to cross the negative stiffness region and reach the positive equilibrium position. This results in a clear change in the transmissibility, where a softening effect can be seen, in accordance with the theoretical studies that show a similar behavior in the case of in-well motion [22].
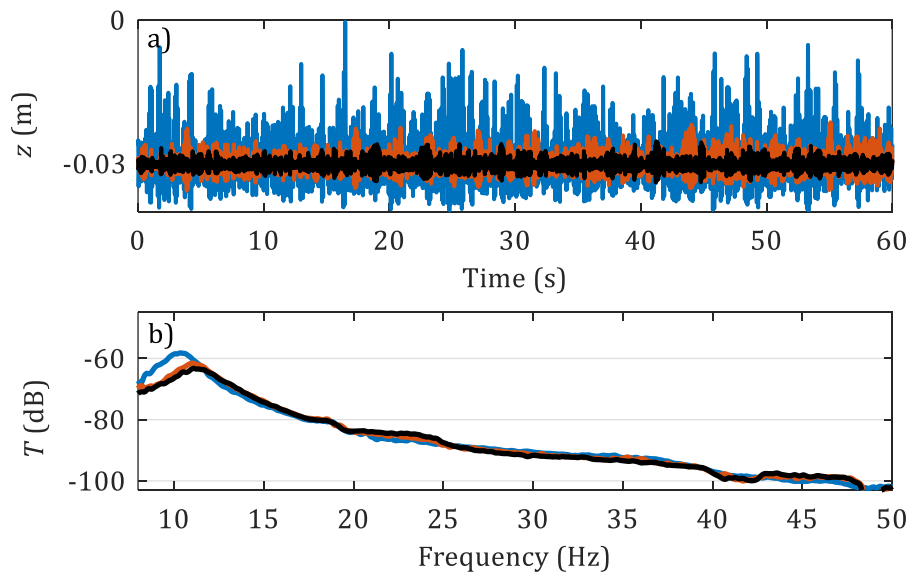
Figure 6.12: Random tests. Black line: $\ddot{b}$=7 m/s² RMS; orange line: $\ddot{b}$=9 m/s² RMS; blue line: $\ddot{b}$=26 m/s² RMS. a) Time history of the displacement (first 60 seconds); b) Transmissibility T in dB scales.

Cross-well random oscillations can be obtained when the energy given to the system is high enough. This situation is depicted in Figure 6.13, where the displacement $z(t)$ clearly shows repeated crossings between negative and positive values.
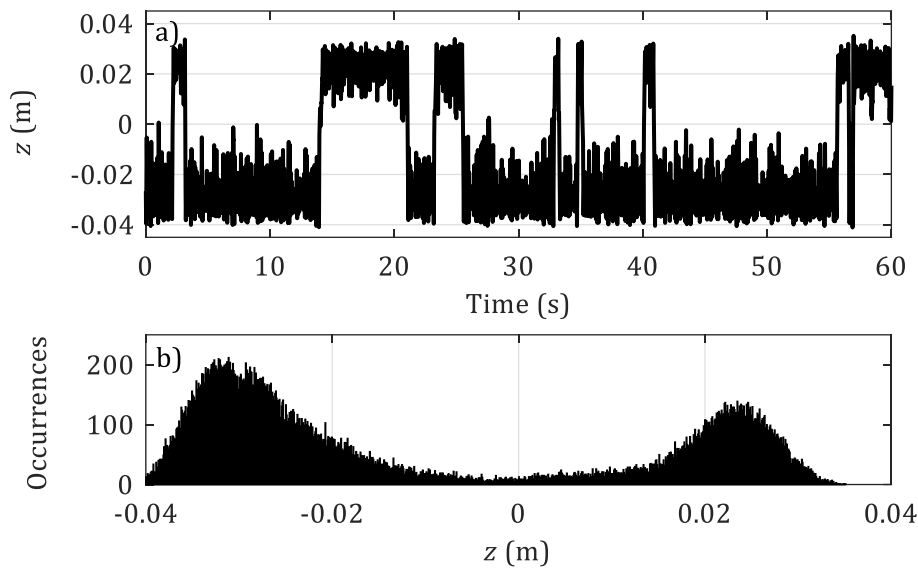
Figure 6.13: Random test at the highest amplitude, $\ddot{b}$=38 m/s² RMS. a) Time history of the displacement (first 60 seconds); b) Statistical distribution of the displacement.

Sine-sweep and harmonic tests

As discussed in Chapter 2, nonlinear systems theory was developed upon harmonically excited systems. For the case considered here it is particularly interesting to see what happens when the device is driven through harmonic excitations, given its bi-stable nature.

Up and down sine sweeps are considered first, in the frequency range 5 – 21 Hz. The sampling frequency is 512 Hz and the length of the up-down sweep is 240 s. Two forcing levels are taken into account, expressed as the amplitude b_0 of the base displacement, and the starting position is the negative equilibrium z_-^*. The up and down sweeps are shown in Figure 6.14. The softening effect can be seen when the system vibrates with in-well oscillations around one equilibrium position (Figure 6.14a): an increase in the forcing amplitude corresponds to an earlier occurrence of the jump-up. As in Chapter 2, the jump phenomenon is symptomatic of the existence of multiple solutions and unstable paths in the response of the system, as it suddenly tries to reach a stable path with different amplitude. Also, two distinct jumps can be noticed, corresponding to the dominant frequency $(10 - 11$ Hz) and its second harmonic $(20 - 21$ Hz).

Cross-well oscillations can be obtained also in this case for higher excitation levels (Figure 6.14b, orange line). It is interesting to look at the harmonic contributions in this case by computing the spectrogram of the relative displacement. The result is reported in Figure 6.15, where the first two minutes refer to the sweep-up, while the second two minutes refer to the sweep-down.
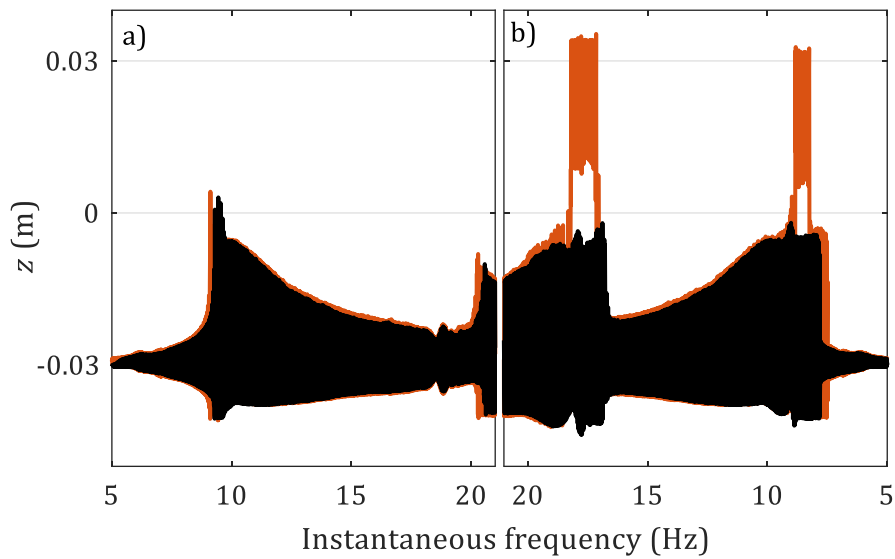
Figure 6.14: Sine-sweep tests. Black line: b_0=4.5 mm; orange line: b_0=5 mm. a) Sweep up; b) Sweep down.
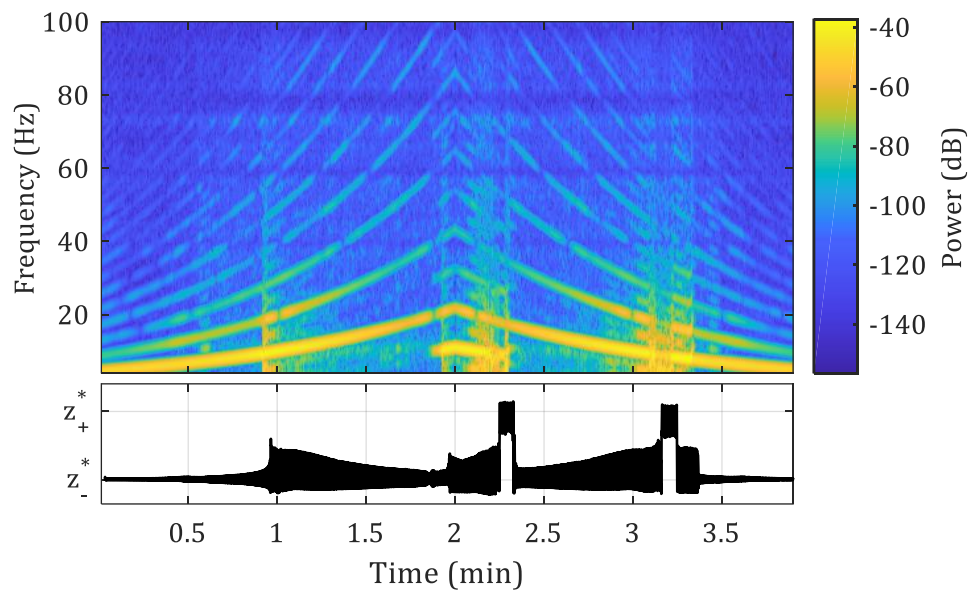
Figure 6.15: Spectrogram of the highest level sine-sweep test and corresponding time-domain response.

Both even and odd harmonics of the instantaneous frequency are present along the whole acquisition, confirming the asymmetrical behavior of the nonlinear system. Subharmonics are also visible in some regions, in particular around 1 and 2 minutes. As stated in Chapter 2, they are generally symptomatic of the possibility of bifurcations and chaotic motion, thus a series of harmonic tests with constant frequency is performed to analyze these effects. The excitation frequency is $\nu = 9$ Hz and three different amplitudes b_0 are considered. Results are presented in the phase diagrams in Figure 6.16.

When the amplitude of the sine excitation is $b_0 = 2$ mm (Figure 6.16a) the phase plane shows one closed orbit centered around the equilibrium position, i.e. one periodic solution [1]. Instead, nested orbits can be noted in Figure 6.16b, when $b_0 = 4.7$ mm. Two paths in a closed loop are generally representative of the period doubling effect [1], so that a period-2 solution is also present (see Chapter 2). This is the case of Figure 6.16b, as demonstrated also by the power spectral density of the signal depicted in Figure 6.17. It can be seen that the system responds at both integer multiples of the dominant frequency v ($2v, 3v, \dots$) and of its subharmonic $\frac{1}{2}v$ $\left(\frac{3}{2}v, \frac{5}{2}v, \dots\right)$.
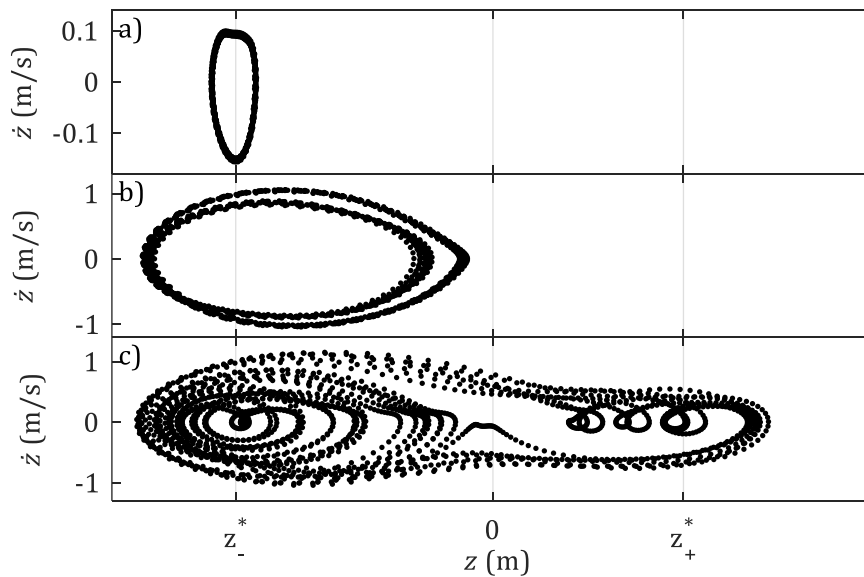
Figure 6.16: Phase diagrams of the response under harmonic excitation. a) b_0=2 mm; b) b_0=4.7 mm; c) b_0=5 mm.
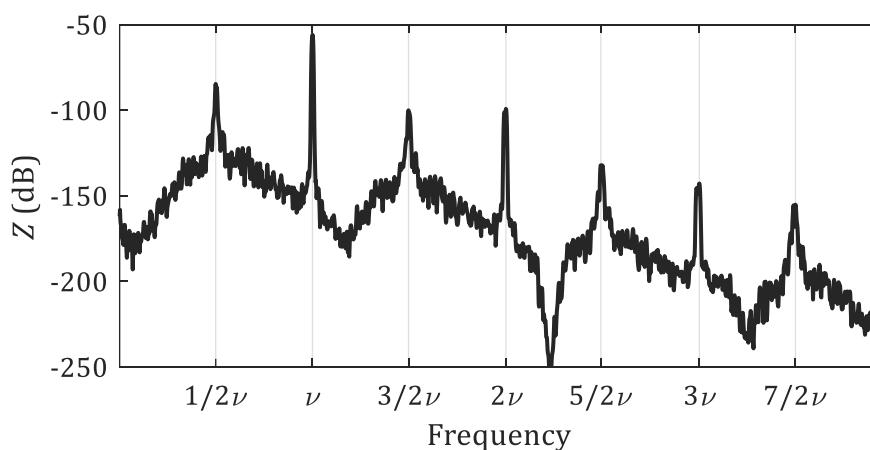
Figure 6.17: Power spectral density of the harmonic response in dB scales (ref. 1 m^2/Hz), b_0=4.7 mm.

Eventually, cross-well oscillations are obtained with an amplitude of $b_0 = 5$ mm. The solution in this case is bounded but not periodic, and it continuously

crosses the stable equilibrium points (cross-well motion) for all the acquisition length, which is 10 minutes. As already seen in Chapter 2, this kind of response is a symptom of *chaotic* behavior. A portion of the time response is depicted in Figure 6.18.
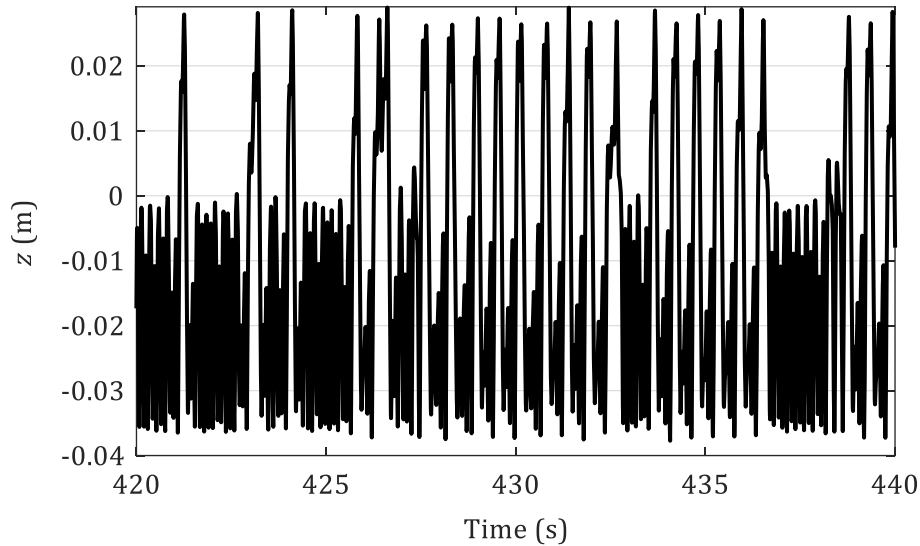
Figure 6.18: Time response under harmonic excitation, b_0=5 mm.

Of course, this case is different from the one seen in Chapter 2, for experimental measurements to be considered here. Indeed, the system is not *strictly* deterministic in this case due to the presence of noise in the acquisition data and possible small harmonic distortions in the input. For these reasons, the largest Lyapunov exponent (LLE) λ is computed from the measured time series following the method proposed in [136]. The result is shown in Figure 6.19, recalling that a positive sign of λ means chaotic motion, while a negative sign is representative of a periodic orbit.
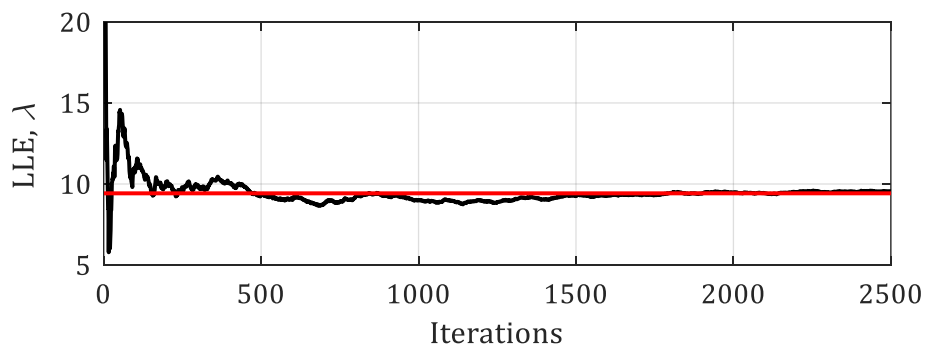
Figure 6.19: Estimation of the Lyapunov exponent. Red line: convergence mean value.

The positive sign of the estimation of the LLE confirms that the system is exhibiting a chaotic motion. The experimental Poincaré sections are computed for different phase synchronizations ϕ of the data with the forcing term [137].

The typical shape of a strange attractor is retrieved [32] and depicted in Figure 6.20a in a polar plot, while three of its sections are represented in Figure 6.20b,c,d.
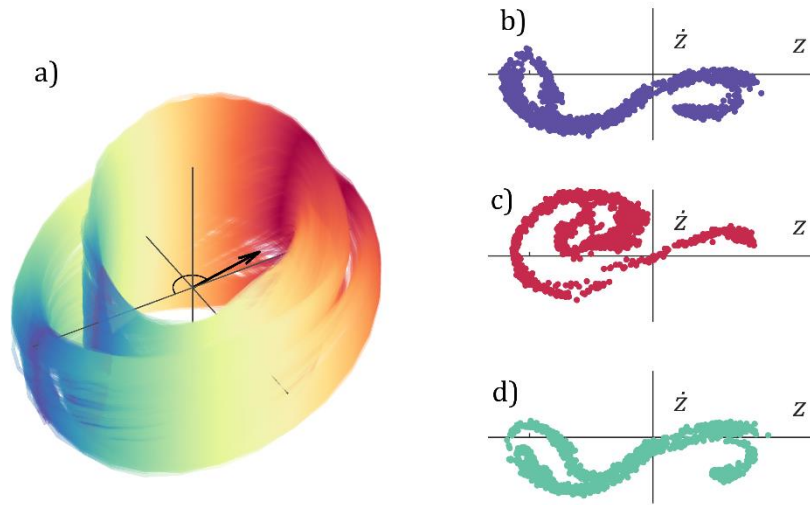
Figure 6.20: Experimental Poincaré sections, b_0=5 mm. a) Polar representation of the attractor surface; b) Poincaré section, φ=0°; c) Poincaré section, φ=170°; d) Poincaré section, φ=320°.

6.2.2. Nonlinear system identification

As expected, the device under test can exhibit rich nonlinear dynamics, allegedly governed by the polynomial restoring force of Eq. (6.8a). The identification of the coefficients of the polynomial expansion is therefore a key step in the design process of the dropper, as it allows the comparison with the physical model.

The identification is performed using two different algorithms: the restoring force surface (RFS) and the nonlinear subspace identification method (NSI). As briefly introduced in Chapter 3, RFS is a basic nonlinear system identification method, based on the representation of the restoring surface from the measured signals. Despite being useful to easily visualize the nonlinearity, it does not actually provide a robust model structure, nor any modal parameters of interest. The identified restoring force with RFS will be therefore compared with the one obtained using NSI, the latter being able to provide also the nonlinear state-space model and the modal parameters of the underlying-linear system, as already discussed several times throughout this thesis.

Restoring force surface (RFS)

The equation of motion describing the dynamical system considered here can be written in the form:

$$m\ddot{z} + R(z, \dot{z}) = f(t) \tag{6.10}$$

where $f(t)$ is the forcing term and $R(z, \dot{z})$ is the restoring surface, function of displacements and velocities. If the inertial term is shifted to the right-hand side of the equation, the restoring surface can then easily be visualized, and its features extracted. In particular, it can be sliced along two different directions, obtaining:

- An approximation of the restoring force $K(z)$ for small velocities ($|\dot{z}| < \varepsilon_s$);
- An approximation of the damping force, called $D(\dot{z})$, for small displacements around one equilibrium position ($|z - z^*| < \varepsilon_d$).

The experimental restoring surface $R(z, \dot{z})$ is built from the cross-well measurements previously seen. The velocity $\dot{z}$ is obtained by integrating and subtracting $\ddot{y}$ and $\ddot{b}$. The resulting restoring surface is reported in Figure 6.21, together with its sections $K(z)$ and $D(\dot{z})$ computed by setting $\varepsilon_s = \varepsilon_d = 0.1\%$.
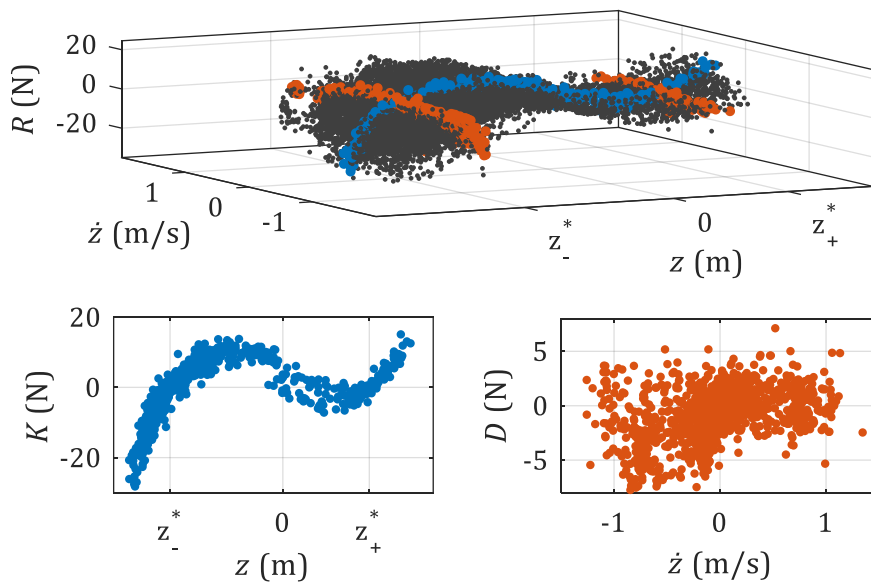
Figure 6.21: Experimental restoring surface. Blue dots: restoring force; orange dots: damping force.

The restoring force is fitted to a polynomial expansion of degree 3 as in Eq. (6.8a), yielding:

$$\begin{aligned} K^{RFS}(z) &= k_3 z^3 + k_2 z^2 - k_1 z + k_0 \\ &= 7.35 \cdot 10^5 \, z^3 + 1.56 \cdot 10^3 \, z^2 - 550 \, z + 2.4 \end{aligned} \tag{6.11}$$

The potential U^{RFS} can be estimated as well once the coefficients of the polynomial expansion are known. Both K^{RFS} and U^{RFS} are depicted in Figure 6.22.
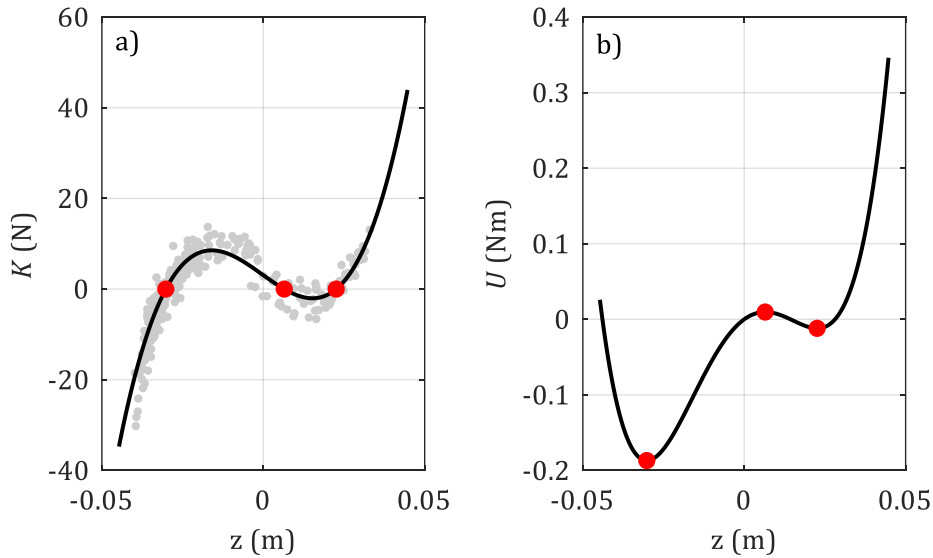
Figure 6.22: RFS estimation of the restoring force *K(z)* (a) and the corresponding potential *U(z)* (b). Gray dots: restoring surface for $|\dot{z}|<\varepsilon_s$. Red dots: stable and unstable equilibrium positions. Black lines: $K^{RFS}(z)$ and $U^{RFS}(z)$.

As for the damping plot in Figure 6.21, no damping model can be easily inferred due to the high dispersion of the measured restoring surface. Indeed, damping estimation is always a tricky task, and it becomes even more difficult in the presence of nonlinear damping phenomena. In the considered case, for instance, it is likely that friction is present between the bushing of the moving mass and the vertical steel guide.

Nonlinear subspace identification (NSI)

As previously seen, one of the cornerstones of NSI is the possibility of splitting the nonlinear equation of motion into an underlying-linear part and a nonlinear feedback. Looking at Eq. (6.7), this leads to:

$$m\ddot{z} - k_1 z = f(t) - (k_3 z^3 + k_2 z^2 + k_0) = f(t) - f^{nl}(t) \tag{6.12}$$

Unfortunately, the subspace technique cannot be directly applied to such equation of motion, because the ULS here described has a negative linear stiffness, i.e. it is unstable. In order to use the NSI method, a shift of the reference axis is therefore needed, considering the oscillations of the moving point around one *reference position*. This reference position is chosen as one of the two stable equilibrium points $z_\pm^*$, and it is generally referred to as z^*. A new variable $x(t)$ can therefore be defined as:

$$x(t) = z(t) - z^* \tag{6.13}$$

and Eq. (6.7) can be written as:

$$m\ddot{x} + K(x + z^*) = -m\ddot{b} \tag{6.14}$$

where $K(x + z^*)$ is equal to:

$$K(x + z^*) =$$
$$k_3 x^3 + (k_2 + 3k_3 z^*)x^2 + \left(3k_3 z^{*2} + 2k_2 z^* - k_1\right)x \tag{6.15}$$
$$= k_3 x^3 + \tilde{k}_2 x^2 + \tilde{k}_1 x$$

The equation of motion in the variable x is therefore:

$$m\ddot{x} + c\dot{x} + k_3 x^3 + \tilde{k}_2 x^2 + \tilde{k}_1 x = -m\ddot{b} \tag{6.16}$$

where a linear viscous damping is also added. This formulation is compatible with the NSI requirements, as a stable ULS is gained. To be more precise, the ULS depends here on the choice of the reference position z^*, therefore:

- When $z^* = z_-^*$ the modal parameters of the underlying-linear small oscillations around the *negative* equilibrium position can be estimated;
- When $z^* = z_+^*$ the modal parameters of the underlying-linear small oscillations around the *positive* equilibrium position can be estimated;

Consequently, two mutually exclusive ULSs can be obtained if one cross-well measurement is used with NSI. The nonlinear state-space model is also gained, with the possibility of extracting the coefficients of the nonlinearities. The coefficients of the two elastic nonlinear basis functions are k_3 and $\tilde{k}_2$, and nonlinear damping is also included in the form $\dot{x}|\dot{x}|$. The latter is the most common polynomial damping form, with the absolute value term to ensure that the force is always opposed to the velocity [3]. The nonlinear restoring surface $R^{nl}(x, \dot{x})$ is therefore:

$$R^{nl}(x, \dot{x}) = k_3 x^3 + \tilde{k}_2 x^2 + c^{nl}\dot{x}|\dot{x}| \tag{6.17}$$

The cross-well random test with amplitude 38 m/s² RMS is considered for the nonlinear system identification with NSI. In particular, the last 60 seconds are used as a validation set for the evaluation of the residuals over the measured output, while the rest of the acquisition is used for the identification.

The stabilization diagrams of the two ULSs associated to the two equilibrium positions are depicted in Figure 6.23. Stability is checked for frequencies, damping rations, MACs, and modal masses and a model order equal to 2 is chosen for both ULSs. The identified modal parameters of the two underlying-linear systems are listed in Table 6.1 in terms of natural frequencies and damping ratios.

Table 6.1: Modal parameters of the two underlying-linear systems identified with NSI.

Reference position	Natural frequency (Hz)	Damping ratio (%)
z_-^*	11.41	11.2
z_+^*	9.19	20.3
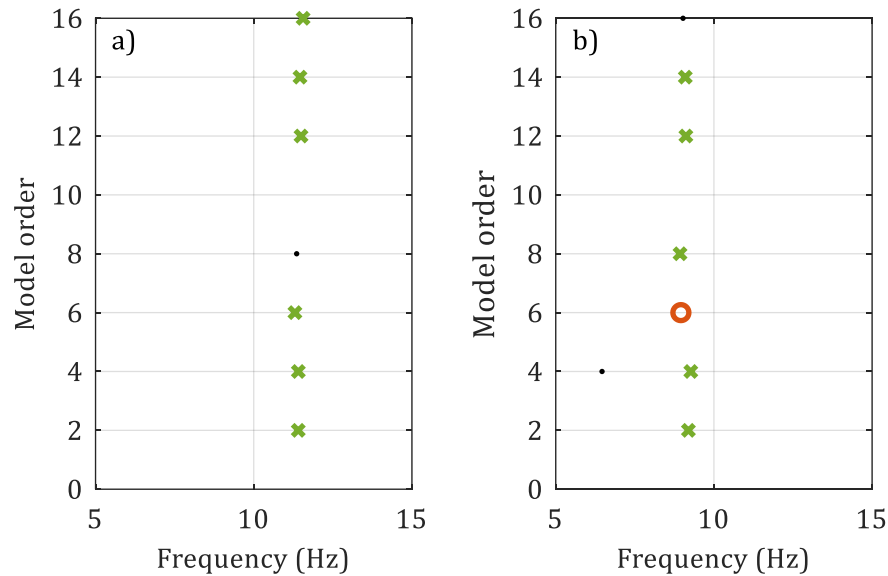
Figure 6.23: Stabilization diagram of the two ULSs with reference positions z_-^* (a) and z_+^* (b). Stabilization thresholds for natural frequency, damping ratio, MAC and modal mass are 1%, 20%, 99.5%, 20%, respectively. Black dot: new (not stable) pole; blue plus: pole stable in frequency; red square: pole stable in frequency and MAC; orange circle: pole stable in frequency, MAC and damping; green cross: pole stable in frequency, MAC, damping and modal mass.

The FRFs of the two underlying-linear systems are depicted in Figure 6.24 together with the measured (nonlinear) one.

Running NSI for the two different reference values means that not only two independent underlying-linear systems are obtained, but also two nonlinear state-space models. This result in a double estimation of the coefficients of each nonlinearity. In particular, the estimation of the coefficients k_3 and c^{nl} should be the same when NSI is applied to the two reference positions, as they are both invariant in the equation of motion (Eqs. (6.16)-(6.17)). On the contrary, $\tilde{k}_2$ depends on the choice of z^*. The identified coefficients are depicted in Figure 6.25 in their real parts for the two reference positions.
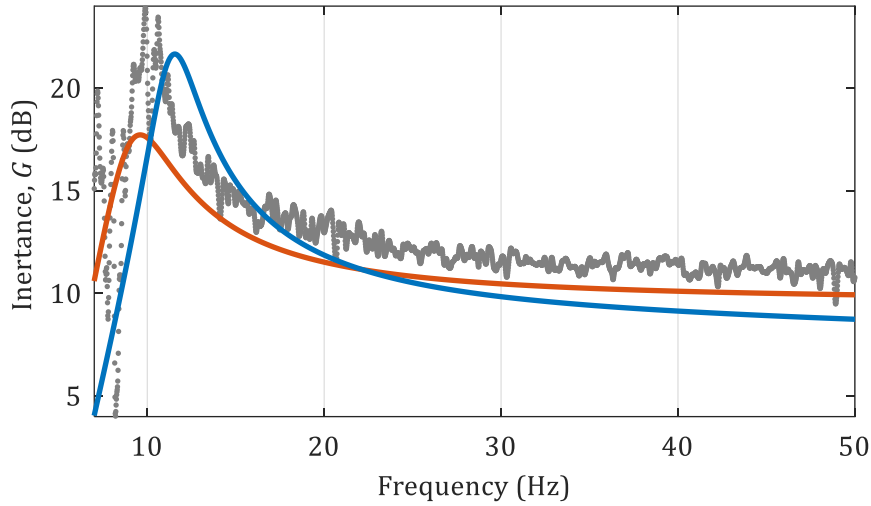
Figure 6.24: Inertances of the two ULSs in dB scales (ref. 1 m²s⁻¹/N). Gray dots: measured inertance of the nonlinear test; blue line: NSI estimation of the linear inertance associated to the negative equilibrium z^*_-; orange line: NSI estimation of the linear inertance associated to the positive equilibrium z^*_+.
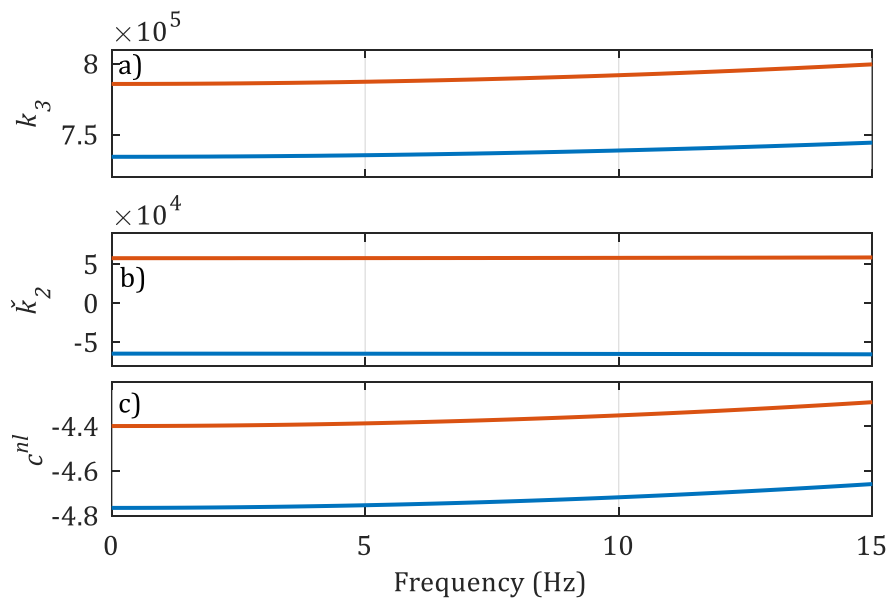
Figure 6.25: Real parts of the identified coefficients of cubic stiffness (a), quadratic stiffness (b) and nonlinear damping (c) as frequency dependent quantities. Blue line: NSI with reference position z^*_-; orange line: NSI with reference position z^*_+.

These coefficients can be compared with the ones estimated by the RFS method, and the comparison is reported in Figure 6.26 in terms of estimated restoring force. The damping force identified by NSI is also shown.
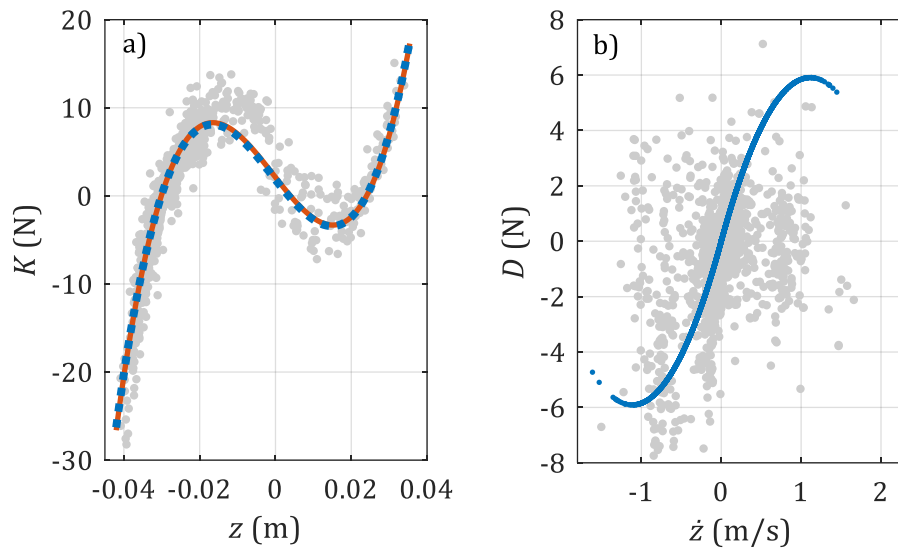
Figure 6.26: Estimation of the restoring force (a) and the damping force (b). Gray dots: sliced restoring surface; orange line: RFS estimation (only in a); blue dots: NSI estimation.

The outcomes of RFS and NSI show a very good agreement on the restoring force, the two curves being almost overlapped in Figure 6.26a. As for the damping, it is difficult to evaluate the goodness of the its estimation due to the high dispersion of the points of the restoring surface. In any case, the damping force has a non-negligible contribution, its peak amplitude (in Newton) being roughly 25% of the maximum amplitude of the restoring force K. It should be highlighted though that the resulting damping force is not valid outside the given range of velocity, as it starts exhibiting a negative slope around ± 1 m/s in Figure 6.26b. Higher velocities are not expected to occur in the considered system, but the user should be aware of possible instabilities of the assumed damping model. A workaround might be to regularize the damping force for velocities $|\dot{z}| > 1$ m/s, for instance keeping a constant value of $\pm$ 6 N.

The final validation of the adopted nonlinear basis functions can be done by generating the response of the system using the identified state-space model on the validation set. Calling x^{NSI} the simulated output, a comparison with the measured one can be carried out in both time and frequency domains. Results are depicted in Figure 6.27, showing an 8% average RMS deviation between predictions and measurements. Noticeably, the estimated state-space model is capable of predicting the crossings between positive and negative oscillations with a very good accuracy.
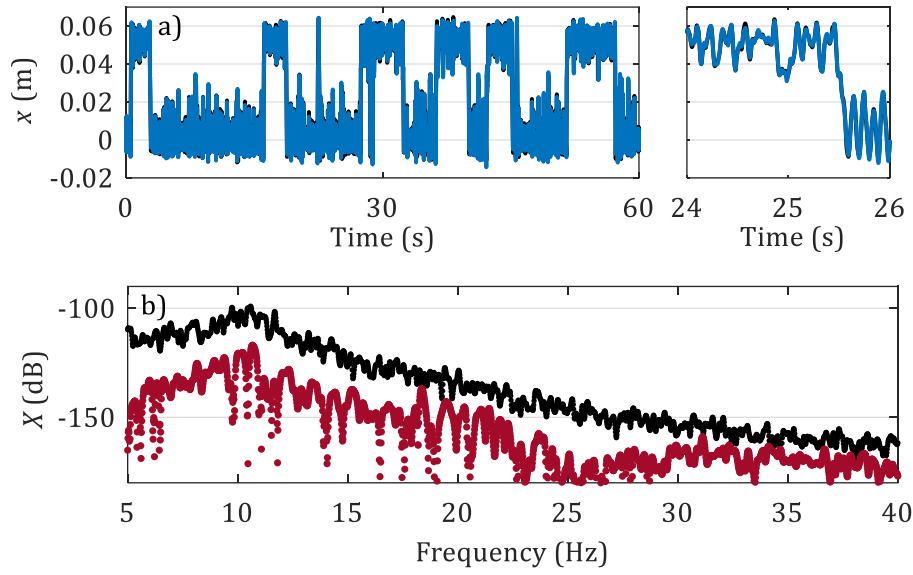
Figure 6.27: Validation of the nonlinear identification in the time domain (a) and frequency domain (b). Black line: measured output; blue line: simulated output; red line: residual with the measured output spectrum in dB scales (ref. 1 m²/Hz).

6.2.3. Model updating

Once the parameters of the restoring force have been estimated from the experimental measurements, a comparison with the originally designed ones is carried out to validate the model adopted during the design process. A model updating procedure is eventually implemented to adjust the physical parameters of the model and minimize the difference between simulated and identified behaviors. A genetic algorithm (GA) [101] is adopted to find the global optimum set of parameters. The selected fitness function ε to be minimized is defined as the sum of two relative error functions ε_ω and ε_{z^*}. The function ε_ω is associated to the residuals on the positive and negative natural frequencies $\omega_\pm$, while ε_{z^*} is related to the residuals on the positive and negative equilibrium positions:

$$\varepsilon_\omega = \text{RMS}\left\{100\left|\frac{(\omega_-^{MOD} - \omega_-^{EST})}{\omega_-^{EST}}\right|, 100\left|\frac{(\omega_+^{MOD} - \omega_+^{EST})}{\omega_+^{EST}}\right|\right\}$$

$$\varepsilon_{z^*} = \text{RMS}\left\{100\left|\frac{(z_-^{*MOD} - z_-^{*EST})}{z_-^{*EST}}\right|, 100\left|\frac{(z_+^{*MOD} - z_+^{*EST})}{z_+^{*EST}}\right|\right\} \tag{6.18}$$

$$\varepsilon = \varepsilon_\omega + \varepsilon_{z^*}$$

The parameters to be optimized are the Young's modulus E, the frame angle α and the moving mass m. The updating of the parameters is depicted in Figure 6.28, while the results of the optimization are reported in Figure 6.29 and Figure 6.30.

The optimization reduces the residual between model and experimental characteristics, providing a good match between the final restoring force and potential curves. The updated model is used as a starting point for the final prototype design to work with a full high-speed OCL, in section 6.3.
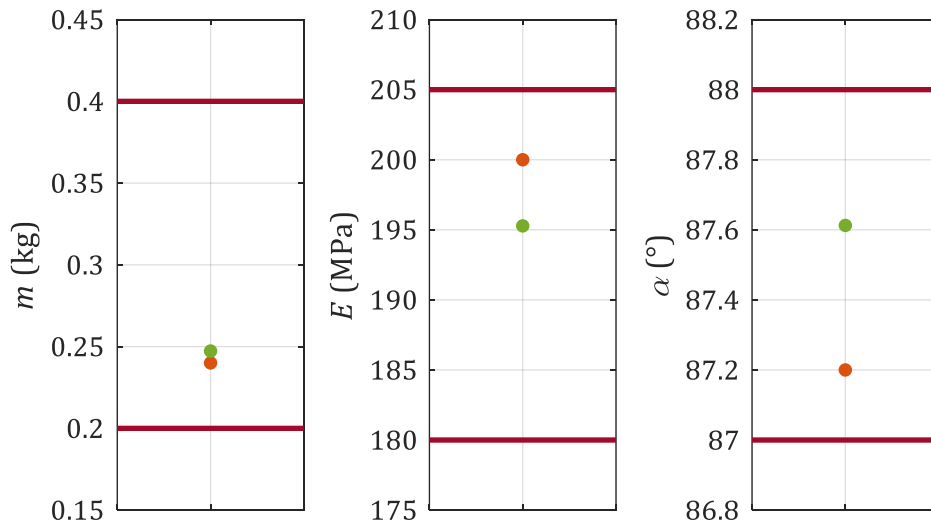
Figure 6.28: Parameters of the GA optimization. Red lines: upper and lower boundaries of the parameters; orange dots: starting values; green dots: final values.
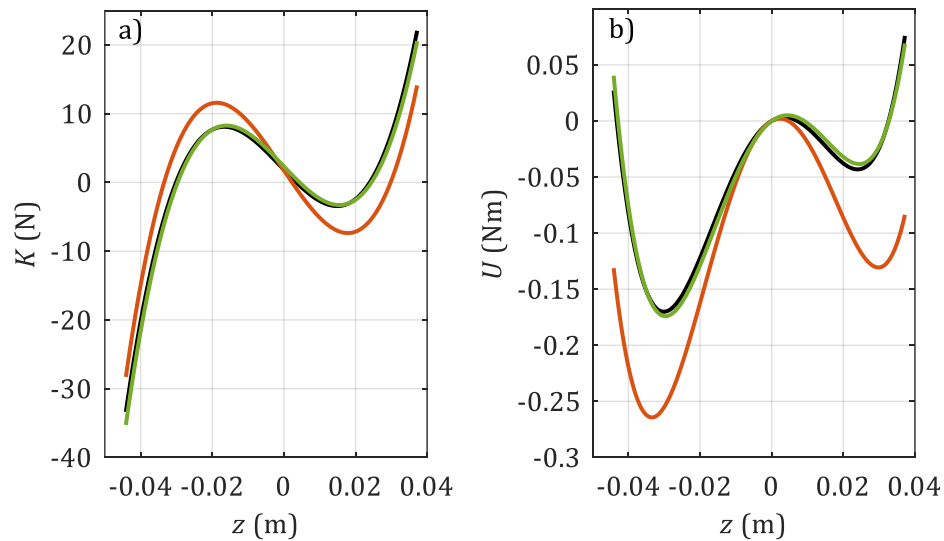
Figure 6.29: Results of the optimization in terms of restoring force in (a) and potential in (b). Black line: identified curves; orange line: starting values; green line: final values.
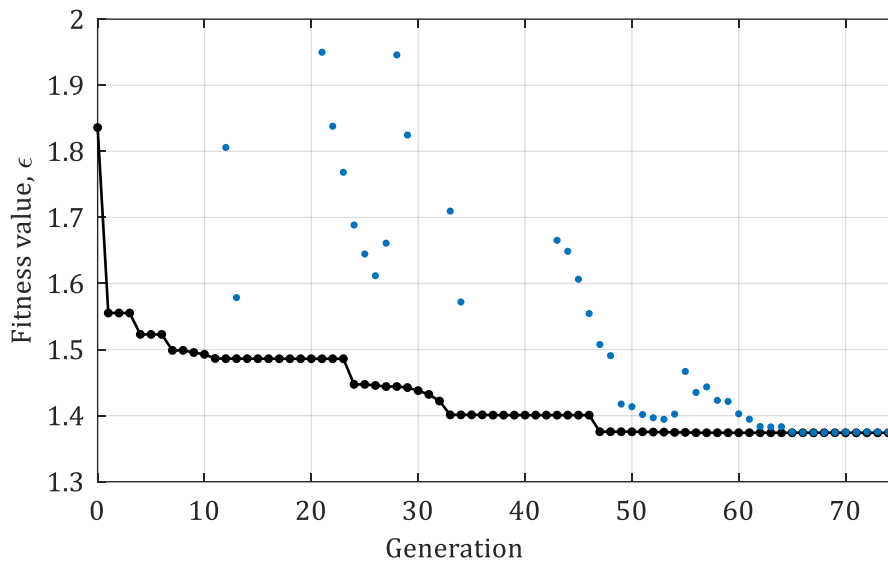
Figure 6.30: Values of the fitness function across the generations of GA. Black line: best fitness; blue dots: mean fitness values.

6.2.4. Experimental test with a contact wire

The damping capabilities of the improved dropper are checked in this section from an experimental point of view, by considering a test set involving a 30 m long tensioned railway contact wire. Measurements are taken with and without the dropper, the latter being positioned at 13 m from one end. The experimental set is depicted in Figure 6.31, where the sub-part of the dropper containing the frame is drafted as a rectangle.
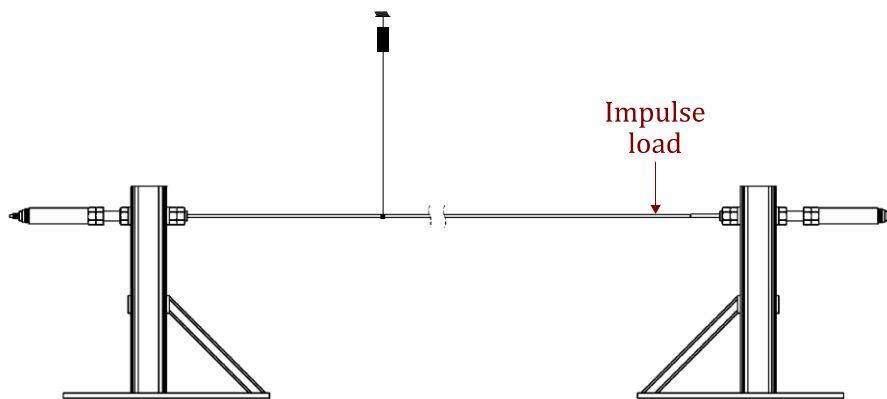
Figure 6.31: Sketch of the experimental setup (not to scale).

A tensile force of 15 kN is applied to the wire with the tensioning device shown in Figure 6.32, based on a simple screw-nut mechanism. The applied tension is measured by means of a through-hole load cell. Furthermore, a thrust bearing on each end is used to assure that no torsion is transferred to the wire.
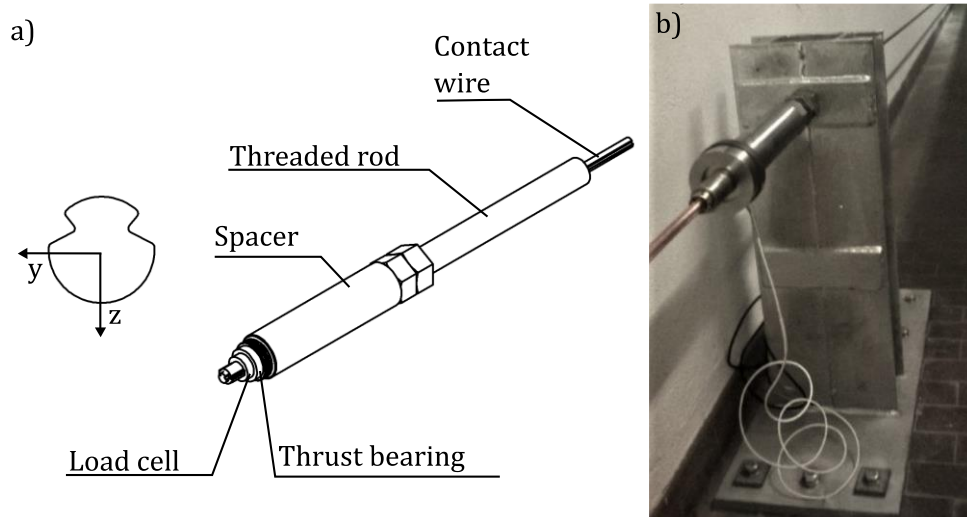
Figure 6.32: a) Scheme of the tensioning device and section of the contact wire. b) Photo of the test bench.

Tests are performed by applying an impulse load to the contact wire along the z-axis (see Figure 6.31 and the reference system in Figure 6.32) and recording the accelerations of five points along the contact wire, whose positions are listed in Table 6.2. The sampling frequency is set to 81.92 Hz.

Table 6.2: Position of the accelerometers along the contact wire.

Sensor n°	1	2	3	4	5
Position (m)	1.5	9	13	17	27

The acceleration of the third sensor and its displacement are reported in Figure 6.33 when the improved dropper is attached and detached. Displacements are obtained by double numerical integration of the measured accelerations.

The additional damping induced by the dropper is evident from Figure 6.33, where a much faster decay is obtained in the presence of the device.

Some more insights can be gained when performing the system identification of the structure in both cases to extract the modal parameters. Given the considerable length of the contact wire, vibrations occur also in the y-axis when the excitation is applied on the z-axis. Since only the vertical vibrations are of interest in the current analysis, the horizontal modes must be excluded from the identification, as shown in [81].

The identification is performed using the stochastic subspace identification technique (Appendix A), and the stabilization diagrams related to the cases without/with the dropper are depicted in Figure 6.34. It is possible to notice the high modal density, which is a common characteristic of cable-based structures. The model order is selected for each identified mode according to the median-damping criterion [81].
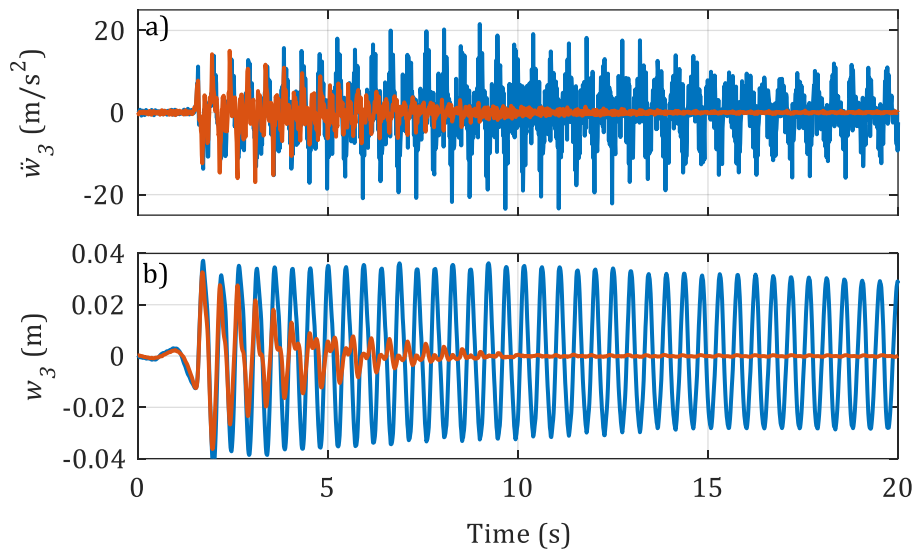
Figure 6.33: Response of the contact wire to an impulse load without the improved dropper (blue line) and with the improved dropper (orange line), sensor 3. a) Measured acceleration; b) Displacement.
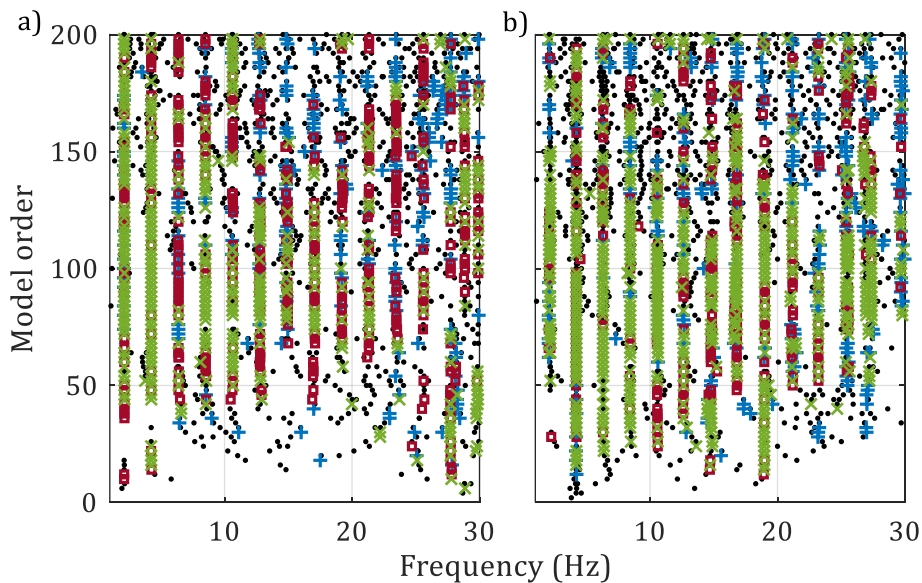
Figure 6.34: Stabilization diagrams without the dropper in (a) and with the dropper in (b). Stabilization thresholds: 0.5%, 10% and 99.5% for frequencies, damping ratios and MACs respectively. Black dot: new pole; blue plus: pole stable in frequency; red square: pole stable in frequency and MAC; green cross: pole stable in frequency, MAC and damping.

Eventually, natural frequencies and damping ratios are extracted and fitted to a proportional damping distribution in both without/with cases. Results are shown in Figure 6.35, where the proportional fit is also depicted for the two abovementioned cases. The identified proportional damping coefficients α and β are listed in Table 6.3.
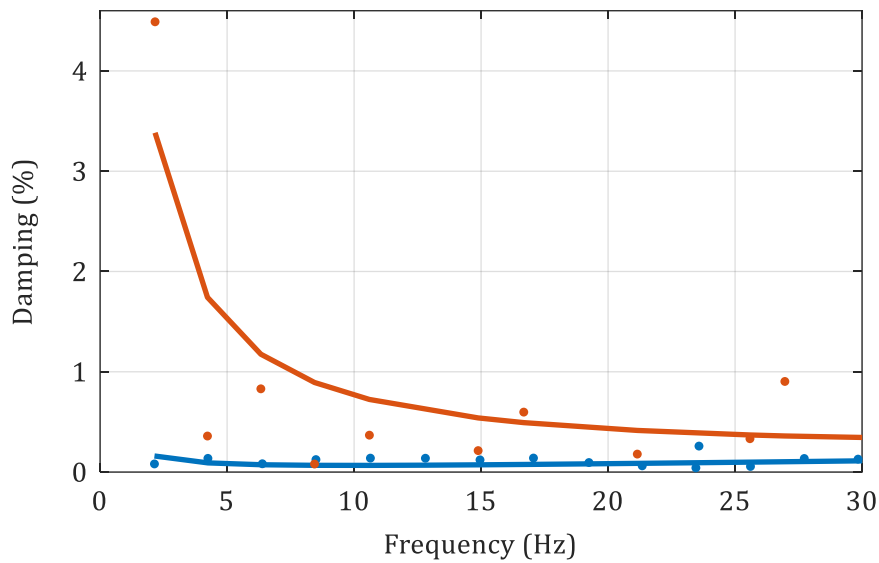
Figure 6.35: Damping estimation (dots) and fit to the proportional model (continuous lines). Blue: without the dropper; orange: with the dropper.

Table 6.3: Identified proportional damping coefficients.

	α (s^{-1})	β (s)
Without the dropper	0.04	$1 \cdot 10^{-5}$
With the dropper	0.92	$1 \cdot 10^{-5}$

The experimental tests confirm the effectiveness of the dropper in damping out the low-frequency modes of the contact wire, and thus its macro-oscillations.

6.3. An improved dropper for OCLs

The effects of the improved droppers on a high-speed overhead contact line are investigated in this section, combining the information acquired with the experimental tests with a FE model of the pantograph-catenary system. A new design of the dropper is sought starting from the updated model to maximize its effectiveness when coupled with the model of a high-speed OCL, and detailed information about the new design steps can be found in the master thesis [127].

The objective of the simulation is to quantify the improvements in the contact force when simulating the response of the pantograph-catenary system with the designed droppers.

The software adopted for the simulations of the dynamical interaction between pantograph and catenary is called *Cateway* and is currently developed at Politecnico di Torino by the Dynamics and Identification

Research Group. Information about its FE formulation can be found in the two master theses [135,138]. Its main characteristics are listed in the following:

- 2D or 3D Euler-Bernoulli beam elements for contact wire and messenger wire;
- Nonlinear spring model for the droppers: activated in normal conditions, deactivated in case of slackening;
- 3 DOFs lumped mass-damper-spring system for the pantograph;
- Penalty contact model;
- Numerical integration performed with the Generalized-α method [139] or the Bathe method [140]. An iterative procedure is also implemented to account for nonlinear phenomena.

As for the parameters of the numerical integrator(s), the guidelines published in [141] are followed, which relate spatial and time discretizations to the wave propagation speed along the wires via the Courant-Friedrichs-Lewy (CFL) number. The software has been validated according to the standard EN50318:2002 [142], and a screenshot of its main interface is shown in Figure 6.36.
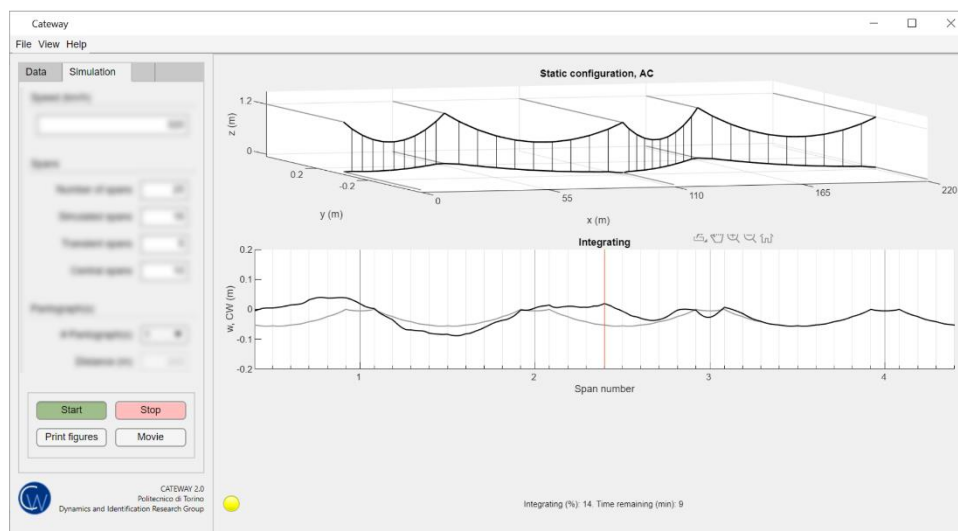
Figure 6.36: Main interface of Cateway. Blurred parts contain sensible information.

The outcomes of Cateway are the contact force, the displacements of the nodes of the OCL and the displacements of the DOFs of the pantograph(s).

As for the state-of-the-art about models for the simulation of the pantograph-catenary interaction, the reader can refer to the reviews [108,110]. Among the others, 3D elements to describe the OCL, nonlinear iterative time solvers and multibody models for the pantographs seem to be the most important recent achievements in this field. The modeling of structural damping instead is still a crucial point, as OCLs are very lightly damped structures, and the estimation of their damping distribution remains a non-trivial task [81,123,124]. Despite their limitations, nonlinear FE models

are a powerful tool to design and simulate OCLs under various operational conditions, especially given the difficulties and the costs of performing direct tests on the lines [108,143].

6.3.1. Simulations with Cateway

Simulations are performed considering the characteristics of the benchmark OCL proposed in [110], with spans of 55 m. The benchmark catenary is of the same type of the French LN2 or the Italian C270 systems, with a tensile force of 22 kN on the 150 mm² contact wire, and 16 kN on the 120 mm² messenger wire. A schematic representation of one span of the catenary is depicted in Figure 6.37, while all the details can be found in [110].

Compared to the catenary system of Figure 6.1, the one proposed here is slightly different, mainly because of the curvature of the contact wire. The curved profile is called *pre-sag*, and it can be adopted to reduce the stiffness discrepancies along the OCL [144].

As for the pantograph, the same 3 DOFs lumped-mass model of the abovementioned benchmark is adopted, with a mean value $\bar{f}_c$ of the contact force obtained from the quadratic law seen in section 6.1.1. The considered speed of the pantograph is 320 km/h, and simulations are conducted on a total of 20 spans. Only the 10 central spans are used for the evaluation of the parameters defining the contact force though.
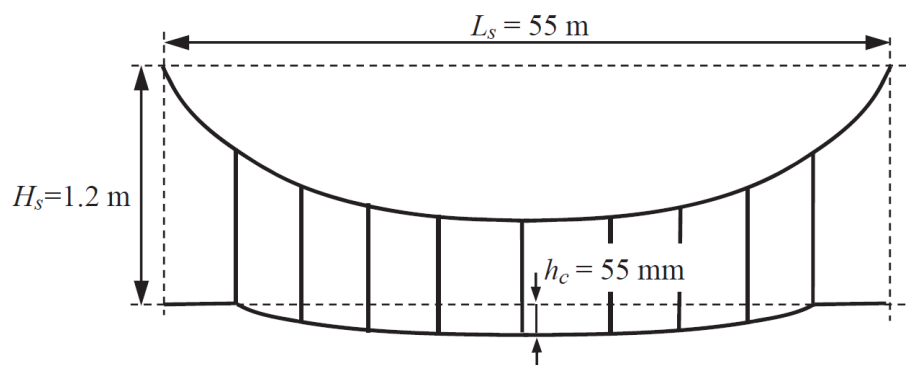
Figure 6.37: Schematic representation of the benchmark catenary, from [110].

The effectiveness of the improved droppers is quantified in terms of improvements in the contact force. The latter is filtered in the range $0 - 20$ Hz, as commonly done for this kind of structures. The contact force is depicted in Figure 6.38 for both the simulations without the improved droppers and with the improved droppers, and its main parameters in the spans of interest are listed in Table 6.4.
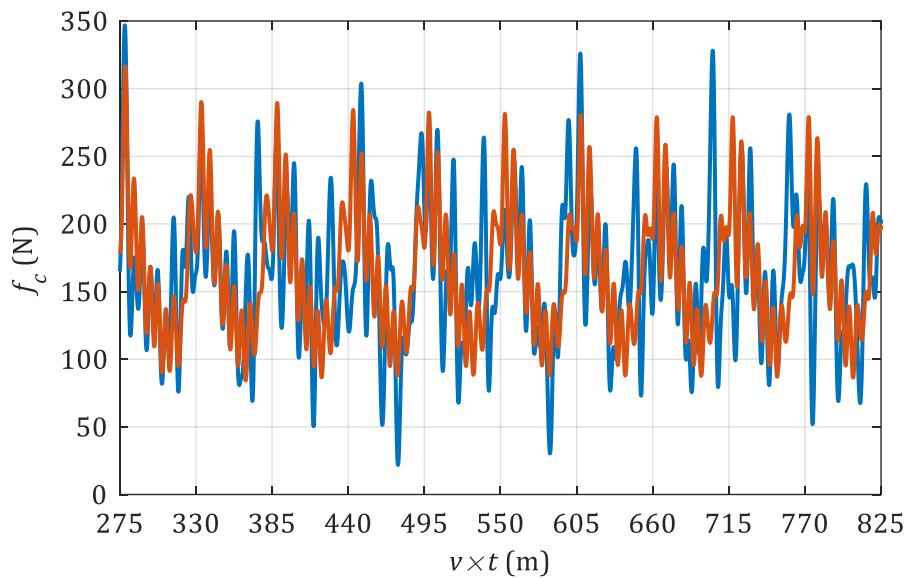
Figure 6.38: Simulated contact force at 320 km/h. Blue line: without the improved droppers; orange line: with the improved droppers.

The positive effects of the added droppers are evident both from the graphical representation and the table values of the contact force f_c. In particular, the minimum of f_c is definitely increased with the new droppers, avoiding the risk of losses of contact. Also, the maximum is decreased, with allegedly lower wear of the surfaces in contact. This is translated in a lower ratio between the standard deviation σ_c and the mean value $\bar{f}_c$, which goes from 0.31 to 0.27.

Table 6.4: Parameters of the contact force.

	Without the droppers	With the droppers
Mean value $\bar{f}_c$ (N)	166	165
Standard deviation σ_c (N)	52	45
$\sigma_c/\bar{f}_c$	0.31	0.27
$\max(f_c)$ (N)	347	317
$\min(f_c)$ (N)	22	84

The additional damping induced by the droppers is clear from Figure 6.39, where the displacement of one support of the catenary is shown for the two cases. All the supports show a similar behavior, with the peak of the displacement associated to the passage of the pantograph.
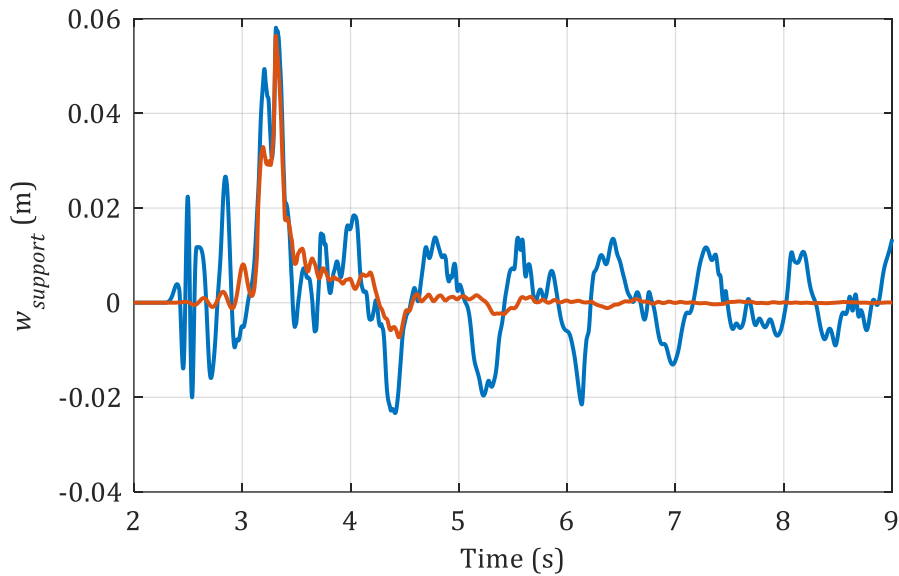
Figure 6.39: Simulated displacement of one support. Blue line: without the improved droppers; orange line: with the improved droppers.

6.4. Concluding remarks

The experimental characterization and subsequent model updating of a nonlinear improved dropper for high-speed overhead contact lines have been conducted. The device is based on negative-stiffness absorbers, with a nonlinear elastic restoring force expressed by a polynomial expansion. When the central spring is removed, a variety of different kind of motions can be obtained because of the intrinsic bi-stable nature of the device, from in-well to cross-well oscillations, including chaotic motion. These dynamical behaviors have been confirmed by the experimental observations, gathering linear, nonlinear and chaotic motions. Eventually, the parameters defining the nonlinear restoring force have been recognized via nonlinear system identification, adopting two different methods. A first guess has been obtained using the restoring force surface method, whose implementation allows to easily visualize the nonlinear behavior and the asymmetric double-well potential of the system. The final identification has been performed using the nonlinear subspace identification method with a cross-well random measurement. The identified parameters have been used to update the physical model of the dropper via genetic algorithms. Eventually, the effectiveness of the designed droppers is tested on a reduced test rig and on a simulated overhead contact line with the pantograph interaction. Future developments will involve experimental tests on a real overhead contact line with high-speed trains, to measure the contact force between the pantograph and the contact wire and experimentally evaluate the induced damping distribution on the structure.

Chapter 7

Conclusions

This doctoral thesis attempts to progress towards the development of techniques for nonlinear vibrating structures, with the aim of filling the gap between the vast achievements in nonlinear systems theory and the practical implementations of nonlinear features in structural engineering. Complex nonlinear dynamical phenomena have been investigated and experimentally characterized in a variety of scenarios, including demonstrative and real-life applications.

Chapters from 1 to 3 are introductory to the topics of the conducted research and present an overview of nonlinear dynamical phenomena and nonlinear system identification techniques. In particular, numerical examples have been proposed in Chapter 2 to describe classical nonlinear phenomena and to ease the description of features such as harmonic distortions, nonlinear frequency response curves, stability issues, bifurcations and chaos. Instead, the identification of nonlinear structure from measured data has been discussed in Chapter 3, starting from a literature review about the major contributions in the field. The nonlinear subspace identification (NSI) method has been presented, together with a demonstrative experimental application with a clearance nonlinearity.

Novel techniques are presented in chapters 4 and 5, to give a contribution to the current unsolved topics in the research community. In particular, the problem of output-only nonlinear system identification has been faced in Chapter 4. A novel technique working with free-decay measurements has been presented, called Free-decay-NSI. The methodology has been first tested on a

numerical example with Coulomb friction, and subsequently on an experimental test rig involving a scaled five-levels building with a polynomial nonlinearity on the top floor. Whilst the presented method is not able to deal with *true* output-only measurements (meaning unmeasured stochastic input), it is a step towards this direction, and it can be used whenever an external excitation source should be avoided.

In Chapter 5 the problem of identifying a distributed nonlinear behavior has been faced and a strategy proposed. The suggested identification technique, called Modal-NSI, has been tested on a slender clamped-clamped beam subjected to large-amplitude vibrations with multiple modes excited simultaneously. The structure has been modeled using a modal approach, and the outcome of the identification has been compared to the one obtained with the Polynomial Nonlinear State-Space method (PNLSS), which is a black-box technique.

Eventually, a real-life application has been proposed in Chapter 6, where the design process of a nonlinear damping system for railway overhead contact lines has been chased. The challenge here was in the dynamical behavior of the device, which ranged from linear to strongly nonlinear and chaotic. Nonlinear system identification has been performed to extract the restoring force of the system, in order to compare experimental results with designed ones. A model updating procedure has been eventually implemented to update the design choices based on the experimental outcomes, and to build the final prototype of the device.

7.1. Future perspectives

The potentialities of nonlinear design and analysis in structural dynamics are so wide that the current state of research can be fairly considered at the early stages of its path, and numerous are the challenges ahead. Some of these have been discussed in this doctoral dissertation, and new solutions have been sought. Looking forward in the years, two points seem to be the most critical ones:

- The development of a general framework for nonlinear system analysis and identification in contrast to ad-hoc solutions for specific issues. Of course, this would require a way broader overall vision of nonlinear dynamical phenomena in engineering structures than the one we currently understand. An encouraging approach seems the expansion of the linear frameworks we are used to, obtaining, for instance, nonlinear normal modes [99,100,145] or modal derivatives [87,95,146]. Despite their current limitations, the above-cited tools are promising in terms of applicability and flexibility.

- The development of commercial and industrial tools for nonlinear dynamical analysis in order to bridge the gap between academics and industries. Steps towards this direction have been already taken, for instance with the startup Nolysis [147]. Nevertheless, we are very far away from this achievement, and surely new engineers should be trained towards this direction in the near future.

While these two points are long-run objectives, other issues can be surely faced in the near future:

- Distributed nonlinearities represent a wide range of nonlinear phenomena, as already discussed. The proposed methodology to deal with them has been tested on a laboratory structure to assess its validity, but further tests with real-life structure should be implemented as well. Also, other reduction basis might be adopted, including for instance the modal derivatives of the mode shapes.

- The *true* output-only nonlinear system identification is still an open point in the research community. The methodology proposed in this thesis is valid for free-decay measurements, but it does not cover the wide case of stochastic identification. This would certainly boost the use of nonlinear system identification techniques in real-life scenarios, as stochastic identification is generally easier to be performed in-situ.

- Nonlinear damping phenomena are still extremely difficult to characterize and identify. It is fair to say that this is generally true also for linear structures, because the classical proportional model, despite its popularity, is not necessarily realistic. Cases exist where a non-proportional damping distribution better represents the structure under test, although it is certainly more difficult to identify and carries the need of a more complex model [81]. Things get much more difficult when nonlinear damping models are taken into account, such as friction between surfaces or fluid flows through an orifice [3]. Surely, the knowledge of nonlinear damping phenomena is far from being exhaustive yet, but it is known for instance that the increase of damping with the vibration amplitude of nonlinear structures represents a common and important phenomenon [148]. Further research in this sense seems therefore mandatory.

- The identification of strong nonlinear behaviors remains a challenging topic, as many of the methods developed so far perform well with weak nonlinear phenomena. This is true for instance for the methods that necessitate an optimization starting from a "known" state, such as the best linear approximation in PNLSS. The identification of a bi-stable system with a strong nonlinear behavior associated to cross-well oscillations has been performed in Chapter 6, but despite its complex nonlinear dynamics

the system was quite easy to model, as essentially being based on a Duffing oscillator. More complex systems with strong nonlinearities are worth to be analyzed, to understand how far an identification method can be pushed and to promote even more the design of structures having nonlinear features.

- Uncertainties associated to the estimation of the model parameters are of use to understand the confidence in the obtained results. Techniques exist to estimate the model uncertainties in linear system identification, like the one in [149], but things get tougher when nonlinearity comes in. This is because nonlinear methods are generally more complex, and uncertainties are present not only in the estimated parameters, but also in the model of the nonlinearity itself. It is worth mentioning that an approach that intrinsically lead to uncertainties estimation is the Bayesian one, which already showed promising results [58].

The suggested list covers the open points that are believed to be among the most important in the field of nonlinear vibrating structures, but new applications and research opportunities are constantly emerging, confirming the spread of this topic in the current years. The direction for future research proposed here has the objective of enhancing the knowledge of nonlinear phenomena in engineering structures and providing at the same time consistent techniques to deal with them. Eventually, easy-to-use tools and software interfaces would likely lead to the spread of industrial applications.

Appendix A:
Overview of subspace identification

System identification via subspace method has become increasingly popular starting from the mid-90s, due to its robustness and effectiveness. The method has been introduced in the time domain by Van Overschee and De Moor [60], and in the frequency domain by McKelvey, Akçay and Ljung [61]. Subspace methods identify state-space models from (input and) output data by applying robust numerical techniques such as QR factorization, SVD and least squares. The principal steps of the time domain version are illustrated in the following. The reader can refer to [60,150] for more detailed information.

Let us consider a deterministic-stochastic state-space model:

$$\begin{cases} \boldsymbol{x}_{k+1} = \boldsymbol{A}\boldsymbol{x}_k + \boldsymbol{B}\boldsymbol{u}_k + \boldsymbol{w}_k \\ \boldsymbol{y}_k = \boldsymbol{C}\boldsymbol{x}_k + \boldsymbol{D}\boldsymbol{u}_k + \boldsymbol{v}_k \end{cases} \tag{A1}$$

where:

- The vectors $\boldsymbol{u}_k \in \mathbb{R}^m$ and $\boldsymbol{y}_k \in \mathbb{R}^l$ are the observations at time instant k of the m inputs and the l outputs, respectively;
- The vector $\boldsymbol{x}_k \in \mathbb{R}^n$ is the state-vector and it contains n states;
- $\boldsymbol{w}_k \in \mathbb{R}^m$ and $\boldsymbol{v}_k \in \mathbb{R}^l$ are the unmeasurable process and measurement errors, respectively. They are assumed to be zero-mean, stationary, uncorrelated white vector sequences.
- The matrices $\boldsymbol{A} \in \mathbb{R}^{n \times n}$, $\boldsymbol{B} \in \mathbb{R}^{n \times m}$, $\boldsymbol{C} \in \mathbb{R}^{l \times n}$, $\boldsymbol{D} \in \mathbb{R}^{l \times m}$ are the dynamical, input, output and direct feedthrough matrices, respectively. The matrix pair $(\boldsymbol{A}, \boldsymbol{C})$ is assumed to be *observable*, which implies that all modes in the system can be observed in the output $\boldsymbol{y}_k$ and thus can be identified.

The objective of the algorithm is to determine the order n of the system and to identify the abovementioned matrices up to a similarity transformation,

given s (input and) output observations. In particular, the *state sequence* $\boldsymbol{X}_i \in \mathbb{R}^{n \times j}$ can be defined as:

$$\boldsymbol{X}_i \doteq \begin{pmatrix} \boldsymbol{x}_i & \boldsymbol{x}_{i+1} & ... & \boldsymbol{x}_{i+j-2} & \boldsymbol{x}_{i+j-1} \end{pmatrix} \tag{A2}$$

where i is a user defined index, large enough with respect to the maximum order of the system ($i > n$). The system matrices in Eq. (A1) do not have to be known to determine the state sequence, as it is obtained directly from the measured data via geometric manipulation. Once these states are known, the identification problem becomes a linear least squares problem in the unknown system matrices, that can therefore be estimated.

In the so-called data-driven approach, the core of the algorithm is the projection of the row space of "future" observations into the row space of "past" observations, both for inputs and outputs. This is accomplished by recasting the measured data into Hankel block matrices:

$$\boldsymbol{Y}_{0|2i-1} \doteq \begin{bmatrix} y_0 & y_1 & ... & y_{j-1} \\ y_1 & y_2 & ... & y_j \\ \vdots & & \ddots & \vdots \\ y_{i-1} & y_i & ... & y_{i+j-2} \\ \hline y_i & y_{i+1} & ... & y_{i+j-1} \\ y_{i+1} & y_{i+2} & ... & y_{i+j} \\ \vdots & & \ddots & \vdots \\ y_{2i-1} & y_{2i} & ... & y_{2i+j-2} \end{bmatrix} \doteq \begin{bmatrix} \boldsymbol{Y}_p \\ \hline \boldsymbol{Y}_f \end{bmatrix} \tag{A3}$$

The subscript p denotes the "past" and the subscript f denotes the "future". A similar operation can be done with the input block matrices $\boldsymbol{U}_{0|2i-1}$, $\boldsymbol{U}_p$, $\boldsymbol{U}_f$.

The state sequence can be obtained by considering the oblique projection $\boldsymbol{O}_i$ of the row space of future outputs $\boldsymbol{Y}_f$ along the row space of future inputs $\boldsymbol{U}_f$ into the joint row space of past inputs and past outputs $\begin{pmatrix} \boldsymbol{U}_p \\ \boldsymbol{Y}_p \end{pmatrix}$:

$$\boldsymbol{O}_i = \boldsymbol{Y}_f / _{U_f} \begin{pmatrix} \boldsymbol{U}_p \\ \boldsymbol{Y}_p \end{pmatrix} \tag{A4}$$

Eq. (A4) can be solved using the LQ decomposition, and detailed steps can be found in [60,150]. Moreover, if:

- process and measurements noise are uncorrelated with the input;
- the rank of $\boldsymbol{U}_{0|2i-1}$ is full;
- the sample size goes to infinity

it can be shown that the oblique projection $\boldsymbol{O}_i$ is equal to the product between the so-called *extended observability matrix* $\boldsymbol{\Gamma}_i$ and a sequence of Kalman filter states $\widetilde{\boldsymbol{X}}_i$. In particular, the matrix $\boldsymbol{\Gamma}_i$ is defined as:

$$\boldsymbol{\Gamma}_i \doteq \begin{bmatrix} \boldsymbol{C} \\ \boldsymbol{CA} \\ \boldsymbol{CA}^2 \\ \vdots \\ \boldsymbol{CA}^{i-1} \end{bmatrix} \tag{A5}$$

Therefore:

$$\boldsymbol{O}_i = \boldsymbol{\Gamma}_i \widetilde{\boldsymbol{X}}_i \tag{A6}$$

Calling $\boldsymbol{\Pi}_{\boldsymbol{U}_f^\perp}$ the projection on the orthogonal complement of the row space of $\boldsymbol{U}_f$, the quantity $\boldsymbol{O}_i \boldsymbol{\Pi}_{\boldsymbol{U}_f^\perp}$ can be computed by SVD decomposition:

$$\boldsymbol{O}_i \boldsymbol{\Pi}_{\boldsymbol{U}_f^\perp} = \boldsymbol{USV}^{\mathrm{T}} = [\boldsymbol{U}_1 \; \boldsymbol{U}_2] \begin{bmatrix} \boldsymbol{S}_1 & \boldsymbol{0} \\ \boldsymbol{0} & \boldsymbol{S}_2 \end{bmatrix} \begin{bmatrix} \boldsymbol{V}_1^{\mathrm{T}} \\ \boldsymbol{V}_2^{\mathrm{T}} \end{bmatrix} \tag{A7}$$

The model order n can be chosen by inspecting the singular values with different orders and fixing a threshold. Another possibility is to use a stabilization diagram, for which although the system matrix $\boldsymbol{A}$ is needed. It is possible to show that an estimation $\widehat{\boldsymbol{\Gamma}}_i$ of the matrix $\boldsymbol{\Gamma}_i$ can be computed by:

$$\widehat{\boldsymbol{\Gamma}}_i = \boldsymbol{U}_1 \boldsymbol{S}_1^{1/2} \tag{A8}$$

The state sequence $\widetilde{\boldsymbol{X}}_i$ is then equal to:

$$\widetilde{\boldsymbol{X}}_i = \boldsymbol{\Gamma}_i^\dagger \boldsymbol{O}_i \tag{A9}$$

with $\cdot^\dagger$ being the pseudo-inverse matrix. Corresponding columns of $\widetilde{\boldsymbol{X}}_i$ are state estimates of $\boldsymbol{X}_i$, therefore it is possible to re-write the initial state-space formulation as:

$$\begin{pmatrix} \widetilde{\boldsymbol{X}}_{i+1} \\ \boldsymbol{Y}_{i|i} \end{pmatrix} = \begin{pmatrix} \widehat{\boldsymbol{A}} & \widehat{\boldsymbol{B}} \\ \widehat{\boldsymbol{C}} & \widehat{\boldsymbol{D}} \end{pmatrix} \begin{pmatrix} \widetilde{\boldsymbol{X}}_i \\ \boldsymbol{U}_{i|i} \end{pmatrix} + \begin{pmatrix} \boldsymbol{\rho}_w \\ \boldsymbol{\rho}_v \end{pmatrix} \tag{A10}$$

where $\boldsymbol{\rho}_w$ and $\boldsymbol{\rho}_v$ are residual matrices associated with noise. Since these residuals are uncorrelated with $\widetilde{\boldsymbol{X}}_i$, solving Eq. (A10) in a least square sense results in an asymptotically unbiased estimate of the state matrices (as $j \rightarrow \infty$).

It should be recalled that the modal parameters of the system can be extracted by eigenvalue decomposition of $\widehat{\boldsymbol{A}}$.

If there is no external input in Eq. (A1), i.e. $\boldsymbol{u}_k = \boldsymbol{0}$, the identification is usually referred to as *stochastic subspace identification* (SSI), and a similar procedure to the one just showed can be implemented. Of course, only the $\widehat{\boldsymbol{A}}$ and $\widehat{\boldsymbol{C}}$ matrices will be estimated in this case, as no input is given.

Appendix B: Polynomial nonlinear state-space models

The polynomial nonlinear state-space (PNLSS) model is a quite recent black-box identification method proposed by Paduart et al. in 2010 [34]. It is a non-parametric method based on a multivariate polynomial nonlinear state-space representation of the system, obtained by optimizing the state-space matrices over the residuals between measured and simulated outputs. Given flexible nature of the model structure, the method suits a wide range of scenarios, such as a magnetorheological damper [34], a wet-clutch device [151] and hysteretic systems [152]. The method relies on the assumptions that the input signal is stationary and belongs to the family of Gaussian excitations, and that the considered system belongs to the class of Wiener systems. The latter in particular implies that the system responds with the same period of the excitation, which is not generally the case for nonlinear systems (e.g. in the case of chaotic behavior and bifurcations).

Considering a N DOFs nonlinear system, with output $\boldsymbol{y}(t)$ and forcing input $\boldsymbol{f}(t)$, a polynomial nonlinear state space model can be defined as:

$$\begin{cases} \boldsymbol{x}(\tau + 1) = \boldsymbol{A}\boldsymbol{x}(\tau) + \boldsymbol{B}\boldsymbol{f}(\tau) + \boldsymbol{E}\boldsymbol{\chi}(\tau) \\ \boldsymbol{y}(\tau) = \boldsymbol{C}\boldsymbol{x}(\tau) + \boldsymbol{D}\boldsymbol{f}(\tau) + \boldsymbol{F}\boldsymbol{\varphi}(\tau) \end{cases} \tag{B1}$$

where $\boldsymbol{x}$ is the state vector, τ is the sampled time, and the matrices $\boldsymbol{A}$, $\boldsymbol{B}$, $\boldsymbol{C}$, $\boldsymbol{D}$ are the classical state-space matrices. The vectors $\boldsymbol{\chi}(\tau)$ and $\boldsymbol{\varphi}(\tau)$ contain nonlinear monomials in $\boldsymbol{x}$ and $\boldsymbol{f}$ of degree up to a chosen value p. The coefficients associated to these nonlinear terms are given by the matrices $\boldsymbol{E}$ and $\boldsymbol{F}$. It is assumed that $\boldsymbol{f}(t)$ is a random-phase multisine signal [6], which is a periodic signal defined as a sum of harmonically related sine waves, where the phase is a realization of a zero-mean random process. Usually, the phase is uniformly distributed in the range $[0, 2\pi)$.

Eq. (B1) derives from the assumption that the nonlinear system can be modeled as the sum of a linear system plus a noise source y_s, representing the part of the system response that cannot be captured by the linear model. This is called *best linear approximation* (BLA) [6,153], and can be imagined as the *best* possible linear model of the considered nonlinear system, essentially corresponding to the linearization of the nonlinear system around its operating point. A parametrized expression for $\boldsymbol{G}^{BLA}$ can be eventually obtained by performing, for instance, the linear subspace identification on the nonlinear data set.

Once the BLA is computed, the algorithm is essentially an optimization of the full state-space model of Eq. (B1). The optimization is initialized with the linear matrices defining the BLA and with the monomials coefficients set to zero, i.e. $\boldsymbol{E} = \boldsymbol{F} = \boldsymbol{0}$. A weighted least squares cost function $\boldsymbol{V}^{id}$ is defined as:

$$\boldsymbol{V}^{id} = \sum_{k=1}^{N_f} \boldsymbol{\varepsilon}_k^{\mathrm{H}}(\boldsymbol{\theta}) \boldsymbol{W}_k \boldsymbol{\varepsilon}_k(\boldsymbol{\theta}) \tag{B2}$$

where k is the frequency line index up to N_f, $\boldsymbol{W}_k$ is a weighting matrix and $\boldsymbol{\varepsilon}_k$ is the error measure in the frequency domain:

$$\boldsymbol{\varepsilon}_k(\boldsymbol{\theta}) = \boldsymbol{Y}_k^{id}(\boldsymbol{\theta}) - \boldsymbol{Y}_k \tag{B3}$$

with $\boldsymbol{Y}_k^{id}(\boldsymbol{\theta})$ and $\boldsymbol{Y}_k$ modelled and measured output DFT spectra, respectively. The vector $\boldsymbol{\theta}$ contains all the parameters to be optimized, i.e. $\boldsymbol{\theta} = \mathrm{vec}(\boldsymbol{A}, \boldsymbol{B}, \boldsymbol{C}, \boldsymbol{D}, \boldsymbol{E}, \boldsymbol{F})$. The final set of matrices $\boldsymbol{A}$, $\boldsymbol{B}$, $\boldsymbol{C}$, $\boldsymbol{D}$, $\boldsymbol{E}$, $\boldsymbol{F}$ is eventually retrieved by minimizing the cost function $\boldsymbol{V}^{id}$ with a Levenberg-Marquardt optimization routine.

Recently, a Matlab [154] toolbox has been released to implement PNLSS, called PNLSS 1.0 [155]. This toolbox has been adopted throughout the thesis to compute the BLA and to perform the PNLSS algorithm in Chapter 5.

Differences between BLA and ULS

At a first glance, the nonlinear state-space models of NSI (Chapter 3) and PNLSS look quite similar: they both have a "linear" state-space model plus some other terms defining the nonlinear behavior. Nevertheless, the meaning of these two parts is completely different for the two methods.

The linear part in NSI defines the underlying-linear system (ULS), which represents the same system with the nonlinearity set to zero. In the theoretical case of no nonlinear modeling errors, the ULS is invariant with respect to the excitation level, as it preserves all the properties of linear systems.

Instead, PNLSS refers to the best linear approximation (BLA), which is the best possible linearization of the system around its operating point. Therefore,

the BLA depends on both excitation type and level. It is used as a starting point for the nonlinear optimization, but it does not give any information about the underlying linear behavior of the system.

An illustrative example is here considered. A Duffing oscillator is excited with a random-phase multisine [6] having an RMS of 5 N. A total of 5 realizations with 6 periods each and 65536 samples at 2048 Hz are simulated. The system parameters are reported in the numerical example of [53] and Newmark algorithm is used to numerically integrate the equation of motion. Also, 1% Gaussian noise is added to the response. The nonlinear FRF is depicted in Figure B1 in grey dots, while both BLA and ULS estimations are reported with continuous lines (orange and blue, respectively).
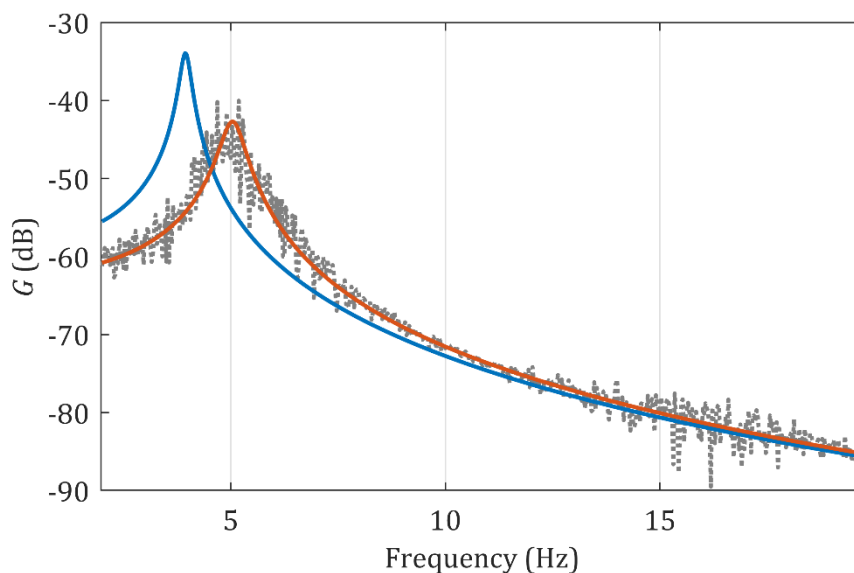
Figure B1: Difference between ULS and BLA for a Duffing oscillator. Grey dots: nonlinear FRF in dB scales (ref. 1 m/N); blue line: ULS estimation; orange line: BLA estimation.

It is clear that the ULS and the BLA represent two entirely different things, and so do the state-space models retrieved by NSI and PNLSS. Also, NSI is a grey-box method, due to the required knowledge of the nonlinear basis functions. PNLSS instead is a black-box method, providing a flexible model structure based on multivariate polynomials in the states and in the inputs. It is not fully "automatic" though, because the user must decide the degree of these polynomials. Based on the above considerations, a physical interpretation of the outcome of NSI is possible, as the description nonlinearity is indeed physically-based (friction, contacts, nonlinear springs, ...). The same cannot be generally stated for PNLSS, although work has been done to reduce the number nonlinear terms via polynomial decoupling [156].

Bibliography

[1]   S.H. Strogatz, R.F. Fox, Nonlinear Dynamics and Chaos: With Applications to Physics, Biology, Chemistry and Engineering, 2nd ed., CRC Press, 2018, https://doi.org/10.1201/9780429492563.

[2]   T. Butlin, J. Woodhouse, A.R. Champneys, The landscape of nonlinear structural dynamics: An introduction, Philosophical Transactions of the Royal Society A: Mathematical, Physical and Engineering Sciences, 373 (2015), https://doi.org/10.1098/rsta.2014.0400.

[3]   K. Worden, G.R. Tomlinson, Nonlinearity in Structural Dynamics, IOP Publishing, CRC Press, 2001, https://doi.org/10.1201/9780429138331.

[4]   C.R. Farrar, K. Worden, Structural Health Monitoring: A Machine Learning Perspective, John Wiley & Sons, 2012, https://doi.org/10.1002/9781118443118.

[5]   S.A. Billings, Nonlinear system identification: NARMAX methods in the time, frequency, and spatio-temporal domains, John Wiley & Sons, 2013, https://doi:10.1002/9781118535561.

[6]   J. Schoukens, M. Vaes, R. Pintelon, Linear System Identification in a Nonlinear Setting: Nonparametric Analysis of the Nonlinear Distortions and Their Impact on the Best Linear Approximation, IEEE Control Systems, 36 (2016) 38–69, https://doi.org/10.1109/MCS.2016.2535918.

[7]   T.K. Caughey, Equivalent Linearization Techniques, The Journal of the Acoustical Society of America, 35 (1963) 1706–1711, https://doi.org/10.1121/1.1918794.

[8]   A.H. Nayfeh, P.F. Pai, Linear and Nonlinear Structural Mechanics, 2005, John Wiley & Sons, https://doi.org/10.1002/9783527617562.

[9]   G. Kerschen, K. Worden, A.F. Vakakis, J.C. Golinval, Past, present and future of nonlinear system identification in structural dynamics, Mechanical Systems and Signal Processing, 20 (2006) 505–592, https://doi.org/10.1016/j.ymssp.2005.04.008.

[10]   P. Argoul, T.P. Le, Instantaneous indicators of structural behaviour based on the continuous Cauchy wavelet analysis, Mechanical Systems and Signal Processing, 17 (2003) 243–250, https://doi.org/10.1006/mssp.2002.1557.

[11]   G. Kerschen, V. Lenaerts, J.C. Golinval, Identification of a continuous structure with a geometrical non-linearity. Part I: Conditioned reverse path method, Journal of Sound and Vibration, 262 (2003) 889–906, https://doi.org/10.1016/S0022-460X(02)01151-3.

[12]   V. Lenaerts, G. Kerschen, J.C. Golinval, Identification of a continuous structure with a geometrical non-linearity. Part II: Proper orthogonal decomposition, Journal of Sound and Vibration, 262 (2003) 907–919, https://doi.org/10.1016/S0022-460X(02)01132-X.

[13]   S. Atluri, Nonlinear Vibrations of a Hinged Beam Including Nonlinear Inertia Effects, Journal of Applied Mechanics, 40 (1973) 121–126, https://doi.org/10.1115/1.3422909.

[14]   M. Rasekh, S.E. Khadem, Pull-in analysis of an electrostatically actuated nano-cantilever beam with nonlinearity in curvature and inertia, International Journal of Mechanical Sciences, 53 (2011) 108–115, https://doi.org/10.1016/j.ijmecsci.2010.11.007.

[15]   M. Liu, W.C. Tai, L. Zuo, Toward broadband vibration energy harvesting via mechanical motion-rectification induced inertia nonlinearity, Smart Materials and Structures, 27 (2018), https://doi.org/10.1088/1361-665X/aac238.

[16]   R. Singh, P. Davies, A.K. Bajaj, Identification of Nonlinear and Viscoelastic Properties of Flexible Polyurethane Foam, Nonlinear Dynamics, 34 (2003) 319–346, https://doi.org/10.1023/B:NODY.0000013511.07097.87.

[17]   C.M. Richards, R. Singh, Characterization of rubber isolator nonlinearities in the context of single- and multi-degree-of-freedom experimental systems, Journal of Sound and Vibration, 247 (2001) 807–834, https://doi.org/10.1006/jsvi.2001.3759.

[18]   M. Vaes, J. Schoukens, Y. Rolain, B. Peeters, J. Debille, T. Dossogne, J.P. Noël, C. Grappasonni, G. Kerschen, Nonlinear ground vibration identification of an F-16 aircraft part I: Fast nonparametric analysis of distortions in frf measurements, International Forum on Aeroelasticity and Structural Dynamics, IFASD 2015, 2015.

[19]   S. Marchesiello, L. Garibaldi, Identification of clearance-type nonlinearities, Mechanical Systems and Signal Processing, 22 (2008) 1133–1145, https://doi.org/10.1016/j.ymssp.2007.11.004.

[20]   A.H. Nayfeh, D.T. Mook, Nonlinear Oscillations, John Wiley & Sons,
         1995, https://doi.org/10.1002/9783527617586.

[21]   D.W. Jordan, P. Smith, Nonlinear Ordinary Differential Equations: An
         Introduction for Scientists and Engineers, 4th ed., Oxford University
         Press, New York, 2007.

[22]   I. Kovacic, M.J. Brennan, The Duffing Equation, John Wiley & Sons,
         Chichester, UK, 2011, https://doi.org/10.1002/9780470977859.

[23]   A.H. Nayfeh, B. Balachandran, Modal interactions in dynamical and
         structural systems, Applied Mechanics Reviews, 42 (1989) 175–201,
         https://doi.org/10.1115/1.3152389.

[24]   M. Ducceschi, C. Touzé, S. Bilbao, C.J. Webb, Nonlinear dynamics of
         rectangular plates: Investigation of modal interaction in free and
         forced vibrations, Acta Mechanica, 225 (2014) 213–232,
         https://doi.org/10.1007/s00707-013-0931-1.

[25]   C.I. VanDamme, B. Moldenhauer, M.S. Allen, J.J. Hollkamp, Computing
         nonlinear normal modes of aerospace structures using the multi-
         harmonic balance method, Conference Proceedings of the Society for
         Experimental Mechanics Series, (2019) 247–259,
         https://doi.org/10.1007/978-3-319-74280-9_26.

[26]   T. Detroux, L. Renson, L. Masset, G. Kerschen, The harmonic balance
         method for bifurcation analysis of large-scale nonlinear mechanical
         systems, Computer Methods in Applied Mechanics and Engineering,
         296 (2015) 18–38, https://doi.org/10.1016/j.cma.2015.07.017.

[27]   M. Claeys, J.J. Sinou, J.P. Lambelin, R. Todeschini, Modal interactions
         due to friction in the nonlinear vibration response of the "Harmony"
         test structure: Experiments and simulations, Journal of Sound and
         Vibration, 376 (2016) 131–148,
         https://doi.org/10.1016/j.jsv.2016.04.008.

[28]   G. Von Groll, D.J. Ewins, The harmonic balance method with arc-
         length continuation in rotor/stator contact problems, Journal of
         Sound and Vibration, 241 (2001) 223–233,
         https://doi.org/10.1006/jsvi.2000.3298.

[29]   N.M. Newmark, A Method of Computation for Structural Dynamics,
         Journal of the Engineering Mechanics Division, 85 (1959) 67–94.

[30]   T. Detroux, Performance and Robustness of Nonlinear Systems Using
         Bifurcation Analysis, University of Liège, 2016,
         https://orbi.uliege.be/handle/2268/195883.

[31]   L. Peletan, S. Baguet, M. Torkhani, G. Jacquet-Richardet, A comparison of stability computational methods for periodic solution of nonlinear problems with application to rotordynamics, Nonlinear Dynamics, 72 (2013) 671–682, https://doi.org/10.1007/s11071-012-0744-0.

[32]   F.C. Moon, P.J. Holmes, A magnetoelastic strange attractor, Journal of Sound and Vibration, 65 (1979) 275–296, https://doi.org/10.1016/0022-460X(79)90520-0.

[33]   J. Schoukens, R. Pintelon, E. Van Der Ouderaa, J. Renneboog, Survey of Excitation Signals for FFT Based Signal Analyzers, IEEE Transactions on Instrumentation and Measurement, 37 (1988) 342–352, https://doi.org/10.1109/19.7453.

[34]   J. Paduart, L. Lauwers, J. Swevers, K. Smolders, J. Schoukens, R. Pintelon, Identification of nonlinear systems using Polynomial Nonlinear State Space models, Automatica, 46 (2010) 647–656, https://doi.org/10.1016/j.automatica.2010.01.001.

[35]   L. Ljung, System Identification: Theory for the User, 2nd ed., Prentice Hall, Upper Saddle River, NJ, 1999.

[36]   L. Ljung, Perspectives on system identification, Annual Reviews in Control, 34 (2010) 1–12, https://doi.org/10.1103/PhysRevE.59.3958.

[37]   J.P. Noël, G. Kerschen, Nonlinear system identification in structural dynamics: 10 more years of progress, Mechanical Systems and Signal Processing, 83 (2017) 2–35, https://doi.org/10.1016/j.ymssp.2016.07.020.

[38]   S.F. Masri, T.K. Caughey, A Nonparametric Identification Technique for Nonlinear Dynamic Problems, Journal of Applied Mechanics, 46 (1979) 433–447, https://doi.org/10.1115/1.3424568.

[39]   E.F. Crawley, K.J. O'donnell, Force-state mapping identification of nonlinear joints, AIAA Journal, 25 (1987) 1003–1010, https://doi.org/10.2514/3.9733.

[40]   K. Worden, Data processing and experiment design for the restoring force surface method, part I: integration and differentiation of measured time data, Mechanical Systems and Signal Processing, 4 (1990) 295–319, https://doi.org/10.1016/0888-3270(90)90010-I.

[41]   K. Worden, Data processing and experiment design for the restoring force surface method, part II: Choice of excitation signal, Mechanical Systems and Signal Processing, 4 (1990) 321–344, https://doi.org/10.1016/0888-3270(90)90011-9.

[42]   W.-J. Kimm, Y. Park, Non-linear joint parameter identification by applying the force-state mapping technique in the frequency domain, Mechanical Systems and Signal Processing, 8 (1994) 519–529, https://doi.org/10.1006/mssp.1994.1037.

[43]   G. Kerschen, J.C. Golinval, K. Worden, Theoretical and experimental identification of a non-linear beam, Journal of Sound and Vibration, 244 (2001) 597–613, https://doi.org/10.1006/jsvi.2000.3490.

[44]   T. Dossogne, J.P. Noël, C. Grappasonni, G. Kershen, B. Peeters, J. Bebille, M. Vaes, J. Schoukens, Nonlinear Ground Vibration Identification of an F-16 Aircraft - Part II Understanding Nonlinear Behaviour in Aerospace Structures Using Sine- sweep Testing, International Forum on Aeroelasticity and Structural Dynamics, 2015.

[45]   I.J. Leontaritis, S.A. Billings, Input-output parametric models for non-linear systems Part II: Stochastic non-linear systems, International Journal of Control, 41 (1985) 329–344, https://doi.org/10.1080/0020718508961130.

[46]   S.A. Billings, H.B. Jamaluddin, S. Chen, Properties of neural networks with applications to modelling non-linear dynamical systems, International Journal of Control, 55 (1992) 193–224, https://doi.org/10.1080/00207179208934232.

[47]   H.J. Rice, J.A. Fitzpatrick, A generalised technique for spectral analysis of non-linear systems, Mechanical Systems and Signal Processing, 2 (1988) 195–207, https://doi.org/10.1016/0888-3270(88)90043-X.

[48]   H.J. Rice, J.A. Fitzpatrick, A procedure for the identification of linear and non-linear multi-degree-of-freedom systems, Journal of Sound and Vibration, 149 (1991) 397–411, https://doi.org/10.1016/0022-460X(91)90444-O.

[49]   C.M. Richards, R. Singh, Identification of multi-degree-of-freedom non-linear systems under random excitations by the "reverse path" spectral method, Journal of Sound and Vibration, 213 (1998) 673–708, https://doi.org/10.1006/jsvi.1998.1522.

[50]   S. Marchesiello, Application of the conditioned reverse path method, Mechanical Systems and Signal Processing, 17 (2003) 183–188, https://doi.org/10.1006/mssp.2002.1554.

[51] P. Muhamad, N.D. Sims, K. Worden, On the orthogonalised reverse path method for nonlinear system identification, Journal of Sound and Vibration, 331 (2012) 4488–4503, https://doi.org/10.1016/j.jsv.2012.04.034.

[52] D.E.E. Adams, R.J.J. Allemang, Frequency domain method for estimating the parameters of a non-linear structural dynamic model through feedback, Mechanical Systems and Signal Processing, 14 (2000) 637–656, https://doi.org/10.1006/mssp.2000.1292.

[53] S. Marchesiello, L. Garibaldi, A time domain approach for identifying nonlinear vibrating structures by subspace methods, Mechanical Systems and Signal Processing, 22 (2008) 81–101, https://doi.org/10.1016/j.ymssp.2007.04.002.

[54] J.P. Noël, G. Kerschen, Frequency-domain subspace identification for nonlinear mechanical systems, Mechanical Systems and Signal Processing, 40 (2013) 701–717, https://doi.org/10.1016/j.ymssp.2013.06.034.

[55] M. Peeters, G. Kerschen, J.C. Golinval, Dynamic testing of nonlinear vibrating structures using nonlinear normal modes, Journal of Sound and Vibration, 330 (2011) 486–509, https://doi.org/10.1016/j.jsv.2010.08.028.

[56] S.W. Shaw, C. Pierre, Normal Modes for Non-Linear Vibratory Systems, Journal of Sound and Vibration, 164 (1993) 85–124, https://doi.org/10.1006/jsvi.1993.1198.

[57] P.L. Green, Bayesian system identification of a nonlinear dynamical system using a novel variant of Simulated Annealing, Mechanical Systems and Signal Processing, 52–53 (2015) 133–146, https://doi.org/10.1016/j.ymssp.2014.07.010.

[58] P.L. Green, K. Worden, Bayesian and Markov chain Monte Carlo methods for identifying nonlinear systems in the presence of uncertainty, Philosophical Transactions of the Royal Society A: Mathematical, Physical and Engineering Sciences, 373 (2015), https://doi.org/10.1098/rsta.2014.0405.

[59] J.P. Noël, S. Marchesiello, G. Kerschen, Subspace-based identification of a nonlinear spacecraft in the time and frequency domains, Mechanical Systems and Signal Processing, 43 (2014) 217–236, https://doi.org/10.1016/j.ymssp.2013.10.016.

[60] P. Van Overschee, B. De Moor, Subspace Identification for Linear Systems, Springer US, 1996, https://doi.org/10.1007/978-1-4613-0465-4.

[61]   T. McKelvey, H. Akçay, L. Ljung, Subspace-based multivariable
         system identification from frequency response data, IEEE
         Transactions on Automatic Control, 41 (1996) 960–979,
         https://doi.org/10.1109/9.508900.

[62]   B. Peeters, G. De Roeck, Stochastic System Identification for
         Operational Modal Analysis: A Review, Journal of Dynamic Systems,
         Measurement, and Control, 123 (2001) 659,
         https://doi.org/10.1115/1.1410370.

[63]   W. Heylen, S. Lammens, P. Sas, Modal Analysis Theory and Testing,
         Department of Mechanical Engineering, Katholieke Universiteit
         Leuven, Leuven, Belgium, 1997.

[64]   R.J. Allemang, D.L. Brown, A correlation coefficient for modal vector
         analysis, Proceedings of the First International Modal Analysis
         Conference, 1982 110–116.

[65]   S. Marchesiello, A. Fasana, L. Garibaldi, Modal contributions and
         effects of spurious poles in nonlinear subspace identification,
         Mechanical Systems and Signal Processing, 74 (2016) 111–132,
         https://doi.org/10.1016/j.ymssp.2015.05.008.

[66]   G. De Filippis, J.P. Noël, G. Kerschen, L. Soria, C. Stephan, Model
         reduction and frequency residuals for a robust estimation of
         nonlinearities in subspace identification, Mechanical Systems and
         Signal Processing, 93 (2017) 312–331,
         https://doi.org/10.1016/j.ymssp.2017.01.020.

[67]   D. Lisitano, S. Jiffri, E. Bonisoli, J.E. Mottershead, Experimental
         feedback linearisation of a vibrating system with a non-smooth
         nonlinearity, Journal of Sound and Vibration, 416 (2018) 192–212,
         https://doi.org/10.1016/j.jsv.2017.11.047.

[68]   D. Lisitano, S. Jiffri, E. Bonisoli, J.E. Mottershead, Experimental
         feedback linearisation of a non-smooth nonlinear system by the
         method of receptances, Mathematics and Mechanics of Solids, 0
         (2018) 1–18, https://doi.org/10.1177/1081286517744601.

[69]   D. Lisitano, E. Bonisoli, J.E. Mottershead, Experimental direct spatial
         damping identification by the Stabilised Layers Method, Journal of
         Sound and Vibration, 437 (2018) 325–339,
         https://doi.org/10.1016/j.jsv.2018.08.055.

[70]   M. Haroon, D.E. Adams, Y.W. Luk, A.A. Ferri, A time and frequency domain approach for identifying nonlinear mechanical system models in the absence of an input measurement, Journal of Sound and Vibration, 283 (2005) 1137–1155, https://doi.org/10.1016/j.jsv.2004.06.008.

[71]   J. Iwaniec, Output-Only Technique for Parameter Identification of Nonlinear Systems Working under Operational Loads, Key Engineering Materials, 347 (2007) 467–472, https://doi.org/10.4028/www.scientific.net/KEM.347.467.

[72]   K.S. Mohammad, K. Worden, G.R. Tomlinson, Direct parameter estimation for linear and non-linear structures, Journal of Sound and Vibration ,152 (1992) 471–499, https://doi.org/10.1016/0022-460X(92)90482-D.

[73]   E. Reynders, G. Wursten, G. De Roeck, Output-only structural health monitoring in changing environmental conditions by means of nonlinear system identification, Structural Health Monitoring, 13 (2014) 82–93, https://doi.org/10.1177/1475921713502836.

[74]   D. Anastasio, S. Marchesiello, Free-Decay Nonlinear System Identification via Mass-Change Scheme, Shock and Vibration, 2019 (2019) 1–14, https://doi.org/10.1155/2019/1759198.

[75]   E. Parloo, P. Verboven, P. Guillaume, M. Van Overmeire, Sensitivity-based operational mode shape normalisation, Mechanical Systems and Signal Processing, 16 (2002) 757–767, https://doi.org/10.1006/mssp.2002.1498.

[76]   D. Bernal, Modal Scaling from Known Mass Perturbations, Journal of Engineering Mechanics, 130 (2004) 1083–1088, https://doi.org/10.1061/(asce)0733-9399(2004)130:9(1083).

[77]   M. López-Aenlle, R. Brincker, F. Pelayo, A.F. Canteli, On exact and approximated formulations for scaling-mode shapes in operational modal analysis by mass and stiffness change, Journal of Sound and Vibration, 331 (2012) 622–637, https://doi.org/10.1016/j.jsv.2011.09.017.

[78]   R. Brincker, J. Rodrigues, P. Andersen, Scaling the Mode Shapes of a Building Model by Mass Changes, International Modal Analysis Conference (IMAC) - 26-29 January 2004, 2004.

[79] H. Shahverdi, C. Mares, J.E. Mottershead, Model structure correction and updating of aeroengine casings using fictitious mass modifications, Proceedings of the Institution of Mechanical Engineers, Part C: Journal of Mechanical Engineering Science, 219 (2005) 19–30, https://doi.org/10.1243/095440605X8342.

[80] G. Gatti, M.J. Brennan, I. Kovacic, On the interaction of the responses at the resonance frequencies of a nonlinear two degrees-of-freedom system, Physica D: Nonlinear Phenomena, 239 (2010) 591–599, https://doi.org/10.1016/j.physd.2010.01.006.

[81] D. Anastasio, A. Fasana, L. Garibaldi, S. Marchesiello, Analytical investigation of railway overhead contact wire dynamics and comparison with experimental results, Mechanical Systems and Signal Processing, 116 (2019) 277–292, https://doi.org/10.1016/j.ymssp.2018.06.021.

[82] Advisory Council for Aviation Research and Innovation in Europe, ACARE, Flightpath 2050 - Europe's vision for aviation, 2011, https://doi.org/10.2777/50266.

[83] F. Wenneker, P. Tiso, A substructuring method for geometrically nonlinear structures, Conference Proceedings of the Society for Experimental Mechanics Series, 1 (2014) 157–165, https://doi.org/10.1007/978-3-319-04501-6_14.

[84] M. Amabili, M.P. Païdoussis, Review of studies on geometrically nonlinear vibrations and dynamics of circular cylindrical shells and panels, with and without fluid-structure interaction, Applied Mechanics Reviews, 56 (2003) 349, https://doi.org/10.1115/1.1565084.

[85] M. Sathyamoorthy, Nonlinear analysis of structures, CRC Press, New York, 1998.

[86] C. Touzé, O. Thomas, A. Huberdeau, Asymptotic non-linear normal modes for large-amplitude vibrations of continuous structures, Computers and Structures, 82 (2004) 2671–2682, https://doi.org/10.1016/j.compstruc.2004.09.003.

[87] C.S.M. Sombroek, P. Tiso, L. Renson, G. Kerschen, Numerical computation of nonlinear normal modes in a modal derivative subspace, Computers and Structures, 195 (2018) 34–46, https://doi.org/10.1016/j.compstruc.2017.08.016.

[88]   M. Claeys, J.J. Sinou, J.P. Lambelin, B. Alcoverro, Multi-harmonic
        measurements and numerical simulations of nonlinear vibrations of
        a beam with non-ideal boundary conditions, Communications in
        Nonlinear Science and Numerical Simulation, 19 (2014) 4196–4212,
        https://doi.org/10.1016/j.cnsns.2014.04.008.

[89]   X. Wang, T.L. Hill, S.A. Neild, Frequency response expansion strategy
        for nonlinear structures, Mechanical Systems and Signal Processing,
        116 (2019) 505–529, https://doi.org/10.1016/j.ymssp.2018.06.027.

[90]   D. Piombino, M.S.M.S. Allen, D. Ehrhardt, T. Beberniss, J.J. Hollkamp,
        System Identification to Estimate the Nonlinear Modes of a Gong,
        Conference Proceedings of the Society for Experimental Mechanics
        Series, 1 (2019) 121–136, https://doi.org/10.1007/978-3-319-
        74280-9_10.

[91]   D. Anastasio, S. Marchesiello, G. Kerschen, J.P. Noël, Experimental
        identification of distributed nonlinearities in the modal domain,
        Journal of Sound and Vibration, 458 (2019) 426–444,
        https://doi.org/10.1016/j.jsv.2019.07.005.

[92]   ANSYS, Theory Reference for ANSYS Mechanical APDL, ANSYS Inc.,
        2013, www.ansys.com.

[93]   D. Anastasio, J. Dietrich, J.P. Noël, G. Kerschen, S. Marchesiello, J.
        Häfele, C.G. Gebhardt, R. Rolfes, Dynamics of Geometrically-Nonlinear
        Beam Structures, Part 1: Numerical Modeling, G. Kerschen, M.R.W.
        Brake, L. Renson (Eds.), Nonlinear Structures and Systems, Volume 1,
        Springer International Publishing, Cham, 2020 213–216.

[94]   L. Meirovitch, Principles and techniques of vibrations, Prentice Hall,
        1997.

[95]   S. Jain, P. Tiso, J.B. Rutzmoser, D.J. Rixen, A quadratic manifold for
        model order reduction of nonlinear structural dynamics, Computers
        and Structures, 188 (2017) 80–94,
        https://doi.org/10.1016/j.compstruc.2017.04.005.

[96]   P.F. Pai, A.H. Nayfeh, Non-linear non-planar oscillations of a
        cantilever beam under lateral base excitations, International Journal
        of Non-Linear Mechanics, 25 (1990) 455–474,
        https://doi.org/10.1016/0020-7462(90)90012-X.

[97]   A.Y.T. Leung, S.G. Mao, A symplectic Galerkin method for non-linear
        vibration of beams and plates, Journal of Sound and Vibration, 183
        (1995) 475–491, https://doi.org/10.1006/jsvi.1995.0266.

[98]   A.H. Nayfeh, R.A. Ibrahim, Nonlinear Interactions: Analytical, Computational, and Experimental Methods, Applied Mechanics Reviews, 54 (2001) B60–B61, https://doi.org/10.1115/1.1383674.

[99]   G. Kerschen, M. Peeters, J.C. Golinval, A.F. Vakakis, Nonlinear normal modes, Part I: A useful framework for the structural dynamicist, Mechanical Systems and Signal Processing, 23 (2009) 170–194, https://doi.org/10.1016/j.ymssp.2008.04.002.

[100]   M. Peeters, R. Viguié, G. Sérandour, G. Kerschen, J.C. Golinval, Nonlinear normal modes, Part II: Toward a practical computation using numerical continuation techniques, Mechanical Systems and Signal Processing, 23 (2009) 195–216, https://doi.org/10.1016/j.ymssp.2008.04.003.

[101]   K. Deb, Multi-objective Optimisation Using Evolutionary Algorithms: An Introduction, Multi-Objective Evolutionary Optimisation for Product Design and Manufacturing, Springer London, 2011, https://doi.org/10.1007/978-0-85729-652-8_1.

[102]   M. Feldman, Hilbert transform in vibration analysis, Mechanical Systems and Signal Processing, 25 (2011) 735–802, https://doi.org/10.1016/j.ymssp.2010.07.018.

[103]   J.P. Massat, T.M.L. Nguyen-Tajan, H. Maitournam, E. Balmès, Fatigue analysis of catenary contact wires for high speed trains, 9th World Congress on Railway Research, Lille, 2011 1–11.

[104]   European Committee for Electrotechnical Standardization, EN 50317. Railway applications - Current collection systems - Requirements for and validation of measurements of the dynamic interaction between pantograph and overhead contact line, 2012.

[105]   European Committee for Electrotechnical Standardization, EN50367. Railway applications — Current collection systems — Technical criteria for the interaction between pantograph and overhead line, 2012.

[106]   European Commission, Commission Regulation (EU) No 1303/2014 of 18 November 2014 concerning the technical specification for interoperability relating to 'safety in railway tunnels' of the rail system of the European Union, Official Journal of the European Union, 57 (2014) 394–420.

[107]   J. Ambrósio, J. Pombo, M. Pereira, P. Antunes, A. Mósca, J. Pombo, A. Mósca, M. Pereira, A computational procedure for the dynamic analysis of the catenary-pantograph interaction in high-speed trains, Journal of Theoretical and Applied Mechanics, 50 (2012) 681–699. http://www.ptmts.org.pl/jtam/index.php/jtam/article/view/v50n3 p681.

[108]   S. Bruni, G. Bucca, M. Carnevale, A. Collina, A. Facchinetti, Pantograph–catenary interaction: recent achievements and future research challenges, International Journal of Rail Transportation, 6 (2018) 57–82, https://doi.org/10.1080/23248378.2017.1400156.

[109]   T. Dahlberg, Moving force on an axially loaded beam - With applications to a railway overhead contact wire, Vehicle System Dynamics, 44 (2006) 631–644, https://doi.org/10.1080/00423110500165523.

[110]   S. Bruni, J. Ambrosio, A. Carnicero, Y.H. Cho, L. Finner, M. Ikeda, S.Y. Kwon, J.P. Massat, S. Stichel, M. Tur, W. Zhang, The results of the pantograph-catenary interaction benchmark, Vehicle System Dynamics, 53 (2015) 412–435, https://doi.org/10.1080/00423114.2014.953183.

[111]   UIC, High speed lines in the world, https://uic.org/IMG/pdf/20190328_high_speed_lines_in_the_world. pdf (accessed September 23, 2019).

[112]   R. Nunno, High Speed Rail Development Worldwide, 2018, https://www.eesi.org/papers/view/fact-sheet-high-speed-rail-development-worldwide.

[113]   BBC, French set new rail speed record, http://news.bbc.co.uk/2/hi/6521295.stm (accessed September 23, 2019).

[114]   Wikipedia, TGV world speed record, https://en.wikipedia.org/wiki/TGV_world_speed_record (accessed September 23, 2019).

[115]   F. Pupke, Optimization and development of contact wire for high speed lines, 8th World Congress on Railway Research, Seoul, 2008.

[116]   European Court of Auditors, A European high-speed rail network: not a reality but an ineffective patchwork, 2018, http://publications.europa.eu/webpub/eca/special-reports/high-speed-rail-19-2018/en/.

[117] J. Erik, I. Trabo, A. Landex, O. Anker Nielsen, J. Erik Schneider-Tilli, Cost benchmarking of railway projects in Europe – can it help to reduce costs?, International Seminar on Railway Operations Modelling and Analysis, Copenhagen, 2013.

[118] G. Bucca, A. Collina, A procedure for the wear prediction of collector strip and contact wire in pantograph-catenary system, Wear, 266 (2009) 46–59, https://doi.org/10.1016/j.wear.2008.05.006.

[119] Z. Liu, S. Stichel, A. Rønnquist, Application of tuned-mass system on railway catenary to improve dynamic performance, Engineering Structures, 165 (2018) 349–358, https://doi.org/10.1016/j.engstruct.2018.03.060.

[120] Z. Liu, P.A. Jönsson, S. Stichel, A. Rønnquist, On the implementation of an auxiliary pantograph for speed increase on existing lines, Vehicle System Dynamics, 54 (2016) 1077–1097, https://doi.org/10.1080/00423114.2016.1187278.

[121] J. Pombo, J. Ambrósio, M. Pereira, Influence of pantograph components on the contact quality of the overhead system for high speed trains, 10th International Conference on Computational Structures Technology, Valencia, 2010, https://doi.org/10.4203/ccp.93.1.

[122] W. Wang, Y. Liang, W. Zhang, S. Iwnicki, Effect of the nonlinear displacement-dependent characteristics of a hydraulic damper on high-speed rail pantograph dynamics, Nonlinear Dynamics, 95 (2019) 3439–3464, https://doi.org/10.1007/s11071-019-04766-4.

[123] P. Nåvik, A. Rønnquist, S. Stichel, Identification of system damping in railway catenary wire systems from full-scale measurements, Engineering Structures, 113 (2016) 71–78, https://doi.org/10.1016/j.engstruct.2016.01.031.

[124] Y.H. Cho, J.M. Lee, S.Y. Park, E.S. Lee, Robust Measurement of Damping Ratios of a Railway Contact Wire Using Wavelet Transforms, Key Engineering Materials, 321–323 (2006) 1629–1635, https://doi.org/10.4028/www.scientific.net/KEM.321-323.1629.

[125] B. Villen, Progettazione di uno smorzatore per cavi tesi, Politecnico di Torino, 2017.

[126] L. Dellavalle, Progettazione di un dispositivo per lo smorzamento dei cavi tesi, Politecnico di Torino, 2017.

[127] D. Lucio, Progettazione di un dispositivo per lo smorzamento di cavi tesi e misure sperimentali, Politecnico di Torino, 2018. https://webthesis.biblio.polito.it/7103/.

[128]   R.S. Lakes, Extreme Damping in Composite Materials with a Negative Stiffness Phase, Physical Review Letters, 86 (2001) 2897–2900, https://doi.org/10.1103/PhysRevLett.86.2897.

[129]   I. Antoniadis, D. Chronopoulos, V. Spitas, D. Koulocheris, Hyper-damping properties of a stiff and stable linear oscillator with a negative stiffness element, Journal of Sound and Vibration, 346 (2015) 37–52, https://doi.org/10.1016/j.jsv.2015.02.028.

[130]   C.M. Lee, V.N. Goverdovskiy, A.I. Temnikov, Design of springs with "negative" stiffness to improve vehicle driver vibration isolation, Journal of Sound and Vibration, 302 (2007) 865–874, https://doi.org/10.1016/j.jsv.2006.12.024.

[131]   T.D. Le, K.K. Ahn, A vibration isolation system in low frequency excitation region using negative stiffness structure for vehicle seat, Journal of Sound and Vibration, 330 (2011) 6311–6335, https://doi.org/10.1016/j.jsv.2011.07.039.

[132]   H. Iemura, M.H. Pradono, Advances in the development of pseudo-negative-stiffness dampers for seismic response control, Structural Control and Health Monitoring, 16 (2009) 784–799, https://doi.org/10.1002/stc.345.

[133]   A.A. Sarlis, D.T.R. Pasala, M.C. Constantinou, A.M. Reinhorn, S. Nagarajaiah, D.P. Taylor, Negative Stiffness Device for Seismic Protection of Structures, Journal of Structural Engineering, 139 (2013) 1124–1133, https://doi.org/10.1061/(ASCE)ST.1943-541X.0000616.

[134]   A. Carrella, M.J. Brennan, T.P. Waters, Static analysis of a passive vibration isolator with quasi-zero-stiffness characteristic, Journal of Sound and Vibration, 301 (2007) 678–689, https://doi.org/10.1016/j.jsv.2006.10.011.

[135]   D. Anastasio, Studio dell'interazione dinamica tra pantografo e catenaria tramite l'implementazione di un modello non lineare agli elementi finiti, Politecnico di Torino, 2016.

[136]   A. Wolf, J.B. Swift, H.L. Swinney, J.A. Vastano, Determining Lyapunov exponents from a time series, Physica D: Nonlinear Phenomena, 16 (1985) 285–317, https://doi.org/10.1016/0167-2789(85)90011-9.

[137]   F.C. Moon, Experiments on Chaotic Motions of a Forced Nonlinear Oscillator: Strange Attractors, Journal of Applied Mechanics, 47 (1980) 638, https://doi.org/10.1115/1.3153746.

[138]   A. Strauss, Development of numerical models for the dynamic analysis of pantograph-catenary interaction, Politecnico di Torino, 2014.

[139]   J. Chung, G.M. Hulbert, A Time Integration Algorithm for Structural Dynamics With Improved Numerical Dissipation: The Generalized-α Method, Journal of Applied Mechanics, 60 (1993) 371–375, https://doi.org/10.1115/1.2900803.

[140]   K.J. Bathe, G. Noh, Insight into an implicit time integration scheme for structural dynamics, Computers and Structures, 98–99 (2012) 1–6, https://doi.org/10.1016/j.compstruc.2012.01.009.

[141]   S. Sorrentino, D. Anastasio, A. Fasana, S. Marchesiello, Distributed parameter and finite element models for wave propagation in railway contact lines, Journal of Sound and Vibration, 410 (2017) 1–18, https://doi.org/10.1016/j.jsv.2017.08.008.

[142]   European Committee for Electrotechnical Standardization, EN50318. Railway application - Current collection systems - Validation of simulation of the dynamic interaction between pantograph and overhead contact line, 2002.

[143]   C.J. Cho, Y. Park, New Monitoring Technologies for Overhead Contact Line at 400 km·h−1, Engineering, 2 (2016) 360–365, https://doi.org/10.1016/J.ENG.2016.03.016.

[144]   Y.H. Cho, K. Lee, Y. Park, B. Kang, K.N. Kim, Influence of contact wire pre-sag on the dynamics of pantographrailway catenary, International Journal of Mechanical Sciences, 52 (2010) 1471–1490, https://doi.org/10.1016/j.ijmecsci.2010.04.002.

[145]   J.P. Noël, L. Renson, C. Grappasonni, G. Kerschen, Identification of nonlinear normal modes of engineering structures under broadband forcing, Mechanical Systems and Signal Processing, 74 (2016) 95–110, https://doi:10.1016/j.ymssp.2015.04.016.

[146]   P.M.A. Slaats, J. de Jongh, A.A.H.J. Sauren, Model reduction tools for nonlinear structural dynamics, Computers & Structures, 54 (1995) 1155–1171, https://doi:10.1016/0045-7949(94)00389-K.

[147]   Nolysis, University of Liège, http://www.nolisys.com (accessed November 28, 2019).

[148]   M. Amabili, Nonlinear damping in nonlinear vibrations of rectangular plates: Derivation from viscoelasticity and experimental validation, Journal of the Mechanics and Physics of Solids, 118 (2018) 275–292, https://doi:10.1016/j.jmps.2018.06.004.

[149]   E. Reynders, R. Pintelon, G. De Roeck, Uncertainty bounds on modal
         parameters obtained from stochastic subspace identification,
         Mechanical Systems and Signal Processing, 22 (2008) 948–969.
         https://doi:10.1016/j.ymssp.2007.10.009.

[150]   K. De Cock, B. De Moor, Subspace identification methods, Control
         systems, robotics and automation - Vol. V, EOLSS Publications, 2009.

[151]   W.D. Widanage, J. Stoev, A. Van Mulders, J. Schoukens, G. Pinte,
         Nonlinear system-identification of the filling phase of a wet-clutch
         system, Control Engineering Practice, 19 (2011) 1506-1516,
         https://doi.org/10.1016/j.conengprac.2011.09.002.

[152]   J.P. Noël, A.F. Esfahani, G. Kerschen, J. Schoukens, A nonlinear state-
         space approach to hysteresis identification, Mechanical Systems and
         Signal Processing, 84 (2017) 171–184,
         https://doi.org/10.1016/j.ymssp.2016.08.025.

[153]   R. Pintelon, J. Schoukens, System identification: a frequency domain
         approach, John Wiley & Sons, 2001.

[154]   MATLAB (R2019b), The MathWorks Inc., Natick, Massachusetts,
         2019.

[155]   K. Tiels, PNLSS 1.0: A polynomial nonlinear state-space toolbox for
         Matlab®, http://homepages.vub.ac.be/~ktiels/pnlss.html (accessed
         July 30, 2019).

[156]   A.F. Esfahani, P. Dreesen, K. Tiels, J.P. Noël, J. Schoukens, Polynomial
         State-Space Model Decoupling for the Identification of Hysteretic
         Systems, IFAC-PapersOnLine, 50 (2017) 458–463,
         https://doi.org/10.1016/j.ifacol.2017.08.082.